Technische Universität München

TUM School of Engineering and Design

A material model for the compaction process simulation of carbon fiber preforms

Dennis Bublitz

Technische Universität München
TUM School of Engineering and Design
Lehrstuhl für Carbon Composites
Boltzmannstraße 15
D-85748 Garching bei München

Tel.:   +49 (0) 89 / 289 – 15092
Fax.:   +49 (0) 89 / 289 – 15097
Email: info.lcc@ed.tum.de
Web: www.asg.ed.tum.de/lcc

ACKNOWLEDGMENTS

KURZFASSUNG

Stetig steigende Kraftstoffpreise und ein wachsender Druck zur Einsparung von klimaschädlichen Gasen führen besonders in der Luft- und Raumfahrtindustrie zu einem vermehrten Einsatz von Leichtbaustrukturen. Kohlenstofffaserverstärkte Kunststoffe bieten aufgrund ihrer hervorragenden gewichtsspezifischen mechanischen Eigenschaften ein besonders großes Leichtbaupotenzial und werden in modernen Flugzeugen zunehmend eingesetzt. Neben der Verarbeitung von vorimprägnierten Halbzeugen, sogenannten Prepregs, sind Harzinjektionsprozesse eine der am weitesten verbreiteten Methoden zur Herstellung von Composite Bauteilen. Obwohl diese Verfahren einige Vorteile bieten, bringen sie aufgrund prozessbedingter Defekte Nachteile mit sich, wie zum Beispiel Reinharzgebiete in engen Radien, Trockenstellen oder große prozessinduzierte Verformungen. Diese Defekte lassen sich oft auf Faservolumengehaltgradienten zurückführen, die aus einer ungleichmäßigen Kompaktierung beim Schließen des Werkzeugs resultieren.

In dieser Dissertation wurde eine Kompaktierungsprozesssimulation für trockene Carbonfaservorformlinge, auch Preforms genannt, mit einem orthotropen nichtlinearen Materialmodell entwickelt, die es ermöglicht, die oben genannten Defekte vorherzusagen. Zuerst wurden die verwendeten Materialen mit Experimenten charakterisiert und eine neue Testmethode für die Schubsteifigkeit in Dickenrichtung erarbeitet. Mit den gewonnenen Daten wurde ein Kompaktierungsmodell für die Vorhersage des zeitabhängigen Verhaltens in Dickenrichtung entwickelt und validiert. Darüber hinaus wurde gezeigt, dass mit dem Modell durch Anpassung des Schließprozesses die erforderliche Schließkraft bei gleichem finalen Faservolumengehalt um 50% reduziert werden kann.

Anschließend wurde das Kompaktierungsmodell um die Verformungszustände in den verbleibenden Richtungen wie der Scherung in Dickenrichtung erweitert. Das kalibrierte Modell zeigt eine hervorragende Übereinstimmung mit den experimentellen Ergebnissen aus Kompaktierungsversuchen mit engen Werkzeugradien. Die Schließkräfte aus der Simulation stimmen für unterschiedliche Radien und Faservolumengehalte sehr gut mit den Werten der Versuche überein. Auch die sich einstellende Geometrie der Preform aufgrund von Kompaktierung, Scherung und Reibung ist in guter Übereinstimmung für kraft- und weggesteuerte Versuche. Das validierte Modell wurde anschließend für eine virtuelle Studie von Preform- und Werkzeugeigenschaften genutzt. Es konnte gezeigt werden, dass besonders dicke Preforms und solche mit hohem Faservolumengehalt zu einem hohen Risiko von Reinharzgebieten im Radius führen. Weitere Erkenntnisse aus der Studie wurden in Designrichtlinien für Kompaktierungsprozesse zusammengefasst.

Mit der entwickelten Kopplung der Ergebnisse aus der Kompaktierungs- zur Füllsimulation wurde gezeigt, dass die Berücksichtigung der Kompaktierungsergebnisse

einen entscheidenden Einfluss auf die Bauteilfüllung hat. Das entwickelte Simulationsmodell kann angewandt werden, um Kompaktierungsdefekte zu vermeiden und die Bauteilqualität zu verbessern. Die Erkenntnisse aus der Parameterstudie liefern wertvolle Richtlinien in frühen Entwicklungsstadien ohne zeitaufwändige Simulationen verwenden zu müssen. Mit der Anwendung auf komplexere Geometrien und weitere Materialien kann die entwickelte Simulationsmethode noch weiter verbessert werden. Experimente mit getränkten Preforms ermöglichen die Erweiterung des Simulationsmodells für andere Herstellprozesse wie Compression Resin Transfer Molding.

ABSTRACT

Continuously rising fuel prices and the growing pressure to save climate-damaging emissions are leading to an increased use of lightweight structures, especially in the aerospace industry. Due to their outstanding weight-specific mechanical properties, carbon fiber-reinforced plastics offer particularly high lightweight potential and are increasingly used in modern aircraft. In addition to the processing of pre-impregnated semi-finished products, the so-called prepregs, resin injection processes are one of the most widely used methods for manufacturing composite parts. Although these processes offer some benefits, they still have limitations due to process-related defects, such as pure resin areas in tight radii, dry spots and large process-induced deformations. These defects are often caused by fiber volume content gradients resulting from a non-uniform compaction during mold closing.

In this thesis, a compaction process simulation for dry carbon fiber preforms with an orthotropic nonlinear material model was developed that allows to predict the defects mentioned above. The materials used were experimentally characterized and a new test method for out-of-plane shear stiffness was designed. Based on the obtained data, a compaction model for predicting the time-dependent behavior in thickness direction was developed and validated. By adjusting the closing process, it was shown that the model can be used to reduce the required closing force by 50% while achieving the same final fiber volume content.

Subsequently, the compaction model was extended to include the deformation modes in the remaining directions such as out-of-plane shear. The calibrated model shows an excellent agreement with the experimental results from compaction tests with tight tool radii. The predicted closing forces agree well with the values from the experiments for varying radii and fiber volume contents. The resulting geometry of the preform due to compaction, shear and friction is in good agreement for both force-controlled and displacement-controlled tests. The validated model was further used for a virtual study of preform and tool properties, revealing that preforms with high thickness and high fiber volume content are particularly prone to pure resin regions in the radius. Further findings of the study were summarized in design guidelines for compaction processes.

With the developed coupling of the results from the compaction simulation with the filling simulation, it was shown that the consideration of the compaction results has a significant influence on the part filling. The developed simulation model can be applied to avoid compaction defects and to improve part quality. The findings from the parameter study provide valuable guidelines in early development stages without having to use time-consuming simulations. The application to more complex geometries and different materials, can improve the developed simulation method. Experiments with impregnated preforms allow the extension of the simulation model to other manufacturing processes, such as compression resin transfer molding.

Contents

Nomenclature

Symbol	Unit	Description
Greek letters		
α	-	Weighting factor for parameter fitting
γ	rad or °	Shear angle
ϵ	-	Strain
ϵ_e	-	Elastic strain
$\dot{\epsilon}_e$	s^{-1}	Elastic strain rate
ϵ^{rel}	-	Relative strain
$\dot{\epsilon}_v$	s^{-1}	Viscous strain rate
η	MPa·s	Dynamic viscosity
Θ	-	Heaviside function
λ	MPa	Normalized sum of the stress differences
λ_{tot}	MPa	Total normalized sum of the stress differences
μ_D	-	Static friction coefficient
μ_s	-	Dynamic friction coefficient
ν	-	Poisson's ratio
ρ_{fiber}	g/cm^3	Density of a fiber
σ_e	MPa	Elastic stress
σ_{exp}	MPa	Experimental stress
σ_{model}	MPa	Model stress
σ_v	MPa	Viscous stress
σ_Y	MPa	Yield stress

Symbol	Unit	Description
τ	s	Relaxation time
τ	MPa	Shear stress
Latin letters		
A	mm^2	Area
A	MPa	Fitting parameter for the *viscous exp* model
a_j	MPa	Fitting parameter for the *viscous exp* model of branch j
A_s	MPa	Constant in Gutowski's model
AW	g/m^2	Areal weight
B	-	Fitting parameter for the *viscous exp* model
b_j	-	Fitting parameter for the *viscous exp* model of branch j
C_j	m	Fitting parameter of the Kozeny-Carman equation
E	MPa	Young's modulus
E_f	MPa	Fiber Young's modulus
G	MPa	Shear modulus
G_A, G_B	MPa	Shear modulus in the first and second section of the bilinear shear model
f_α, f_β	-	Strain and strain rate dependent functions
F_{DT}	N	Dynamic tangential force
$f_{E_{11}}$	-	In-plane stiffness reduction factor
$f_{E_{33}}$	-	Compaction stiffness scaling factor
$f_{E_{55}}$	-	Out-of-plane shear stiffness scaling factor

Symbol	Unit	Description
F_N	N	Normal force
F_{ST}	N	Static tangential force
F_T	N	Tangential force
h	MPa	Total stress in a Maxwell element
h_{ini}	mm	Initial preform thickness
$h_{r,max}$	mm	Maximum gap height in small tool radii
j	-	Subscript for the number of the Maxwell branch
$\boldsymbol{J}$	-	Jacobian matrix
k	-	Subscript for the number of the curve in the fitting algorithm
K	m^{-1}	Permeability
$\boldsymbol{K}$	-	Stiffness matrix
L_{pf}	mm	Length of the preform
N	-	Number of branches in a generalized Maxwell Model
N	-	Number of layers in a preform
n	-	Design parameter for mesh convergence study
n_j	m	Fitting parameter of the Kozeny-Carman equation
P	N	Mold closure force
r	mm	Radius
r_i, r_o	mm	Inner and outer tool radius
t	s	Time
t_r	s	Ramp time

Symbol	Unit	Description
u	mm	Displacement
u_{pf}	mm	Displacement of the preform
u_{tot}	mm	Total displacement
u_{tp}	mm	Displacement of the tape
V_f	-	Fiber volume content
V_{f0}	-	Initial fiber volume content
w_{pf}	mm	Width of the preform

Abbreviations

Abbreviation	Description
1D, 2D, 3D	One-, Two-, Three-dimensional
APDL	Ansys Parametric Design Language
ASTM	American Society for Testing and Materials
CAD	Computer Aided Design
CFM	Continuous Filament Mat
CFRP	Carbon Fiber-Reinforced Plastic
CO_2	Carbon Dioxide
COVID-19	Coronavirus Disease 2019
CPU	Central Processing Unit
CNC	Computer Numerical Control
CRTM	Compression Resin Transfer Molding
CSM	Chopped Strand Mat
CST	Compression Shear Test
CT	Computed Tomography
DIN	German Institute for Standardization Registered Association
FACC	Fischer Advanced Composite Components
FVC	Fiber Volume Content
FE	Finite Element
FEA	Finite Element Analysis
GFRP	Glass Fiber Reinforced Plastic
ISO	International Organization for Standardization

Abbreviation	Description
LCM	Liquid Composite Molding
LIMS	Liquid Injection Molding Simulation
LRZ	Leibniz Rechenzentrum
LVDT	Linear Variable Differential Transformer
NCF	Non-Crimp Fabric
NO_x	Nitrogen Oxide
RTM	Resin Transfer Molding
SAMPE	Society for the Advancement of Material and Process Engineering
SBS	Short Beam Shear
TUM	Technical University of Munich
WV	Weave material
VARI	Vacuum Assisted Resin Infusion
VARTM	Vacuum Assisted Resin Transfer Molding
UDF	User-Defined Function
UTM	Universal Testing Machine
ZIM	Zentrales Innovationsprogramm Mittelstand

List of figures

List of tables

1 Introduction

Lightweight design and the utilization of lightweight materials have always been key factors for the development of airplanes since the very first motor-powered aircraft, the Wright Flyer, which was mainly composed of wood. These key factors are still valid for modern airplanes. Besides aerodynamical advantages of light aircraft, monetary and environmental reasons are major drivers towards lighter designs. A 1% saving in the structural weight reduces the fuel consumption by 0.7 to 0.75% [1]. According to the Advanced Materials Research Program by the Federal Aviation Administration (FAA), one pound of weight saved on a commercial aircraft saves 100 $ to 300 $ over its service life [2]. An excellent example to illustrate the importance of weight saving in the aerospace industry comes from the US-based airline, American Airlines. By replacing nearly 20 kg pilot bags, containing operating manuals, checklists and logbooks, with 0.6 kg iPads, the airline could save 1.2 million dollars of fuel cost annually [3,4].

The utilization of modern lightweight materials has an enormous potential to reduce the structural weight of airplanes. In recent decades, the weight percentage of fiber-reinforced composites in aviation has risen continuously. Due to their excellent specific mechanical properties, composite materials offer great potential for more efficient aircraft. Fig. 1-1 shows the proportion of composites in the total weight of civil and military aircraft over the last 60 years. Starting in the 1960s and 1970s, the share of fiber-reinforced plastics was in the range of single digits. However, in modern civil aircraft such as Airbus A350 or Boeing 787, composites now account for more than 50% of the total weight [5]. According to Boeing, 20% of the total empty weight of the 787 Dreamliner could be saved by using composite materials compared to a conventional aluminum design [6]. Besides a reduction of operational cost, fuel saving leads to reduced emissions of harmful nitrogen oxides (NO_x) and carbon dioxide (CO_2). With an increasing awareness of sustainable aviation, saving emissions is becoming more and more important. The European Flightpath 2050 [7] passed by the European Commission outlines the following goals relative to a typical new aircraft in 2000:

- 75% reduction in CO_2
- 90% reduction in NO_x
- 65% reduction in noise

Together with the European Green Deal, aiming for a climate-neutral EU by 2050, this emphasizes the need to design more efficient aircraft. For the next-generation single-aisle (NGSA) aircraft, it is assumed that the weight percentage of composites will further increase [8].
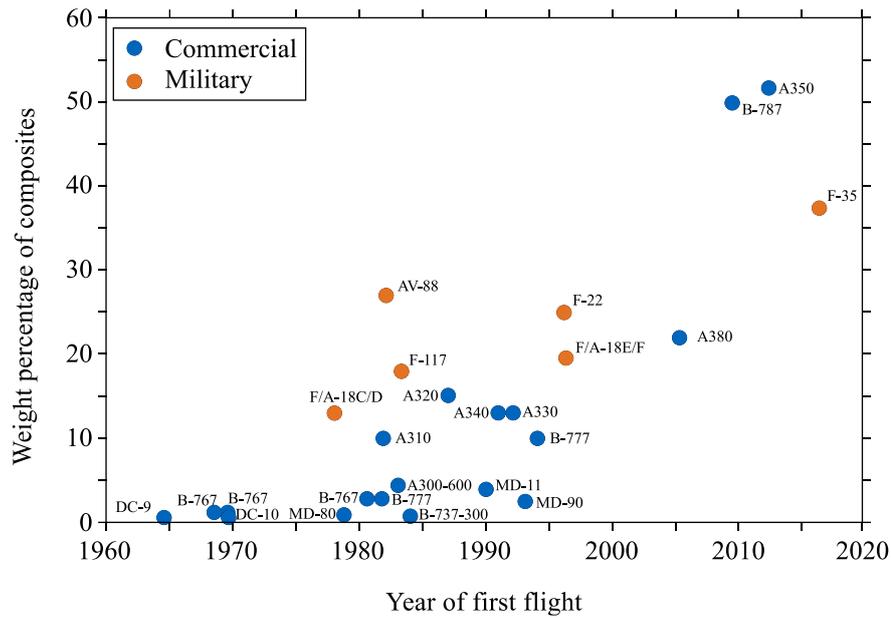
Fig. 1-1: **Weight ratio of composite materials in military and civil aircraft (adapted from [8–10]).**

1.1 Composite manufacturing technologies in the aviation industry

In the early civil aircraft models shown in Fig. 1-1, composites were mainly used in secondary structures such as rudder and trailing wing edge [11]. In the Airbus A310, carbon fiber-reinforced plastics (CFRP) were applied for the vertical fin and brakes [10]. For modern aircraft, primary structural components, such as the ribs or the center wing box, are also made of carbon composites [11,12]. In addition, the entire wings and fuselage of the Airbus A350 and the Boeing 787, for example, are manufactured with carbon composites [5,13].

With the development towards larger and more load carrying composite structures, the requirements for high part quality and robust processes are increasing. The use of pre-impregnated semi-finished products (prepregs) is currently the most widely applied process for manufacturing components in the aerospace industry. However, liquid composite molding (LCM) processes are gaining in importance for the manufacture of complex parts. Both processes enable the production of very high-quality components that meet aerospace requirements. Production with prepregs is usually carried out by tape laying or hand layup with subsequent curing in an autoclave. One of the main advantages of prepreg processes is the excellent quality of the produced part due to the homogenous

high pressure in the autoclave. However, the use of the autoclave requires a lot of energy and the occupancy of the autoclave for curing can limit the production rate [5].

Fig. 1-2 compares the possible production volume for different composite part production processes. In addition, the performance, i.e. the possible mechanical properties of the manufactured components, is indicated. It can be seen that resin transfer molding (RTM) and resin infusion, which belong to the group of LCM processes, can produce high-quality components comparable to those made with prepregs. Moreover, RTM allows for higher production rates according to some authors [5,14]. The advantages of RTM processes are particularly evident for thick components with high geometrical complexity [13].

In coming decades, the demand for civil aircraft will continue to grow. According to the Airbus global market forecast 2021 [15], the global passenger traffic grows at the same rate as before the COVID-19 pandemic with a two years lag. Airbus expects to deliver 39,000 new aircraft until 2040 with a share of 76% single-aisle aircraft [15]. This corresponds to an average production rate of 120 small aircraft per month. Currently, Airbus aims to produce 67 A320s per month in 2023 [16].

Considering that several parts appear multiple times in a certain airplane, such high production rates are only possible with processes that allow short cycle times. The prepreg autoclave process has clear limits regarding cycle times. One cycle including heating and cooling takes four to five hours for a typical aerospace material such as Hexcel M21 [17]. One additional drawback of the prepreg material is the required energy consumption for cooling during storage and transportation [5].
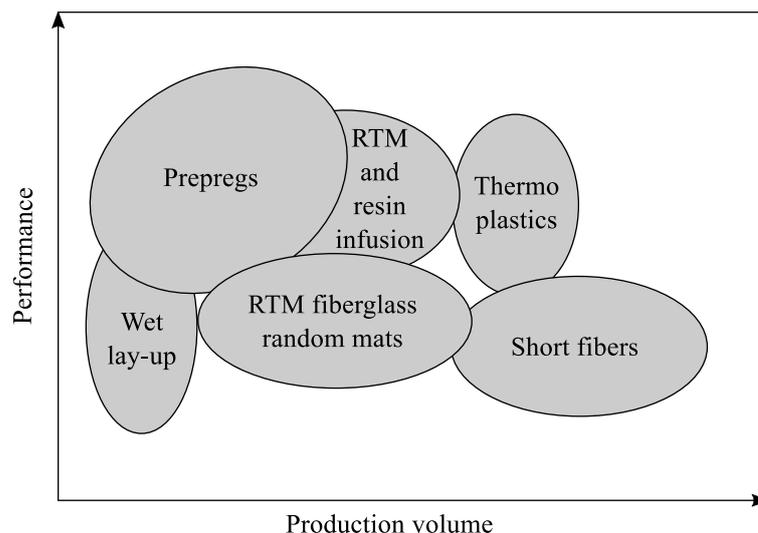
Fig. 1-2: **Production volume and mechanical properties of manufactured parts for various aerospace production processes (adapted form [14]).**

Because of the advantages mentioned above, especially for complex geometries, several parts are nowadays produced with LCM processes, mostly RTM. RTM is a variant of LCM with two rigid molds, ensuring high part quality on both sides. For this purpose, a dry textile preform is placed inside the tool before the resin is injected via a pressure difference between inlet and outlet. In civil aviation, the following aircraft components are currently manufactured using the RTM process [5,11,18,19]:

- Window frame Airbus A350XWB
- Leading edge on the horizontal stabilizer Airbus A350XWB
- Passenger doors Airbus A350XWB
- Main attachment pieces for wing flaps Airbus A330/A340/ A350XWB
- Landing gear struts Boeing 787
- Spoiler Airbus A320
- Door pillars, stringers, stiffened panels, rudders

According to Airbus, further reasons for manufacturing structural components using RTM processes include [13]:
- Reproducible laminate thickness even for thick components (> 50 mm)
- Production of close-to-final contour without post-processing
- Compared to prepreg, a higher degree of integral construction
- Very high degree of automation

RTM is a process that can offer advantages in the manufacture of components for the aerospace industry. Especially for components with high wall thickness or geometric complexity, cost advantages can be expected in addition to the process-related aspects mentioned above. The Austrian supplier FACC recently produced a five meter long multicell flap in an integral design avoiding assembly cost [20]. The US supplier Spirit delivered the first set composite spoilers for the A320 series manufactured in a fully automated RTM process in 2021 [21]. Airbus started the assembly of the first Wing of Tomorrow prototype in 2021 that contains further large-scale RTM parts such as trailing edge and spars [22].

1.2 Motivation

LCM processes offer several advantages, especially for manufacturing complex and thick parts, yet they face some limitations. According to [23], the biggest challenges of RTM processes are mold design, filling strategy and resin-rich edges. A clearance between the edge of the preform and the edge of the tool leads to a higher flow velocity during resin injection in this channel [24]. The resin flow through a hollow path within a cavity is referred to as race-tracking that can lead to dry spots or resin-rich corners in the final part [25]. McIlhagger et al. emphasized that one of the most critical problems

in RTM are dry spots in the finished part [5]. FACC reported that issues with race-tracking were the main challenge during the manufacture of a five-meter-long multicell flap [20]. All mentioned challenges can be explained with variations of the fiber volume content (FVC) and geometrical variations of the dry preforms. Fig. 1-3 demonstrates how FVC gradients are generated in curved tools. Fig. 1-3a shows the tool geometry and Fig. 1-3b displays a micrograph of a cured part. It can be seen that the reinforcement is more compacted in the radius, leading to a significantly higher FVC. Regions with high degree of compaction slow down the resin flow front and have a significant influence on the preform infiltration. Variations of the FVC can lead to unfilled regions and create dry spots or empty spaces in the tool, leading to race-tracking and resin-rich corners. Mesogitis et al. [26] performed a review on uncertainties in the manufacturing process of thermosetting composites. They concluded that FVC variations play a dominant role in the manufacturing process. Due to the high variability of the preform properties, race-tracking channels can appear at different locations and different dimensions. This leads to a low reproducibility of the process [27]. Besides affecting the filling behavior, FVC gradients are one of the main drivers of part distortions after the demolding of the cured part [28,29]. Moreover, FVC gradients have a significant influence on the mechanical properties of the finished part [26].

(a)   (b)
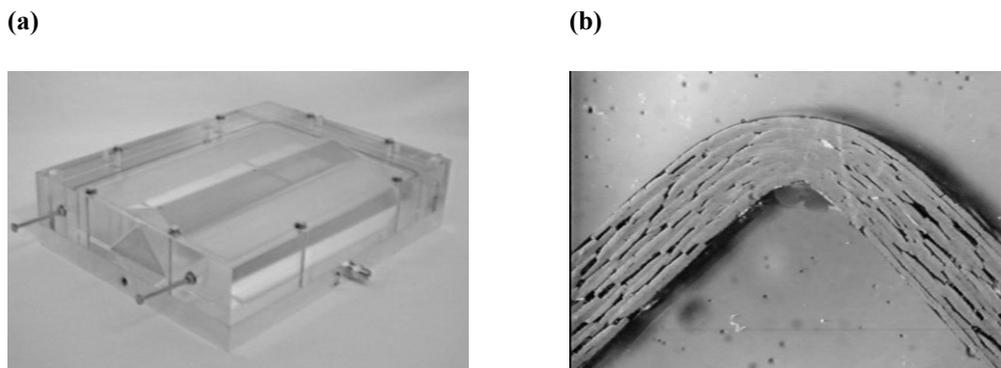
Fig. 1-3:   **Development of FVC gradients in curved preforms: (a) transparent tool; (b) micrograph of cured part [30].**

Numerical simulations are widely used to optimize the manufacturing process and avoid defects in the finished part. Filling simulations have been used to minimize filling times and avoid dry spots [31,32]. In order to accurately predict the filling behavior, it is important to account for previous manufacturing steps. For instance, the influence of fiber orientation from the preceding draping process has been investigated in filling simulations [33,34]. However, compaction simulations that define the FVC distribution in the finished part are not included in the current state of the art. This is neither part of commercial solutions such as ESI PAM Composites [35] nor included in academic virtual LCM process chains [33,34]. Thus, there is an evident need for compaction simulations to avoid defects and design stable manufacturing processes.

1.3 Objectives

The goal of this thesis is to develop a simulation method to predict the compaction behavior of dry carbon fiber preforms in LCM processes. Understanding and predicting effects that occur during tool closing will assure a more robust process and avoid compaction induced defects. Using the results from compaction simulations, such as FVC gradients and deformed shape, will enhance the predictive capabilities of filling simulations. Deriving guidelines from the developed methodology, can be helpful in the process development if complex simulations are not possible or are too time consuming. This novel simulation method can be a building block of overcoming the current challenges in a wider application of LCM processes in the aerospace industry.

In order to achieve the above-mentioned goals, the following objectives for this thesis are identified:

- Development of a material model capable of describing the behavior of dry preforms during compaction.
- Implementation of the novel material model into a finite element software and application of the validated model to derive guidelines.
- Integration of the compaction simulation method into a manufacturing process simulation chain.

1.4 Thesis outline

The outline of this thesis is illustrated in Fig. 1-4, showing the interaction of the seven chapters of this work. A brief overview of each chapter is described as follows:

Chapter 1 introduces the use of composite materials in the aerospace industry and current trends in manufacturing processes. This chapter highlights the need for compaction simulations for LCM processes. Based on this, the objectives for the thesis are derived.

Chapter 2 reviews the state of the art, necessary to address the objectives defined in Chapter 1. This chapter starts with an overview of the LCM processes, emphasizing compaction induced part defects. Afterwards, this chapter shows the characterization methods for the most relevant material properties. The overview of compaction material models reviews one-dimensional models for the through-thickness compaction, followed by approaches for three-dimensional non-planar geometries.

Chapter 3 presents the experiments conducted within this work. First, characterization experiments for planar geometries are described that are used as input for the process simulations. For this purpose, through-thickness compaction, out-of-plane shear and tool-preform friction were characterized. Second, compaction experiments, using nonplanar geometries, are presented, with results being used for the validation of the nonplanar model.

Chapter 4 shows the development of a time-dependent material model for the through-thickness compaction. Experimental data from Chapter 3 is used for the model fitting and validation. The model is applied to displacement-controlled and force-controlled setups.

Chapter 5 extends the one-dimensional description of the compaction behavior to an orthotropic three-dimensional model, including deformation modes in the remaining directions. The model is calibrated to a single configuration of the non-planar compaction experiments. The remaining configurations are used for the validation of the model. Guidelines are derived from parameter studies of materiel properties and geometrical dimensions.

Chapter 6 presents a methodology to transfer results from compaction simulations to subsequent filling simulations. In addition to the FVC, the material orientation and the deformed mesh, the contact status is transferred, allowing to create race-tracking channels in empty spaces in the cavities. The approach is applied to two different cases, highlighting the importance of compaction data in filling simulations.

Chapter 7 summarizes the main contributions of this work, achieving the objectives defined at the beginning. Furthermore, this chapter gives an outlook on future work to enhance the methods developed within this thesis. A brief overview of two research projects following up on the current work, is given.
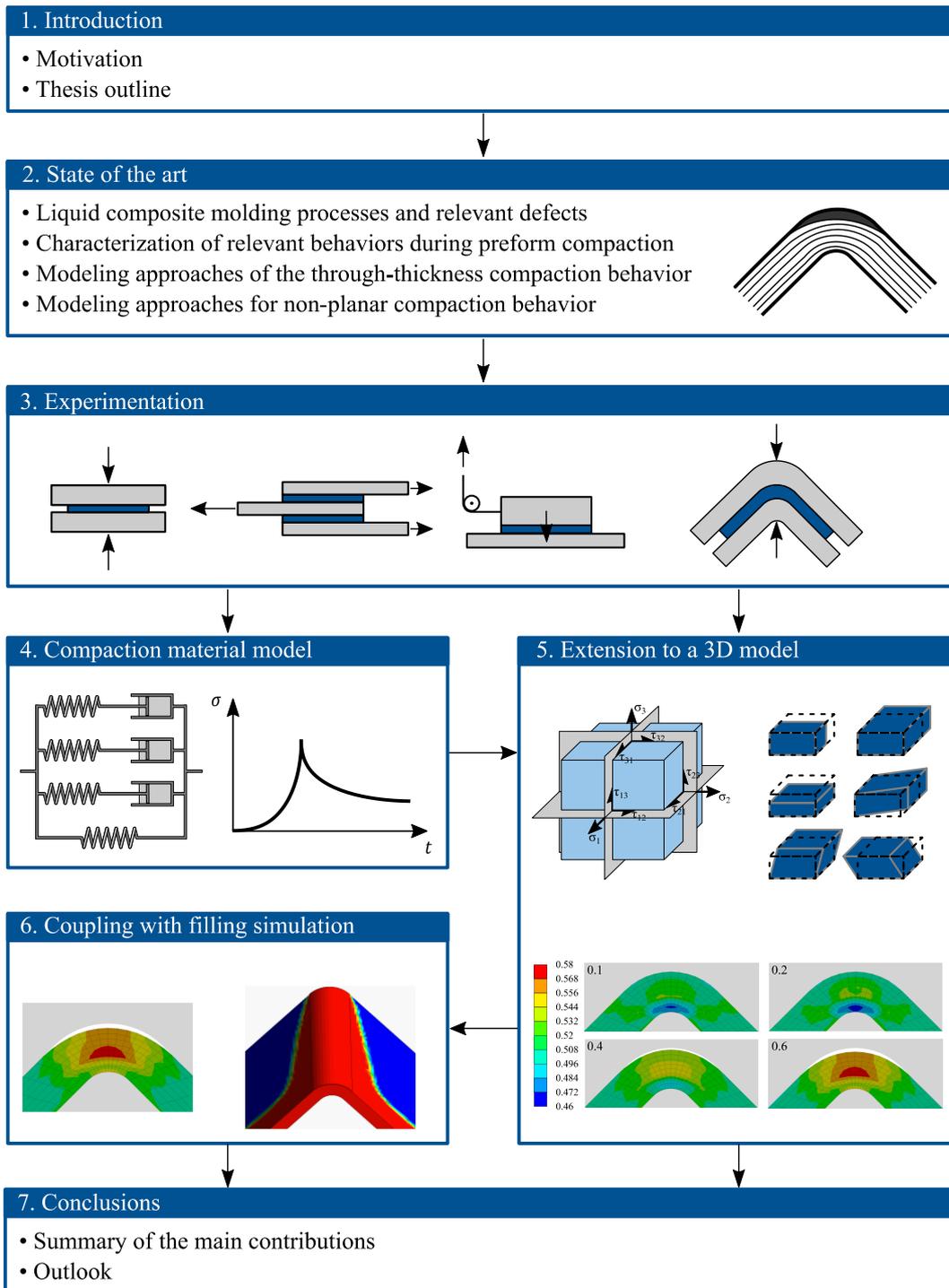
Fig. 1-4:   **Outline of the thesis.**

2 State of the art and research questions

This chapter reviews the state of the art and provides necessary information for the prediction of the compaction behavior of fibrous reinforcements. First, an overview of LCM processes is given, discussing current developments and unresolved challenges. Special emphasis is placed on compaction-induced defects and contributing deformation mechanisms of the preforms. Based on these findings, the material behavior and state of the art characterization methods for these deformation mechanisms are presented. Because the focus of this work is to accurately predict the out-of-plane compaction behavior, a thorough review of modeling approaches on different scales is presented. Methods on macroscopic level and rheological models are described more in detail. Furthermore, the review is extended to non-planar compaction behavior of reinforcement materials. Finally, research questions are derived from the gap identified in the literature.

2.1 Liquid composite molding processes and relevant defects

Most LCM processes have in common that the matrix is added to the fibers during part manufacturing. Typically, the fiber reinforcement is preformed before it is positioned on the lower mold surface of the tool. These so-called preforms can either be produced directly, for instance by braiding, or sequentially by draping stacked layers onto a surface. The driving force for the impregnation of the dry preforms in LCM processes is a pressure gradient between the resin inlet and the cavity. This gradient can either be realized by injecting the resin with pressure or by applying vacuum to the cavity that pulls the resin into the preform. Besides different possibilities of applying a pressure gradient, the characteristic of the upper mold can categorize LCM processes. There are different terminologies found in literature for each variant of LCM. In this work the definition proposed by Advani and Sozer in [32] and Long in [36] is used for the classification of LCM processes. Fig. 2-1 shows basic LCM processes with different upper mold stiffness. In RTM processes, the resin is injected into a cavity between an ideally rigid upper and lower mold. In contrast, the upper mold in vacuum assisted RTM (VARTM) is a flexible membrane. In some literature, this process is also referred to as vacuum assisted resin infusion (VARI) [36,37]. Applying vacuum ensures that the membrane remains in contact with the preform. Light RTM processes (see Fig. 2-1b), which have a semi-rigid upper mold lie between the two variants mentioned before. A common characteristic of all variants is that the final FVC of the part results from the compaction of the preform

9

between upper and lower mold. The FVC is either defined by the distance between two rigid molds or the atmospheric pressure and resin pressure acting on the vacuum membrane.

(a)   **(b)**   **(c)**
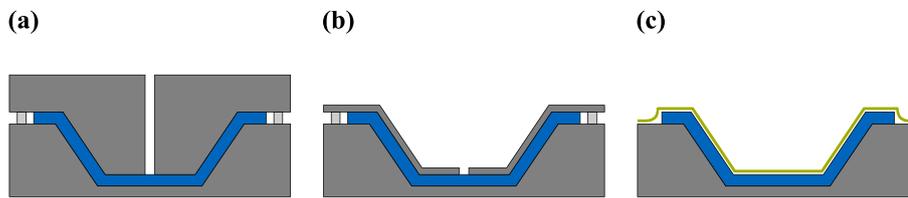
Fig. 2-1:   **Basic LCM processes based on the characteristic of the upper mold: (a) RTM; (b) Light RTM; (c) VARTM.**

2.1.1   State of the art RTM processes

The main process steps of a classical RTM process are illustrated in Fig. 2-2. First, the preform is placed onto the lower mold, before the upper mold closes the tool. During the tool closing, the preform is compacted to its final FVC. Generally, the thickness of the preform is defined by the distance between the lower and upper mold. However, material and process-related defects, which are outlined in Subsection 2.1.3, can cause deviations in thickness. After the preform is compacted to the final FVC, the resin is injected with a pressure ranging from 1 bar up to 150 bar in high pressure applications [38]. Sealing around the preform prevents the tool from leaking. When the preform is fully impregnated with the matrix, the resin is cured in the closed mold. Depending on the resin system, the tool needs to be heated during injection and curing. After the curing stage, the finished part is demolded. Chemical cure shrinkage of the resin and different coefficients of thermal expansion of reinforcement and resin can lead to residual stresses in the part [39,40]. After demolding, these stresses are partly released and can lead to part distortions [39,41,42]. Higher FVC gradients within the part lead to higher gradients of the residual stresses and thus, potentially stronger part distortion.

The RTM process is suitable for the production of large and complex structures guaranteeing high mechanical performance for the aerospace industry [23,32,37,43,44]. Further advantages include the ability to produce near-net-shaped parts with good surface quality on both sides and short cycle times [11,32,37,44,45]. The combination of high volume production and comparably low cost makes the process interesting for a broad range of applications [43]. Its high potential for automation has led to a wide use in the automotive industry [43,46]. Moreover, recent developments of new resins allow a broader application of RTM processes. With new resin systems which cure in less than 60 seconds, high volume production of up to 150,000 parts per year is possible [47]. With new polyimide resins, high temperature RTM parts can be manufactured for operating temperatures above 300°C [48,49]. Furthermore, the RTM process is being

adapted to thermoplastic matrix systems, enabling better recyclability of composite parts [44,50]. Furthermore, using thermoplastic resins allows for subsequent welding or thermoforming of the produced part [44].

Some of the major challenges of RTM are related to process instabilities because of variations of the preforms originating from fabric cutting, stacking and placement in the mold [32]. This leads to permeability variabilities reducing the process robustness and having a major impact on the reproducibility of parts produced with RTM [27]. Further drawbacks are the sensitivity of the process to the mold and injection strategy design [23,32]. Both factors can lead to incomplete filling and thus, dry spots in the final part [23,51]. Moreover, the preform deformation during tool closing can lead to resin-rich edges in the final part [23,51,52].
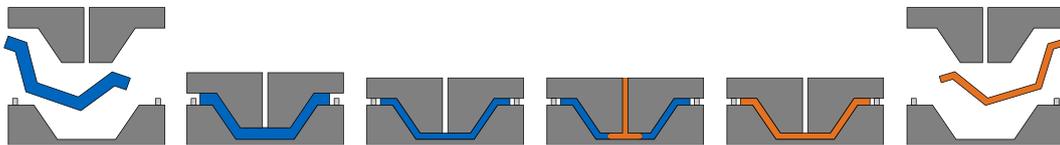
Fig. 2-2:   **Schematic illustration of the process steps in an RTM process (adapted from [32]).**

2.1.2   State of the art VARTM processes

Fig. 2-3 illustrates the main process steps of the VARTM process. In comparison to the RTM process, the upper rigid mold is replaced by a flexible vacuum membrane. In terms of compaction, the main difference to RTM is that the final FVC is defined by the position of the membrane. The local membrane position results from the force equilibrium of the compacted fiber bed, the resin pressure and the atmospheric pressure. One of the main advantages of the VARTM process is the reduced investment cost, because no upper mold and no press to close the tool are required [53]. This advantage becomes more important with increasing part dimensions, which makes the process extremely attractive for the wind turbine industry. Wind turbine blades of up to 120 m length can be produced using state of the art VARTM processes [54,55]. The flexible membrane enables manufacturing of complex geometries with the possibility to easily modify the upper mold [56,57]. Moreover, a transparent vacuum bag makes dry spots in the part visible during the process and allows for counteractive measures [57]. Using an elevated temperature VARTM process, Menta et al. [53] proved that high performance parts with less than 1% void content can be produced in this low cost technique. The Airbus A220, with wings manufactured in resin-infusion process, has been in service since 2016 [58].

One of the major challenges in the VARTM process is that the pressure inside the vacuum bag varies with distance from the injection point and that the compaction stiffness of the preform depends on its saturation with resin [36,59]. The pressure gradient from inlet to outlet can lead to an uneven thickness distribution in the finished part [60].

Because of the maximum compaction pressure of one bar, it is generally not possible to reach the same high FVC as in RTM processes. Additionally, the low pressure gradient leads to comparably long process times [57]. Having a flexible membrane, reduces the surface quality on one side of the finished part compared to a rigid mold [32]. Another challenge in VARTM processes is the high chance of leakage between the flexible membrane and the rigid lower mold [57]. Further compaction-related defects, which can occur due to corner effects are outlined in Subsection 2.1.3.
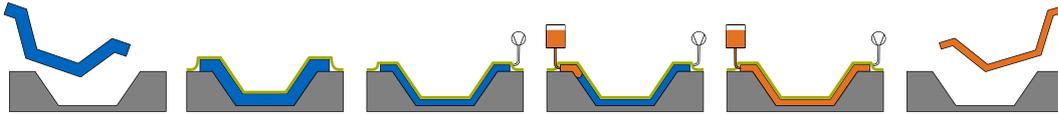
Fig. 2-3:   **Schematic illustration of the process steps in a VARTM process (adapted from [32]).**

2.1.3   Compaction induced defects in LCM processes

After reviewing the state of the art of LCM processes, this subsection focuses on part defects induced by the compaction of the preform. The overview of the manufacturing induced defects that can be related to FVC gradients highlights the importance of compaction process simulations. Moreover, understanding the underlying mechanisms of defect generation is valuable for setting up simulation models and understanding which properties need to be characterized. This subsection is divided into two parts, focusing on closed mold processes and open mold processes. For the open mold processes, pre-pregs are also considered, since the effects in mold radii are the same and more literature is available.

2.1.3.1   Closed mold processes

Holmberg and Berglund [61] reported that different defects can occur in sharp tool corners (see Fig. 2-4). Due to high in-plane compression loads, fibers can break at the inner radius. During tool closing, the reinforcement is pulled tight around convex corners in the tool [61,62]. Hence, the material is over-compacted in the radius, leaving a gap between the molds. Fig. 2-4b shows how this effect can result in a race-tracking channel and a resin-rich corner after the infiltration [32,37,63]. These unwanted flow channels can significantly affect the filling behavior and can cause incomplete infiltration of the preform [64–67]. Potter [68] reported that resin accumulations can also appear on flat sections due to movements of the preform. Besides resin-rich corners, the compaction in tight radii can also cause dry spots, which is shown in Fig. 2-4c [61]. This effect can be explained by extremely high local FVC in the radius causing very low permeability.

Causse et al. [56] studied the influence of preforming on the quality of curved parts. The specimens were manufactured by flexible injection process, which is an RTM process with a flexible membrane in the tooling allowing faster through-thickness impregnation. Their experimental study showed that fibers oriented in 0° direction cause significant corner thinning on convex tools. The effect was more dominant for smaller tool radii and decreased with further compaction.

(a)   **(b)**   **(c)**

Broken fibers   Resin-rich zone   Resin flow direction

                                                                      Dry or porous inner radius
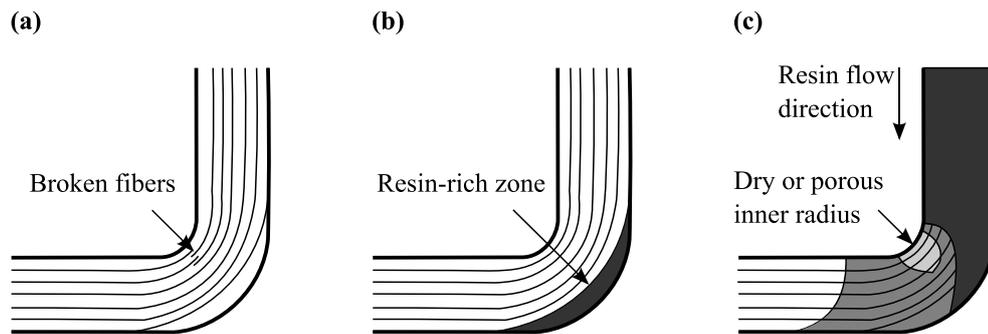
Fig. 2-4:   **Defect types in sharp corners (adapted from [61]).**

Walbran et al. [69] performed compaction experiments with non-planar geometries concluding that with increasing tool angles, the shear component of compaction stress becomes more important. The shear is introduced by the friction between the tool and preform. In a more recent publication, Walbran et al. [70] studied the out-of-plane shear behavior in a Compression Resin Transfer Molding (CRTM) process utilizing a truncated-pyramid tool geometry. Other authors came to the same conclusion that tool-ply friction and shear stress in thickness direction significantly influence the compaction behavior for non-planar geometries [56,61,63,71,72].

Dong et al. [52] studied the formation of resin-rich corners of dry glass fiber preforms without binder by varying geometry and material parameters. They found that FVC, stacking sequence and tool radius are the most significant factors influencing the gap height (see Fig. 2-5). In addition to race-tracking channels, the combination of very low permeability in the inner radius and an unwanted flow-channel in the outer radius can lead to dry zones in the part [37,61]. Fong et al. [73] suggest to either clamp several preform layers or to adjust the tool design in order to avoid wrinkles or thickness reduction in tight tool radii.

Bickerton and Advani [74] studied race-tracking effects in tight radii with different preform materials on a box-shaped mold. Bickerton et al. [30] performed an experimental study on curvature effects on mold filling in RTM processes. By using a transparent tool with an L-shaped cavity (see Fig. 2-6), they investigated the influence of tool radii on the flow front progression. The evolution of the flow front in Fig. 2-6b clearly shows how the flow is slowed down by higher FVC and accordingly low permeability due to over-compaction in the radius.

(a)   **(b)**
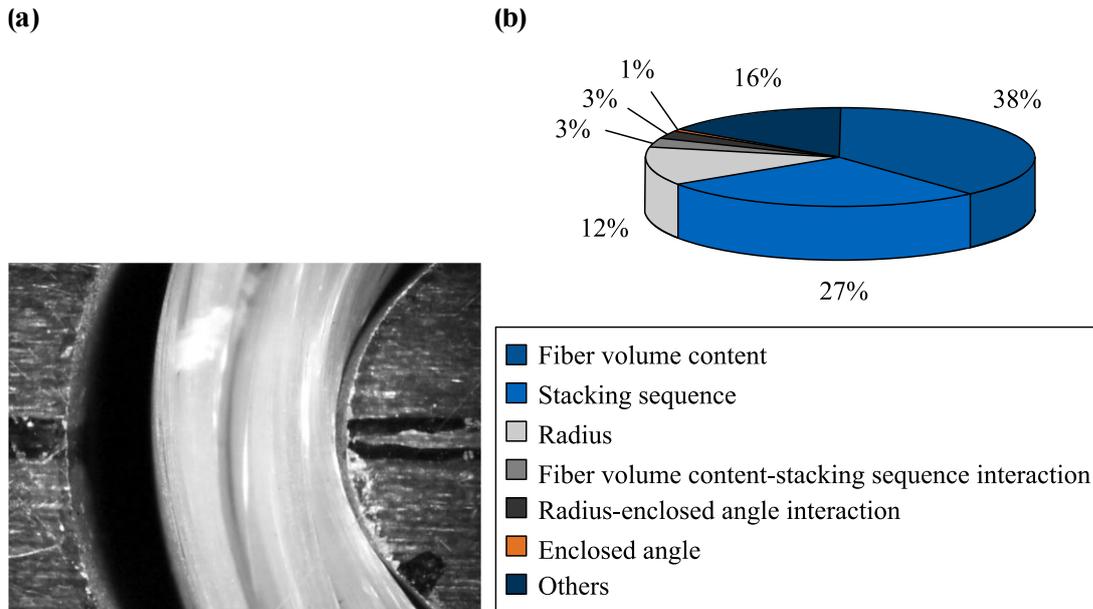
Fig. 2-5:   Development of gaps in the small tool radii: (a) example 90° corner, 5 mm radius
              and 0.39 FVC; (b) contributing effects (adapted from [52]).

           (a)   **(b)**
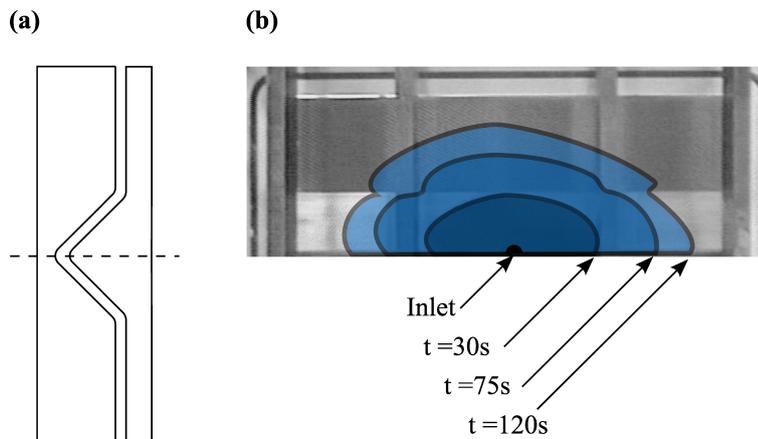
Fig. 2-6:   Flow front distribution in an angled preform: (a) side view of the tool; (b) top view of
              the flow front with tool (adapted from [30]).

Local FVC gradients do not only influence the mold filling process, they also affect the
part deformation after demolding. Jain et al. [75] found that resin-rich layers in the con-
cave mold cause large spring in angles for L-shaped profiles produced in RTM. FVC
gradients in the final part are one of the main drivers for process-induced deformations
of complex parts in RTM processes [29,76]. Causse et al. [77] concluded that through-
thickness FVC gradients and resin-rich zones have a major impact on part distortions
for composites manufactured by flexible injection. The defects mentioned above also
have a negative influence on mechanical properties of the manufactured part [26,68,78].

However, Karahan performed tensile tests on woven carbon-epoxy composites stating that damage initiation was not affected by FVC variations [79]. According to Khan et al. [80], the tensile strength due to resin-rich regions was reduced by 32%.

2.1.3.2 Open mold processes

Contrary to closed mold processes, the thickness of the parts is not defined by the cavity height in open mold processes. This leads to more pronounced thickness gradients for VARTM [36,59,81] or prepreg processes [82–84] compared to RTM. A literature review by Hassan et al. [85,86] showed that thickness gradients, resin-rich zones and wrinkling are the most common defects for complex-shaped laminates. Resin-rich zones can occur in open mold processes in concave corners because of bridging effects. As shown in Fig. 2-7b, compressing a laminate on a convex tooling can lead to corner thinning [82,83,86–88]. Hubert and Poursartip [87] explain the corner thinning effect with the reaction stress which is larger in the corner than in the flat section. In another publication, Hubert et al. [89] concluded that corner thinning is increased with increasing percentage of 0° layers. However, some authors also report layer separation and wrinkles in corners of convex tools, which lead to an increased thickness [87,90–92]. Geng et al. [81] observed the formation of gaps when preforms were placed on a convex tool. During resin injection in a VARTM process, these gaps act as race-tracking channels.

For layups on a concave tooling, authors report bridging effects, which lead to corner thickening (Fig. 2-7a) [82,83,88,91,93]. According to Hubert and Poursartip [87], this defect can be explained with reduced reaction stress in the corner of the mold. The thickening effect can lead to resin accumulations in the corner [56,83,94,95]. Hubert and Poursartip [87] observed the formation of wrinkles for prepregs which were cured on a concave tool. Wrinkles in concave molds have also been reported by Lightfoot et al. [90]. According to their findings, shearing between the plies is the main mechanism for this defect. Other authors also concluded that out-of-plane shear has a major impact on the formation of corner defects for concave and convex tools [86,87,91,96,97]. The influence of out-of-plane shearing of the tool-part interface has been studied in order to predict spring-back and warpage for prepreg processes [98,99].

The corner effects described above have a major influence on part distortion after the curing stage. Svanberg et al. [94] studied the influence of thickening and thinning of different prepreg systems on the shape distortions. Oakeshott [95] compared experimental with numerical results of the warpage of U-shaped profiles, concluding that a resin layer on the outer surface has a significant influence on the distortion. With experiments and numerical studies, authors proved that thickness reduction and FVC gradients in the radius have a significant influence on the spring-in effect [28,101–103]. Moreover, the above-mentioned defects can reduce the mechanical performance of the produced parts [84,104].

(a)   (b)
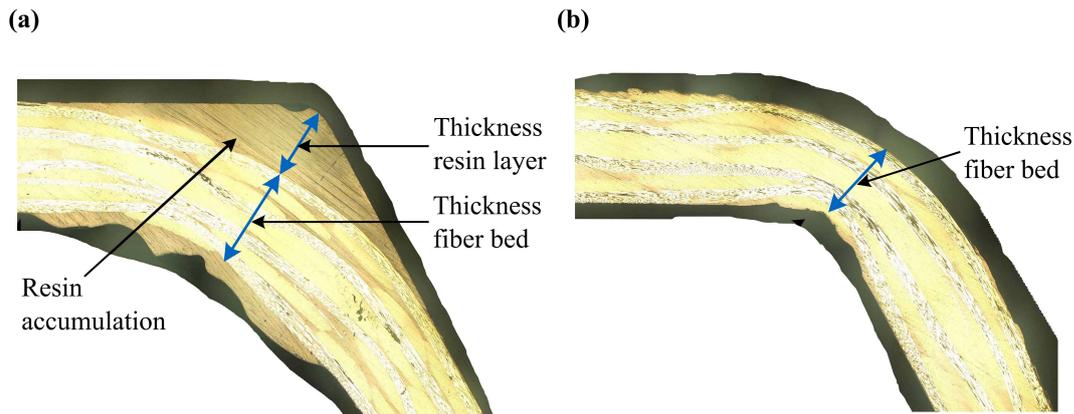
Fig. 2-7:   **Defects in corner laminates: (a) concave corner; (b) convex corner (adapted from [100]).**

2.1.3.3   Conclusions on the non-planar compaction behavior

The main defects occurring during the compaction of complex shaped layups are wrinkles and FVC gradients. Corner thinning or thickening effects lead to FVC gradients in thickness direction, whereas uneven compaction pressure can cause in-plane gradients. Resulting FVC gradients can lead to different effects during the resin injection in closed mold processes. On the one hand, gaps in the tool cause unwanted race-tracking channels during the resin injection. These unwanted flow channels can cause incomplete filling of the entire part. On the other hand, very low permeability in the corner causes slower resin propagation. An extremely high FVC on the inner tool radius can lead to dry spots near the radius. Moreover, mechanical properties are significantly decreased by compaction-related defects.

According to the reviewed literature, the most relevant behaviors defining the presence of compaction defects are:

- Through-thickness compaction
- Out-of-plane shear
- Tool-preform friction

The compaction influences the thickness and FVC of the preform, whereas the friction defines how much tangential load is transferred from the tool into the preform. The lower the shear stiffness is, the more shear deformation will appear due to this tangential load. Therefore, it is important that compaction models for non-planar parts include these material characteristics in order to accurately predict the preform behavior.

2.2 Material behavior and characterization methods of relevant preform deformation modes

This section reviews the characteristic material behavior of preforms and presents the state of the art for experimental characterization tests. Based on the conclusions in Subsection 2.1.3, characterization methods for the through-thickness compaction behavior, the out-of-plane shear behavior and tool-preform friction are highlighted. Material characteristics in the remaining directions are briefly discussed in the last subsection.

2.2.1 Through-thickness compaction behavior

Compaction experiments are conducted in order to characterize the mechanical behavior in thickness direction of fibrous preforms. Generally, the specimens are compressed between two steel plates in a universal testing machine (UTM). The force is measured by the load cell and the displacement is determined by the UTM or an external measurement system. One major difference in the experimental setups found in literature is the ratio of the size of the specimen and the compaction plates. Some authors used compaction plates, which were smaller than the preform specimens [105–108]. Other authors performed the experiments with plates that were larger than the specimen dimensions [109–111]. Kabachi et al. [112] used a setup for dry and wet compaction measurement where specimen and compression plates have the same diameter. According to an international benchmark on the experimental characterization of the preform compressibility, there was no significant influence of the ratio between specimen and plates on the measured stress response [113].

The stresses acting during the compression to high FVC can reach the order of several megapascals [114]. These high stresses cause the deformation of the specimen as well as the testing equipment. Thus, the displacement-measurement from the cross-head of the testing machine can have a significant error at high compression forces. Moreover, compaction experiments show that the stress increases sharply near the maximum compression [115]. Thus, small uncertainties in the thickness measurement can lead to extremely high variations of the stress near the minimum sample thickness. Consequently, an accurate and reliable thickness measurement method is crucial for the characterization of the compaction behavior.

Several methods have been applied to account for the machine compliance during compaction experiments. A very common method is using the cross-head displacement data from the UTM of an empty compaction test without specimen. This data can be used to correct the displacement measurement after the experiment [105,107,108]. However, it is also possible to use the compliance data for calibrating the UTM prior to testing [113].

Other authors have used the displacement recorded by the UTM without mentioning measures accounting for machine deformation [109,111,116–118]. Another method to account for machine compliance during the experiments is an external measurement of the cross-head position. A widely used approach utilizes linear variable differential transformers (LVDTs) [113]. The displacement of the cross head can also be measured with optical systems, such as laser sensors [119–121] or video analysis [112,114,122]. Using external devices to measure the cross-head displacement offers the possibility to control the closing of the compaction plates. This makes data correction after testing unnecessary and allows compacting the sample to a defined FVC during the experiment. Moreover, the utilization of LVDTs or laser sensors allows for quantifying the parallelism of the compaction plates [113]. The international benchmark on textile compression with 26 participating institutes [113] revealed a large scatter in the measured maximum compaction stresses. The coefficient of variation was 38% for two different dry materials. One outcome of the study was that machine compliance can be very high and thus, has a major influence on the accuracy of the test results. May et al. [123] developed a reference specimen for compression tests in order to identify the specific sources of the variability between the different test methods. As their suggested design is 86 mm and thus, significantly thicker than normal specimens and does not account for time-dependent behavior, the comparability to textile preforms is limited.

Various investigations on the compaction response of different kinds of textile reinforcements showed that they exhibit a time-dependent behavior. A very common procedure to characterize this behavior is to apply a constant compaction speed followed by a holding phase with constant plate position. A schematic displacement-controlled compaction experiment with the corresponding stress-response is shown in Fig. 2-8. Fibrous preforms exhibit an exponential stress increase during the compaction with constant cross-head speed. When the distance between the compaction plates is kept constant after the compression, the stress is relaxing. This time-dependent behavior has been observed for woven fabrics, random mats, knitted textiles and non-crimp fabrics [108,115,124–126]. Also natural fibers such as flax or jute exhibit the same time-dependent behavior when they are compacted in thickness direction [120,127,128]. Wei et al. [126] found that the binder content has a significant influence on the preform thickness compaction behavior. Schauer et al. [C8] concluded that higher binder content increases the compaction force.

Compaction experiments have also been conducted on wet specimens. For dry and wet compaction experiments, the same qualitative time-dependent behavior was observed [113,119,129]. The comparison shows that the stress level during compaction and relaxation is lower for the wet preforms. Lower stresses can be explained with the lubrication effect due to the present fluid. The drop of compaction pressure because of lubrication is of special importance for CRTM processes. Buntain and Bickerton [130] performed compaction experiments during the resin injection in order to characterize tooling forces in CRTM processes. Their results show a significant drop of the clamping force during the holding phase compared to dry experiments.

Because of their special importance in the aerospace industry, there have been various investigations on the compaction behavior of prepregs showing the same qualitative behavior [131–133]. Lukaszewicz and Potter characterized the relaxation behavior of uncured prepreg at different displacements in dependency of the temperature [134]. Nixon-Pearson et al. measured the time-dependent thickness evolution of uncured prepregs using creep experiments [135]. Etchegaray Bello et al. [P2] performed cyclic compaction experiments with uncured prepreg showing an increasing thickness reduction with each cycle.
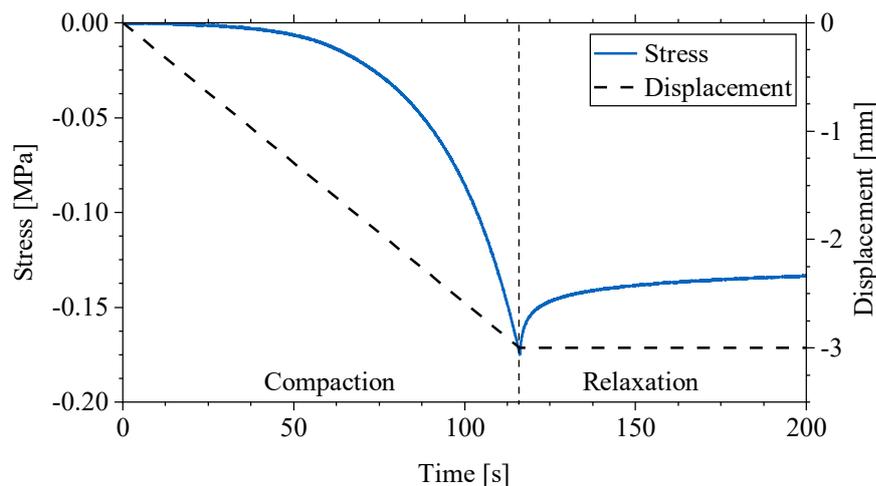
Fig. 2-8:   **Compaction stress progression during relaxation test.**

The compaction phase of displacement-controlled experiments can be divided into three sections, which are shown in Fig. 2-9. The first section is characterized by an almost linear stress increase with a small slope. It is followed by a nonlinear increase of the compaction stress in the second section. During the third phase, stress is rising rapidly with a nearly linear proportion. There are different deformation modes which have an influence on the compaction response of a textile. The four main factors are shown in Fig. 2-9.

By means of micrographs, individual mechanisms can be related to different stages of the compaction process. The initial state before compaction is characterized by large voids between the individual layers and more or less bended fiber bundles depending on the fabric structure. The first phase of the compaction is dominated by the closing of large voids between the layers caused by two different effects. On the one hand, the distance between two adjacent layers is reduced by small horizontal displacements increasing the so called nesting [108,136]. On the other hand, the yarns show varying curvature after handling and stacking the material, leading to gaps between adjacent layers. These small gaps are closed by balancing the crimp of the individual yarns [136,137]. In the second section, mesoscopic voids between yarns in one layer are

gradually reduced [111,137]. This phase is dominated by bending of the yarns and in-compressible yarn deformation maintaining the cross sectional which leads to a nonlin-ear stress increase [136,138]. In the last section, microscopic voids inside individual yarns are closed. The further compaction is dominated by the yarn compression and cross-section deformation causing a sharp stress increase [137–139].

The stress release during the following relaxation phase can be explained by the reorientation of the bended fibers after the compaction [108,140]. The relaxation starts with a rapid stress decrease because of yarn rearrangement followed by a slower decrease due to fiber rearrangement inside the yarns [141].
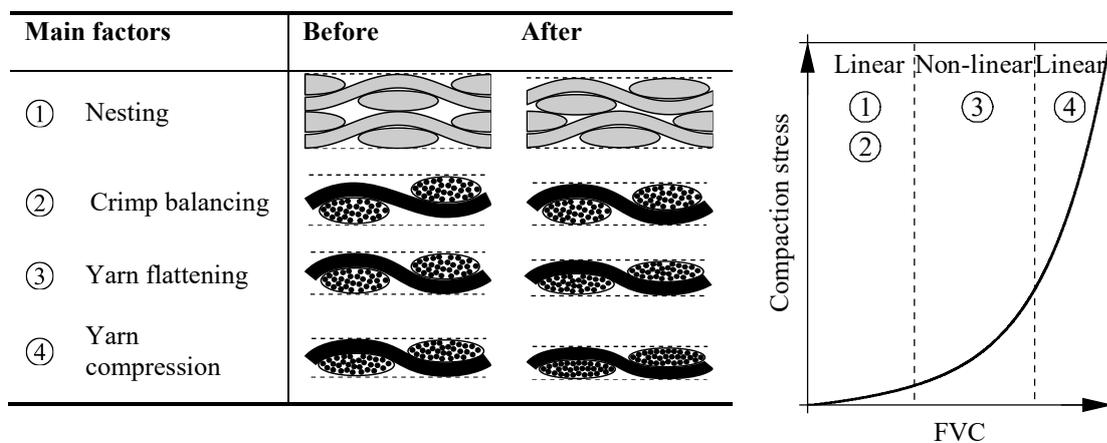
Fig. 2-9:   **Basic compaction effects during the compaction of textiles (adapted from [108,137]).**

2.2.2 Out-of-plane shear behavior

According to the author's knowledge, there is no test method available which has been designed for the characterization of out-of-plane shear behavior of dry fabrics. However, there are several out-of-plane shear characterization methods described for cured com-posites, foams and adhesives. Fig. 2-10 gives an overview of methods to test shear prop-erties found in literature.

Gras et al. [142] characterized the out-of-plane shear behavior of a 3D woven composite with epoxy matrix. They used a standard three-point bending test with short coupons to measure the out-of-plane shear stiffness (see Fig. 2-10a). This short beam shear (SBS) test is a very common method to measure interlaminar shear strength of cured compo-sites described in ASTM D2344/D2344M [143] and in DIN EN ISO 14125:2011-05 [144]. The SBS test has been applied by several authors [145–147]. The idea behind this method is having a short and thick specimen, in which shearing is the predominant de-formation mode when bending load is applied. Another commonly used method for the characterization of out-of-plane shear properties of composites is the compression shear

test (CST) illustrated in Fig. 2-10b [145,148]. Contrary to the SBS test, pure shear load is introduced into the specimen. Further methods for the characterization of shear properties are the single lap shear and double lap shear test shown in Fig. 2-10c and Fig. 2-10d respectively. The test method is described in ISO 1922:2018 [149] for rigid cellular plastics. Lap shear tests are widely used to characterize shear stiffness and shear strength of adhesives and foams [150–152]. The advantage of the double lap shear compared to single lap shear is that no rotational moment is introduced due its symmetry.

(a)   **(b)**   **(c)**

(d)
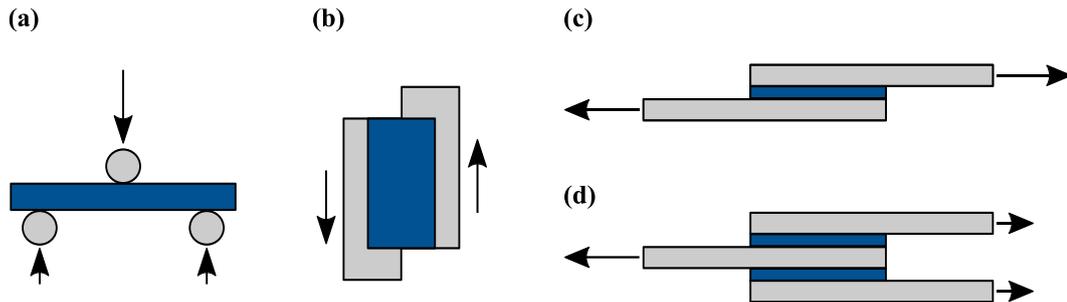
Fig. 2-10:   **Test methods for the characterization of out-of-plane shear properties: (a) short beam shear; (b) compression shear; (c) single lap shear; (d) double lap shear (adapted from [145,151]).**

2.2.3   Tool-ply friction

The friction between two rigid bodies can be characterized by the relation between the normal force F_N pressing the two bodies against each other and the tangential force F_T acting on the interface. According to Coulomb, the frictional behavior can be characterized by two phenomena, the static friction and the dynamic friction [153]. The static friction is defined by the static tangential force F_{ST} which needs to be overcome to bring a rigid body into motion [153–155].

$$\mu_S = \frac{F_{ST}}{F_N} \tag{2-1}$$

The dynamic friction is characterized by the dynamic tangential force F_{DT} which is needed after the body started to move [153–155].

$$\mu_D = \frac{F_{DT}}{F_N} \tag{2-2}$$

The characteristic behavior of the tangential force F_T for increasing displacement s is shown in Fig. 2-11a. Until no tangential movement occurs, the force increases until the static frictional force F_{ST} is reached. The force drops immediately when the body starts to move and reaches the constant dynamic friction force F_{DT}. However, experiments

with fibrous reinforcements often do not show constant dynamic friction with a more or less pronounced oscillating characteristic [156,157]. Significant oscillations occur for plastic materials, which can be explained with the so-called stick-slip behavior [158]. The same phenomenon has been reported for textile materials [159]. Fig. 2-11b shows the repetitive change between stick and slip phase during friction characterization. In such cases, the dynamic friction is given by the mean value over a defined sliding distance [158].
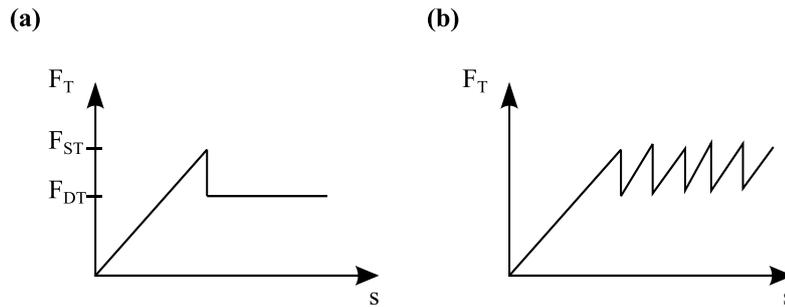
Fig. 2-11:   **Development of the tangential force versus displacement: (a) static and dynamic friction; (b) stick-slip behavior.**

Various methods have been developed for the characterization of the friction behavior between two rigid bodies. The sled test method, which is described in DIN 14882 [154] and ASTM D1894-01 [155] has been developed for the determination of the friction coefficients of textile materials. This test method, shown in Fig. 2-12a, is based on a sled with one contact material on the bottom which is pulled along a flat surface with the second contact material. The normal force results from the weight of the sled and a load cell measures the tangential force. By using a filament and low friction pulley, the test setup can easily be installed in a universal testing machine. This setup has been applied by various authors to characterize the friction behavior of fibrous reinforcements [156,157,159,160]. Further test methods are the pull-through and pull-out test, which are shown in Fig. 2-12b and Fig. 2-12c respectively. Both methods rely on the principle that a material is pulled between two surfaces which are pressed against each other. Thus, the friction between two contact surfaces is measured. The pull-through setup where the contact area remains constant during the experiment has been applied for the characterization of textile materials [161,162]. During a pull-out test, the contact area changes during the experiment, which has been used for thermoplastic composites in [163].
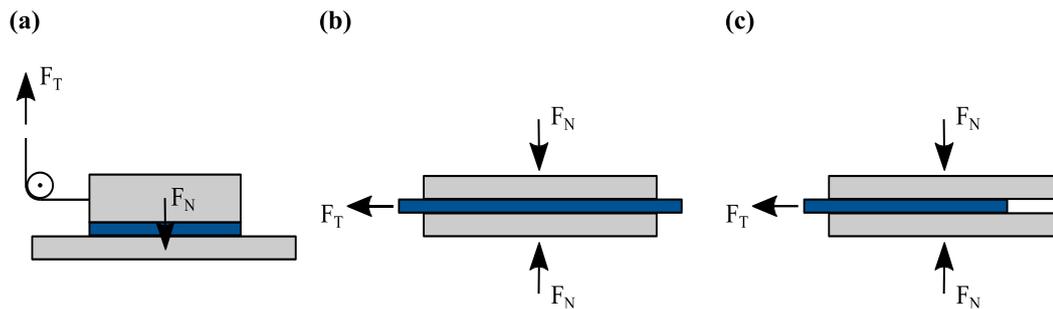
Fig. 2-12:   Experimental methods for the characterization of the friction behavior: (a) sled setup; (b) pull-through test; (c) pull-out test.

2.2.4   Overview on remaining material properties

In-plane stiffness

The characterization of in-plane tensile properties for textile materials is documented in DIN EN ISO 13934 T1 [164]. The tests are performed in a UTM which pulls the specimen at constant velocity while the force reaction is measured [165]. A good estimation of the tensile properties can be made by applying the rule of mixture as proposed in [56]:

$$E_1 = V_{f1} \cdot E_f \tag{2-3}$$

The in-plane stiffness E_1 is defined by the Young's modulus of the fibers E_f and the FVC of fibers parallel to direction 1 V_{f1}. More advanced models of the tensile behavior of dry fibrous reinforcements on various scales are presented in [166].

In-plane shear

There are two common methods for the characterization of the in-plane shear properties of textiles. On the one hand, the behavior can be characterized with the so-called picture-frame test [167]. This test utilizes a rigid quadratic frame and frictionless joints with the fabric mounted inside the frame. By applying a displacement on one end of the frame, pure shear is introduced into the specimen. The whole test setup can be mounted into a UTM. On the other hand, the shear behavior can be characterized with the bias extension test [168]. For this test method, the fabric is cut into a rectangular geometry with a ±45° fiber orientation. Applying tensile load, introduces shear indirectly in the middle section of the specimen. Independent on the test method, the shear angle vs. shear force relation is usually strongly nonlinear for biaxial fabric materials [167–169]. Initially, the material behaves very soft with low stiffness. Due to shear locking, the stiffness increases at a certain shear angle to significantly higher values.

Poisson's ratios

The Poisson's ratios describe the mechanical coupling between two normal deformation modes. Due to material symmetries in an orthotropic material, one in-plane Poisson's ratio ν_{12} and two out-of-plane Poisson's ratios ν_{23} and ν_{31} have non-zero entries in the stiffness matrix [170].

Penava et al. [171] describe a test to characterize the in-plane Poisson's ratio ν_{12} of a cotton and a wool woven fabric. They used rectangular specimens applying tensile load in a UTM. The strain in the perpendicular direction was measured with an optical system. They concluded that the Poisson's ratio shows a nonlinear behavior and a significant difference for warp and weft direction. Sun et al. developed an analytical mechanical model to calculate the in-plane Poisson's ration of woven fabrics [172].

Very few publications can be found on characterization of the out-of-plane Poisson's ratios. Dixit at al. [173] used a mesoscopic unit cell model to predict the macroscopic elastic properties of a woven fabric.

2.3 Modeling approaches of the through-thickness compaction behavior

Different models have been developed to predict the compaction behavior of fibrous preforms. The models can be classified according to the level of detail on which the compaction is investigated. Micro-scale models look at the behavior of a textile on the level of individual fibers. The compaction is described with the bending and frictional contacts of filaments. On a higher level, yarns are modeled as continuums with homogenized properties. Meso-level models compute the deformation and interaction of individual yarns. As according to Fig. 2-9 most of the compaction effects occur on meso-scale, the literature review on small scale models focuses on the meso-level. Macro-models offer the possibility to compute the compaction behavior of a multi-layer preform as a single continuum. This allows to model more complex structures, as macro-models are in general computationally more efficient. Most of the macro-models use viscoelastic material descriptions to model the time-dependent behavior. Thus, it is interesting to not only look at macro-models specifically developed for fibrous preforms but also to review viscoelastic material models which were designed for materials with comparable behavior.

The analysis of the compaction behavior in Subsection 2.2.1 showed that most of the contributing effects take place in the yarns or the individual fibers. Thus, it is obvious to build simulations on yarn and filament scale to gain deeper understanding of the compaction behavior of textiles. Because there is no consistent definition of the different levels in composite simulations in literature, the following definitions illustrated in Fig. 2-13 are used here:

- Macroscopic scale:

  On a macroscopic scale, the properties of the textile layer are homogenized to a single continuum. The mechanical behavior of the continuum is usually described with an anisotropic constitutive law. This allows to describe the different properties in fiber direction and perpendicular to it in a single element. The smeared approach does not allow to model effects which occur on yarn level, such as gaps between yarns. Simulations on macroscopic level can either be performed with 2D or 3D elements depending on the desired output. For instance, draping simulation models are usually discretized with shell or membrane elements because the focus is mostly on in-plane deformations. However, for compaction simulations, the focus is on the out-of-plane behavior. Thus, compaction models are mostly discretized with 3D continuum elements. Here, no differentiation is made if each layer of the reinforcement is modeled individually or all layers are homogenized over the thickness. In both cases the simulation is on a macroscopic level.

- Mesoscopic scale:

  On a mesoscopic scale, each yarn of the reinforcement is modeled separately. This allows to simulate the interactions between the tows in a textile. The individual yarns are usually discretized with 3D continuum elements, but depending on the application also 2D element approaches are possible. Simulations on mesoscopic level do not allow to simulate the behavior of individual filaments inside a yarn.

- Microscopic scale:

  Models on microscopic scale provide the highest level of detail. Because a single tow usually consists of thousands of individual filaments, discretizing every individual fiber leads to extremely complex models. Hence, it is a common approach to model yarns with a lower number of filaments. Each of those filaments represents a certain number of fibers in the yarn. The filaments are usually discretized with chains of beam or bar elements. These models are called microscopic scale here as well.
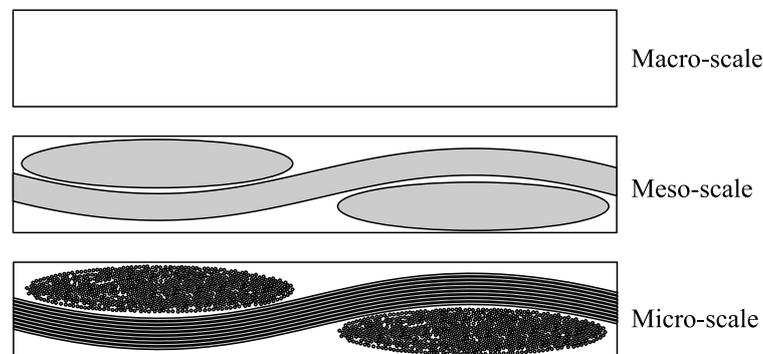
Fig. 2-13:   **Different scales for modeling a plain weave composite (adapted from [174]).**

2.3.1   Models on microscopic scale

Van Wyk [175] was one the first authors who presented a compaction model for fibrous textiles on a microscopic scale. He developed an analytical model which describes the compressibility of wool. In his model, he assumes that the acting pressure can be derived from the bending of individual fibers. Fig. 2-14 shows an overview of different numerical models on micro-scale to describe different kinds of fabrics. Green et al. [176] modeled the compaction of 3D woven preforms numerically on unit cells. They used multiple chains of beam elements for each yarn. The comparison with CT scan images from experiments showed very good agreement. A very similar approach was chosen by Thompson et al. [177] to model the compression behavior of woven fabrics. They used chains of beam elements representing a certain number of fibers in a yarn. The mechanical behavior of the yarn was modeled with a hyper-elastic constitutive model. They were able to predict the compaction pressure for different FVC very well. Durville et al. [178] developed a numerical framework to model 3D angle-interlock fabrics. They used so-called macro-filaments discretized with beam elements to model bundles of filaments in a fabric. The interactions of the individual filaments were modeled with frictional contacts. With a numerical compaction simulation, they were able to predict a nonlinear stress increase during compaction. However, the numerical results were not validated against experimental data. Colin et al. [179] used chains of truss elements to model NCFs on filament scale. They used virtual compaction of the textile to create a model of the manufactured fabric including local defects.
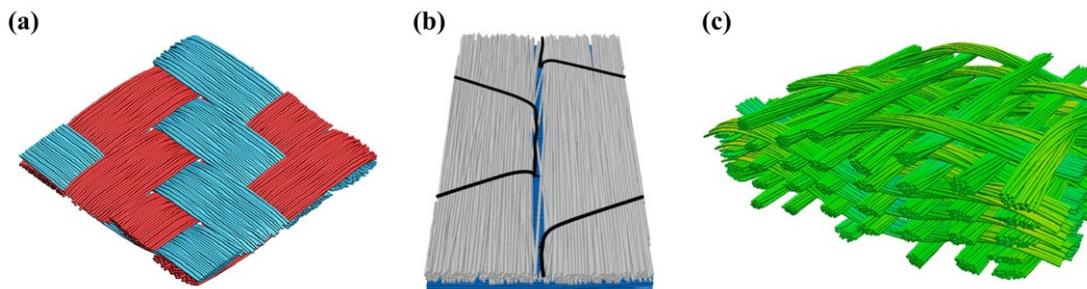
Fig. 2-14:   **Examples of FE models on microscopic scale: (a) woven fabric (adapted from [177]); (b) NCF (adapted from [179]); (c) 3D angle-interlock fabric (adapted from [178]).**

An interesting combination of microscopic and mesoscopic modeling approach was suggested by Chen et al. [180]. They developed an analytical model for the compaction behavior of woven fabrics. In their model shown in Fig. 2-15, they include the bending of the individual fibers in the yarn and the deformation of the yarn cross-section. For the yarn bending, each fiber in the yarn is approximated with an elastic curved beam. However, the compaction of the yarn cross-section is modeled on a mesoscopic level. Their model showed good results compared to experimental data for a plain weave glass fiber fabric. Chen et al. [181] evolved their model to investigate the compaction behavior of multilayer preforms. With the multilayer model, they were able to investigate on nesting

effects and the influence of different numbers of layers. By shifting individual layers, they found that nesting has a significant influence on the compaction behavior of multi-layer preforms.
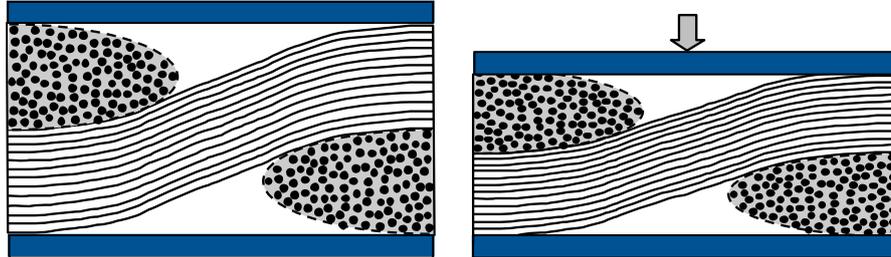
Fig. 2-15:   Deformation of a plain weave unit cell during the compaction (adapted from [180]).

2.3.2   Models on mesoscopic scale

Jeong and Kang [182] studied the compression behavior of a plain weave using a mesoscopic unit cell model (see Fig. 2-16). They applied an isotropic elastic material to the cylindrical yarns and validated their model with compaction experiments from wool and nylon fabrics.
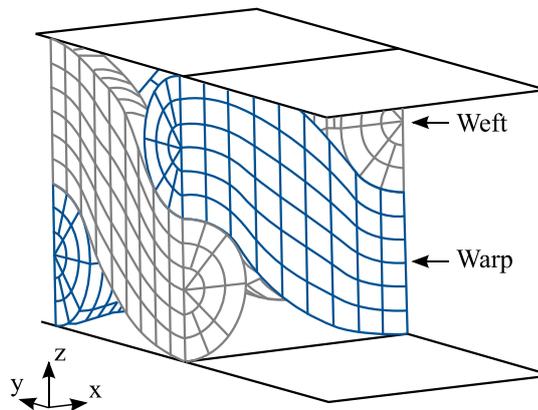
Fig. 2-16:   Mesoscopic unit cell model of a plain weave (adapted from [182]).

Sherburn [183] used a mesoscopic finite element model to simulate the compression behavior of different reinforcement fabrics. He modeled the yarns with 3D continuum elements with a transversally isotropic material. Nonlinear behavior was assumed in longitudinal and transversal direction. The model was accurate in compression and tension of the fabrics. Potluri and Sagar [137] proposed an energy based numerical analysis to compute the compaction behavior of woven fabrics. They used springs to represent the compression of yarns in a unit cell and beam elements for the bending of the yarns. The thickness of the unit cell is computed by minimizing the potential energy function for a given compression force. Grail et al. [184] developed a method to generate finite

element models for several plain weave fabric layers. They modeled the layups on a mesoscopic level focusing on computing the tensile strains of the unit cell after compaction. The did not model the compaction process and thus, did not predict the evolution of the stress during the compression.

Lin et al. [185] used numerical simulations to model the compression behavior of woven fabrics. They modeled the yarns in a unit cell as a continuum with solid elements. They achieved satisfactorily results by using a nonlinear material model for the Young's modulus in yarn thickness direction and the transverse yarn shear behavior. Fig. 2-17 shows models on meso-scale from Nguyen et al. [186] to predict the compaction behavior of textile preforms. The mechanical behavior of the yarn was modeled with a hypoelastic constitutive law. They performed a study on the effect of nesting and in-plane shear on the compaction response of the layup.

(a)   (b)
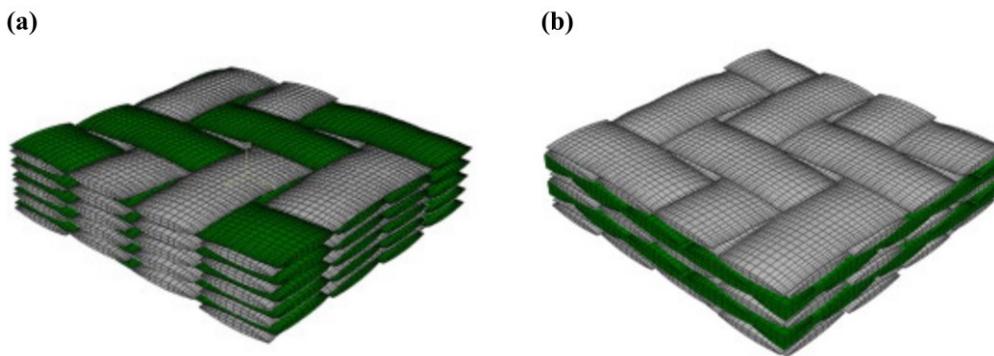
Fig. 2-17:   **Five layer stack of a twill carbon fiber fabric: (a) without nesting; (b) with maximum nesting (adapted from [186]).**

Another mesoscopic approach for modeling biaxial NCF was proposed by Sirtautas et al. [187]. They modeled the mechanical behavior of the tows by superimposing two independent constitutive laws. A linear elastic law was used in fiber direction and a nonlinear law for the transverse behavior. They used the model to predict the draping behavior of a biaxial NCF layer. Wijaya et al. [188] developed a finite element model for the compaction of multi-layer textiles. With a transversally isotropic nonlinear elastic constitutive model they were able to predict the mechanical behavior of the tows. They used a meso-scale model of the textile to simulate the compression behavior.

The models on microscopic and mesoscopic scale have shown excellent capabilities in predicting the internal structure of textile materials. They are extremely useful to gain deeper understanding of effects inside the fabric. These models can also be used for virtual characterization of the material behavior to generate input for simulations on a larger scale. However, the presented models were not capable of predicting the time-dependent behavior which can be observed in experiments. Due to their complexity, small-scale models are extremely computationally expensive and therefore not suitable for process simulations of complex structures.

2.3.3 Modeling approaches on macroscopic level

Macroscopic models are appropriate for the calculation of larger and more complex structures. It is important to keep in mind that simplifications and homogenization lead to a loss of information on a larger scale. An overview of rheological models is given, because many models on macroscopic scale rely on them to predict the time-dependent behavior. Afterwards, approaches to model the through-thickness compaction behavior are reviewed. Special emphasis is placed on the implementation of compaction models into FE codes.

2.3.3.1 Rheological models for viscoelasticity

When modeling the compaction behavior on a smaller scale, the stress response of the fabric is a result of the deformation of fibers or fiber bundles. However, if the compaction is modeled on a macroscopic level, the time-dependent behavior of the textile (see Fig. 2-8) must be inherent in the material model of the continuum. A very common method to describe the constitutive equations for the stress-strain relationship is using rheological models.

Basic rheological elements

In rheology, three basic elements describe the fundamental properties elasticity, viscosity and plasticity. The corresponding elements are the elastic spring or Hooke-element, the viscous dashpot or Newton-element and the friction or Coulomb element [189,190].

Hooke-element

The Hooke-element, which is symbolized by a spring, describes the elastic deformation of a material. If a stress is applied to a purely elastic element, it will deform and once the stress is removed, it returns to its initial shape. In case of a linear elastic material the elastic stress σ_e is described by Hooke's law: [191]

$$\sigma_e = E \cdot \epsilon_e \tag{2-4}$$

With the Young's modulus E and the elastic strain ϵ_e.

Newton-element

The Newton-element is represented by a dashpot and describes the viscous deformation of a material. Viscous materials typically show a strain rate dependent stress response. A Newtonian fluid is defined by a linear dependency of the viscous stress σ_v on the viscous strain rate $\dot{\epsilon}_v$: [190]

$$\sigma_v = \eta \cdot \dot{\epsilon}_v \tag{2-5}$$

Where η is the dynamic viscosity of the material.

Coulomb-element

The Coulomb element describes the plastic or permanent deformation of a material. It can be represented by a frictional element, which deforms only if the applied stress is above the yield stress σ_Y. The strain of a Coulomb element can be given as follows: [190]

$$\epsilon = \begin{cases} 0 \\ \epsilon(t) \end{cases} \quad for \quad \begin{matrix} \sigma < \sigma_Y \\ \sigma > \sigma_Y \end{matrix} \tag{2-6}$$

Different material behaviors can be modeled by connecting these basic elements in series or in parallel. Most of the material models found in literature that describe the compaction behavior of preforms are based on rheological models consisting of springs and dashpots. Consequently, the focus in this subsection is on these models.

Tab. 2-1 shows the characteristic model response for different rheological elements. If a spring element is subjected to a constant strain, it will respond with a constant stress. If a dashpot is subjected to an instantaneous strain ϵ, it sees an infinite strain rate and consequently with Eq. (2-5) infinite stress. If a spring and a dashpot element are connected either in series or in parallel, two basic viscoelastic elements can be created.

Maxwell element

A spring and a dashpot connected in series is called Maxwell element. In a serial combination, the stresses in both elements are the same, whereas the total strain in the Maxwell element is the sum of elastic and viscous strain. The strain rate of the Maxwell element $\dot{\epsilon}$ can be written as follows:

$$\dot{\epsilon} = \dot{\epsilon}_e + \dot{\epsilon}_v \tag{2-7}$$

Thus, combining Eqs. (2-4), (2-5) and (2-7) leads to the differential equation:

$$\dot{\epsilon} = \frac{1}{E}\dot{\sigma} + \frac{1}{\eta}\sigma \tag{2-8}$$

By introducing the relaxation time $\tau = \frac{\eta}{E}$, the homogenous solution of the differential equation yields:

$$\sigma_h(t) = C \cdot exp\left(-\frac{t}{\tau}\right) \tag{2-9}$$

For a relaxation test with the total strain $\epsilon(t) = const$ and thus, $\dot{\epsilon} = 0$, the particular solution of (2-8) is:

$$\sigma_p(t) = 0 \tag{2-10}$$

With the initial condition of the Maxwell element $\sigma(0) = E\epsilon(0)$, the constant can be derived as $C = E\epsilon(0)$. Thus, the solution of the differential equation (2-8) can be written as [192–195]:

$$\sigma(t) = E \cdot exp\left(-\frac{t}{\tau}\right)\epsilon(0) \tag{2-11}$$

In a relaxation test, the stress in the Maxwell element relaxes exponentially according to Eq. (2-11). For times $t \rightarrow \infty$, the stress in the element becomes zero. During a creep test, the stress in the Maxwell element and its constituents remains constant. Thus, according to Eq. (2-4) the elastic strain is constant, whereas the viscous strain increases at constant rate according to Eq. (2-5). Hence, the total strain increases linearly starting at $\epsilon(0) = \frac{\sigma}{E}$.

Kelvin-Voigt element

A spring and a dashpot connected in parallel is called Kelvin-Voigt element. The parallel connection leads to equal strains in the two branches, whereas the total stress is the sum of the elastic and viscous stress. This assumption together with Eqs. (2-4) and (2-5) leads to the differential equation:

$$\sigma = E\epsilon + \eta\dot{\epsilon} \tag{2-12}$$

The differential equation can be solved for a creep test with $\sigma(t) = \sigma(0) = const$. The homogeneous and particular solution can be written as follows:

$$\epsilon_h(t) = C \cdot exp\left(-\frac{t}{\tau}\right) \quad \text{and} \quad \epsilon_p(t) = \frac{\sigma(0)}{E} \tag{2-13}$$

By using the initial condition $\epsilon(0) = 0$ for the creep test, the constant $C = -\sigma(0)/E$ can be determined. Thus, the solution of the differential equation (2-12) is [192–194]:

$$\epsilon(t) = \frac{1}{E} \cdot \left(1 - exp\left(-\frac{t}{\tau}\right)\right)\sigma(0) \tag{2-14}$$

During a relaxation test, the stress in the spring remains constant according to Eq. (2-4). However, the stress in the dashpot is zero due to zero strain rate. Thus, the total stress during the relaxation is only determined by the elastic stress. In a creep test, the total strain increases according to Eq. (2-14) at constant stress $\sigma(0)$. When the stress is removed, the strain is completely recovered going back to zero.

Tab. 2-1: **Rheological elements with characteristic model responses (adapted from [192,196,197]).**

Element	Input	Output
Spring element		
Dashpot element		
Maxwell element		
Kelvin-Voigt element		
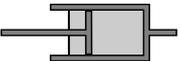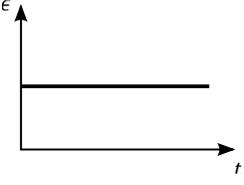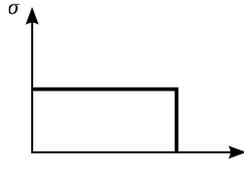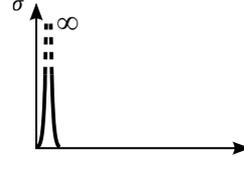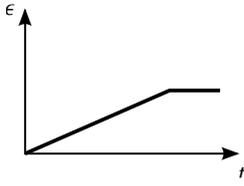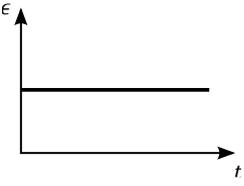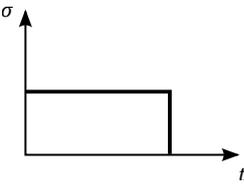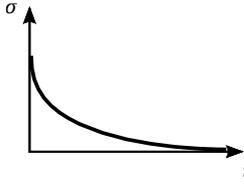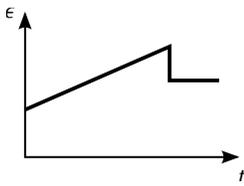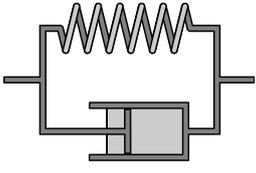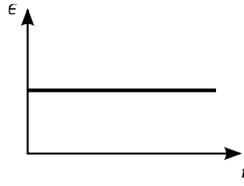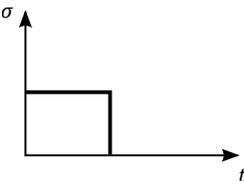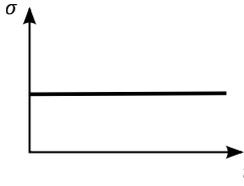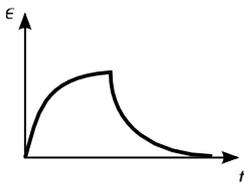
There are various possibilities of combining the rheological elements from Tab. 2-1 to larger structures. Two models which have shown the best suitability for modeling the compaction of fabrics are discussed in more detail, the Burgers and the generalized Maxwell model [198].

Burgers model

The Burgers model is a four-element model consisting of a Maxwell and a Kelvin element connected in series (see Tab. 2-2).

By combining Eqs. (2-4), (2-5) and (2-14), the strain of the creep test can be given as follows [192]:

$$\epsilon(t) = \frac{\sigma(0)}{E_1} \cdot \left(1 + \frac{t}{\tau_1} + \frac{E_1}{E_2}\left(1 - exp\left(-\frac{t}{\tau_2} \right) \right) \right) \tag{2-15}$$

Where E_1, τ_1 and E_2, τ_2 are the elastic and viscous parameters in the Maxwell element and Kelvin-Voigt element respectively.

Tab. 2-2:   **Model response of a Burgers model [192,199].**

As stated in Eq. (2-15), the initial strain $\epsilon(0)$ at $t = 0$ is the strain in the spring with stiffness E_1. During the creep test, the strain increases as a sum of the linear increase from the Maxwell element and the exponential increase from the Kelvin Voigt element. When the stress is released, the strain in the spring E_1 goes back to zero instantaneously. This leads to a jump in the strain response at the beginning of the recovery. The strain decreases and converges to the permanent strain deformation of the dashpot τ_1. As stated in Eq. (2-15), the initial strain $\epsilon(0)$ at $t = 0$ in a relaxation test is the strain in the spring with stiffness E_1. The model response of a relaxation test is defined by the free dashpot causing the strain in the remaining elements to recover. Thus, the total stress converges to zero.

Generalized Maxwell model

As depicted in Tab. 2-3, the generalized Maxwell model consists of several Maxwell elements and a spring element, which are connected in parallel. The number of so-called Maxwell-branches is arbitrary and can be chosen to fit experimental data best. As the number of parameters increases with more parallel branches, a sensitivity analysis is usually performed to determine a reasonable number of branches. Due to the parallel connection, the strains in all branches of the generalized Maxwell model are the same. The total stress can be calculated by the sum of the stresses in the individual branches. Thus for N Maxwell branches the total stress can be determined from Eqs. (2-4) and (2-11):

$$\sigma(t) = E_0\epsilon(0) + \sum_{j=1}^{N} E_j \, exp\left(-\frac{t}{\tau_j}\right)\epsilon(0) \tag{2-16}$$

Tab. 2-3:   **Model response of a generalized Maxwell model [198].**

Element	Input	Output
generalized Maxwell model		
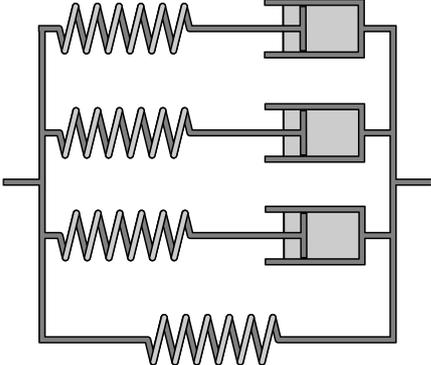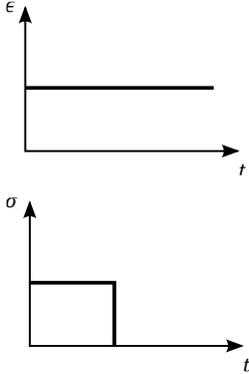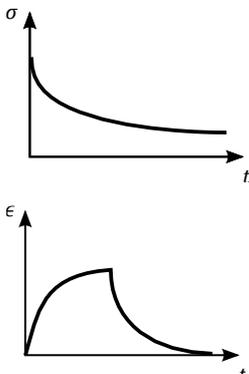
In a relaxation experiment, the stress in a generalized Maxwell model decreases exponentially according to (2-16). Because of the free spring E_0, the total stress does not relax to zero. For $t \to \infty$, the total stress equals the stress in the free spring, $\sigma = E_0\epsilon(0)$. Because of the free spring, the response of the creep test shows an instantaneous strain. During the creep test, the dashpots are slowly releasing their initial stress. The generalized Maxwell model reaches an equilibrium state when all dashpots have zero strain rate und thus, zero viscous stress. The following stress release leads to an instantaneous recovery of the elastic stress of the spring E_0. In the further course, the strain which is stored in the dashpots goes back to zero. Contrary to the Burgers model, the strain converges to zero without any permanent deformation [198].

A general formulation for the stress during a relaxation test has been reported by Schapery in [200]:

$$\sigma(t) = E(\infty)\epsilon + \Delta E(t)\epsilon \tag{2-17}$$

Where $E(\infty)$ is the final or equilibrium value of the so-called relaxation modulus. $\Delta E(t)$ is the transient value of the modulus. The stress response to an arbitrary strain input can be calculated as follows by means of the Boltzmann superposition integral [200]:

$$\sigma(t) = E(\infty)\epsilon + \int_0^t \Delta E(t-s)\frac{d\epsilon}{ds}ds \tag{2-18}$$

Where $\Delta E(t-s)$ is the relaxation function. In a similar way the strain response in a creep experiment can be calculated with the creep compliance $D(t)$ [200]:

$$\epsilon(t) = D(0)\sigma + \int_0^t \Delta D(t-s)\frac{d\sigma}{ds}ds \tag{2-19}$$

With the creep function $\Delta D(t-s)$. According to Eq. (2-16) the relaxation function of a generalized Maxwell-model is defined as:

$$\Delta E(t-s) = E_0 + \sum_{j=1}^{N} E_j \, exp\left(-\frac{t-s}{\tau_j}\right) \tag{2-20}$$

Thus, the stress in the integral representation can be given as [195]:

$$\sigma(t) = E_0\epsilon(t) + \sum_{j=1}^{N}\int_0^t E_j exp\left(-\frac{t-s}{\tau_j}\right)\frac{d\epsilon}{ds}ds \tag{2-21}$$

Solving the integral leads to the recursive formulation of the stress $h_j(t)$ in one Maxwell branch as presented by Kaliske and Rothert [195]:

$$h_{j,t+\Delta t} = exp\left(-\frac{\Delta t}{\tau_j}\right)h_{j,t} + \frac{E_j}{E_0}\frac{1 - exp\left(-\frac{\Delta t}{\tau_j}\right)}{\frac{\Delta t}{\tau_j}}\left[\sigma_{0,t+\Delta t} - \sigma_{0,t}\right] \quad (2\text{-}22)$$

With this formulation the current stress at time $t + \Delta t$ in one Maxwell branch $h_{j,t+\Delta t}$ can be given in dependency of the stress of the previous time step $h_{j,t}$. The parameter $\sigma_{0,t}$ is the stress in the free spring at time t. By introducing the "initial stress" $s_0 = \sigma_0\frac{E_j}{E_0}$, the following recursive formulation by Simo and Hughes [201] can be derived:

$$h_{j,t+\Delta t} = exp\left(-\frac{\Delta t}{\tau_j}\right)h_{j,t} + \frac{1 - exp\left(-\frac{\Delta t}{\tau_j}\right)}{\frac{\Delta t}{\tau_j}}\left[s_{0,t+\Delta t} - s_{0,t}\right] \quad (2\text{-}23)$$

The total stress in the generalized Maxwell model with N branches at time $t + \Delta t$ can be given as [195,201]:

$$\sigma_{t+\Delta t} = E_0\epsilon_{t+\Delta t} + \sum_{j=1}^{N} h_{j,t+\Delta t} \quad (2\text{-}24)$$

Finite element implementation of rheological models

The incremental formulation of the stress is well suited for an implantation into a finite element code. Kaliske and Rothert [195] used their formulation to predict time-dependent deformations of rubber structures. Careglio et al. [202] used the recursive formulation in Eq. (2-24) in a finite element code and validated it with analytical results. They achieved very good results for relaxation and creep tests. In [203] Schapery extends his viscoelastic model to three-dimensional cases based on thermodynamic principles. Lai and Bakker [204] extended the one-dimensional Schapery representation for creep to a three-dimensional model. They showed that the time step size has no influence on the accuracy and that numerical results matched experimental data very well.
In a publication from 1997 [205] Schapery included nonlinear viscoelastic and viscoplastic behavior into the constitutive equations. Varna et al. [206] analyzed Schapery's nonlinear viscoelastic model to simulate strain-controlled boundary conditions. They used the incremental form of the model for an implementation into a finite element software. Haj-Ali and Muliana [207] implemented Schapery's three-dimensional model in its incremental form into a finite element environment. Their numerical results for creep and recovery strain response were in good agreement with the experiments. In [208] Monsia used a single Maxwell element with nonlinear spring and nonlinear dashpot to model the time-dependent behavior of viscoelastic materials. In 2019, Birzle and Wall [209] used nonlinear viscoelastic models to predict the

compression behavior of biomedical materials. Their model is based on a generalized Maxwell element with an additional fractional term. Xia et al. [210] modeled the compaction behavior of an epoxy polymer using a nonlinear viscoelastic model. Their model consists of a series of Kelvin-Voigt elements with an additional spring. The comparison of their model and Schapery's model with experimental results showed generally a good agreement. However, Schapery's model could not predict stress unloading at high stress levels accurately.

2.3.3.2 Macroscopic modeling approaches of fibrous materials

Besides the material models which generally describe viscoelastic material behavior, there are material models which have been specifically developed to predict the response of fibrous preforms. Tab. 2-4 gives an overview of the most relevant compaction models in literature for preforms and prepregs. Most of the macroscopic formulations are based on rheological models presented in Subsection 2.3.3.1 or the decomposition of strain and strain rate dependent stresses.

Formulations based on rheological models

Kim et al. [117] performed compression and relaxation tests on different rovings, a plain weave and a random mat. They fitted the experimental relaxation data to a Maxwell-Wiechert model, which corresponds to the generalized Maxwell model without the free spring. For the compression, they propose the following model from Gutowski to calculate the stress in thickness direction [211]:

$$\sigma = A_s \frac{\sqrt{\frac{V_f}{V_0}} - 1}{\left(\sqrt{\frac{V_a}{V_f}} - 1\right)^4} \tag{2-25}$$

Where A_s is a constant, V_f the FVC, V_0 the initial FVC and V_a the maximum possible FVC. A very similar approach with different formulations for compaction and relaxation was suggested by Bickerton and Kelly in [116]. Similar to Kim et. al, they used a parallel connection of several Maxwell-elements to model the relaxation behavior. Vangheluwe and Kiekens [212] developed a model which describes the relaxation behavior after dynamic loading of the preforms. They used a nonlinear generalized Maxwell model with a single Maxwell element. The stress in the free spring is proportional to the square of the strain. Vangheluwe's model has been adapted by Ghosh et al. [213] to model the strain rate dependent behavior of different spun yarns. They assumed the nonlinear behavior of the free spring to be dependent on ϵ^n, with $n > 0$.

Kelly et al. [119,214] investigated on the viscoelastic compaction behavior of continuous glass filament mats. They derived a formulation for the stress response from a finite strain thermomechanical model. They obtained a model which corresponds to a generalized Maxwell model with nonlinear springs in the branches. Their formulation allows to model compression and relaxation in a single equation. A comparison of experimental and model results for a compaction of dry and wet CFM preforms to a FVC of 0.35 is shown in Fig. 2-18. The model matches the qualitative behavior very well. However, there are significant deviations during the relaxation, especially for the dry material. More recently, Khan et al. [215] used Kelly's model and extended it with an additional material parameter. They applied the model to predict the compaction response of different kinds of 3D woven fabrics.
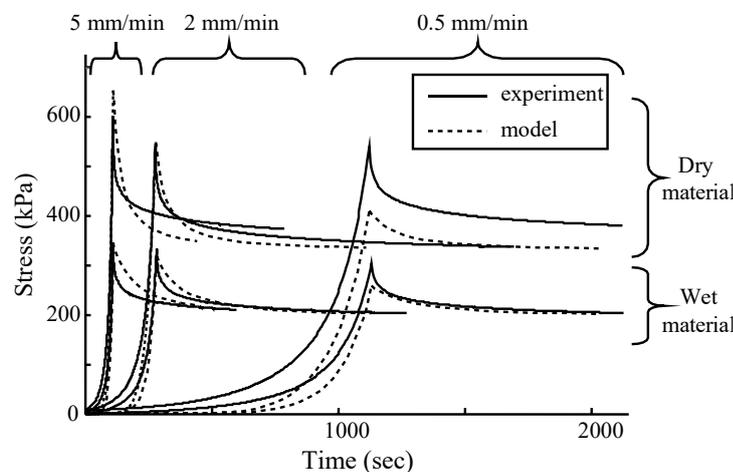
Fig. 2-18:   **Experimental and model stress response for CFM preforms at different compaction speeds [119].**

Matsuo et al. [216] modeled the relaxation behavior of different knitted fabrics with a Burgers model. Relaxation experiments were performed at different rotation angles from the normal axis in thickness direction. Their results were in good agreement with experimental data. Somashekar et al. [217] used various glass fiber reinforcements, such as plain weave, biaxial stitched fabric, CSM and CFM for compaction experiments. They applied a linear generalized Maxwell model to predict the stress response during the relaxation. However, their model did not account for the influence of different compaction velocities on the relaxation behavior. Xiong et al. [218] used a model based on a generalized Maxwell approach to predict the compaction behavior of thermoplastic prepregs. They used the recursive formulation Eqs. (2-23) and (2-24) by Simo and Hughes [201] to calculate the stress response. They implemented the model into a commercial FE software to model the consolidation behavior of thermoplastic prepregs during thermoforming.

Danzi et al. [107] published a compaction model for dry woven carbon fiber fabrics. Their formulation uses a single formula for compression and relaxation, which is based on a nonlinear generalized Maxwell model with three branches. The springs and dashpots in the model are nonlinear. They used a Heaviside function to activate a second term for the stress relaxation after the compression step. They defined the stress response in dependency of the ramp time t_r as follows:

$$
\begin{aligned}
\sigma(t) = \dot{\epsilon} \Big\{ & E_0 t + \tau_1 E_1 \left(1 - \exp\left(-\frac{t}{\tau_1} \right) \right) + \tau_2 E_2 \left(1 - \exp\left(-\frac{t}{\tau_2} \right) \right) + \\
& \tau_3 E_3 \left(1 - \exp\left(-\frac{t}{\tau_3} \right) \right) - \Theta(t_r - t) \Big[E_0 (t_r - t) + \\
& \tau_1 E_1 \left(\exp\left(-\frac{t_r - t}{\tau_1} \right) - 1 \right) + \tau_2 E_2 \left(\exp\left(-\frac{t_r - t}{\tau_2} \right) - 1 \right) + \\
& \tau_3 E_3 \left(\exp\left(-\frac{t_r - t}{\tau_3} \right) - 1 \right) \Big] \Big\}
\end{aligned}
\tag{2-26}
$$

The predicted stress response for a ramped strain input was in very good agreement with experimental results. However, there are two main drawbacks, which make an implementation of the model into an FE code difficult. On the one hand, Eq. (2-26) requires a constant strain rate limiting the model to cases with constant strain rate during the compaction. On the other hand, the ramp time needs to be known in advance. This might be difficult in cases, where not all preform surfaces are in contact with the tool at the same time (e.g. in small tool radii). More recently Werlen et al. [219] validated Danzi's model for different fabrics in dry and wet condition. They solved the model numerically and linearized it over small time increments. This way they could overcome the drawbacks of Danzi's original model mentioned above. The model predictions of the stress response were accurate compared to the experimental data. Mei et al. [220] developed a compaction model for glass fiber fabrics for varying temperatures. They propose to use a generalized Maxwell model for relaxation experiments and a series connection of two Kelvin-Voigt elements with a spring for creep experiments.

Formulations based on strain and strain rate dependent functions

Besides rheological models, the decomposition of the stress into a strain and a strain rate dependent function is a commonly used method in literature to describe time-dependent behavior.

Saunders et al. [221] developed a compaction model for resin-impregnated fiber cloths. They split the compaction pressure into one component to compress the fiber bed and one representing the resin pressure. Their model for the viscoelastic deformation of the fiber network is summing an elastic and a viscous stress component. They validated their model only for the compression phase. A very similar approach was chosen by Hubert et al. [131] to describe the compaction response of carbon fiber prepregs. They assumed that the fiber bed deformation is purely elastic, whereas the viscous component of the response comes from the compaction of the resin. The total compaction stress is composed of the sum of the elastic stress in the fiber bed and the resin pressure. The

additively composition of strain and strain rate dependent stress can also be interpreted as a Kelvin-Voigt element (see Fig. 2-19).
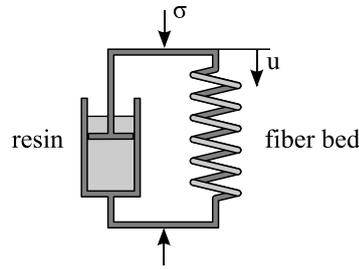
Fig. 2-19:   **Kelvin-Voigt representation of an additively composition of stresses (adapted from [131]).**

Furthermore, a multiplicative decomposition has been used to combine strain and strain rate dependent responses in a constitutive law. Accordingly, the viscoelastic behavior can generally be described as [222]:

$$\sigma(\epsilon, \dot{\epsilon}) = f_\alpha(\dot{\epsilon}) f_\beta(\epsilon) \tag{2-27}$$

For compaction experiments, Eq. (2-27) can be interpreted as the multiplicative decomposition of FVC and compaction speed dependent functions. Kelly [222] developed a model for the compaction phase based on Eq. (2-27). For the stress relaxation phase, Kelly proposes a different model based on his formulation in [119]. According to the author, the model only applies for materials, for which the normalized stress curves collapse to a single master curve.

Belnoue et al. [223] developed a hyper-viscoelastic compaction model for thermoset prepregs based on Kelly's findings for impregnated preforms. They used the following formulation to calculate the stress response [223]:

$$\sigma(\epsilon, \dot{\epsilon}) = f_\alpha(\dot{\epsilon}) f_\beta(\epsilon) \dot{\epsilon} = f_\alpha(\dot{\epsilon}) f_{micro}(\epsilon) f_{macro}(\epsilon) \dot{\epsilon} \tag{2-28}$$

In their phenomenological model, the strain dependent term is composed of a term accounting for deformation on macro-scale and a term for micro-scale. The model from Belnoue was later used by Valverde et al. [224] to model the compaction behavior of reinforced thermoplastic UD tapes. Blößl and Schledjewski [225] developed an empirical model based on the compaction work for different natural fiber textiles. Their model is only applicable to predict the stress response during the compression phase.

Tab. 2-4 gives an overview of the most relevant compaction and relaxation models reviewed in this section. The table shows that most models that can predict compaction and relaxation for glass and carbon fiber preforms are based on generalized Maxwell models. However, some of these approaches use separate models for the two phases. As pointed out by Kelly et al. [119], it is advantageous to have a single model for compaction and relaxation. The model from Danzi et al. [107] is not considered as a single

model, because two models are connected with a Heaviside function. This would require a case distinction when implemented in a subroutine. The models from Belnoue et al. [223] and Valverde et. al [224] show a very promising approach for prepregs.

Tab. 2-4: **Overview of macroscopic material models for the compaction behavior of fibrous textiles**

Materials	Generalized Maxwell/ Maxwell Wiechert	Burgers and Voigt model	Decomposition of strain and strain rate	Empirical
Dry carbon fiber fabric	**Khan et al [215]** Danzi et al. [107] **Werlen et al. [219]**			
Dry glass fiber reinforcements	Kim et al. [117] Bickerton and Kelly [116] **Kelly et al. [119]** Somashekar et al. [217] Mei et al. [220]		Kelly [222]	
Natural fiber and other fiber materials	Vangheluwe and Kiekens [212] Ghosh et al. [213]	Saunders et al. [221] Matsuo et al. [216]		Blößl and Schladjewski [225]
Pre-impregenated fibers (thermoset and thermplastic)	Xiong et al. [218]		Hubert and Poursartip [131] **Belnoue et al. [223]** **Valverde et al. [224]**	

compaction   relaxation   both   **single model**

Comparative studies:

Šajn et al. [226] performed stress relaxation experiments with several kinds of woven wool/lycra fabrics. They used different rheological models to predict the stress response of the tested materials. They found that a generalized Maxwell model with a nonlinear free spring shows the most accurate results. Yenilmez et al. [198] compared different rheological models to analyze their capability to predict the compaction behavior of woven fabrics. They included Maxwell, Kelvin-Voigt, Zener, Burgers and generalized Maxwell model for the study. A Zener model is a simplified generalized Maxwell models with a single viscoelastic branch. The models were tested for a stress input consisting of load increase, settling at constant load, unloading and strain relaxation at zero stress. They concluded that Burgers and generalized Maxwell models have the highest performance. However, there was a significant difference in the performance of these two models. Burgers model showed good performance for the material spring-back when the stress was released, but failed to model the creep behavior at constant stress accurately. The characteristics of the generalized Maxwell model were exactly the opposite with good prediction of the creeping and poor results for the spring-back. Dörr et al. [227] implemented two different nonlinear viscoelastic models in a commercial FE code, a Kelvin-Voigt and a generalized Maxwell model. They analyzed both approaches for the applicability to model the intra-ply behavior of thermoplastic UD-tapes. They concluded that only the generalized Maxwell model can describe the whole material characteristic.

2.3.3.3   Planar compaction process simulation models

Several macroscopic compaction models presented in Subsection 2.3.3.2 have been implemented into FE codes in order to simulate composite manufacturing processes. Solving the models numerically enables the possibility to analyze different geometries and applying non-constant displacement or force boundary conditions. Moreover, many authors coupled the compaction analysis with a resin filling simulation [228–232]. This allows for considering the effect that the permeability is dependent on the FVC of the preform [233–235]. In force-controlled setups, such as VARTM, the coupling allows to predict the thickness increase due to lubrication effects in the preform [236–238].
Models designed for simulating closed mold processes mostly focus on the prediction of tooling forces. With the numerical analysis, setup costs can be optimized and the usage of press capabilities can be maximized [239]. Bickerton and Buntain [228] developed an FE model to predict forces in RTM and injection compression molding processes. Their model assumes that the total clamping force F_{clamp} consists of the force in the fiber bed F_{fiber} and the fluid force F_{fluid} from the resin pressure:

$$F_{clamp} = F_{fiber} + F_{fluid} \qquad\qquad (2\text{-}29)$$

They used a simple model with a Taylor series for the compaction stress. Their model is capable of predicting clamping forces during the whole process from dry compaction to the complete filling of the part. Gupta et al. [229] improved the model presented in [228] in order to consider rate dependency of the preform. They used Eq. (2-29) and applied a bilinear model for the dependency of the fiber compaction stress on the compaction velocity. A similar approach based on Eq. (2-29) was chosen by Walbran et al. [230] to model forces in RTM and compression RTM processes. They implemented the viscoelastic compression model from Kelly [222] in an FE code. A separate model for stress relaxation based on the decomposition of strain and strain rate dependent stress was applied in the code.

Further research focused on predicting the thickness in force-controlled processes such as VARTM or resin film infusion. Kang et al. [231] developed a model to compute the swelling of the preform during infusion in a VARTM process. Similar to previous authors, they assume that the load is shared by a purely elastic fiber bed and the viscous resin. The fiber bed compaction stress is defined by a nonlinear expression depending and the FVC. The impregnated fiber bed is modeled with a viscoelastic element consisting of a spring in series with a Kelvin-Voigt element. Park and Kang [232] used the same approach and applied it to resin film infusion processes. Correira et al. [240] developed a process simulation model to predict resin flow and compaction in VARTM processes. They describe the compaction pressure with a power law in dependency of the FVC. Their model does not account for stress relaxation or material creep. Another process simulation model was developed by Acheson et al. [236]. They coupled a filling and compaction simulation to predict the thickness in VARTM processes. They used a model from Gutowski, Eq. (2-25), to relate the compaction stress to the FVC. Givignon et al. [237] presented a coupled filling and compaction simulation approach for VARTM which uses a one-dimensional FE model for the compaction. They use a simple power law which describes the FVC in dependency of the compaction stress. More recently Chang [238] presented a coupled injection and compaction approach for force-controlled RTM processes. He related compaction stress to the FVC with experimental data without using a model.

In most of the discussed approaches, rather simple compaction models were used. This is motivated by an easier implementation and shorter calculation times. Moreover, the material characterization for a complex model requires extensive testing. However, most of the simple compaction models do not allow predicting time-dependent effects. Furthermore, the models presented here were only applied for planar geometries. Effects which occur during the compaction of non-planar preforms are not considered.

2.4 Modeling approaches for non-planar compaction behavior

During the compaction of more complex shaped preforms, further effects occur in addition to the viscoelastic behavior in thickness direction. Different in-plane tension or compression on the inner and outer preform layers lead to shear strains in the preform. Consequently, compaction models need to be extended in order to predict the behavior of non-planar cases. In this section, modeling approaches to predict the compaction response of non-planar reinforcements are presented. After a brief overview of analytical models, the focus is placed on numerical process simulations. Because the material behavior during LCM and prepreg processes is very similar and compaction simulation approaches are nearly the same, both processes are included in the review. Moreover, there is more literature published on prepreg processes.

2.4.1 Analytical models for the prediction of thickness gradients

Gao and Young [241] developed a simple model for the prediction of the layup height after bending around a small convex tool radius. Their model takes fiber stretching, fiber straightening, shear slip and buckling into account to calculate the thickness after preforming. Bickerton et al. [242] used an analytical model to account for FVC and permeability changes in curved preforms. They assume a uniform FVC in all layers, which is increased due to in-plane compression of the preform after bending. They calculate the FVC in dependency of the inner tool radius, the total thickness of the preform, the initial FVC and the FVC of the tows.

Dong [71] suggested the following analytical model to calculate the gap height $h_{r,max}$ in a closed curved RTM tool:

$$h_{r,max} = \frac{hP\mu sin\phi}{r^a V_f^b} \tag{2-30}$$

Where h is the thickness of the mold cavity, P is the mold closure force, μ the friction coefficient, ϕ the curvature angle, r the mid-plane radius as depicted in Fig. 2-20 and V_f the FVC. With parameters a and b the model is fitted to experimental data.

Koutsonas [63] used a power law with two fitting parameters to calculate the preform height in dependency of the compaction pressure. The gap height was determined by fitting the simulation results to experimental data. Levy and Hubert [88] developed an analytical model for the prediction of thickness variations of out-of-autoclave prepreg processes. Their model calculates the thickness based on two geometric ratios, the radius to flange length and the thickness to radius ratio.
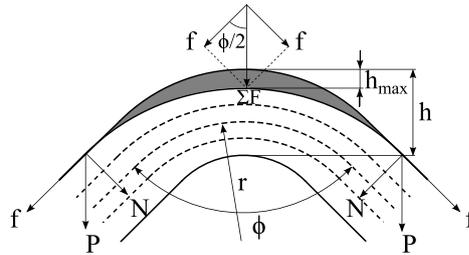
Fig. 2-20:   **Preform deformation and resulting gap height in tool radii (adapted from [71]).**

2.4.2   Finite element modeling approaches for non-planar compaction

There are viscoelastic material models available in commercial FE software tools, such as Abaqus/CAE or ANSYS [243,244]. However, the provided models offer only the possibility to use isotropic material properties. Thus, in order to use a material model with viscoelastic out-of-plane and elastic in-plane behavior with different stiffness, programming a user-defined material is necessary. A compaction model from Kelly and Bickerton [245] has been implemented in LIMS. LIMS is the liquid injection molding simulation tool developed at the University of Delaware [246].

LCM processes

The compaction response of non-planar preforms in LCM process has not been modeled by many authors. Bickerton and Kelly [245] implemented their viscoelastic model presented in [119] in a FE software to predict tooling forces in RTM process. They extended the model to complex geometries by adding a shear stress component τ according to:

$$\tau = \begin{cases} 0 & \alpha = 0 \\ \mu_f \sigma_f & \alpha > 0 \end{cases} \tag{2-31}$$

With the known draw angle α of the tool, the shear stress component in closing direction is calculated from the friction coefficient μ_f and the normal stress σ_f. One of the main drawbacks is, that the angle between surface and tool closing direction needs to be known for every element.

In a later publication, the same authors [239,247] presented a tooling force analysis for RTM and injection compression molding processes. They applied the same methodology to different geometries and compared numerical results to experimental data. Fig. 2-21 shows the normal and shear stress distribution after the compaction and before the resin injection in an RTM process.
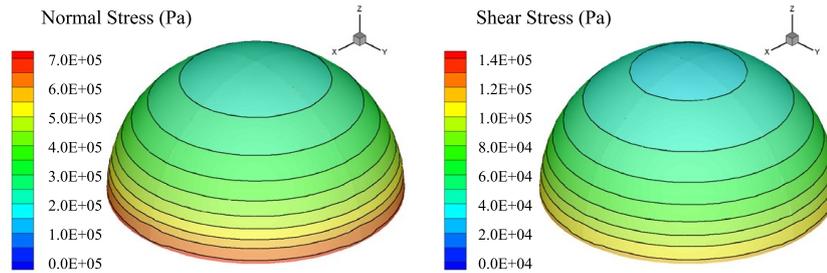
Fig. 2-21:   **Normal and shear stress of a hemisphere after compaction and before resin injection (adapted from [247]).**

Walbran et al. [70] implemented the compaction model described by Kelly in [222] in an FE code. They also accounted for the shear component of the resulting compaction stress by the friction coefficient between tool and preform according to Eq. (2-31).

Some authors applied compaction models in process simulations for compression RTM. Because this process is often force-controlled, predicting the thickness of the final part is of special interest. Most of the reviewed literature showed the implementation of simple models without time-dependency not allowing for the prediction of creep or spring-back effects [248–250]. Verleye et al. [251] presented a model for compression RTM processes applying an iterative method to solve the viscoelastic model from [222]. With this approach, they were able to use a time-dependent model for force-controlled setups. Although the model is applied to complex geometries, it does not account for frictional or out-of-plane shear effects.

Causse et al. [56] developed a process model for the compaction during the flexible injection process. They describe the compaction stress with a power law in dependency of the compaction strain. A simplified 2D plane strain model predicted the preform deformation in concave and convex corners. The longitudinal and the shear behavior were modeled with linear elastic relations. They varied the shear stiffness in the model in order to fit the resulting deformation to experimental results. Fig. 2-22 shows the results of a compaction simulation for different tool radii. It can be seen that high shear stresses appear in the curved section, especially for small tool radii.
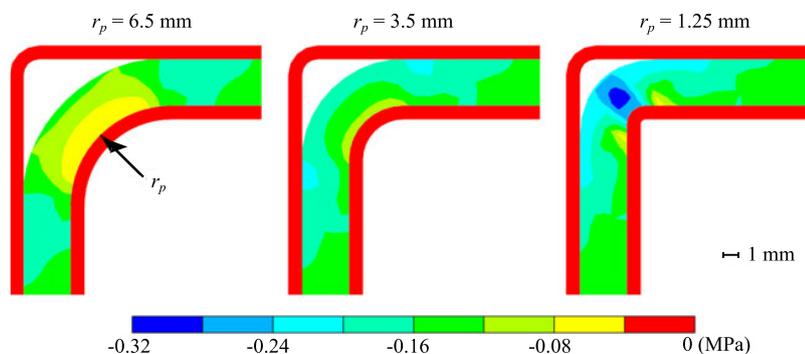
Fig. 2-22:   **Shear stress distribution after compaction for different inner tool radii (adapted from [56]).**

Prepreg processes

Hubert et al. [96] developed a 2D model for the compaction of non-planar prepreg laminates. Their model describes the flow and compaction in a cross section of the laminate during autoclave processing. The whole lay-up is discretized with a single continuum layer. They describe the constitutive law of their model as follows:

$$\begin{Bmatrix} \sigma_1 \\ \sigma_3 \\ \tau_{13} \end{Bmatrix} = \begin{bmatrix} E_1 & 0 & 0 \\ 0 & E_3 & 0 \\ 0 & 0 & G_{13} \end{bmatrix} \cdot \begin{Bmatrix} \varepsilon_1 \\ \varepsilon_3 \\ \gamma_{13} \end{Bmatrix} \tag{2-32}$$

Where ε_1 and σ_1 are stress and strains in-plane and ε_3 and σ_3 describe the behavior in thickness direction. G_{13} is the out-of-plane shear stiffness, which describes the shearing of the modeled continuum. Interestingly, the authors neglected all coupling factors. With a parametric study, they found that the shear modulus of the fiber bed has a significant influence on the compaction behavior in tool radii. Hubert's model with Eq. (2-32) was later used by Qiao et al. [252] to analyze the compaction behavior of thick composite layups during autoclave processing.

Ganapathi et al. [253] used a 3D model to investigate on process-induced thickness variations of GFRP wind turbine caps. They used a nonlinear model for the fiber bed compaction and an FVC dependent out-of-plane shear modulus in their constitutive model. A more recent 2D process model for the consolidation of prepregs was presented by Amini Niaki et al. [254]. They used literature values from Hubert et al. [96] for the out-of-plane shear stiffness. Their model is capable of predicting the thickening effect in 90° corners as well as edge deformations of the stack. Sakhaei et al. [255] developed a 3D model for the deformation of uncured prepregs. Their model allows to define tensile stiffness, shear stiffness and bending stiffness independently.

Belnoue et al. [92] applied the hyper-viscoelastic model presented in [223] to simulate the consolidation of thick composite parts manufactured in autoclave prepreg processes. For their approach each layer was modeled separately with frictional inter layer contacts. As shown in Fig. 2-23, they were able to predict the generation of wrinkles in thick complex structures.
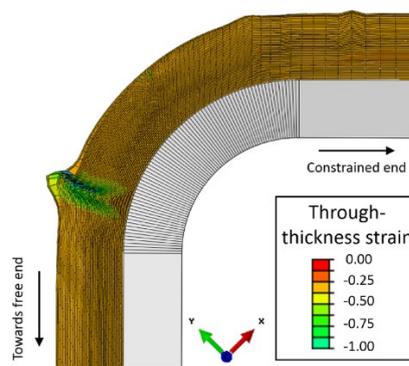
Fig. 2-23:   **Simulation result of a prepreg C-section cured in an autoclave process ([92]).**

Thompson et al. [256] combined shell and membrane elements to model the compaction behavior in autoclave prepreg processes. In their modeling approach each individual layer of the stack is modeled separately. The in-plane behavior of the material is defined by the stiffness of the membrane element, whereas the bending behavior is controlled by the shell elements. In order to account for the through-thickness behavior, they implemented an elastic penalty stiffness of the intra-ply contacts. The underlying compaction model is nonlinear but it is not capable of showing time dependency effects. A result of the compaction induced defect which occurs in the radius is shown in Fig. 2-24.
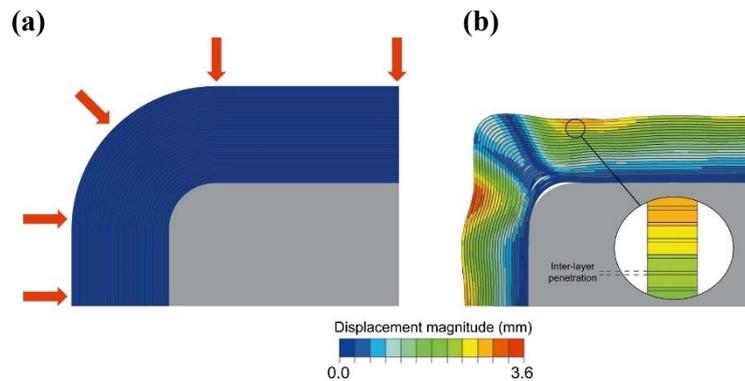
Fig. 2-24:   **Compaction simulation of a prepreg autoclave process: (a) boundary conditions; (b) deformation after pressure application (adapted from [256]).**

2.5 Research questions

The literature review showed the complexity of the orthotropic time-dependent compaction behavior of preforms. There are several promising approaches to model the behavior of preforms. However, none of the reviewed models covered all aspects of the material behavior of dry preforms. Based on the results of the literature review, the following research questions are formulated to accomplish the objectives defined in Section 1.3:

1. How can the main deformation mechanisms of a dry preform be characterized in order to be used as input for mechanical simulations?
2. How can the compaction behavior for relaxation and creep of dry preforms be described in a single formula which is suitable for an efficient FE implementation?
3. How can the one-dimensional model be extended to non-planar compaction cases by including the remaining deformation mechanisms and which guidelines for stable manufacturing processes can be derived?
4. How can results of a compaction simulation be transferred to subsequent filling simulations to enable the integration into a virtual manufacturing process chain?

Each research question is addressed in one of the following chapters of this work.

3 Experimentation

Based on the conclusions on the literature review in Subsection 2.1.3, through-thickness compaction, out-of-plane shear and tool-preform friction are characterized in this chapter. With the results of these experiments research question 1 raised in Section 2.5 is answered. Moreover, non-planar compaction experiments are performed, which will be used for calibration and validation of the 3D-model in Chapter 5.

3.1 Materials

The content of this section is partly derived from the preprint of [P1].

Two different carbon fiber materials were used for the experiments carried out in this work, the woven fabric (WV) HexForce G0926 [257] and the biaxial NCF Tenax-E DRNF PB1 [258]. The carbon fiber satin weave consists of 6k rovings and has 2.5% epoxy powder E01 on each side with an areal weight AW of 375 g/m^2. The NCF material consists of two ±45° layers with 24 k carbon fiber rovings and stitching yarns in a tricot pattern. 1.7% powder binder EP05311 are located on the top side of the material. The areal weight of the NCF is 388 g/m^2.

For the preforms, that were used for the compaction and shear experiments, the fabrics were cut into squares of 440 mm × 440 mm using a Zünd M-1200 CNC-cutting machine. Afterwards, the cut layers were stacked to a symmetric twelve-layer cross-ply layup of alternating 0° and 90° layers. Every second layer was rotated by 90° with two layers of the same orientation in the middle of the preform. The binder of the stacked layups was activated in a hot press with 600 mm × 600 mm plates at 100 °C. For the weave material, a force of 1000 kN was applied for 60 s. The NCF was preformed with 580 kN force for 120 s. In both cases, steel shims with 7.0 mm were used to ensure a uniform sample thickness. The preforms were cooled at room temperature. After preforming, 20 mm was cut from every edge to avoid fringed areas in the specimens. The preformed samples were cut into the final dimensions of the specimens for the experiments using the CNC-cutting machine. For the friction experiments, only single layers of the woven fabric were used. In order to test the material under the same processing conditions, the binder was activated prior to the experiments. The fabrics were compacted with 1 bar pressure at 100 °C for 60 s.Because each specimen for the non-planar compaction experiments needed to be produced individually in the curved tools, the manufacturing process was more complex. The preparation of the L-shaped specimens is described in detail in Subsection 3.5.1.

3.2 Compaction experiments

The content of this section is partly derived from the preprint of [P1].

A UPM 250 universal testing machine from Hegewald und Peschke with a 250 kN load cell was used for the compaction experiments. Two square steel plates with a length of 220 mm ensured a uniform pressure distribution on the surface of the specimen (see Fig. 3-1). A video extensometer with a telecentric lens was used to measure the distance of the two compaction plates during the experiment. Parallel markers with black and white lines together with a monochromatic blue light ensured maximum contrast for the distance measurement. Fig. 3-1 shows the setup with the markers on the two compaction plates.
Preform specimens with 100 mm x 100 mm size were used for the compaction experiments. The tests were performed with the weave material and the NCF. The weave specimens had an average thickness of 8.05 mm with a standard deviation of 0.11 mm, and 6.81 mm with a standard deviation of 0.06 mm for the NCF specimens.
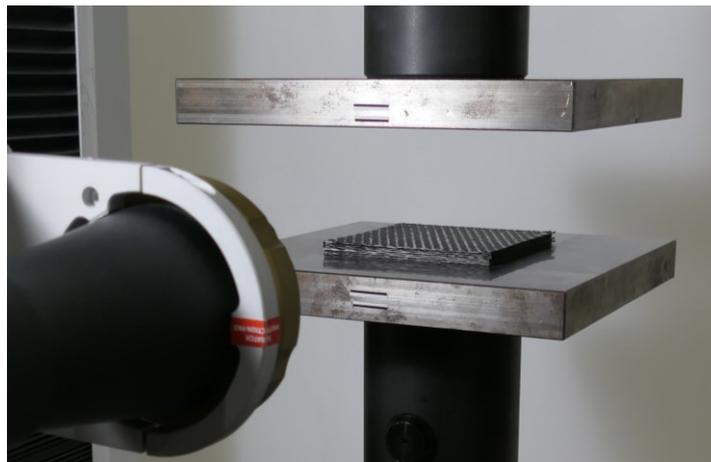
Fig. 3-1:   **Experimental setup for the compaction tests with video extensometer.**

3.2.1 Machine deformation

The literature review in Subsection 2.2.1 showed that machine compliance has a major impact on the accuracy of the measured compaction response. Thus, the machine deformation was determined prior to the experiments. The experiments to characterize the machine deformation were performed with preform specimens similar to the description in Section 3.1.

In order to quantify the machine deformation, the displacement measured by the stepping motor of the UTM was compared to the distance measurement from the video extensometer. Fig. 3-2a compares the relative displacement of the upper plate for both

measurement methods. Zero displacement indicates the initial contact of the upper compaction plate with the specimen. The curve of the video extensometer measurement bends to the right when the compaction force increases. This can be explained by the deformation of the UTM leading to smaller displacement measurements from the video extensometer at high forces. The extent of the machine deformation becomes more evident in Fig. 3-2b. In this diagram, the absolute difference between the two measurements is plotted against the displacement measured by the UTM together with the corresponding compaction force. For small forces below 1 kN, the difference between the UTM and the video extensometer signal is negligible. However, the deformation increases with the compaction force. A compaction force of 20 kN leads to an error in the displacement measurement of nearly 0.2 mm. Characterizing the machine compliance with an empty compaction test and subtracting it from the measurements of the compaction experiments would provide corrected displacement data. This method has been applied by several authors [105,107,108]. However, looking at the measured velocity of the compaction plate in Fig. 3-3 reveals another challenge. In order to reduce the scatter, the floating average of ten data points was used for the two velocities shown. The velocity measured by the video extensometer decreases from 5 mm/min to 2.5 mm/min, whereas the UTM velocity remains constant. However, the algorithm fitting the compaction model developed in Section 4.1 to experimental data requires a constant velocity. Hence, a constant velocity during the experiment is needed in order to derive sufficient model parameters.

(a)   **(b)**
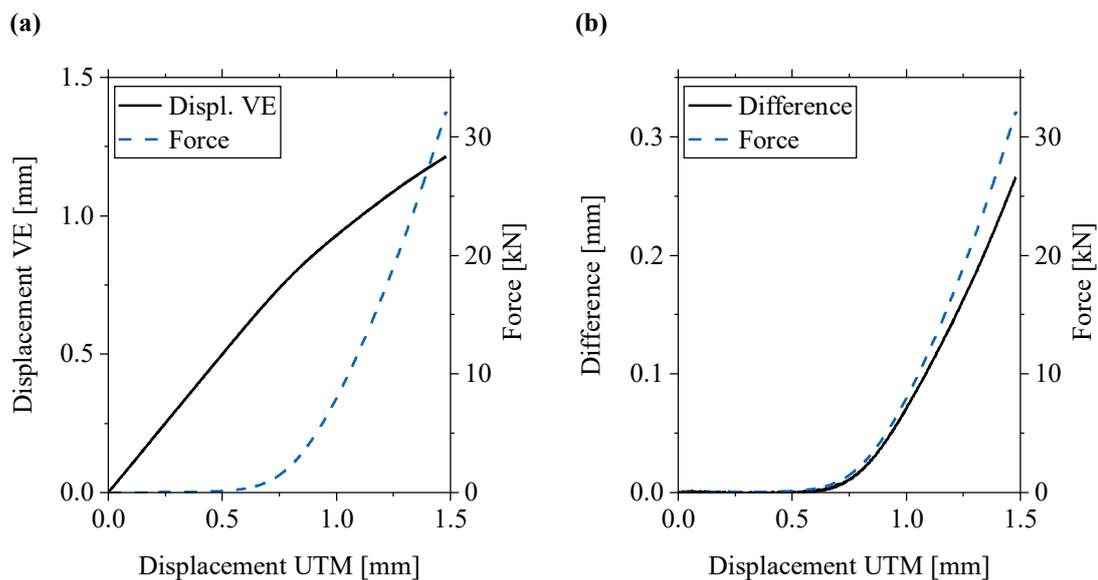
Fig. 3-2:   **Comparison of displacement measured by the UTM and the video extensometer with corresponding force.**
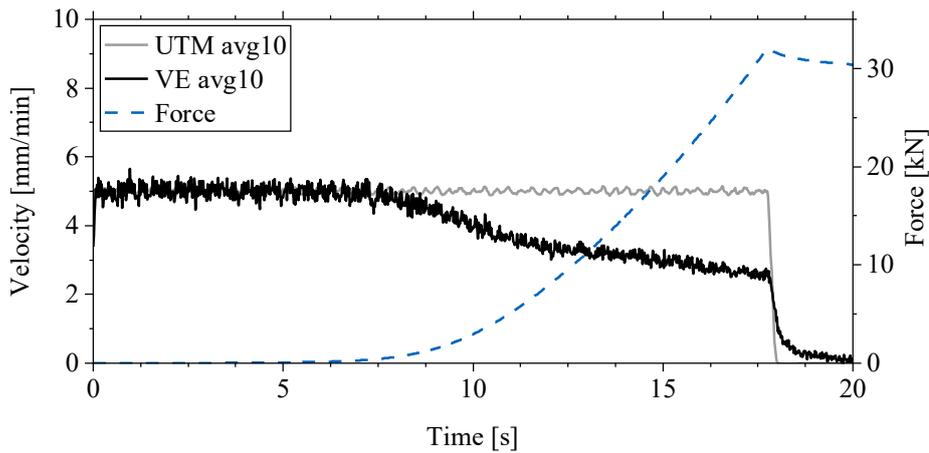
Fig. 3-3: **Floating average of the velocity measured by the UTM and the video extensometer, crosshead movement controlled by the UTM.**

A constant velocity of the upper compaction plate can be achieved by controlling the crosshead position of the UTM with the video extensometer. Fig. 3-4 shows the effect of a video extensometer-controlled compaction experiment. Contrary to the UTM-controlled experiment, the video extensometer velocity is constant and the UTM velocity increases at high forces. For 20 kN compaction force the measured velocity increases to 2.5 mm/min from initially 2.0 mm/min.
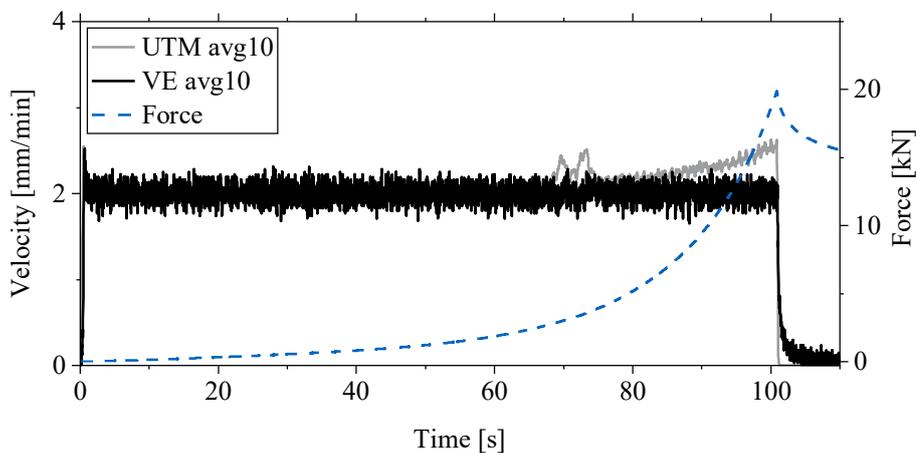
Fig. 3-4: **Floating average of the velocity measured by the UTM and the video extensometer, crosshead movement controlled by the video extensometer.**

3.2.2 Experimental procedure

Tab. 3-1 and Tab. 3-2 provide an overview of all tested configurations for the compaction experiments with displacement-controlled and force-controlled setup. Several basic properties of the specimens were documented before and after the compaction. In case abnormalities occur during the experiment, this data is used to find the root cause.

The following properties were documented for each specimen prior to the experiment:
- In-plane dimensions length and width
- Thickness at five reference locations (center and each corner)
- Weight
- Optical abnormalities (e.g. delamination, loose rovings or fringed edges)

At the beginning of each experiment, the specimen was placed in the center of the lower compaction plate in order to avoid bending moments during the plate closure. All specimens of one material were compacted to the same initial thickness h_{ini} of 7.6 mm for the weave and 6.7 mm for the NCF material. This compensated for potential variability of the preform thickness after manufacturing and ensured a uniform starting point for all experiments with the same material. Fig. 3-5 shows the procedure of the compaction experiments as programmed in the UTM. Following the left branch determines the approach for displacement-controlled experiments. Initially, the upper plate was moved with high velocity to the position of 1.4 mm plus the initial thickness h_{ini} of the material. Afterwards, the plate closed with a low velocity of 1.0 mm/min until the position h_{ini} was reached. The following holding phase of two minutes ensured that the stresses in the material were relaxed after the pre-compaction. Moreover, potential vibrations of the upper plate due to the negative acceleration could decay. The corresponding mean pre-compaction force at the end of the first holding phase was 25 N for the weave and 1.4 N for the NCF. The compression to the final FVC started with a velocity of 1, 2 or 5 mm/min. The compression speed was constant until reaching the final thickness. The final position was held constant for twelve minutes in order to measure the stress relaxation. At the end of the experiment, the plates opened at a constant speed. This compaction test was repeated for six different configurations of each material at different compaction velocities and different final FVC (see Tab. 3-1). Each configuration was repeated with five test samples. The FVC V_f, in dependency of the preform thickness h, can be described as follows:

$$V_f = \frac{N \cdot AW}{\rho_{fiber} \cdot h}$$
(3-1)

where N is the number of plies in the preform, AW is the areal weight, and ρ_{fiber} is the fiber density. With ρ_{fiber} = 1.77 g/cm^3 [257] and the initial thickness h_{ini} = 7.6 mm, the initial FVC of the weave can be calculated as 0.33. A fiber density 1.78 g/cm^3 [258] and an initial thickness of h_{ini} = 6.7 mm lead to an initial FVC of 0.39 for the NCF.

Tab. 3-1:   **Configurations of the displacement-controlled experiments of the weave and the NCF materials.**

Configuration	Final FVC [-]	Compaction velocity [mm/min]	Final thickness weave [mm]	Final thickness NCF [mm]
WV_0.45-2 / NCF_0.45-2	0.45	2.0	5.65	5.81
WV_0.50-1 / NCF_0.50-1	0.50	1.0	5.08	5.23
WV_0.50-2 / NCF_0.50-2	0.50	2.0	5.08	5.23
WV_0.50-5 / NCF_0.50-5	0.50	5.0	5.08	5.23
WV_0.55-1 / NCF_0.55-1	0.55	1.0	4.62	4.76
WV_0.55-2 / NCF_0.55-2	0.55	2.0	4.62	4.76
WV_0.55-5/ NCF_0.55-5	0.55	5.0	4.62	4.76
WV_0.60-2/ NCF_0.60-2	0.60	2.0	4.23	4.36

Similar experiments were conducted for force-controlled tests. Instead of constant compression velocity, a constant force rate compacted the preforms. The distance of the compaction plates was measured using the video extensometer. Additional to configurations 0.50–1 and 0.50–5, which are not used for the model calibration, the force-controlled experiments are used for the model validation. Since the model was being used to predict the final thickness of preforms after compaction, the applicability had to be proved with force-controlled setups. The tested configurations are summarized in Tab. 3-2. The procedure of the force-controlled experiments is shown in Fig. 3-5 following the right branch. As for the displacement-controlled tests, the specimens were compacted to an initial FVC of 0.34 or 0.39. The preforms were compacted at a constant force rate of 100 N/s and 250 N/s, respectively. The force was kept constant for ten minutes after reaching the maximum of 10 kN for the weave material. The NCF was compacted with a maximum force of 4.2 kN. Measuring the thickness evolution at a constant force enabled the quantification of material creep. At the end of the experiment, the force was released at a constant rate of 20 N/s for the slow compacted specimens, and 50 N/s for the faster compaction. The release rate was lower than that of the compaction in order to guarantee continuous contact between the plate and the preform.

```
        ┌─────────────────────────────┐
        │  Go to poition: h_ini + 1.4 mm │
        │     Velocity 100 mm/min      │
        └─────────────────────────────┘
                      │
                      ▼
        ┌─────────────────────────────┐
        │     Go to poition: h_ini     │
        │      Velocity 1 mm/min       │
        └─────────────────────────────┘
                      │
                      ▼
        ┌─────────────────────────────┐
        │       Hold position for      │
        │          2 minutes           │
        └─────────────────────────────┘
```

Displacement-control   Force-control

```
┌──────────────────────────┐        ┌──────────────────────────┐
│  Go to position: h_final │        │       Go to F_max        │
│   Velocity 1/2/5 mm/min  │        │  Force rate 250/100 N/s  │
└──────────────────────────┘        └──────────────────────────┘
            │                                    │
            ▼                                    ▼
┌──────────────────────────┐        ┌──────────────────────────┐
│     Hold position for    │        │       Hold force for     │
│        12 minutes        │        │        12 minutes        │
└──────────────────────────┘        └──────────────────────────┘
            │                                    │
            │                                    ▼
            │                        ┌──────────────────────────┐
            │                        │        Go to 100 N       │
            │                        │   Force rate 100/20 N/s  │
            │                        └──────────────────────────┘
            │                                    │
            └───────────────┬────────────────────┘
                            ▼
            ┌─────────────────────────────┐
            │  Go to poition: h_ini + 30 mm │
            │     Velocity 100 mm/min      │
            └─────────────────────────────┘
```
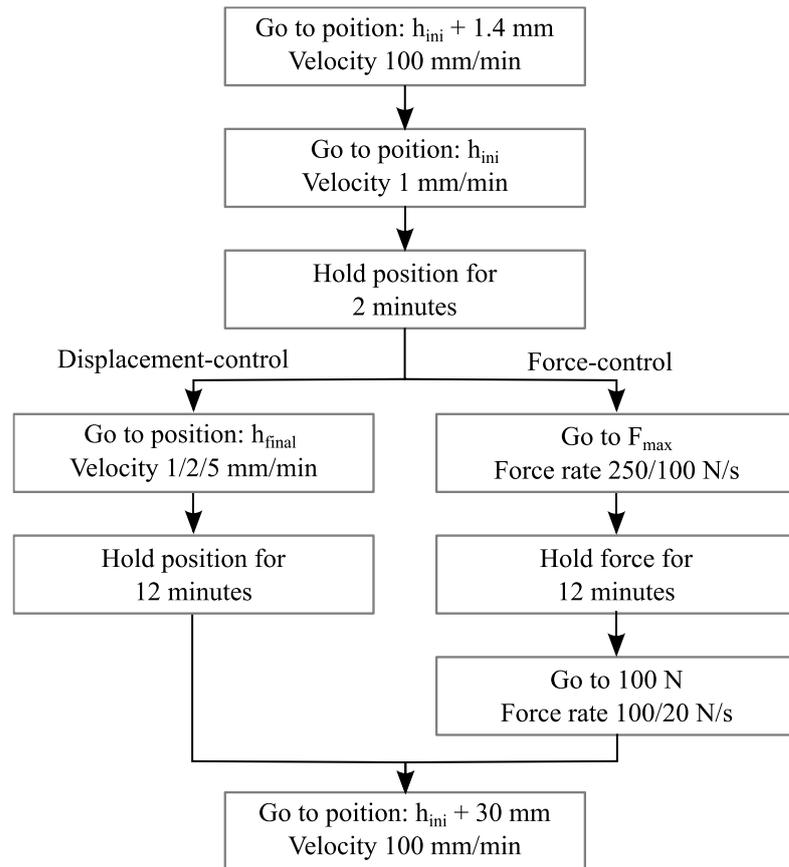
Fig. 3-5:   **Flow chart of the procedure for the displacement-controlled and force-controlled compaction experiments.**

Tab. 3-2:   **Configurations of the force-controlled experiments of the weave and the NCF materials.**

Configuration	Compaction rate [N/s]	Max. force [kN]	Release rate [N/s]
WV_F10-100	100	10	20
WV_F10-250	250	10	50
NCF_F4.2-100	100	4.2	20
NCF_F4.2-250	250	4.2	50

Immediately after each experiment, the tested sample was measured again. The following data was collected for all tested specimens:

- In-plane dimensions length and width after compaction and load release
- Thickness at five reference locations after compaction and load release
- Optical abnormalities after compaction and load release (e.g. delamination, loose rovings or fringed edges)

3.2.3   Results and discussion

3.2.3.1   Displacement-controlled experiments

Fig. 3-6 shows the results of the displacement-controlled experiments with the weave material. Besides the mean curve, the minimum and maximum values at every time point are displayed as scatter areas in the graphs. The coefficient of variation is between 2.6% and 8.1% of the mean curve. The curves with the same final FVC indicate that the peak stresses slightly increase at an increasing compaction speed. The compaction responses of these curves did not relax to the same final stress. For the 50% final FVC, the curves show lower absolute relaxed stresses for lower compaction velocities. For the 55% final FVC, the fastest compaction results in the lowest absolute relaxed stress. The final stresses of all configurations show that the evolution of the relaxed stress in dependency of the FVC was clearly nonlinear. The relation between FVC and relaxed stress seems to be exponential.
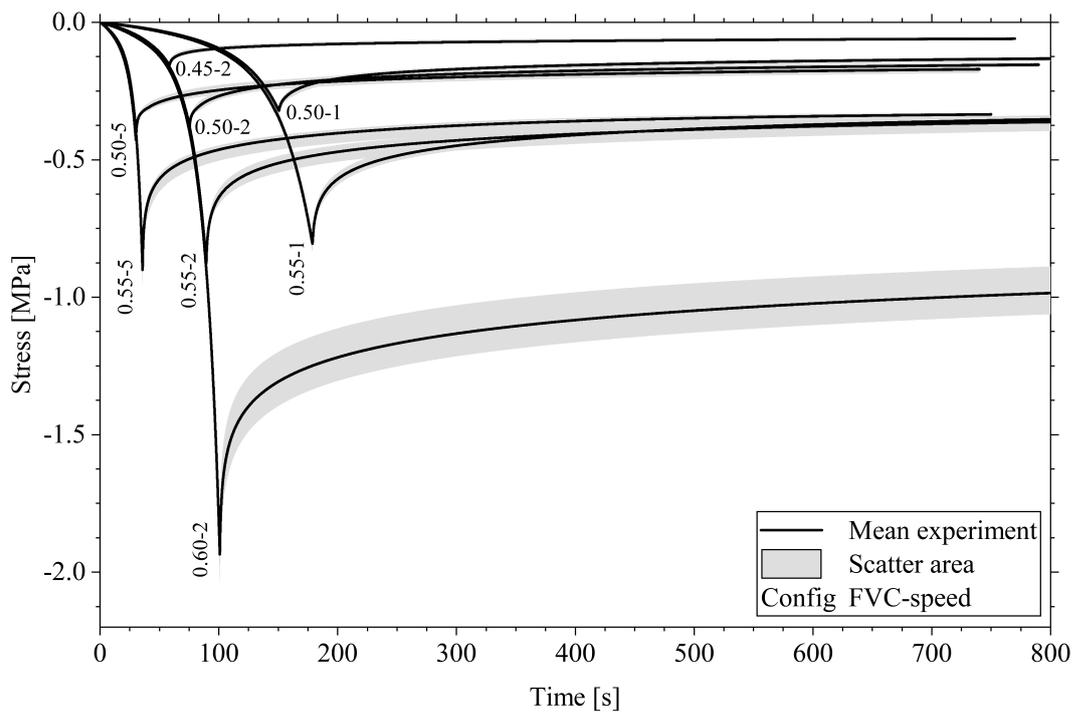
Fig. 3-6:   **Stress response of the displacement-controlled planar compaction experiments of the weave material with varying compaction velocities and final FVC, including minimum and maximum scatter area.**

The results of the displacement-controlled experimental configurations from Tab. 3-1 of the NCF are shown in Fig. 3-7. In comparison with the weave material, the general stress level is significantly lower. Moreover, the scattering of the results is lower compared to the weave material. The coefficient of variation of the relaxed stress of the NCF is

between 1.9% and 4.6% of the mean curve. Furthermore, the qualitative behavior differed from the weave material. During the relaxation, the stress in the NCF preforms decreased by only approximately 30%. In contrast, about 60% of the peak stresses were relaxed for the lower three analyzed FVCs of the weave material. For the NCF, the relaxed stresses at 50% and 55% FVC were lower when the material was compacted at a higher velocity. The same effect was observed for the weave material at 55% FVC.
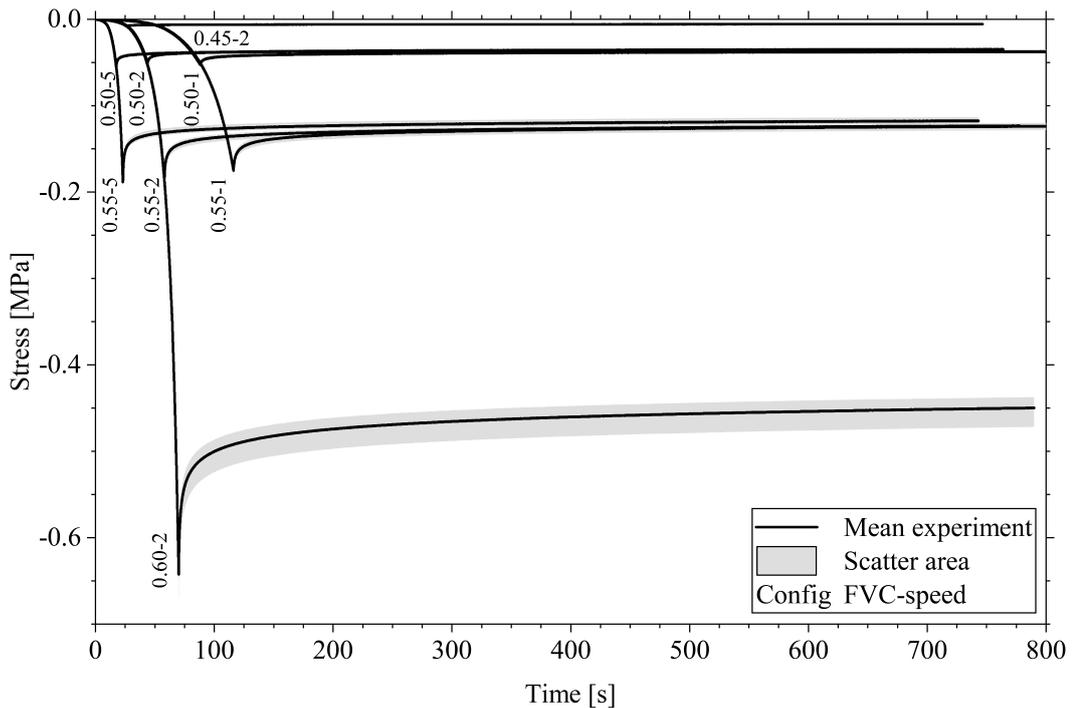
Fig. 3-7: **Stress response of the displacement-controlled planar compaction experiments of the NCF material with varying compaction velocities and final FVC, including minimum and maximum scatter area.**

3.2.3.2 Force-controlled experiments

Fig. 3-8 shows the results of the force-controlled experiments with the weave material. The curves represent the average of five repetitions. The shaded area describes the scatter in which all the single results lay. The coefficient of variation was 1.3% for the low force rate and 0.90% for the high force rate. A creep effect was observable when the force remained at a constant value. For faster compaction, the preforms reached a higher FVC. During the release of the force, the preforms exhibited a spring-back behavior to a higher thickness. A similar behavior was observable for the force-controlled experiments with the NCF material in Fig. 3-9. Likewise, the material was slightly more compacted at a higher force rate. As in the displacement-controlled experiments, the scattering was lower for the NCF material. The coefficient of variation was 0.55% and 0.20% of the mean curve for the low force rate and the high force rate, respectively.
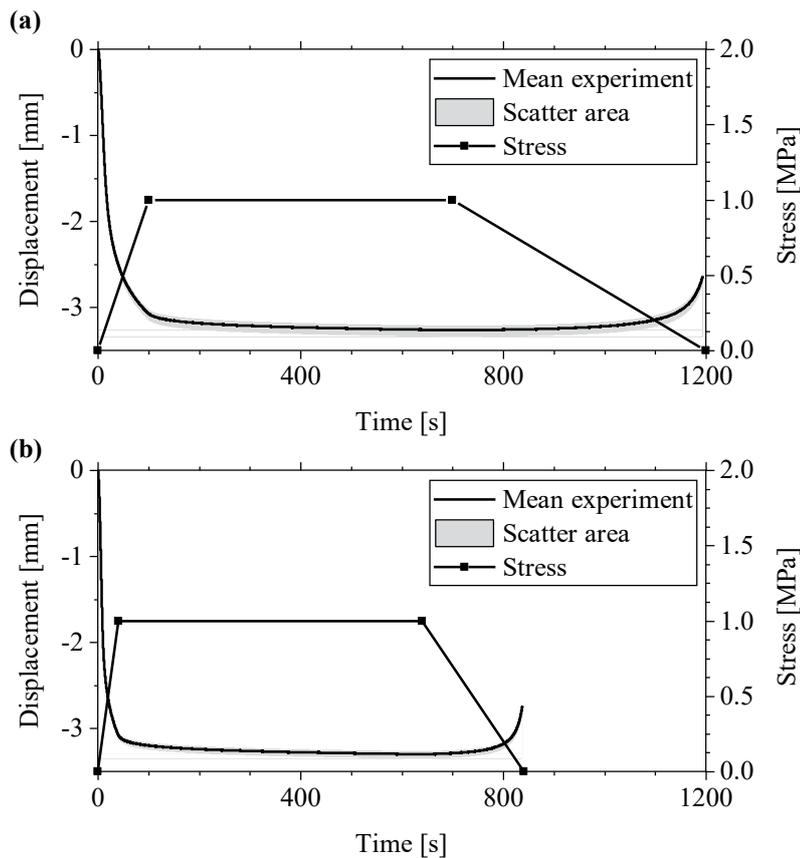
Fig. 3-8:   **Displacement response of the force-controlled planar compaction experiments of the weave material, including minimum and maximum scatter area: (a) slow compaction; (b) fast compaction.**

Measurements of the thickness of the specimens shortly after the compaction experiment showed that the preforms did not reach the initial state. Weave preforms having an average initial thickness of 8.1 mm were compacted to 5.1 mm and showed a spring-back to 7 mm shortly after the experiment. One hour later, the thickness increased to 7.6 mm, which corresponded to an average recovery of 83% of the maximum compaction strain. There thus appeared to be an extremely slow spring-back or an irreversible part of the deformation corresponding to a small plastic contribution in addition to the elastic and viscous behaviors on a macro-scale. On a smaller scale, this can be explained by irreversible nesting effects or the permanent rearrangement of fibers. Another effect could have been the permanent deformation of the binder network. In this study, only the spring-back behavior of preforms shortly after the compaction with the maximum force was characterized and modeled. Therefore, the contribution of the plasticity was neglected for the materials analyzed in this work. Regarding long-term effects or different materials, plasticity might be relevant or can be modeled with an additional viscous element with an extremely long relaxation time.

The scatter of experiments can be explained with different nesting conditions in the specimens. Lomov et al. [259] showed that random nesting has a significant influence on the FVC and the scatter of permeability. Chen and Chou [138] presented a unit-cell model for multi-layer preforms showing the influence of different nesting configurations on the compaction pressure. In a very recent publication, Trochu et al. [260] reported that much of the variation in compaction measurements can be attributed to nesting. Nesting was not reproducible during the layup of large preforms. Consequently, a variation of nesting leads to different compaction responses. This also explains the lower scattering of the experimental data of the NCF compared to the weave material due to less potential nesting between the individual layers. Because of the roving undulations in the weave material, the degree of nesting can vary in a larger range, which can lead to more differing material responses. A comparison of the compaction response with the dimensional properties of the individual specimens did not show any significant relation. There was no relation between higher compaction stress and specimen thickness or in-plane dimensions observable for tests with the same configuration. Likewise, there was no significant relation between the specimen properties and the response to force-controlled experiments for repetitions of one test configuration.
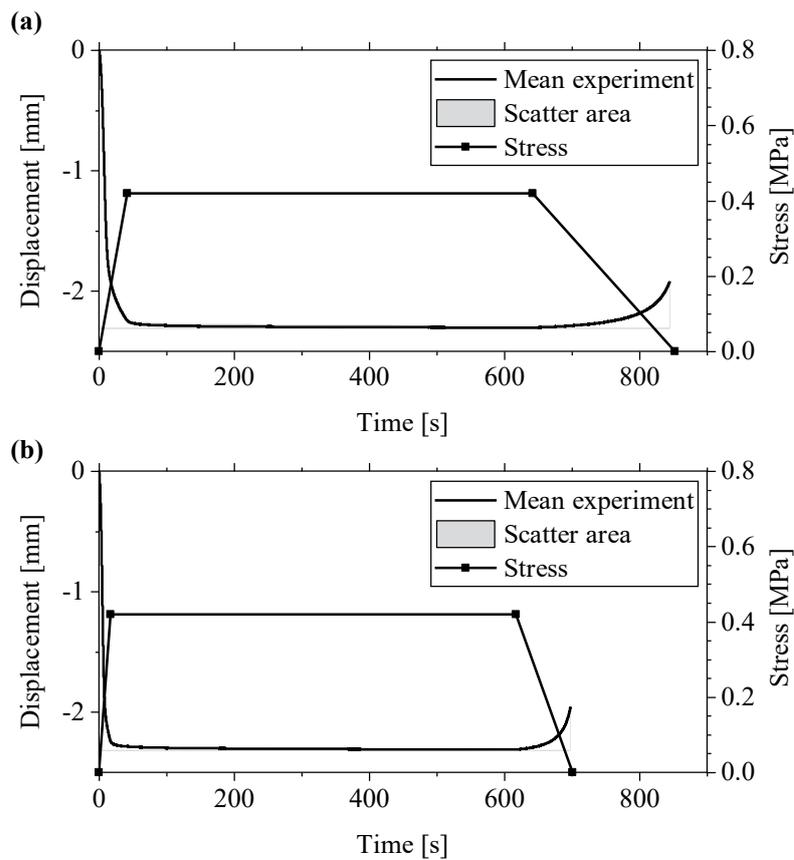
Fig. 3-9:   Displacement response of the force-controlled planar compaction experiments of the NCF material, including minimum and maximum scatter area: (a) slow compaction; (b) fast compaction.

3.3 Out-of-plane shear characterization

The content of this section is partly derived from SAMPE 2021 conference paper [C3].

A major challenge for the characterization of dry preforms is to measure the shear modulus without affecting the compaction state during the test. Moreover, it can be assumed that the shear stiffness increases with an increasing degree of compaction due to nesting effects. Currently available test methods do not provide possibilities to measure the out-of-plane shear stiffness of dry preforms at a defined FVC [143,144,149,261]. Due to spring-back effects, preforms do not maintain their thickness after compaction. Additionally, the low stiffness in thickness direction leads to local compaction during three- or four-point bending tests. Thus, the FVC needs to be kept constant at a defined thickness in the test setup during the experiments. A further challenge is to transfer the shear load into the preform specimens without influencing the material behavior.

The woven carbon fiber fabric Hexcel G0926 [257] with E01 binder was used for these experiments. With the manufacturing procedure described in Section 3.1, the large preforms were cut into specimens of 90 mm x 40 mm size. The extra strong double-faced adhesive tape from Tesa was used to glue the preforms on the plates of the experimental setup. The whole test setup was mounted into a universal testing machine UPM 250 from Hegewald und Peschke with a 500 N load cell.

3.3.1 Development of a novel test method for out-of-plane shear characterization

The test method described in this subsection was developed together with Schletterer in the context of a master's thesis [S14]. Fig. 3-10 shows an exploded view of the experimental setup on the left and built into the testing machine on the right. The concept is similar to a double lap shear test, where two specimens are tested simultaneously. The machine fixtures on the top and bottom connect the experimental setup with the testing machine. The specimens are compacted between the front and the back plate with screws, while the distance plates ensure a defined thickness of the preforms in the setup. Adhesive tape on both sides of the specimens ensures the force transition to the central web and the outer plates respectively. The distance plates were sanded to greater thickness than the specimens to account for 0.2 mm tape thickness on both sides.

The experiments were conducted with four different FVCs. The respective thicknesses according to Eq. (3-1) of the single specimens and the corresponding distance plates are shown in Tab. 3-3. During all experiments the central web was moved upwards with a constant velocity of 1 mm/min. Each configuration was repeated five times. The experiments stopped when the force reached 480 N, which is close to the limit of the used load cell. The central web and the outer plates were cleaned with isopropanol between

the repetitions to remove remains of the adhesive tape. In addition to the preform material, the shearing of the tape was characterized in order to account for its influence on the preform measurements.
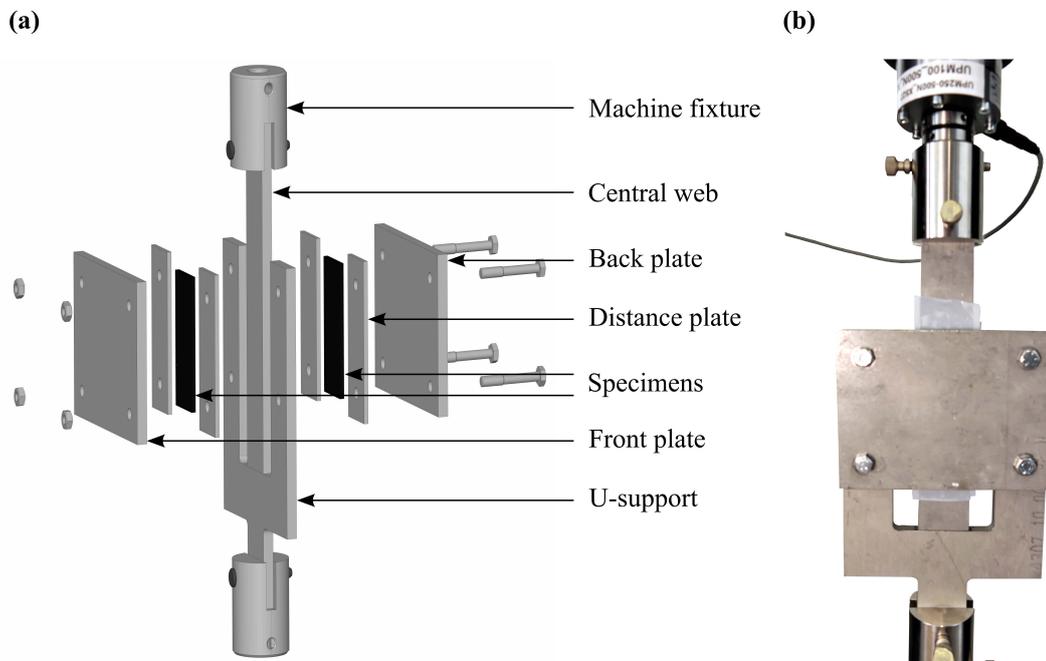
Fig. 3-10: **Experimental setup of the out-of-plane shear measurements: (a) exploded view; (b) mounted into the testing machine.**

Tab. 3-3: **Tested configurations of the out-of-plane shear experiments.**

Configuration	FVC [-]	Specimen thickness [mm]	Distance plate thickness [mm]
HV_45	0.45	5.65	6.05
HV_50	0.50	5.08	5.48
HV_55	0.55	4.62	5.02
HV_60	0.60	4.23	4.63
Tape	-	0.2	-

3.3.2 Evaluation method of the shear stiffness

A schematic illustration of the shear deformation, which acts on a single preform with one layer of adhesive tape is shown in Fig. 3-11. During the experiments, a normal force F_{tot} acts on the central web and leads to a shear displacement of the preform and the adhesive tape.
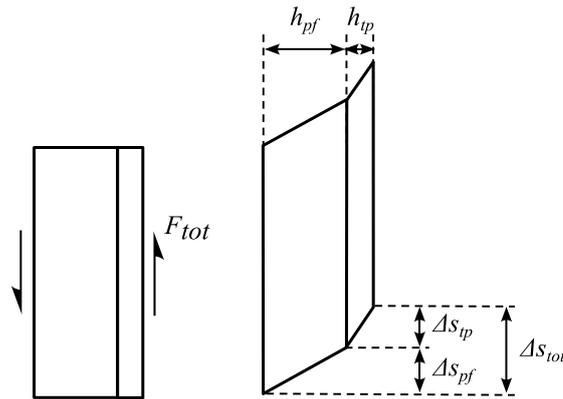
Fig. 3-11:   **Schematic illustration of serial shear displacements of two materials.**

The total displacement Δs_{tot} is the sum of the displacements Δs_{pf} of the preform and Δs_{tp} of the tape:

$$\Delta s_{tot} = \Delta s_{pf} + \Delta s_{tp} \tag{3-2}$$

However, the acting forces F_{pf} and F_{tp} are equal in the preform and the tape, as they are connected in series:

$$F_{tot} = F_{pf} = F_{tp} \tag{3-3}$$

The shear stiffness G in dependency of the shear stress τ and the shear angle γ can generally be given as:

$$G = \frac{\tau}{\tan \gamma} = \frac{\Delta F \cdot h}{A \cdot \Delta s} \tag{3-4}$$

Here h is the thickness and A is the area in which the shear stress acts. In order to obtain the stiffness of the preform, the displacement of the tape Δs_{tp} has to be subtracted from the total displacement Δs_{tot}. Hence, shear experiments for the adhesive tape without preform are necessary.

From five tape measurement repetitions, a mean curve is derived, which is subtracted from each test with preform and tape. Straight lines are fitted to the resulting force-displacement curves of the preform without adhesive tape to derive areas with constant shear stiffness. Linear sections of the curves are identified with a linear regression algorithm. A python script is used which gradually increases the number of data points in a section until the coefficient of determination falls below the threshold of 0.99. Using this approach, two linear sections can be found for each repetition in every test configuration. The linear regression algorithm provides a slope m and an intercept t for every straight line. Because the slope is defined as the quotient of ΔF and Δs, the shear stiffness can be calculated as follows by using Eq. (3-4):

$$G_{pf} = \frac{h_{pf} \cdot m}{2 \cdot l_{pf} \cdot w_{pf}} \qquad (3\text{-}5)$$

With the geometrical dimensions of the specimen length l_{pf} and the width w_{pf}. Because the experimental setup consists of two specimens, only half the force acts on the area $l_{pf} \cdot w_{pf}$.

3.3.3 Results and discussion

3.3.3.1 Experimental results

The experiments were conducted together with Schletterer in the context of a master's thesis [S14]. The results of the five repetitions of the tape measurements are shown as dashed lines in Fig. 3-12a. The solid line represents the mean curve of the measurements. The qualitative behavior of all curves is the same. A steep linear increase of the force is followed by another almost linear section with a less inclined slope. Between the nearly linear sections, a smooth transition zone can be observed. In the first section, the slope of the force shows an apparent variation. In contrast, the variation of the slope in the second section is significantly smaller leading to nearly parallel curves.

Fig. 3-12b shows the results of all the measurements of the preform specimens for the four configurations, which are given in Tab. 3-3. The mean displacement of the tape is subtracted for all experiments shown in the figure. Repetitions of the same configuration are depicted with the same color. It can be seen that the repetitions of each configuration do not show the same level of variation. The experimental results with an FVC of 55% are very close, whereas, the repetitions of the other configurations show larger variations. The most noticeable scatter appears at an FVC of 60%. Generally, a tendency to higher forces can be seen for increasing degrees of compaction. For higher FVC the scatter areas of the repetitions are overlapping. Only the scatter area of HV_45 can clearly be separated from the other configurations. Compared to the second linear section, the first one seems to be nearly independent of the FVC. Moreover, the scatter of the slope is significantly smaller for lower displacements than for larger displacements. Because the specimen thickness influences the shear stiffness according to Eq. (3-5), the slope of the curves does not allow direct conclusions to be drawn about the shear stiffness.

(a)   **(b)**
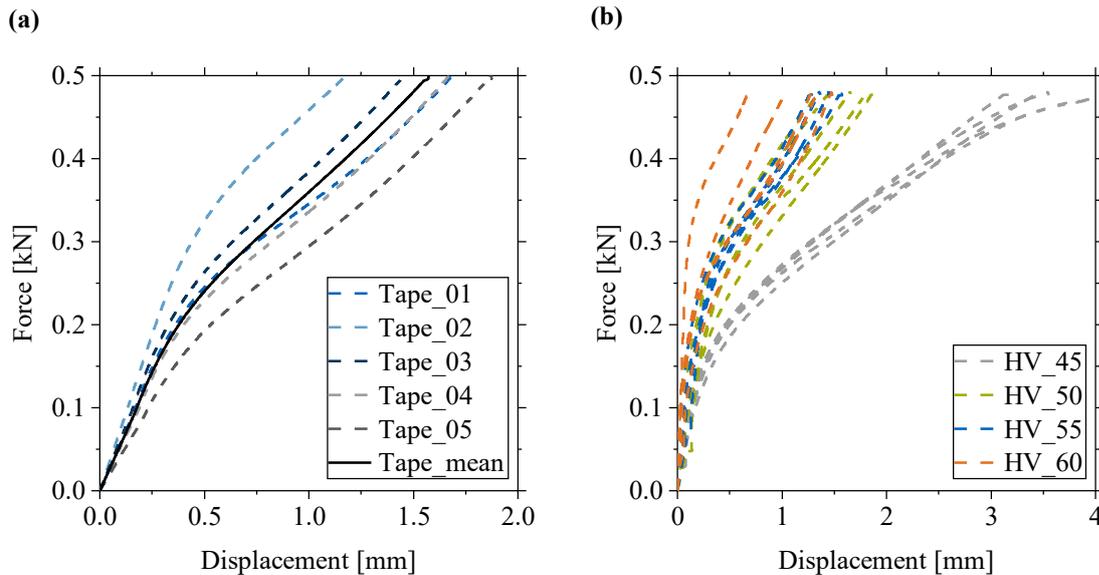
Fig. 3-12: **Force response from displacement-controlled out-of-plane shear experiments: (a) tape measurements; (b) preform measurements with subtracted tape displacement.**

3.3.3.2 Calculation of the shear stiffness

Fig. 3-13a shows how linear sections are identified, using the example of the test configuration HV_55_01. The straight lines cover only the areas where the coefficient of determination is below the threshold. The dashed lines depict the elongation covering the whole measurement interval until the intersection. Section A starts at almost zero displacement and ends where the curve bends to the right. Adding more data points on the right would lead to a less inclined linear fit and a lower coefficient of determination. Another nearly linear section appears for higher displacements. Section B starts after the transition area and continues to almost the end of the force range. Looking at Fig. 3-12b, many curves show a curvature at higher forces. Thus, the linear section B does not cover very high shear displacements in several cases.

Fig. 3-13b shows the results of the shear stiffness calculation for four different FVCs including the minimum and maximum values. G_A describes the shear stiffness of the first section A and G_B is the shear stiffness of the second section B. For G_A a significant increase of stiffness with increasing degree of compaction can be seen. G_B increases between FVC 0.45 and 0.5, whereas there is a plateau for higher degrees of compaction. The averaged results for all configurations are given in Tab. 3-4. Besides the slope of the straight lines, their interception point is of interest. In order to be used in a bilinear model for simulations, the transition from constant high to constant low stiffness needs to be defined. For the interception, the shear angle is given to be independent of the specimen thickness. With an increasing degree of compaction, the intercept moves towards smaller shear angles.

(a)   **(b)**
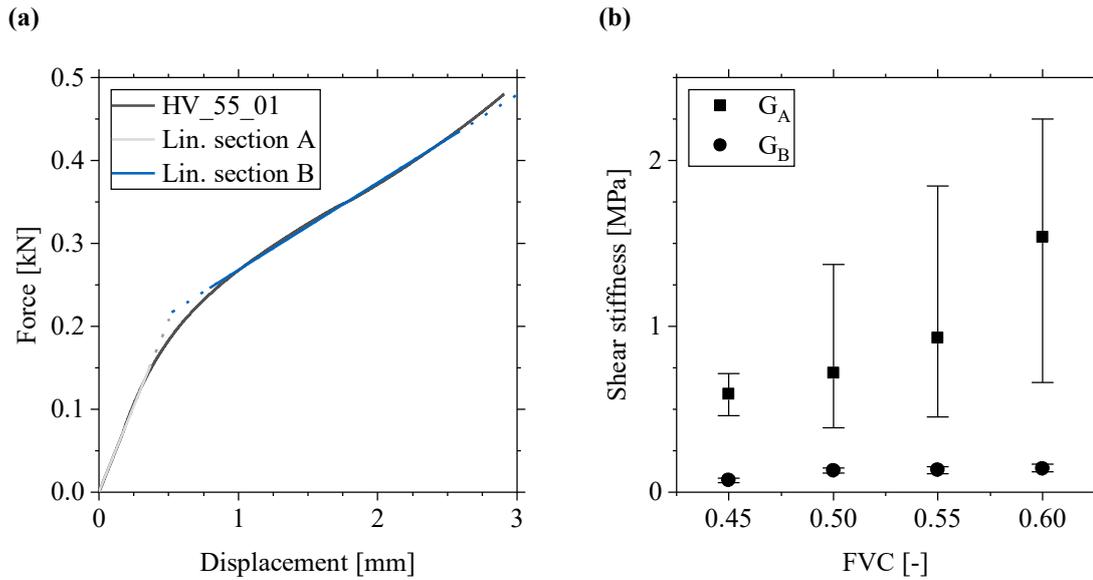
Fig. 3-13: (a) Identification of linear sections for HV_55_01; (b) calculated shear stiffness for different FVC including minimum and maximum values.

Tab. 3-4: Mean shear stiffness and mean interception point for different FVC.

Configuration	G_A [MPa]	G_A [MPa]	Interception [°]
HV_45	0.59	0.07	2.7
HV_50	0.72	0.13	2.5
HV_55	0.93	0.13	1.8
HV_60	1.54	0.14	1.1

The calculated shear stiffnesses clearly show a dependency on the degree of compaction. Especially in the first section the stiffness increases significantly with the FVC. The effect can be explained with nesting of the plies. If the plies are nested into each other, more force is needed for a tangential movement of the plies when the compaction force increases. The results of the shear modulus calculation in Fig. 3-13b show significant scatter, especially for high FVC in section A. This can be explained with the scatter of the measurements of the adhesive tape. Another cause for the variation could be the nesting of the layers. If all layers are perfectly nested into each other, the resulting stiffness is very high. Whereas, a relative movement of the plies with subsequent nesting will lead to lower out-of-plane shear stiffness.

The relative displacements in the section B are very high. With a thickness of the single specimens between 4.2 and 5.7 mm, the maximum displacements correspond to shear angles above 20°. With such high strains, some relative movement between adhesive tape and preform can occur. As these high shear strains are very unlikely in real

processes, the G_A values might be more important for numerical models. Nevertheless, a significant decrease of shear stiffness appears between one and three degrees shear angle for all tested configurations. Thus, the chosen bilinear model covers this effect very well. However, it is important to state that the force response does not show a perfect bilinear behavior, especially in the transition zone.

3.4 Characterization of the tool-ply friction

The friction characterization tests were performed together with Geschwandtner as part of a bachelor's thesis [S15]. The friction was measured for the weave material Hexcel G0926 [257]. The objective was to characterize the friction between the preform and the tool surface. Moreover, the influence of preform orientation, sliding velocity and normal pressure on the friction coefficient was investigated. The measured values were used for the non-planar compaction simulations in Chapter 5.

3.4.1 Method

The specimens were manufactured under the same conditions as the samples for the compaction and shear experiments. The main difference is that only a single layer of the fabric material is needed for the friction tests. An existing test setup with a sled, developed by Margossian [156] was used for the experiments (see Fig. 3-14). The 60 mm x 77 mm fabric layers were cut using the Zünd M-1200 CNC-cutting machine. Afterwards the binder in the single fabric layers was activated in a hot press for one minute with 2 bar pressure at 100 °C. After cooling to room temperature, the specimen was clamped on the sled using an area of 10 mm on each side of the fabric layer. This results in a sliding surface of 40 mm x 77 mm during the experiment. The sled was pulled over a metal plate, which was cleaned with isopropanol after each experiment in order to remove remains of fibers and binder from the surface. Initial tests carried out in [S15] showed that the quality of the results could be improved by removing the guides on the side of the test setup. The whole test setup was mounted into a UPM 250 testing machine from Hegewald und Peschke, as shown in Fig. 3-14b. The force was measured with a 500 N load cell and an HBM QuantumX MX840A measuring amplifier.

The influence of the orientation (defined in Fig. A-9) of the weave material relative to the sliding direction on the friction behavior was investigated. Additionally, the influence of the normal force and the influence of the sled velocity on the friction coefficient was studied. The influence of contact pressure is of special importance, because the results from compaction experiments in Section 3.2 show, that the normal pressure increases strongly with increasing FVC. For this purpose, up to four additional weights were placed on top of the sled. The sled has a weight of 1.58 kg generating a normal

force of 15.50 N. Each weight is a 15 mm thick steel plate with a mass of 1.79 kg corresponding to an additional normal force of 17.56 N. An overview of the tested configurations for the friction measurement is given in Tab. 3-5. Each configuration was tested at five different levels of the normal force. Six repetitions per configuration for each normal force result in 90 individual tests.

Tab. 3-5:   Configurations for the friction experiments.

Configuration	orientation [°]	velocity [mm/min]	Normal force [N]				
FR_0-1	0	1	15.50	33.06	50.62	68.18	85.74
FR_0-10	0	10	15.50	33.06	50.62	68.18	85.74
FR_90-10	90	10	15.50	33.06	50.62	68.18	85.74

(a)   (b)
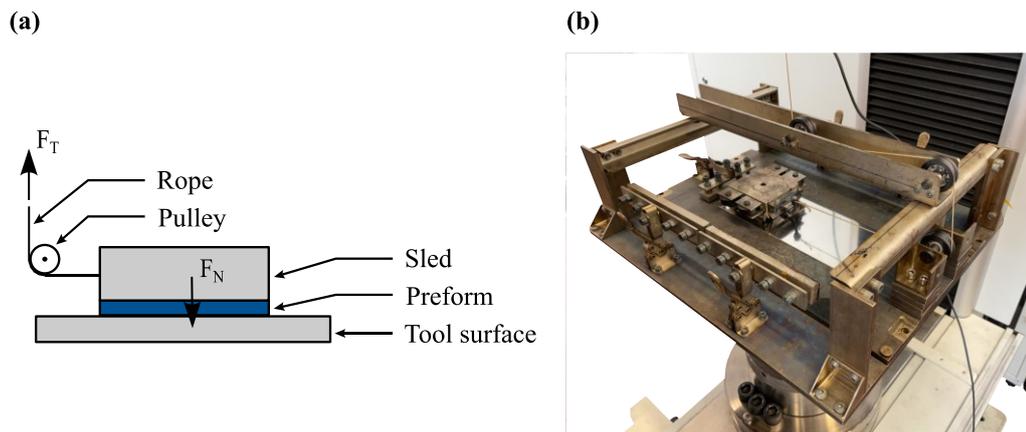
Fig. 3-14:   Sled test setup for friction characterization: (a) schematic illustration; (b) setup mounted into a UTM (photo adapted from [S15]).

3.4.2   Results and discussion

The evaluation of the results is shown using the example of the FR_0-1 configuration with 1 mm/min at 0° orientation. Fig. 3-15 depicts the results of the friction force measurement for all repetitions and four additional weights excluding the outlier FR_0-1-4-04. Fig. 3-15a shows the measured force versus the position of the sled. All five repetitions exhibit the same qualitative behavior with a linear force increase followed by a nearly constant force when the sled starts to slide. Because no drop in the force can be observed after the sled starts to move, a separation of static and dynamic friction is not possible. Moreover, the measurements of the tangential force show an oscillating behavior after the sled started sliding. This can be explained with stick-slip due to tacky behavior of the binder. Another explanation of the stick-slip behavior is the catching of

individual fibers on the metallic surface. All further configurations in Tab. 3-5 showed the same qualitative behavior (see Appendix e). Fig. 3-15b shows the mean friction force values including standard deviation for each repetition from the point the sled started to slide at around 3 mm until the final position of 10 mm. It can be seen that the overall repeatability of the measurements is satisfactory. Some measurements, such as FR_0-1-4-05 show a significantly higher scatter than other measurements. A relation between the scatter of the force signal and the properties of the specimen could not be determined.

The mean value of all repetitions of one configuration with varying additional weights allows investigating on the influence between normal force and frictional force. Fig. 3-16a shows the relation between normal force and frictional force for 10 mm/min at 0° and 90° orientation of the fabric. It can be seen that the mean values for each orientation are located on a straight line. This linear dependency suggests that the friction coefficient is independent on the normal force in the tested range. Moreover, the lines connecting the mean values for both orientations are nearly parallel. The mean force values of the 90° configurations are slightly higher than the 0° values. However, the scatter areas of both orientations are overlapping at all measured normal forces. Thus, it can be assumed that the friction coefficient is independent on tested orientations. The influence of the sled velocity on the frictional force is shown in Fig. 3-16b. The mean friction force values for different sled weights are lying on a straight line for both tested speeds. The slope of the 10 mm/min curve is slightly steeper causing an intersection of both curves at approximately 50 N. However, the range of the standard deviation shows an overlap for all different values of the normal force. This leads to the assumption that the friction coefficient is independent on the tangential velocity of the sled.
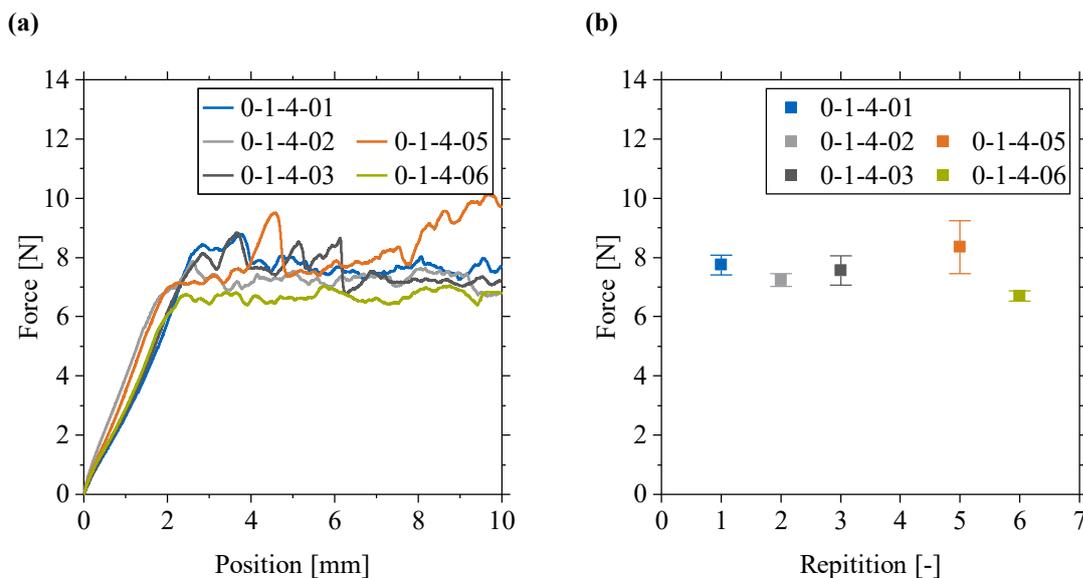
Fig. 3-15:   **Frictional force for 1 mm/min with 0° orientation and four additional weights: (a) force-position; (b) mean value with standard deviation.**

(a)   **(b)**
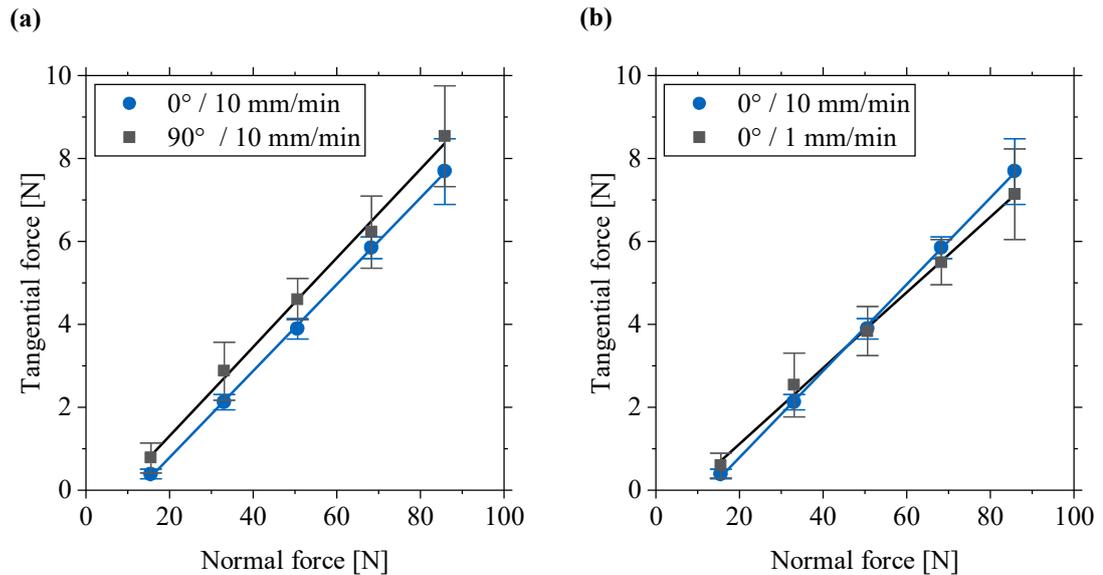
Fig. 3-16:   **Mean tangential force for varying applied normal force: (a) different ply orientations; (b) different sled velocities.**

According to Eq. (2-1), the friction coefficient is defined as the ratio between tangential force and normal force. Hence, the friction coefficient can be calculated from the slope of the curves in Fig. 3-16. Because no distinction between static and dynamic friction can be made for the measured force, only a single friction coefficient was calculated for each configuration. A summary of the mean friction coefficients is given in Tab. 3-6. Because the friction coefficients are nearly identical, the influence of sliding velocity and ply orientation is neglected for the process simulations in Chapter 5. All further compaction simulations that include contact interfaces are calculated with a constant friction value of 0.1.

Tab. 3-6:   **Mean friction coefficient for the tested configurations.**

Configuration	Friction coefficient [-]
FR_0-1	0.10
FR_0-10	0.09
FR_90-10	0.11

3.5 Non-planar compaction experiments

3.5.1 Material and methods

In general, the method of the compaction experiments is very similar to the planar compaction experiments in Section 3.2. Because the individual layers had to be draped and preformed on a radius, the manufacturing process of the preforms was more complex. Each specimen needed to be manufactured individually, because the width of the tool limits the space available. Moreover, the cutting to the final shape could not be done with the CNC cutter and thus, manual cutting was necessary. The manufacturing process of the specimens is described in detail in this subsection. The experimental procedure is the same as for the planar compaction experiments. The objective of selected configurations is to test the influence of the radius, number of layers and the FVC with displacement-controlled and force-controlled experiments.

3.5.1.1 Preform manufacturing

Fig. 3-17 depicts the setup of the preforming device consisting of an upper and a lower tool. The adapter plates on the top and bottom side allow mounting the tools into the hydraulic press. Because the press can only be operated at defined closing pressure, distance plates were needed to ensure a defined preform thickness. Without the adapter plates, the tools can also be directly installed in the universal testing machine. Thus, preform manufacturing and compaction experiments can be performed with the same tools. However, the final preform thickness at the end of the compaction experiment differs from the desired thickness after manufacturing. Hence, different upper tool radii are needed for preforming and testing in order to ensure uniform preform thickness. Two different configurations of the lower tool and three configurations of the upper tool were manufactured. An overview of the inner radius r_i and outer radius r_o configurations is given in Tab. 3-7. Detailed drawings of the tools can be found in Appendix b. For instance, using the $r_i = 3$ mm lower tool and the $r_o = 10$ mm upper tool allows manufacturing a preform with 7 mm thickness. Using the same lower and the $r_o = 8$ mm upper tool enables compacting the preforms to a final thickness of 5 mm in the experiment. Combining different tool radii enables several experimental configurations. However, it is important to ensure that the preforming tool radius is greater than the compaction tool radius. The preforming tool needs a radius which corresponds to the desired thickness of the preform ensuring constant cavity thickness. Additionally, it is important to keep in mind that the preform will show a spring-back behavior, leading to a preform that is thicker than the distance between lower and upper preform tool.
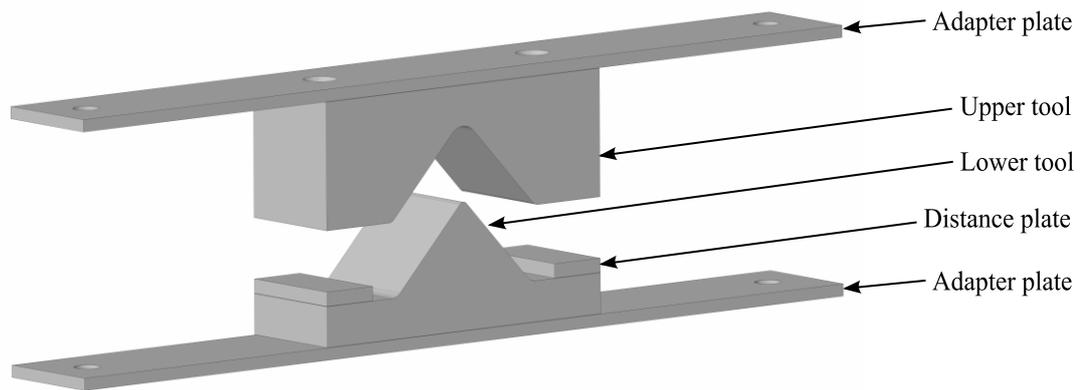
Fig. 3-17: Setup of the preforming device, showing a 3 mm lower tool and 10 mm upper tool.

Tab. 3-7: Tool configuration for the preforming process and the non-planar compaction experiments.

Tool	Parameter	Configurations [mm]
Lower tool	r_i	3 / 6
Upper tool	r_o	8 / 10 / 12

The specimen manufacturing process starts with cutting the individual layers into squares of 100 mm x 60 mm size using the Zünd M-1200 CNC-cutting machine. All preforms were stacked with cross ply layup of alternating 0° and 90° layers, ensuring mid-plane symmetry. Afterwards, the stacked layers were draped on the lower tool. In order to prevent relative movement of the layers, tape was placed on the long edges, as shown in Fig. 3-18a. This ensures that the layers are kept in position during further handling. However, initial trials showed that the taped preforms have a strong tendency to open towards greater angles. This effect was prevented by attaching single rovings on both sides of the layup. With the rovings placed as shown in Fig. 3-18a, the layup was stable enough for further processing. The lower and upper tool were mounted into a hydraulic press from Pinette Emidecau Industries. After heating the tools to a temperature of 100 °C, the preform was placed on the hot lower tool. PTFE foil was placed on the upper and lower tool in order to avoid sticking of the preform on the tool surface. Afterwards, the tool was closed with a pressure of 50 bar. The distance plates between lower and upper tool ensured a defined thickness of the preform. With the binder activated for 60 s, the tool was opened and the preform was removed from the hot tool. After the preform cooled down at room temperature, it was cut into its final dimensions. 5.0 mm were cut off on both long sides of the preform while positioned on the lower tool, resulting in a final preform width of 40.0 mm. Additively manufactured L-shaped positioning devices (see Appendix b) were used to cut the short edges of the preform. Placing these devices on top of the preform allowed cutting at a defined edge. The final

flange length of the specimens with 10 mm upper tool radius is 40 mm. Because of the greater circumference, the 12 mm preforms were cut to a flange length of 38.5 mm. The definition of flange length l, inner preform radius r_i and outer preform radius r_o is illustrated in Fig. 3-19.

(a)   **(b)**
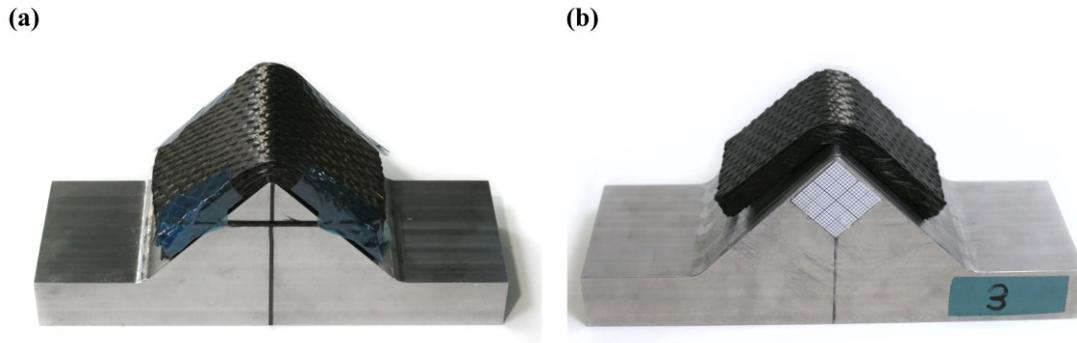
Fig. 3-18: Non-planar preform manufacturing process: (a) stacked and fixed layers on the lower tool; (b) after preforming and cutting into final dimensions.
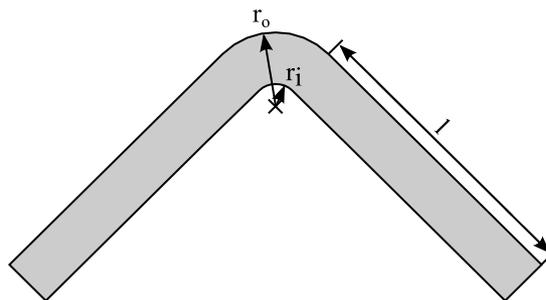
Fig. 3-19: Schematic sketch of a preform specimen with geometry definitions.

Before testing, the following properties of the manufactured specimens were measured and documented:

- Width of the flanges and of the radius
- Thickness of the flanges and of the radius
- Weight of the preform
- Manufacturing defects, such as loose rovings or delamination

3.5.1.2   Experimental procedure

The experimental procedure is the same as for the planar compaction experiments shown in Fig. 3-5. Additionally, a photo was taken of each preform after the preform was pre-compacted to the initial thickness and at the end of the compaction during relaxation.

The photos are used to evaluate the thickness of the preform in the radius. Contrary to the planar experiments, all tests were performed with the same closing velocity of 2 mm/min.

Tab. 3-8 lists all configurations of the non-planar experiments. Six displacement-controlled configurations vary the tool radii and the number of layers. Four of these configurations have the same final thickness of 5 mm with varying final FVC depending on the number of layers. However, combining the smallest lower tool radius with the greatest upper tool radius allows for a final thickness of 7 mm (L_3_10_14). Compacting a preform to 3 mm becomes possible with the larger inner radius and the smallest outer radius (L_5_8_8). For the two force-controlled configurations L_3_8_12_F and L_5_10_12_F, different inner radii with the same final thickness and the same number of layers were chosen.

Tab. 3-8: Configurations of the non-planar compaction experiments.

Configuration	Lower tool radius [mm]	Outer radius pre-form tool [mm]	Outer radius compaction tool [mm]	Number of layers
L_3_8_12	3	10	8	12
L_3_8_14	3	10	8	14
L_3_10_16	3	12	10	16
L_5_10_12	5	12	10	12
L_5_10_14	5	12	10	14
L_5_8_8	5	10	8	8
L_3_8_12_F	3	10	8	12
L_5_10_12_F	5	12	10	12

3.5.2 Evaluation of the specimen dimensions

The thickness of each specimen was measured with a dial gauge. A mean value was calculated from three measurements on both flanges respectively. The distinction between the flanges was chosen randomly with the purpose to verify if significant differences between the flanges appear. A defined measurement of the thickness in the radius was not possible with the chosen method, because the preforms showed different spring-back angles. With the thickness in the radius being dependent on the angle of the preform, the results of a thickness measurement in the radius are not comparable. Tab. 3-9 summarizes the mean values of the thickness measurement on the flanges. The measurements showed that both flanges had comparable thicknesses with variations inside the scatter of the measurements. The values for the initial thickness during the

compaction tests were chosen to be slightly greater than the smallest measured thickness. This ensures initial contact between the preform and the upper mold for all experiments. Moreover, the same initial thickness was chosen for all configurations having the same number of layers to ensure comparability of the test data. Applying Eq. (3-1) allows to calculate the initial and the final FVC for each configuration which are also given in Tab. 3-9.

Tab. 3-9: **Mean flange thickness before testing, initial test thickness and FVC values of the non-planar characterization experiments.**

Configuration	Left flange [mm]	Right flange [mm]	Initial thickness [mm]	Initial FVC [-]	Final FVC [-]
L_3_8_12	8.04	8.35	7.6	0.334	0.508
L_3_8_14	8.74	8.85	8.3	0.357	0.593
L_3_10_16	10.44	10.46	10.0	0.339	0.484
L_5_10_12	8.05	8.08	7.6	0.334	0.508
L_5_10_14	8.58	8.69	8.3	0.357	0.593
L_5_8_8	5.69	5.7	5.4	0.314	0.565
L_3_8_12_F	8.06	8.00	7.6	0.334	0.508
L_5_10_12_F	8.19	8.29	7.6	0.334	0.508

Measuring the thickness on the flanges with the dial gauge was important to detect possible asymmetries and to set the initial thickness for the experiments. However, measuring the thickness in the radius was not possible. Thus, an optical method was applied to measure the thickness of each specimen inside the tool using photographs. For this purpose, millimeter paper was glued onto both lower tools. Using the millimeter paper as reference in a digital image analysis, the thickness of the preform can be measured at different locations. Fig. 3-20 illustrates how the thickness is evaluated with an image showing the preform during the experiment. The photo was taken during the holding phase after the specimen was compacted to the initial thickness and before the final compaction started. The geometry of this state will be taken as input for the compaction simulation in order to account for correct thickness and FVC in the virtual model.

The posttreatment of the images was implemented in a Python routine using the OpenCV [262] package for image analysis. The code opens an image and lets the user select two points with the mouse in a defined distance of 10 mm. With the length/pixel ratio stored in a variable, any distance on the image can then be provided in millimeters. Clicking two further points on the image directly shows their distance as depicted in Fig. 3-20. With this method, the thickness of the flange and the radius was measured for each specimen.
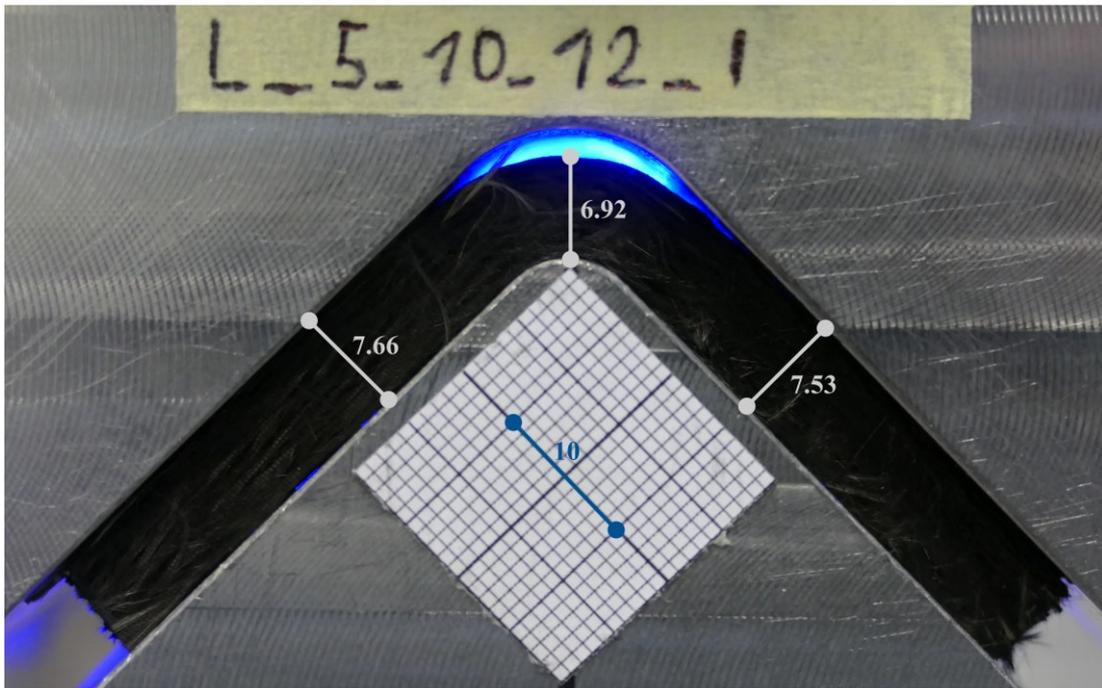
Fig. 3-20: **Digital image length measurement during first holding phase at initial thickness (shown for configuration L_5_10_12_01), length in mm.**

Tab. 3-10 provides the mean specimen dimensions at the beginning of the compaction experiments. The given flange length corresponds to the respective dimension of the additively manufactured positioning device. The width of the specimens was measured manually with a caliper gauge. The values of the flange thickness and the radius thickness were evaluated with the method mentioned above. For all configurations, the mean thickness of the flanges corresponds to the initial thickness being set in the UTM. The most noticeable result is that the radius section is significantly thinner for all configurations. The radius thinning varies from 7.0% to 10.5% with configuration L_3_8_12 showing the greatest thinning. No correlation was identified between the radius thinning and any other specimen properties such as number of layers, weight or FVC.

Additionally to the measurement of specimen dimensions, the pictures taken before and after compaction can be used to quantify the deformation during the experiment. Overlaying pictures before and after compaction enables measuring the shear deformation at the flanges. Fig. 3-21 depicts the overlay of two photographs of configuration L_5_10_12. The detail of the flange in Fig. 3-21b allows to quantify the shear deformation by measuring the angle between the deformed and undeformed specimen. These measurements are used for model calibration and validation in Chapter 5.
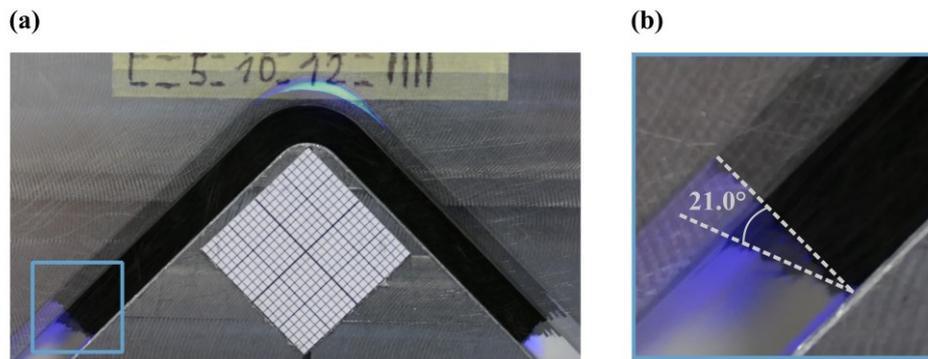
Fig. 3-21: Overlay of pictures before and after compaction for the measurement of the shear angle after compaction (configuration L_5_10_12): (a) entire specimen showing the position of the detail; (b) detail for the measurement.

Tab. 3-10: Mean specimen dimensions at the beginning of the compaction test

Configuration	Flange length [mm]	Width [mm]	Flange thickness [mm]	Radius thickness [mm]	Radius thinning [%]
L_3_8_12	40.0	40.94	7.6	6.8	10.5
L_3_8_14	40.0	40.75	8.3	7.7	7.2
L_3_10_16	38.5	41.51	10.0	9.3	7.0
L_5_10_12	38.5	40.97	7.6	6.9	9.2
L_5_10_14	38.5	40.59	8.3	7.7	7.2
L_5_8_8	40.0	40.84	5.4	5.0	7.4
L_3_8_12_F	40.0	40.87	7.6	6.9	9.2
L_5_10_12_F	38.5	41.22	7.6	6.9	9.2

3.5.3 Experimental results and discussion

All configurations showed a gap between tool and preform on the outer radius at the beginning of the experiment. However, this gap vanished during the compaction to the final FVC during each repetition for all configurations. Fig. 3-22 illustrates the final state of the compaction experiment for one specimen of configurations L_3_10_16 and L_5_8_8. The photographs show that the gap vanishes for thick preforms with low final FVC (0.48) as well as for thin preforms with higher final FVC (0.57). Moreover, the radius of the lower tool does not influence this effect. The same behavior was observed during the force-controlled experiments L_3_8_12_F and L_5_10_12_F.

(a) (b)
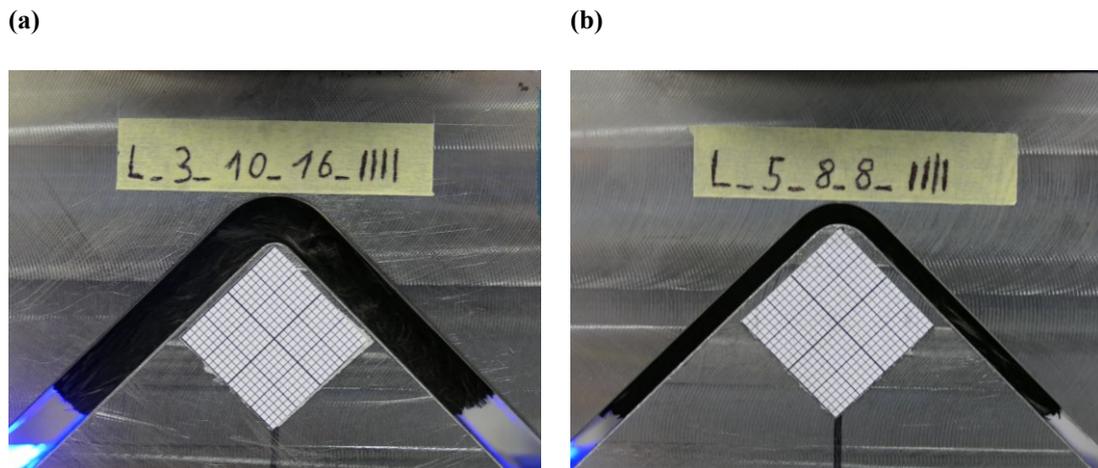
Fig. 3-22:   Front view of the preforms during the holding phase at maximum compaction level:
             (a) configuration L_3_10_16; (b) configuration L_5_8_8.

Because of the vanishing gap in the radius, the contact area between tool and preform changes during the experiment. With a changing area the reaction force acts in, it is extremely difficult to calculate a stress response. Thus, the reaction force over time measured by the load cell is provided for the results analysis. The reaction force is also a direct output from the process simulation and can thus, be used for the model validation in Section 5.5. The force response of all displacement-controlled experiments is shown in Fig. 3-23. Besides the mean value illustrated as continuous line, the scatter between minimum at maximum values is shown with a shaded area. The most noticeable result is that the qualitative behavior is very similar to the planar compaction results in Fig. 3-6. The angled preforms show an exponential stress increase during compaction and a significant stress relaxation during the holding phase. Moreover, a strong dependency of the relaxed stress on the final FVC appeared in the experiments. This leads to the assumption that the material response of the angled preforms is dominated by the through-thickness compaction force.

Having a closer look at the force responses, it is noticeable that not all curves are on top of each other although the compaction speed was the same. This can be explained with varying strain rates due to different preform thicknesses of the configurations L_3_10_16 and the L_5_8_8. A thinner preform compacted with the same velocity leads to higher strain rate. The remaining four curves with the same strain rate are nearly on top of each other during the compaction phase. Interestingly, the material responses of configurations L_3_8_12 and the L_5_10_12 are almost identical, whereas there is a significant difference between L_3_8_14 and the L_5_10_14. It seems that the tool radius has a significant influence on the peak stress and the relaxed stress for high FVC. The coefficient of variation is between 1.0 and 6.2%. Thus, the scatter is smaller than for the planar compaction experiments. The highest coefficient of variation appears for the configuration with 16 layers, whereas the configuration with only 8 layers shows the

lowest scatter. Consequently, there seems to be a relation between the scatter and the number of layers. This supports the hypothesis that nesting effects are a main contributor to the scattering of the experimental results.
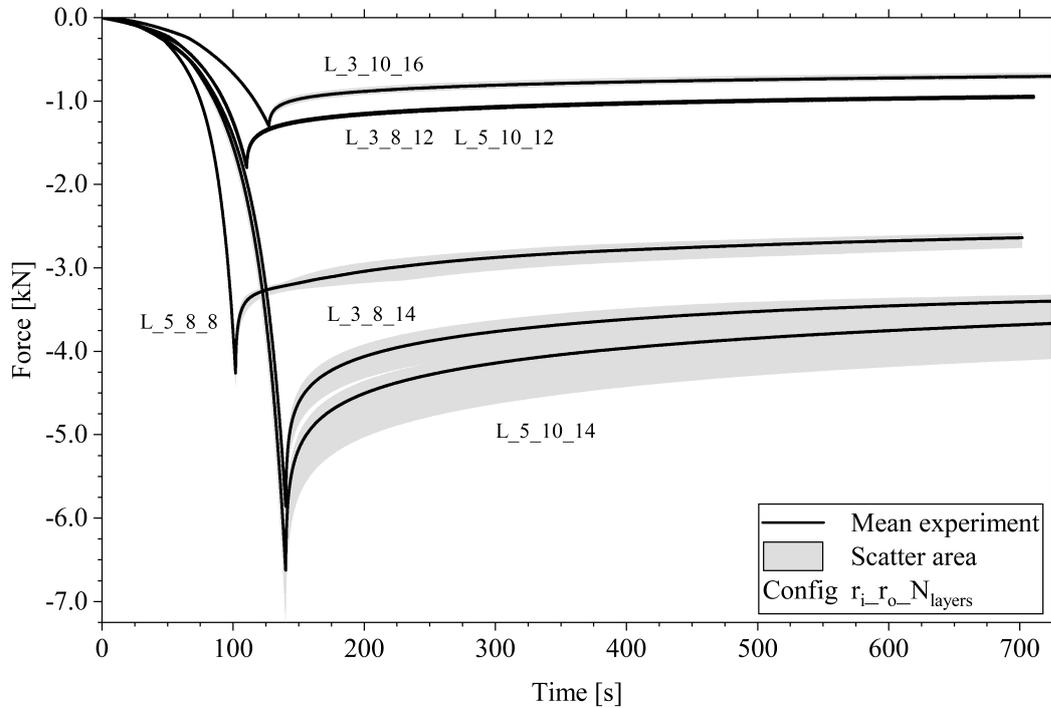
Fig. 3-23: **Force response of the displacement-controlled non-planar compaction experiments for different tool radii and number of layers, including minimum and maximum scatter area.**

The mean displacement response including the scatter area of the force-controlled experiments is shown in Fig. 3-24. As for the displacement-controlled tests, the qualitative behavior is very similar to the planar compaction in Fig. 3-8. The thickness decrease is followed by a creep phase at constant force. The force release leads to a material springback without recovering to the initial thickness. As in the case of displacement-controlled tests, the coefficient of variation is less than for the planar experiments. The coefficients of variation of the 3 mm and the 5 mm configuration are 0.58% and 0.56%, respectively. Comparing Fig. 3-24a and b shows no obvious difference between the results. The mean maximum displacement at the end of the creeping phase differs by only 0.14% and thus, lies inside the scatter range.

(a)

(b)
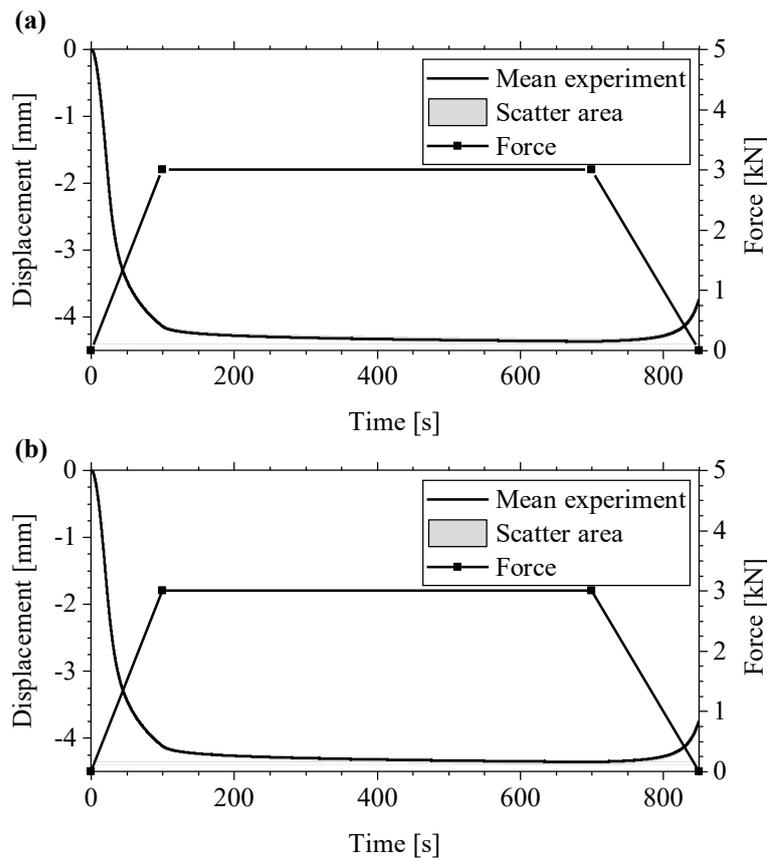
Fig. 3-24: **Displacement response of the force-controlled non-planar compaction experiments, including minimum and maximum scatter area: (a) 3 mm inner tool radius; (b) 5 mm inner tool radius.**

In contrast to some of the reviewed literature, none of the tested configurations showed a gap in the corner. However, in several cases, the appearance of gaps can be explained with poor tool design. As reported by Bickerton et al. in [30], they only observed race-tracking in the corner for one configuration that had significantly higher cavity thickness in the radius. Causse et al. [56] used molds with the outer radius being greater than the inner radius. This tool design enforces gaps, because the cavity thickness is larger in the corner. Koutsonas [63] performed experiments with constant cavity thickness observing race-tracking channels in the radius. Dong [52] could also determine gaps in the cavity with constant height. However, the four examples discussed used layered stacks without activating the binder. This is in good agreement with the radius thinning observed in Subsection 3.5.2.

4 Compaction material model for dry carbon fiber preforms

The objective of this chapter is the development of a one-dimensional material model which is capable of predicting the complex time-dependent compaction behavior of dry carbon fiber preforms. The model should meet the following requirements in order to be applicable in a numerical process simulation:

- Description of the material behavior in a single formula for compaction and relaxation.
- Prediction of the material response for displacement-controlled and force-controlled setups.
- Computational efficiency in order to be used for complex geometries.

After the model is developed and model parameters are identified, it is validated with experimental data. For this purpose, displacement-controlled and force-controlled experiments with the weave and the NCF material are used.

4.1 Model development

As a starting point for the development of a new material model, the approach of Schapery [200] and Kaliske [195] was used, since it already meets most of the objectives mentioned above. On the one hand, the model describes viscoelastic behavior in a single equation. On the other hand, it is computational efficient according to Kaliske and Rothert [195]. However, the capabilities for the prediction of displacement-controlled and force-controlled material response of the selected materials needs to be investigated. In order to evaluate the predictive quality of different models, a fitting approach is developed which is capable of quantifying the distance between curves. Afterwards, a phenomenological model was developed and fitted to experimental data.

The content of this section is partly derived from the preprint of [P1].

4.1.1 Fitting approach

A phenomenological approach was used to modify an existing model in order to better reproduce the experimental data. The starting point of the model development was a

generalized Maxwell model, in which the branch spring stiffness E_j was modified with different formulations. The resulting models were fitted to the test results. For this purpose, an optimization algorithm was used which minimizes the area between experimental and model data. The quality of a certain formulation was evaluated using the results of the objective function. The fitting algorithm reads in the experimental time-stress data and takes the same time steps to calculate the total stress with the developed model. The difference from the experimental curve can then be calculated without interpolation. For every input curve, the difference between experimental and model stress was calculated for each data point. The normalized sum of the stress differences λ for one input curve was calculated as follows:

$$\lambda = \frac{\sum_{i=1}^{P}(\sigma_{i,exp} - \sigma_{i,model})^2}{\sum_{i=1}^{P} \sigma_{i,exp}^2} \qquad (4\text{-}1)$$

The square difference between experiment and model was summed up for every stress data point σ_i. P describes the total number of data points of the current curve. The square difference method was used in order to give areas with greater deviation a higher weight in the optimization. The value was normalized to the square sum of the experimental values to make an evaluation of the quality of a fit at the different stress levels possible. By summing up the normalized stress differences for all input curves, the objective function is defined as follows:

$$\lambda_{tot} = r \cdot \sum_{k=1}^{M} \frac{\left(\sigma_{min,exp} - \sigma_{min,model}\right)_k^2}{\sigma_{min,exp,k}^2} + (1-r) \cdot \sum_{k=1}^{M} \lambda_k \qquad (4\text{-}2)$$

The stress difference λ_{tot} for all input curves k was minimized. M is the number of input curves which are selected for the optimization. In order to receive a better representation of the peak stress, the difference between the minimum stresses σ_{min} of each curve receives a higher weight in the objective function. Therefore, the absolute difference between the experimental and model peak stress was considered with a weighting factor r. A weight $r = 0.1$ for the peak stress has been found to produce the most accurate results. The normalized total difference λ_{tot} was minimized with a sequential least squares programming method implemented in Python. A more detailed description of the fitting procedure is given in Appendix d.

4.1.2   Formulation of the spring stiffness

The development of a new model capable of predicting the compaction behavior of carbon fiber preforms was based on the formulation from Kaliske et al. [195]. They used a generalized Maxwell model to describe the viscoelastic behavior of different rubber materials. The main advantage of their model is that compaction and relaxation can be

described with a single formula. Moreover, the incremental description provides the option of a computational efficient implementation in an FEA code. The rheological representation of the model with three branches ($N = 3$) is depicted in Fig. 4-1. In this model, E_0 denotes the stiffness in the free spring, whereas E_j and τ_j represent the stiffness and relaxation time in the branch j with $j = 1 \dots N$.
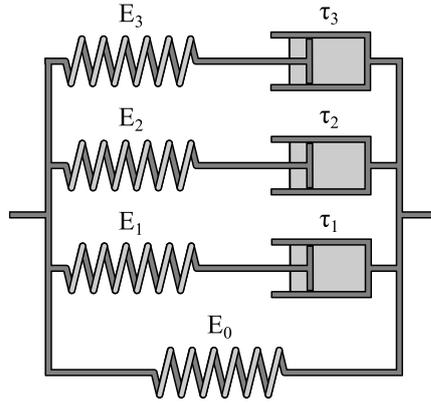
Fig. 4-1:   **Rheological representation of the developed material model with three branches.**

The stress h_j in one Maxwell branch j is given by an incremental formulation in dependency of the previous time step [195]:

$$h_{j,t+\Delta t} = \exp\left(-\frac{\Delta t}{\tau_j}\right) \cdot h_{j,t} + E_j \cdot \left(1 - \exp\left(-\frac{\Delta t}{\tau_j}\right)\right) \frac{\Delta \epsilon}{\Delta t / \tau_j} \qquad (4\text{-}3)$$

Where Δt is the time step size, τ is the relaxation time of the dashpot, E is the stiffness of the spring, and ϵ is the total strain of the Maxwell element.

The total stress σ is defined as the sum of the N branch stresses and the stress in the free spring with stiffness E_0 [195]:

$$\sigma_{j,t+\Delta t} = E_0 \epsilon_{t+\Delta t} + \sum_{j=1}^{N} h_{j,t+\Delta t} \qquad (4\text{-}4)$$

The stiffness E_0 in the free spring ensures that not all the applied stress was relaxed after the compaction. The magnitude of relaxed stresses of the various configurations in Fig. 3-6 and Fig. 3-7 increases sharply with an increasing final FVC. The relation between relaxed stress and FVC was thus strongly nonlinear. Consequently, an expression of the stiffness E_0 with an exponential law in dependency of the FVC V_f was introduced.

$$E_0 = \frac{A}{V_f} \cdot exp(B \cdot V_f^2) \qquad\qquad (4\text{-}5)$$

The variables A and B are fitting parameters which can be derived from the relaxed stresses depending on the final FVC.

With a defined E_0, a novel formulation which describes the stress in one branch can then be developed. Initially, the aforementioned model from Kalsike with three Maxwell branches and a constant spring stiffness E_j was implemented in Python. In order to evaluate the capabilities of the model, it was fitted to configuration WV_0.55-1 of the weave material from Tab. 3-1 using Eq. (4-2). The resulting curve was plotted in Fig. 4-2a (referred to as "*const*") together with the mean value of the experimental data. The fit of the *const* model shows that the exponential stress increase during the compaction phase cannot be well reproduced. Moreover, the model provides a poor fit of the high peak stress. However, the relaxed stress was described very well, which is defined by the stiffness E_0. To gain a deeper understanding of why the model was not capable of showing high peak stresses, it was fitted again with a higher weight for the peak stress, $r = 0.99$. The resulting curve is shown in Fig. 4-2a as "*const peak*". This modification led to a very good description of the peak stress and the stress decrease during relaxation. However, the compaction phase was modeled extremely poorly. The significant difference compared to the experimental curve in the first phase led to higher values λ_{tot} of the objective function during the optimization. The deviation of the model during the compaction phase can be explained by the evolution of the branch stresses. Fig. 4-2b shows the contributions of the four branches to the total stress for the *const peak* fit. Due to the constant FVC in the holding phase, the stress in E_0 remained constant. Thus, high peak stresses could only be achieved with high stresses in the remaining branches. In every branch, the stress increases sharply at the beginning when the deformation is mostly taken by the spring. Since the dashpot takes larger fractions of the deformation, the stress increased more slowly. During the holding phase, the extension of the spring reached its initial state, and the stress returned to zero. The higher the peak stress compared to the relaxed stress of the experimental data, the higher the fraction from the branches in the model needs to be. However, this also caused larger deviations in the compaction phase. Hence, the *const* model might be suitable for materials with low peak stresses, but not for high peak stresses.

Since the stiffness was constant, the elastic branch strains had the same qualitative behavior as the branch stresses shown in Fig. 4-2b. The slope of the branch stress can be adjusted by modifying the stiffness E_j. Thus, in order to achieve a better fit during the compaction phase, a nonlinear stiffness with a flat increase at the beginning and a steep increase towards the peak stress is needed. With a spring and a dashpot connected in series, the viscous strain shows this qualitative behavior. Given that the strain in the dashpot equals the total strain minus the elastic strain, it has the opposite behavior of the strain in the spring. The *viscous lin* model uses a stiffness with a linear dependency on

the viscous strain. The best fit of this model is shown in Fig. 4-2a. Contrary to the two fits with a constant stiffness, the compaction showed a good agreement with experimental results. The peak stress was significantly higher than with the *const* model, but still not as high as the experimental data. The relaxation phase was in good agreement with the test, but the stress was relaxing too slowly. In order to further improve the fit, the stiffnesses E_j were defined with an exponential dependency on the viscous strain. The result of the fitting optimization is shown in Fig. 4-2a. The *viscous exp* model is in very good agreement with the experimental data in the compaction phase as well as in the relaxation phase. A comparison of the best fit results for the four different models is given in Tab. 4-1. The optimized values of the objective function support that the *viscous exp* model agrees extremely well with the experimental data. As a result, only this model was considered for the following study.

Tab. 4-1: **Comparison of the fit optimization for different stiffness formulations.**

Model	E_j formulation	λ_{tot} of best fit [-]
Const	$E_j = a_j$	$21.29*10^{-3}$
Const peak	$E_j = a_j$	$94.33*10^{-3}$
Viscous lin	$E_j = a_j \cdot \epsilon^v$	$4.488*10^{-3}$
Viscous exp	$E_j = a_j \cdot \exp(b_j \cdot \epsilon^v)$	$0.9438*10^{-3}$

In order to account for the stiffnesses E_j, which can vary between two consecutive time steps, Eq. (4-3) was adjusted. The consideration of the time dependency of the stiffness for the integration leads to:

$$h_{j,t+\Delta t} = exp(-\frac{\Delta t}{\tau_j}) \cdot h_{j,t} + \left(E_{j,t+\Delta t} - E_{j,t}exp(-\frac{\Delta t}{\tau_j}) \right)_j \frac{\Delta \epsilon}{\Delta t / \tau_j} \qquad (4\text{-}6)$$

With the total strain ϵ and the elastic branch strain ϵ_j^e, the branch stiffness can be written as:

$$E_j = a_j \cdot exp((\epsilon - \epsilon_j^e) \cdot b_j) \qquad (4\text{-}7)$$

Where a_j and b_j are constants relative to the branch stiffness. For the calculation of the current stress, the stiffness $E_{j,t+\Delta t}$ needs to be known and depends on the strain $\epsilon_{j,t+\Delta t}^e$. From Eq. (4-6), a formulation for the current elastic strain can be derived:

$$\epsilon_{j,t+\Delta t}^{e} = exp(-\frac{\Delta t}{\tau_j}) \cdot \epsilon_{j,t}^{e} + \left(1 - exp(-\frac{\Delta t}{\tau_j})\right) \frac{\Delta \epsilon}{\Delta t/\tau_j} \tag{4-8}$$

The total stress in the system can be calculated with Eq. (4-4) by inserting Eq. (4-5), (4-6), (4-7) and (4-8). The model is described with the fitting parameters A and B for the spring E_0 and the parameters a_j, b_j, and τ_j for each branch.

The derivation of Eq. (4-3) was based on the assumption of linear elastic behavior. Given that a nonlinearity has been introduced later on in order to improve the accuracy of the model, the new formulation does not correspond to a generalized Maxwell model. Thus, the stress which is calculated with Eq. (4-6) is not the same as the stress of a nonlinear Maxwell model with the branch stiffness of Eq. (4-7). There is no simple analytical solution to this nonlinear problem, because the derivation of the stress formulation requires a time integration of the relaxation function. This leads to extremely complex equations if the stiffness itself is time-dependent. A numerical integration is possible, but it results in very long calculation times. However, the goal of this study is to provide a numerically efficient model capable of predicting the behavior of the material. Hence, a phenomenological approach for the derivation of this model was chosen.

(a)   **(b)**
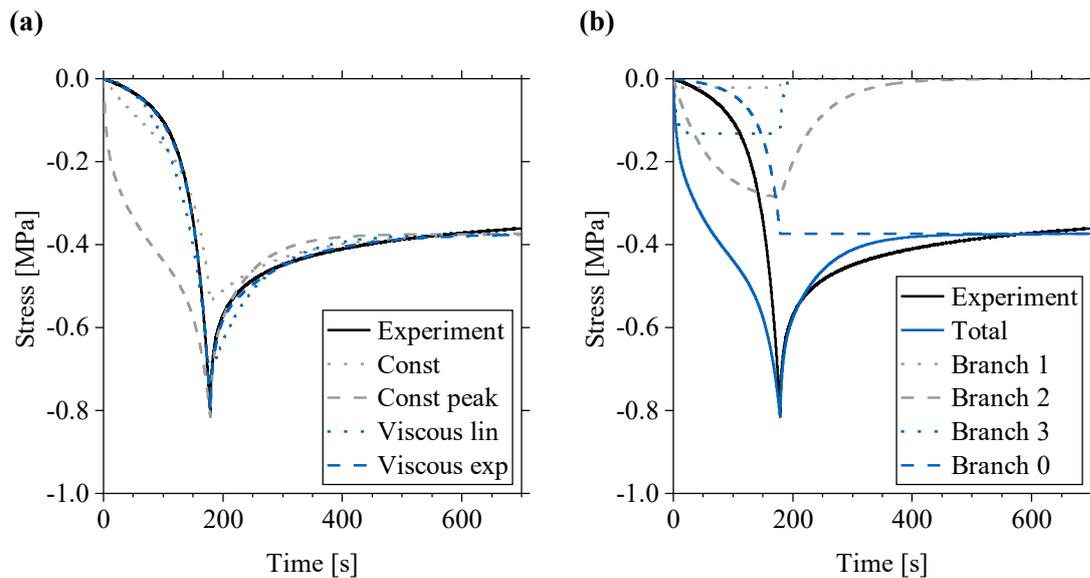
Fig. 4-2:   **(a) Experimental stress evolution of config WV_0.55-1 in comparison with different model formulations; (b) Branch stresses of the *const peak* fit compared to experimental stress data of config WV_0.55-1.**

The recursive formulation of the presented model takes the current strain and the strain rate as inputs for each time increment. This formulation thus enables the calculation of stresses for non-constant compaction velocities. This is useful in case the tool velocity is decreased before the maximum stress is reached in order to minimize peak stresses. The model can also be applied to compute stresses for multi-step compaction processes.

The derivation of the model parameters requires two steps. In the first step, the relaxed stresses for different FVC are fitted to Eq. (4-5). With the derived values for A and B, the remaining branch parameters a_j, b_j, and τ_j can be fitted using Eq. (4-4) and (4-6) in the second step. It is recommended to use at least three configurations with different compaction speeds and the same final FVC for the branch parameter fitting in order to cover the strain rate dependency.

4.2 Numerical solution of the nonlinear equations

The *viscous exp* model in Section 4.1 was derived applying a phenomenological approach by modifying the spring stiffness in an existing generalized Maxwell model. The incremental formulation which was used as a starting point was derived from linear rheological elements. Because nonlinearities were introduced at a later stage, the provided solution of the *viscous exp* model in Eq. (4-6) does not correspond to a rheological Maxwell element. The physically correct description of a nonlinear Maxwell element requires solving Eq. (2-8) with the nonlinear spring from Eq. (4-7):

$$\dot{\epsilon} = \frac{1}{a \cdot \exp(\epsilon^v \cdot b)} \left(\dot{\sigma} + \frac{1}{\tau} \sigma \right) \tag{4-9}$$

However, the model developed in Section 4.1 is capable of predicting the compaction response of different reinforcement materials very well. Moreover, the presented methodology provides a highly efficient analytical solution and meets the goal of this work very well. The objective of this section is to find a numerical solution of Eq. (4-9) in order to gain a deeper understanding of the model. Furthermore, a comparison of the phenomenological model to the numerical solution of the nonlinear Maxwell model allows quantifying the deviation due to the simplifications.

The mathematically correct solution of the nonlinear Maxwell model requires solving the first order differential equation Eq. (4-9). Because according to Eq. (2-5), the viscous strain ϵ^v in the definition of the spring stiffness is a function of the stress rate $\dot{\sigma}$, this function is extremely complex to be solved analytically. However, Eq. (4-9) can be solved with iterative methods such as Newton's method. In order to apply Newton's method, the problem needs to be defined in a way that it can be solved by finding an x-axis intercept. This can be achieved by using the assumption that in any arbitrary series connection of rheological elements, the stresses are equal in all individual elements at an equilibrium state. The equilibrium state of a Maxwell element with the elastic stress σ^e in the spring and the viscous stress σ^v in the dashpot, can be written as follows:

$$\sigma^e - \sigma^v = 0 \tag{4-10}$$

Another possibility to apply Newton's method is to use the assumption that the total strain in a series connection equals the sum of the elastic and viscous strains of the individual elements:

$$\epsilon - \epsilon^e - \epsilon^v = 0 \qquad (4\text{-}11)$$

Assuming that the total strain ϵ of the Maxwell element is known from the boundary condition, the viscous stress can be rewritten by using Eq. (2-5):

$$\sigma^v = \tau \frac{d(\epsilon - \epsilon^e)}{dt} \qquad (4\text{-}12)$$

Thus, a function $f(\epsilon^e)$ can be derived from Eq. (4-10) by inserting Eq. (2-4) and (4-12), which provides the elastic strain ϵ^e at the stress equilibrium state by finding the x-axis intercept of:

$$f(\epsilon^e) = E\epsilon^e - \tau \frac{d(\epsilon - \epsilon^e)}{dt} \qquad (4\text{-}13)$$

Now Newton's method can be applied in the following form in order to find the elastic strain at which the elastic stress equals the viscous stress:

$$\epsilon^e_{t+\Delta t} = \epsilon^e_t - \frac{f(\epsilon^e_n)}{f'(\epsilon^e_n)} \qquad (4\text{-}14)$$

Eq. (4-14) has been implemented in a Python script, which allows solving arbitrary linear and nonlinear Maxwell elements numerically. In order to verify that the numerical approach delivers a sufficient result, it is validated with the analytical solution from Kaliske and Rothert [195] for a linear Maxwell element. The *const* model response for configuration WV_0.55-1 was calculated analytically and numerically for the same set of parameters derived from the fitting in Section 4.1 (A_0=4.00e-3, B_0=1.61e-8, a_1=1.00e-8, a_2=8.15e-1, a_3=1.00e-7, τ_1=7.55e+0, τ_2=1.17e+2, τ_3=1.38e+1). The comparison of the analytical and the numerical solution of the model response is shown in Fig. 4-3a. It can clearly be seen, that the stress responses of the two approaches are the same. Hence, the numerical approach can be applied for nonlinear problems, which do not allow a straight forward analytical solution.

In the next step, the phenomenological *viscous exp* model from Section 4.1 is compared to the numerical solution of the nonlinear generalized Maxwell model with the same spring stiffnesses. The comparison of the stress responses of the two models is shown in Fig. 4-3b. Both curves are calculated for configuration WV_0.55-1 using the same set of model parameters for the weave material from Tab. 4-2. Comparing the stress evolution shows that both models respond nearly identical during the compaction phase. However, the model responses show a significant deviation during the relaxation phase. After similar initial relaxation, the numerical model response shows a second increase of the

absolute stress value, whereas the phenomenological model keeps decreasing. Having a second stress peak at around 240 s, the numerically solved model decreases the stress to the same final relaxed stress. Equal relaxed stresses for both solutions can be explained with zero stresses in the spring-dashpot branches. Moreover, it can be assumed that the compaction phase is also dominated by the stress in the spring E_0. The second stress peak during the relaxation of the numerically solved model can physically not be explained. Because the stress in the spring E_0 is constant during the relaxation, stress increase must be resulting from the spring-dashpot branches.

(a)   **(b)**
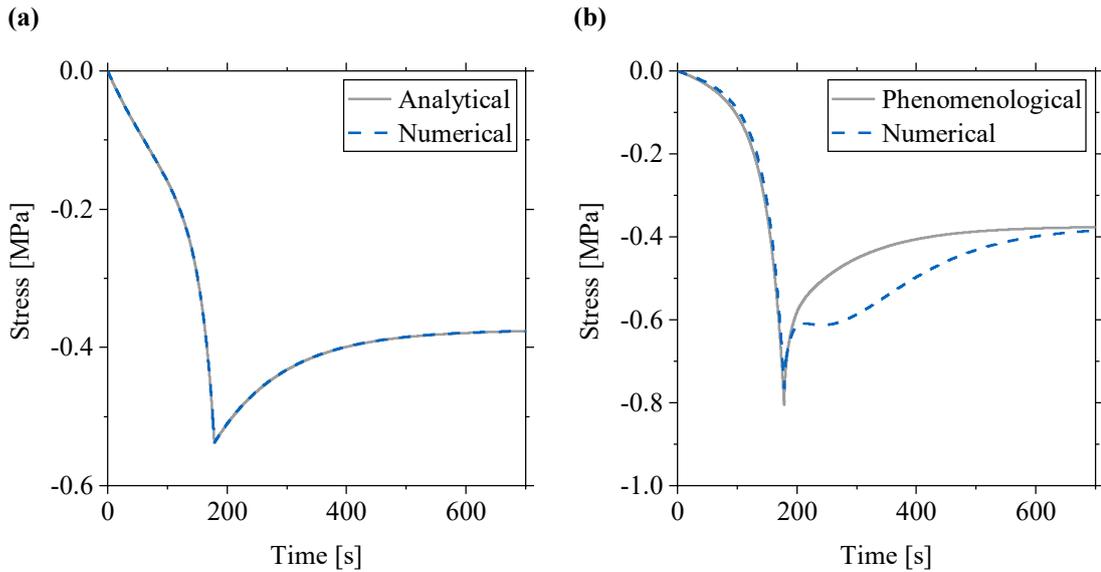
Fig. 4-3:   **Comparison of the stress response for configuration WV_0.55-1: (a) analytical and the numerical solution of the *const* model; (b) phenomenological model and the numerical solution of the *viscous exp* model.**

In order to gain a deeper understanding of the behavior of the numerically solved model, the stress evolution in the individual spring-dashpot branches needs to be analyzed. Fig. 4-4 compares the stress evolution in the individual branches for the phenomenological model and the numerical solution. The comparison shows that the stresses in branches 1 and 3 are nearly identical, whereas stresses in branch 2 show a very different behavior. The difference is particularly striking during the relaxation phase. The delayed stress peak in the second branch explains the behavior of the total stress of the numerical solution in Fig. 4-3b. As shown in Tab. 2-1, a continuous stress decrease is expected at constant strain in a Maxwell model, because the strain is gradually transferred from the spring to the dashpot. However, the absolute stress in branch 2 of the numerical solution keeps increasing at constant total strain. According to Eq. (2-4), an increasing stress in the spring can only be caused by increasing strain or increasing stiffness in the spring.

Taking a closer look into the evolution of the spring stiffnesses explains the behavior that was observed for the branch stresses. The comparison in Fig. 4-5a shows that both,

the phenomenological and with the numerical approach, deliver the same spring stiffnesses. As expected from the stresses in Fig. 4-4, the stiffness in branch 2 increases after the ramp time has been reached. The same but less dominant effect can be seen in branch 1. Looking at the model parameters in Tab. 4-2 leads to the assumption that the effect is related to higher relaxation times in the branches. The root cause can be found by looking at the viscous strains in the individual branches in Fig. 4-5b. Due to the higher relaxation time τ_2, the second branch reacts more slowly and thus, needs more time to transfer the elastic strains to viscous strains. This leads to a slower increase of the branch stiffness and a delayed stress peak in branch 2.
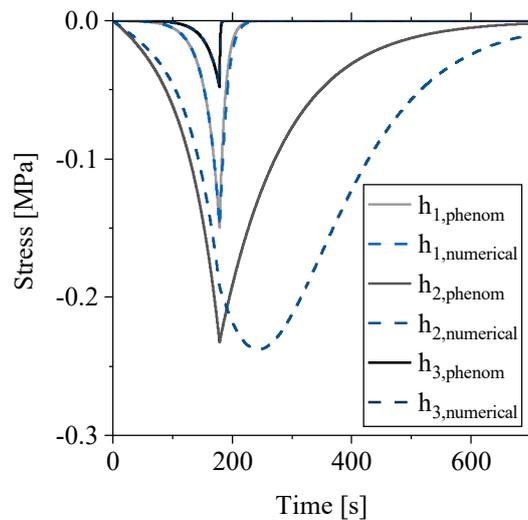
Fig. 4-4: **Comparison of the branch stresses of the analytical and the numerical solution of the** *viscous exp* **model for configuration WV_0.55-1.**

The comparison of the solution of the phenomenological model with the numerical model in Fig. 4-5 shows that strains and stiffnesses are the same for both approaches. The simplification in the derivation of the phenomenological model results in a different computation of the branch stresses. Branches with high relaxation times show a significant delay of the peak stress, whereas the stresses of the branches in the analytical model all start decreasing immediately at constant total strain.
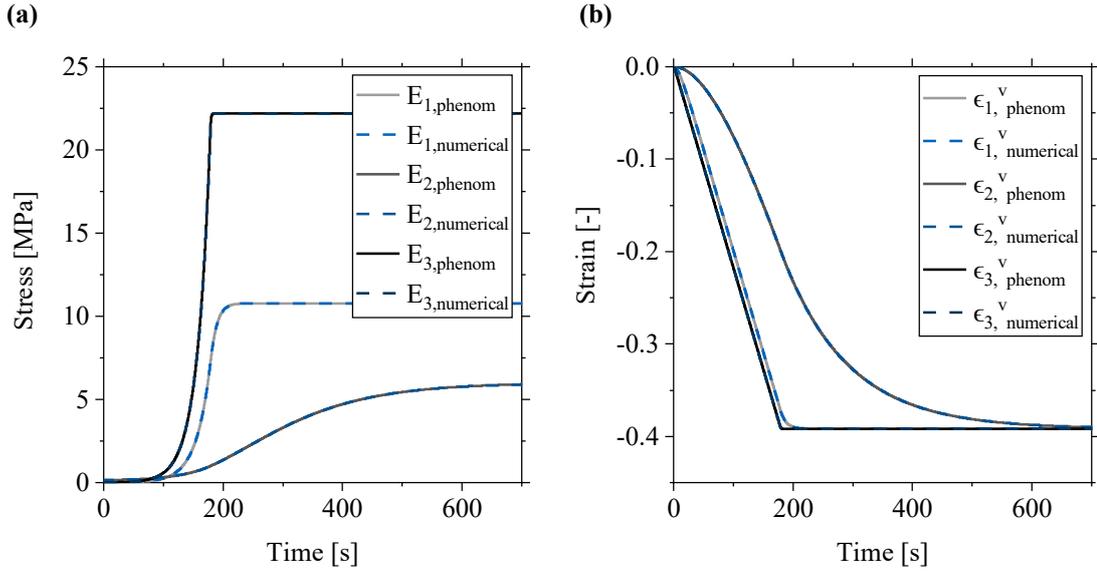
Fig. 4-5: Comparison of the analytical and the numerical solution of the *viscous exp* model for configuration WV_0.55-1: (a) spring stiffness; (b) viscous strain.

The fact that the poor fit of the numerical solution is a result of the viscous strain increasing after the ramp time, raises the question if the model can be improved with a modified strain. Defining the spring stiffness in dependency of a modified strain, which remains constant after the ramp time, eliminates the second peak in the numerical solution. Danzi et al. [107] introduced a relative strain ϵ^{rel} which shows constant values after the ramp time:

$$\epsilon^{rel} = \epsilon - \max(\epsilon^e) \tag{4-15}$$

By subtracting the maximum elastic strain from the total strain, the relative strain shows the desired behavior. Interestingly, Kelly used a similar strain relation in [214] subtracting the branch strain from the maximum possible strain. According to Kelly, this ensures higher viscous stresses when fibers are packed more tightly at higher FVC. Fig. 4-6a shows the different strains appearing in branch 2. It can be seen that the relative strain equals the viscous strain until it remains constant when the ramp time is reached.

The stiffness of the springs in the branches of the *relative exp* model can then be defined as follows:

$$E_j = a_j \cdot exp(\epsilon_j^{rel} \cdot b_j) \tag{4-16}$$

Fig. 4-6b compares the stress response of the phenomenological *viscous exp* model and the numerically solved *relative exp* model with the experimental data of configuration WV_0.55-1. Both models were fitted to the experimental data. The comparison reveals that the *relative exp* model shows a larger deviation from the experimental data during

the compression phase. However, both models show a very similar behavior during the relaxation. The λ_{tot} of the best fit of the *relative exp* model is $1.253*10^{-3}$ compared to $0.9438*10^{-3}$ for the *viscous exp* model. This proves that the *relative exp* model cannot reproduce the experimental data as accurate as the phenomenological *viscous exp* model. A comparison of the run time of the python scripts shows that the numerical solution of the *relative exp* model needs 33.5% more time than the *viscous exp* model. Because the model will be used in numerical simulations with thousands of elements and hundreds of time steps, short calculation times are crucial.

Due to better accuracy and shorter calculation times, the phenomenological *viscous exp* model will be used for the following studies in this work. It is important to state that the *viscous exp* model was derived from a linear generalized Maxwell model, but does not correspond to a rheological model, because nonlinearities were incorporated. Thus, the newly derived constitutive law is considered as a phenomenological model. The Maxwell elements in the model are consequently called branches in order to point out that they are not referred to as rheological elements. Nevertheless, the newly developed phenomenological model provides the best capability to answer research question 2 and the objectives defined at the beginning of this chapter. The applicability to displacement and force-controlled scenarios is proven and discussed in the following sections.
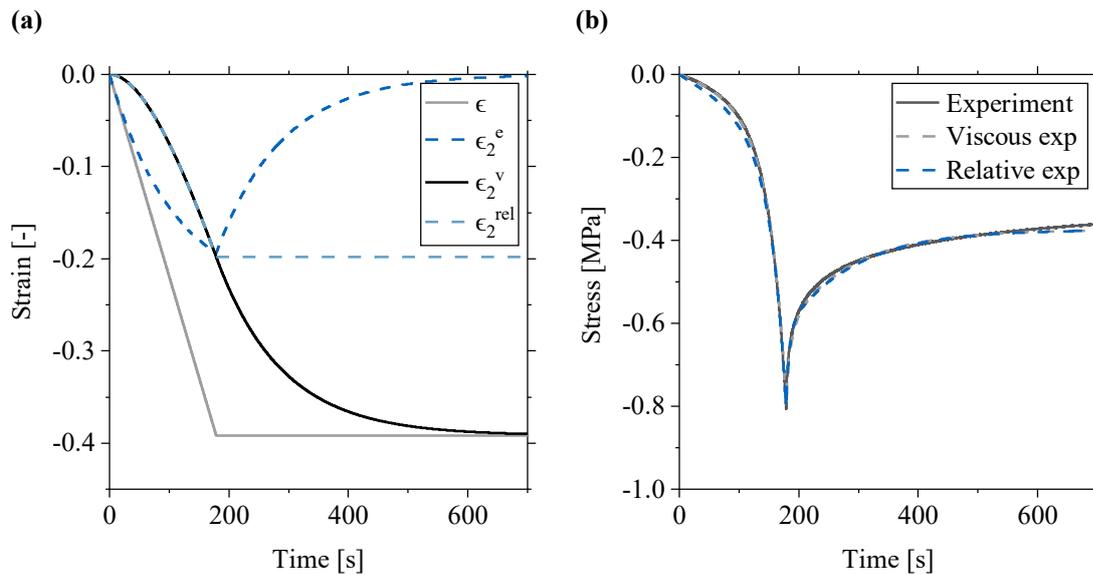
Fig. 4-6: **(a) strains in branch 2 of the *viscous exp* model for configuration WV_0.55-1; (b) Comparison of stress responses of different models with experimental results for configuration WV_0.55-1.**

4.3 Application of the *viscous exp* model to displacement-controlled setups

In this section, the phenomenological *viscous exp* model developed in Section 4.1 is applied to displacement-controlled setups. In order to prove the applicability to various reinforcement materials, the model is used to predict the stress response of the woven fabric and the NCF which have been characterized in Section 3.2. Configurations 0.45-2, 0.50-2, 0.55-1, 0.55-2, 0.55-5 and 0.60-2 from Tab. 3-1 are used for the calibration of the model. The remaining configurations 0.50-1 and 0.50-5 are used for the model validation in Subsection 4.3.3. Moreover, a sensitivity analysis is performed to gain a deeper understanding of the individual model parameters. The parameter study is also used as a base line to decide on the optimum number of branches in the model. The objective of this section is to prove that the model can be applied to different materials capturing the strain rate dependency and the FVC dependent stiffness of the fibrous materials. The content of this chapter is partly derived from the preprint of [P1].

4.3.1 Model calibration

The analytical *viscous exp* model is calibrated in two steps. At first, the parameters of the stiffness of the free spring E_0 are determined. In the second step, the remaining parameters, which define the stress in the branches, are identified. It is assumed that the stress of the fully relaxed state is only stored in the free spring. Thus, the stiffness E_0 can be determined independently of the branches. The relaxed stresses of the compaction experiments with the velocity 2 mm/min are used for the parameter fitting, in order to have four different FVCs. The values A and B in Eq. (4-5) are fitted with the experimental data in dependency of the final FVC. From Eq. (3-1), the strain can be calculated with the initial FVC V_{f0} as:

$$\epsilon = \frac{V_{f0}}{V_f} - 1 \tag{4-17}$$

Fig. 4-7 shows the result of the parameter fitting for the free spring for the two tested materials. The relaxed stress from experimental data was plotted with the scatter of the corresponding configuration. The description of the stiffness E_0 in Eq. (4-5) predicted the relaxed stresses very well. The model curve was in excellent agreement with the experimental data of both materials. Only the stress of the weave at 55% FVC was over-predicted and the stress of the NCF at 45% FVC was slightly under-predicted. Nevertheless, the curve remains within the scatter of the experimental data. The values of the parameter fitting are given in Tab. 4-2.
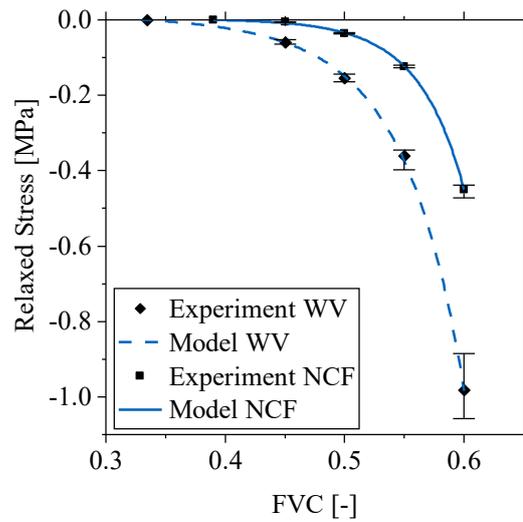
Fig. 4-7:   **Fitting of the model to the relaxed stresses of experimental data with 2 mm/min, including scatter for the weave and the NCF.**

For the second step of the procedure, configurations having different compaction velocities and the same final FVC were fitted. Three configurations were used to cover the strain rate dependent behavior of the material. The optimization algorithm provides the set of parameters having a minimum distance between the experimental and model data according to Eq. (4-2). The resulting parameters which define the elastic branch stiffness from Eq. (4-7) and the branch relaxation times for both materials are provided in Tab. 4-2. The fitting parameters are given for a model with three branches.

Fig. 4-8 shows the three experimental input curves of the fitting algorithm with a final FVC of 55% and different compaction velocities with the corresponding model predictions. The model of the weave in Fig. 4-8a exhibits a good level of accuracy during the compaction phase. Additionally, the model predicted the peak stresses notably well, which is of special importance for tooling force analysis. During the relaxation, the model response matched the experiments very well for the first hundred seconds after the peak stress. In contrast, the model shows some deviations for the subsequent relaxation. For all velocities, a deviation can be seen from the experimental relaxed stress. The difference of the final stresses in the 2.0 mm/min configuration of the weave corresponds to the small deviation of the fit in Fig. 4-7, at 55% FVC. The compaction at 1.0 mm/min exhibited minor deviations at the end of the relaxation. However, for higher compaction velocities, the model response diverged earlier from the experimental results. This behavior can be explained with the parameter fitting to the relaxed stresses in Fig. 4-7. Since the model assumes that the relaxed stress is stored in the free spring, it is independent of the compaction velocity. Thus, the experimental data with different relaxed stresses cannot be perfectly reproduced. Importantly, the relaxed stress of the model prediction is -0.375 MPa, which is still within the scatter area of the experimental data. The modeled material response of the NCF is compared with the experimental data

in Fig. 4-8b. Except for minor deviations at the beginning, the compaction phase of the model was in very good agreement with experimental data. Moreover, the peak stresses were predicted very well for all three compaction velocities. The stress relaxation was in good agreement with the experiments for the 2 mm/min and 1 mm/min compaction velocities, whereas the relaxation behavior for the highest velocity showed a deviation. This can be explained with the strain-rate-independent definition of E_0.

Tab. 4-2:   **Model parameters of weave and NCF material for the three-branch model.**

Model parameter	Value weave material	Value NCF material
A	$4.001*10^{-3}$ MPa	$4.354*10^{-4}$ MPa
B	$1.613*10^{+1}$	$2.078*10^{+1}$
a_1	$5.348*10^{-3}$ MPa	$6.127*10^{-3}$ MPa
b_1	$1.942*10^{+1}$	$2.571*10^{+1}$
a_2	$1.585*10^{-1}$ MPa	$1.095*10^{-8}$ MPa
b_2	9.274	$1.389*10^{-2}$
a_3	$6.409*10^{-3}$ MPa	$6.883*10^{-3}$ MPa
b_3	$2.080*10^{+1}$	$2.127*10^{+1}$
τ_1	9.477 s	$1.452*10^{+2}$ s
τ_2	$1.101*10^{+2}$ s	$3.718*10^{+1}$ s
τ_3	1.034 s	4.635 s
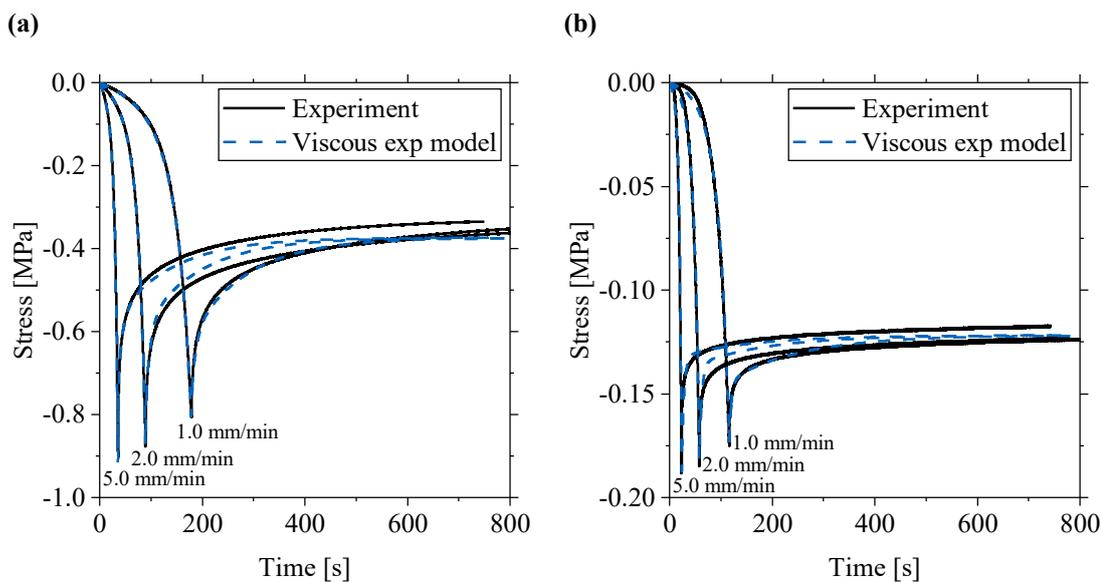
Fig. 4-8:   **Fitting of the branch parameters to different compaction velocities for the three-branch model; (a) weave, (b) NCF.**

4.3.2   Parameter study

A sensitivity analysis was performed in order to gain a better understanding of the model parameters. For this purpose, the optimum elastic and viscous parameters of the weave material in Tab. 4-2 were increased and decreased by 50%.

Fig. 4-9 shows the results of the study, with every column representing one of the branches in the model. Each plot takes the modeled compaction curve from configuration WV_0.55-2 as a reference. The modification of the single parameters clearly shows the influence on different sections of the compaction response. Comparing the a_j values in the first row shows that a_1 influenced the peak stress and the early stress relaxation, whereas the parameter a_2 in the second branch influenced the relaxation behavior at later time points. However, a_3 did not have a significant influence on the characteristic of the curve. Varying the b_j parameters in the second row led to a similar behavior. Modifying b_1 strongly influenced the value of the peak stress. However, b_2 mostly affected the early stress relaxation. It is important to note that the b_j values were the only ones influencing the compaction phase for every branch. Varying the relaxation times τ_j showed that the first branch defined the beginning of the relaxation, and the second one defined the subsequent stress relaxation. In contrast, τ_3 seems to have a minor influence on the compaction response. Generally, all relaxation times influenced the relaxation without having a significant influence on the compaction response or the peak stress.

The parameter study showed that different sections of the response curve can be modified individually by increasing or decreasing different variables. This study supports the outcome from the two tested materials, that very different behavior from strong to weak stress relaxation can be represented very accurately with the developed model.

Interestingly, the third branch was only sensitive to an increased b_3 value. Moreover, it seems that the effect of increasing b_3 can also be achieved by a combination of other parameters. However, decreasing b_3 or varying the other values in the third branch had a minor effect on the model response. This finding indicated that the compaction behavior can also be modeled with only two branches. Thus, the fitting procedure was repeated for the weave with a different number of branches. The normalized total stress difference λ_{tot} of the three input curves was used to evaluate the quality of the fit. Tab. 4-3 compares the results of the objective function for one, two, three, and four branches. The comparison proves that the third branch has a minor influence on the model behavior. The model with two branches decreases the quality of the fit by 7.4% compared to three branches. However, further reduction to a single branch worsens the result significantly. The model with four branches shows a negligible improvement of the fit compared to three branches. Due to the high number of variables, the computational effort for the optimization increases significantly. For the following validation, three branches were used in order to obtain the best possible results with a reasonable amount of CPU effort.
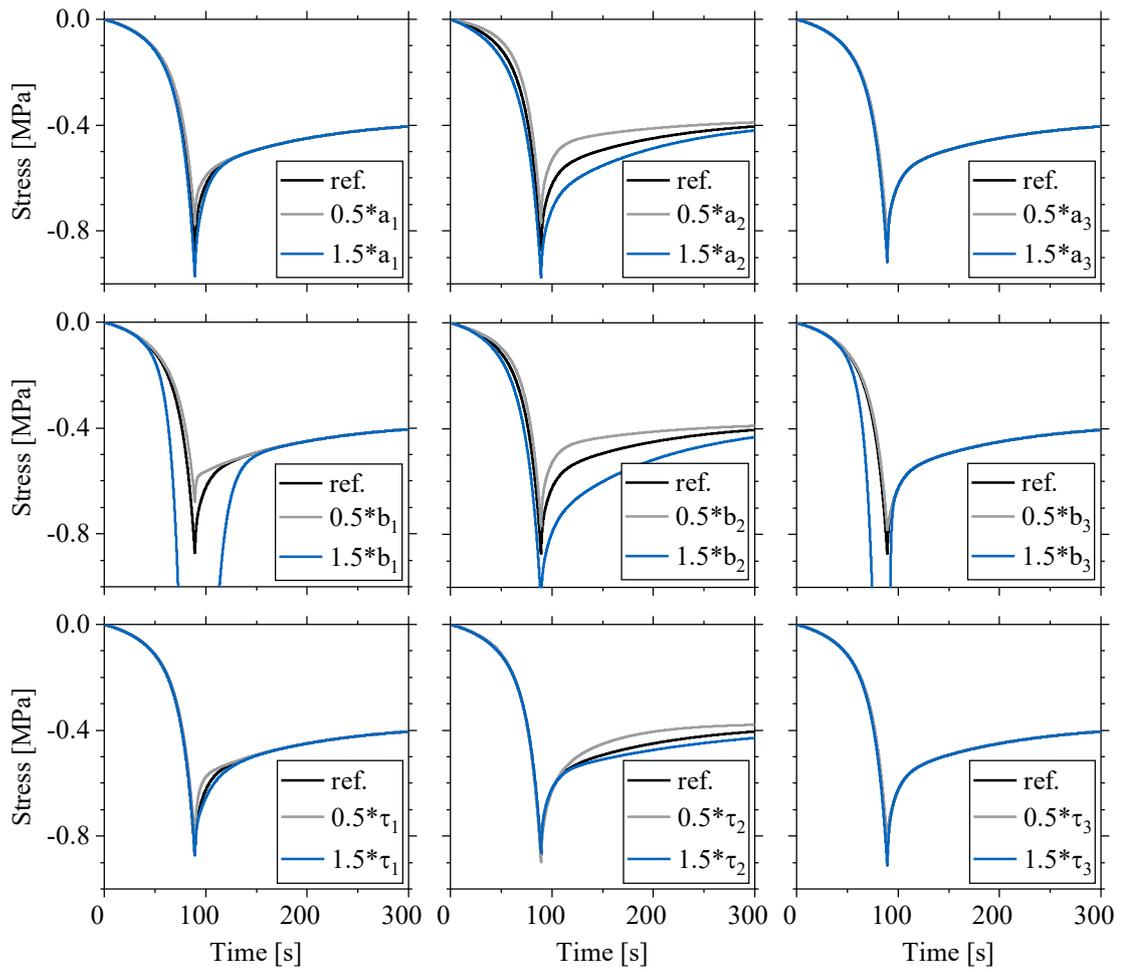
Fig. 4-9: **Variation of elastic and viscous parameters for three branches of ±50% of the fitted optimum (ref.), all curves plotted for 2 mm/min with 0.5 final FVC.**

Tab. 4-3: **Total difference of the parameter fitting of the weave material for different number of branches *N*.**

N	λ_{tot} [-]
1	$24.79*10^{-3}$
2	$6.231*10^{-3}$
3	$5.803*10^{-3}$
4	$5.799*10^{-3}$

4.3.3 Model validation and discussion for displacement-controlled setups

For the derivation of the parameters in the branches, the three configurations 0.55-1, 0.55-2, and 0.55-5 from Tab. 3-1 were used for each material. The remaining experiments can thus be used for validating the model. Fig. 4-10 shows the experimental results and the corresponding model predictions for all displacement-controlled configurations with the weave material. In general, the model with three branches predicted the compaction response of the woven material very well. During the compression phase, there was only a small deviation for configuration WV_0.50-5. The model and the experiments show a good agreement for the peak stresses for both low and high FVC. However, deviations were observed in the relaxation phase. The modeled relaxation response was very accurate for configurations WV_0.50-2, WV_0.55-2, and WV_0.55-5. For lower FVC values, as in configuration WV_0.45-2, the model relaxed the stresses too slowly. In contrast, the higher FVC in configuration WV_0.60-2 causes an overly rapid stress relaxation. The final stresses in all configurations were in very good agreement with the experimental results. For the slower (configuration WV_0.50-5) and faster (configuration WV_0.50-1) compaction velocities with 50% FVC, the stress did not relax to the experimental values, which is due to the model assumption of a purely elastic free spring.
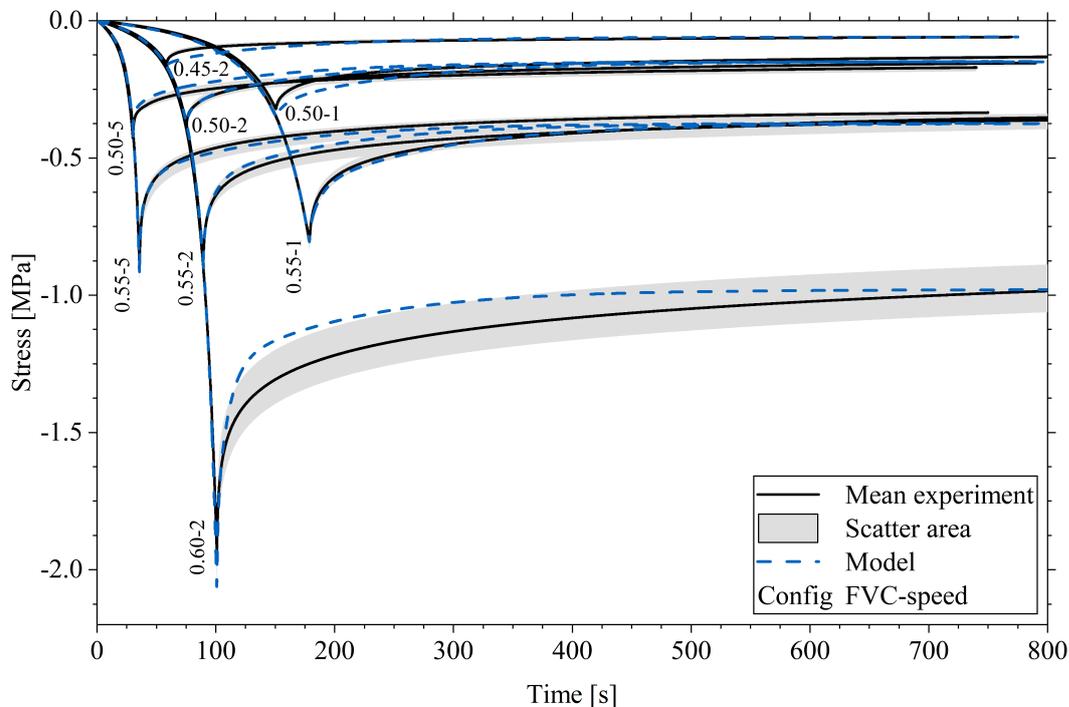
Fig. 4-10: **Experimental data of the weave material tests for different compaction velocities and final FVC, including minimum and maximum scatter area and prediction of the viscous exp model.**

Fig. 4-11 shows the mean experimental data, including scatter, together with the results of the modeled stress response of the NCF material. The modeled compression phase was in very good agreement with experimental results, showing only small deviations at the beginning of the compaction. As for the woven fabric, the model predicted the peak stresses very well for all configurations. During the relaxation, the same effect as that of the weave can be observed. If the material was compacted to a low FVC, the model relaxed the stress too slowly, whereas the stress relaxation was too fast at a high final FVC. This can be explained with the different phases during the compaction as introduced in Section 2.2. During the compaction of configurations NCF_0.45-2 and WV_0.45-2, larger voids remained in the preform without entering the third phase of sharp stress increase, whereas configurations NCF_0.60-2 and WV_0.60-2 exhibited stronger yarn deformation. This effect might be the cause for the deviation in the relaxation behavior. Another parameter could be introduced into the macroscopic model in order to cover the additional strain rate dependency during the stress relaxation. The relaxation of the model agrees very well with experimental data at 50% FVC for all velocities tested. The final stresses were in very good agreement with experimental results for all configurations, except for NCF_0.45-2. The deviation of the relaxed stress came from the fit of the free spring E_0 illustrated in Fig. 4-7.
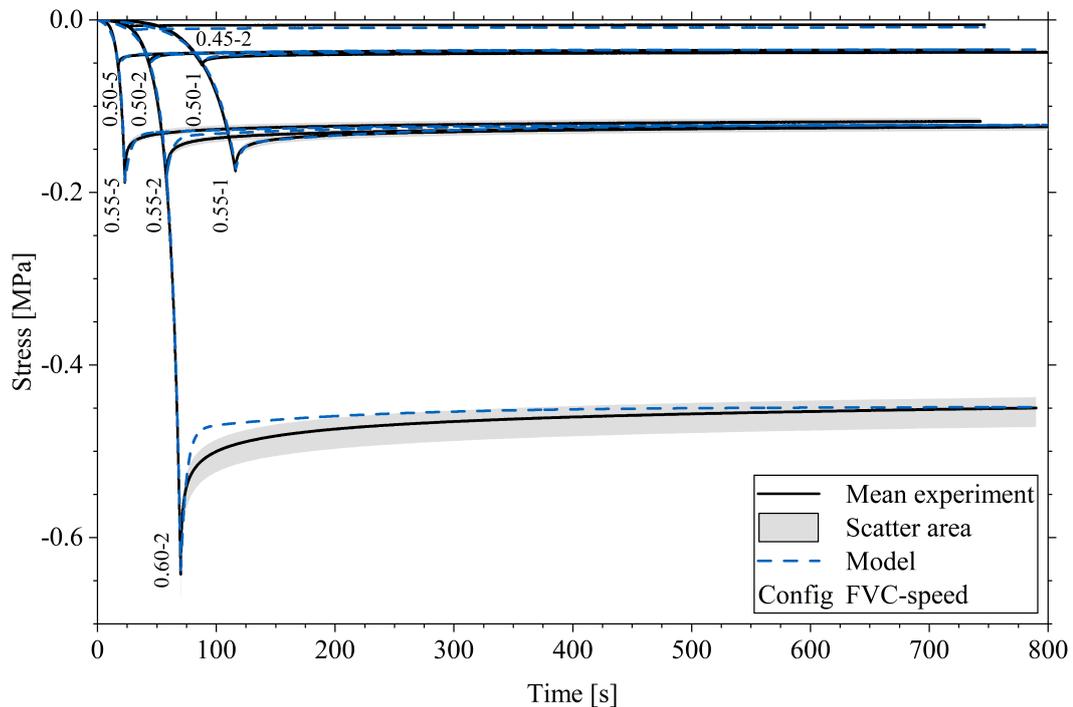
Fig. 4-11:   **Experimental data of the NCF material tests for different compaction velocities and final FVC, including minimum and maximum scatter area and prediction of the viscous exp model.**

4.4 Implementation of the material model in a user-defined subroutine

The formulation in Eq. (4-3) cannot be solved analytically for force boundary conditions to calculate compaction strains. Nevertheless, the calculation of strains is possible in numerical simulations. Thus, the *viscous exp* model developed in Section 4.1 has been implemented in user material routine in ANSYS Mechanical. With the FE simulation, the force-controlled configurations from Tab. 3-2 can be modeled and the strain response can be compared to experimental data. Moreover, it is the basis for geometrically more complex models in Chapter 5.

All structural FE simulations were performed using the commercial software ANSYS Mechanical 2020.R2 [243]. An ANSYS research license held by the TUM LCC was used for all simulations. Computationally more expensive models were solved on the CoolMUC-2 and CoolMUC-3 high performance cluster from the Leibniz Rechenzentrum (LRZ) [263]. User-defined subroutines were compiled using Microsoft Visual Studio Professional 2017 Version 15.0 and Intel Visual Fortran 2019.3.203 compilers.

In order to provide a better understanding of the steps which are necessary for nonlinear materiel modeling, the basic concept of Newton-Raphson iteration is briefly introduced. Generally, in any FE method the following equation is solved for each element [264]:

$$[K]\{U\} = \{R\} \tag{4-18}$$

This equation describes the equilibrium for a linear static analysis, were $[K]$ is the stiffness matrix, $\{U\}$ is the displacement vector and $\{R\}$ is the vector of forces acting in the direction of the displacements. However, finding an equilibrium state becomes more complex if the relation between displacements and applied forces are nonlinear. A nonlinear analysis becomes necessary if:

- Displacements are large and the volume change of the element cannot be neglected
- The material shows a nonlinear elastic behavior
- Boundary conditions are not constant during the response (e.g. change of contact status)

In the present case, the stiffness of the material is a function of strain and time (see Eq. (4-5) and (4-7)). Thus, Eq. (4-18) cannot be solved for a given applied force, because the stiffness can only be calculated for a known displacement and vice versa. Nevertheless, there must be an equilibrium state for the applied load. It is assumed that in the equilibrium, the external loads R equal the internal forces F corresponding to stresses inside the element. The force equilibrium at the time $t + \Delta t$ can be written as [264]:

$$\{R_{t+\Delta t}\} - \{F_{t+\Delta t}\} = 0 \tag{4-19}$$

It is assumed that forces and displacements at time t are known. The force is increased by the increment ΔF [264]:

$$\{F_{t+\Delta t}\} = \{F_t\} + \{\Delta F\} \tag{4-20}$$

The tangent stiffness matrix $[K_t]$, which describes the stress strain relation of the material at time t is defined as follows:

$$[K_t] = \frac{\{\Delta F\}}{\{\Delta U\}} \tag{4-21}$$

With $[K_t]$, Eq. (4-19) can be rewritten as [264]:

$$\{R_{t+\Delta t}\} - \{F_t\} - [K_t]\{\Delta U\} = 0 \tag{4-22}$$

This formulation is only an approximation because it calculates the material response for the applied load $\{R_{t+\Delta t}\}$ with the tangent stiffness of the previous time step. The exact solution of this problem with stiffness $[K_{t+\Delta t}]$ can be found with iterative methods. The following equations can be solved with Newton-Raphson iteration [264]:

$$\{R_{t+\Delta t}\} - \{F_{t+\Delta t}^{i-1}\} - [K_{t+\Delta t}^{i-1}]\{\Delta U^i\} = 0 \tag{4-23}$$

$$\{U_{t+\Delta t}^i\} = \{U_{t+\Delta t}^{i-1}\} + \{\Delta U^i\} \tag{4-24}$$

Where i denotes the iteration number. Following initial conditions are used for the first iteration $i = 0$ [264]:

- $\{U_{t+\Delta t}^0\} = \{U_t\}$
- $\{K_{t+\Delta t}^0\} = \{K_t\}$
- $\{F_{t+\Delta t}^0\} = \{F_t\}$

In order to converge quickly, it is crucial to find a consistent definition of the tangent stiffness matrix, also known as Jacobian matrix. A poor definition of the Jacobian matrix would result in a simulation which does not converge. For the *viscous exp* model, the Jacobian matrix was defined according to the model from Kaliske et al. [195]. Incorporating the nonlinear stiffness from Eq. (4-7) leads to the following representation of the tangent stiffness matrix:

$$\{K_t\} = E_0 + \sum_{j=1}^{m}\left(E_{j,t+\Delta t} - E_{j,t}exp(-\frac{\Delta t}{\tau_j})\right)\frac{\tau_j}{\Delta t} \tag{4-25}$$

With the Jacobian matrix defined, the material model can be implemented in a user-defined material subroutine. This code is executed by the solver for every element in each time step. Using the Jacobian matrix at the end of the subroutine, the solver will

try to find a stable solution and return strains and stresses at the equilibrium for each time step.

The process flow of the code which was implemented in Fortran is shown in Fig. 4-12. The solver passes strains, strain increments and state variables to the subroutine in the respective element coordinate system. [265]. The code begins with an initialization of variables, such as the initial FVC and the model parameters given in Tab. 4-2. Afterwards, the strain rate is calculated from the strain increment provided by the solver and the current FVC can derived from Eq. (4-17). Using the total strain provided by the solver, the elastic branch strains are calculated by applying Eq. (4-8). With all strains known, the stresses in the branches can be computed with Eq. (4-3). However, the stress stored in the free spring E_0 is calculated with Eq. (4-5) using the total strain derived from the solver. Summing up the branch stresses and the stress in the spring E_0 gives the total stress according to Eq (4-4). The corresponding entry in the Jacobian matrix is computed from current and previous time step stiffnesses using the definition from (4-25). At the end, the subroutine provides the updated stresses in the element coordinate system, the Jacobian matrix and the updated state variables back to the solver [265]. The Fortran code of the user material subroutine can be found in Appendix c.
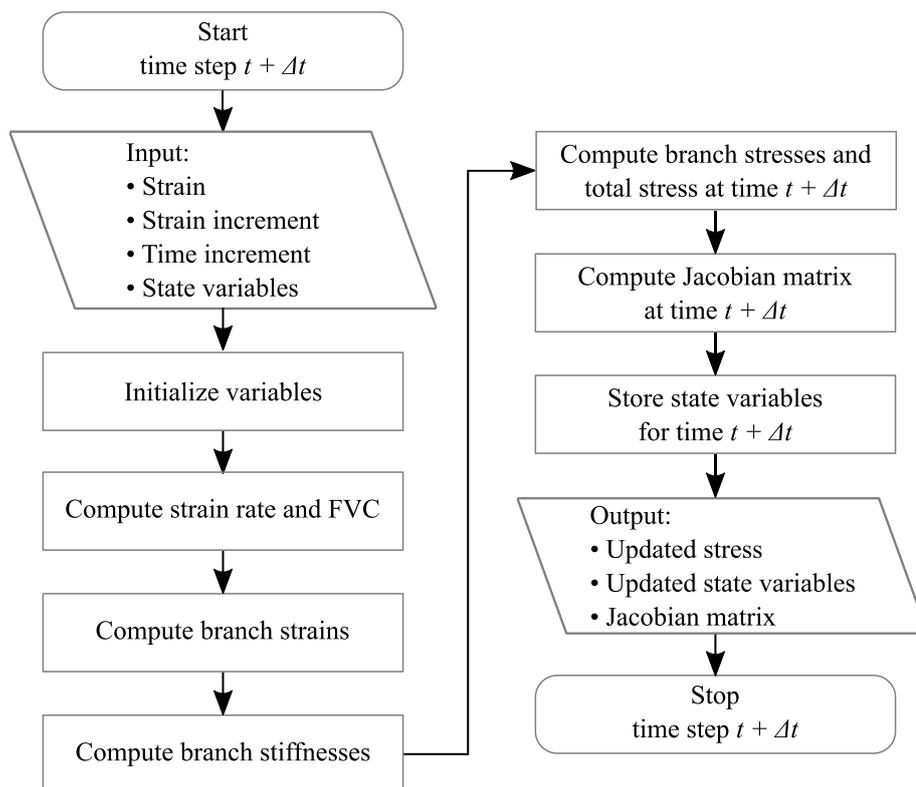
Fig. 4-12: **Flow chart for the computation of stresses in the user-defined material model for one-dimensional compaction model.**

In order to test the subroutine, simulations were conducted using a 1D bar meshed with a single LINK180 element. The model was set up in ANSYS Mechanical APDL with a length corresponding to the initial thickness of the test samples. The cross-sectional area of the bar element was set to the size of the specimens. Thus, the model response can directly be compared with experimental data. One node was fully constrained, and a displacement or force boundary condition was applied to the second node. Tab. 4-4 gives an overview of the simulation parameters used for the one-dimensional simulations.

Before the FE model was used to compute force-controlled setups, it was applied to displacement-controlled simulations. Because displacement-controlled setups can also be calculated analytically with the Python script used for the model calibration in Section 4.3, the comparison shows if the numerical method provides correct results. The Fig. 4-13 clearly shows that the numerical solution implemented in the FE element code provides the same stress response for all configurations. Thus, the numerical method can be applied to validate the model for force-controlled setups in the following section.
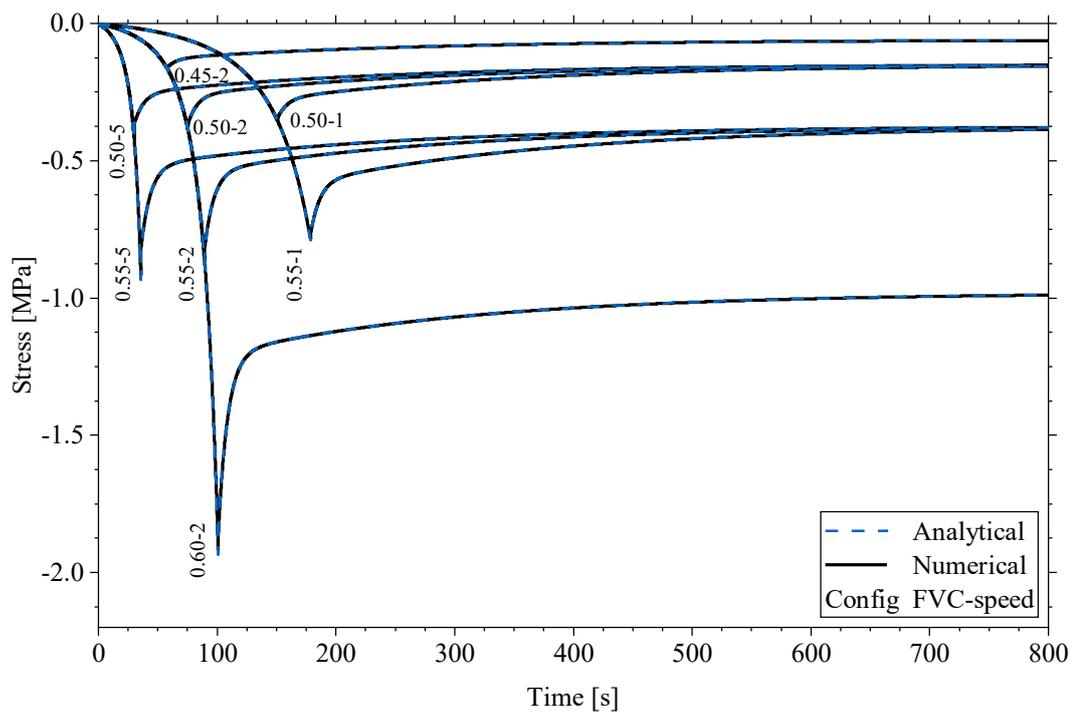
Fig. 4-13: **Comparison of analytical and numerical solution for displacement-controlled experiments with the woven fabric.**

Tab. 4-4: **Settings for the one-dimensional simulation model.**

Parameter	Value
Element type	Link180
Element length	7.6 mm
Element cross section	10 000 mm²
Initial FVC	0.3345
Damping	0.0

4.5 Application of the viscous exp model to force-controlled setups

The content of this section is partly derived from the preprint of [P1].

The force-controlled setups were calculated in ANSYS Mechanical using the user-defined subroutine presented in Section 4.4. Fig. 4-14a shows the results of the numerical one-dimensional simulation and the experimental results of the force-controlled experiments at a 100 N/s compaction rate of the weave material. The numerical simulation predicts the behavior in the three phases of compaction, creeping, and spring-back very well. The compression in the first phase was in good agreement with the experiment and was only slightly over-estimated. The model also showed the creep of the material at a constant force, where the slope of the curve was less than the experimental one. However, the thickness at the end of the creep phase differed by 4.8% from the experiments. Moreover, the simulation predicted the spring-back of the material when the force was released. Although there was a difference in the increase of qualitative thickness, the final thickness was predicted very well, with a difference of 3.0% from the experimental value.

Fig. 4-14b compares the numerical simulation with the force-controlled experiments of the weave at a 250 N/s compaction rate. As for the slower compaction rate, the three phases of the experiment can be seen. During the compaction, the predicted behavior agreed very well with the experimental results. The modeled creeping showed slightly higher displacements than the experimental data, with a deviation of 3.1% of the thickness at the end of this phase. Similar to the slower compaction, the spring-back showed the most significant difference in qualitative behavior. However, the difference in the final thickness compared to the experiments was 6.5%. For both tested configurations, the modeled thickness differed by between 3.0% and 6.5% from the experiments at the end of the creep and the spring-back. This model thus provides a powerful tool for predicting the thickness of preforms in force-controlled setups.
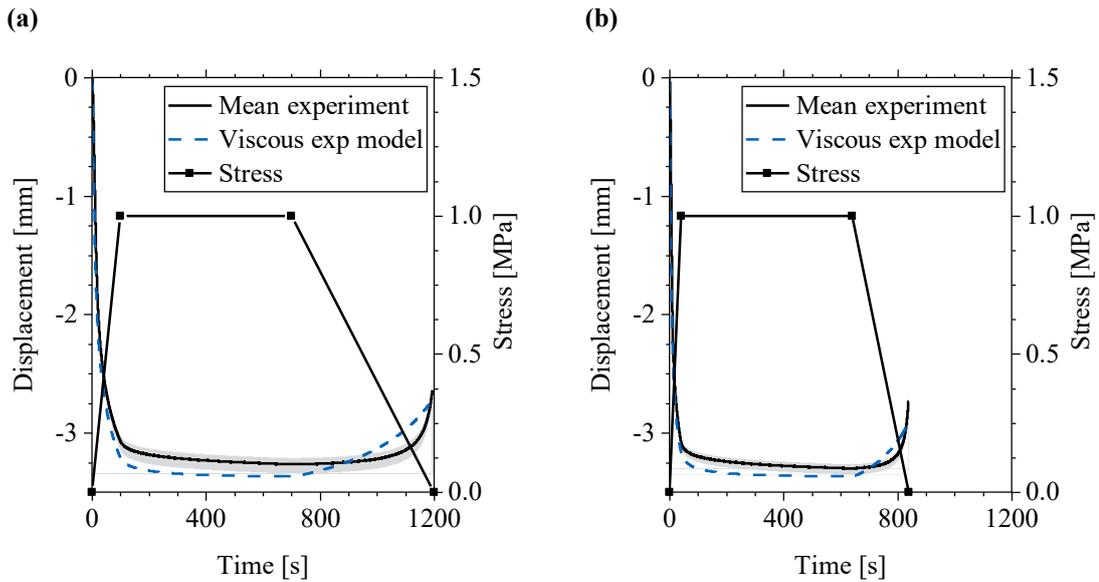
Fig. 4-14: **Experimental data for force-controlled experiments, including minimum and maximum scatter area and results of the model of the weave material: (a) slow compaction; (b) fast compaction.**

Fig. 4-15a compares the modeled displacement response of the NCF with experimental data for the force-controlled configuration at a low force rate. The modeled compression phase was in excellent agreement with the experimental data. The following creep phase at a constant compaction pressure showed small deviations from the experiment, with a difference of 0.7% of the maximum displacement. The modeled thickness slightly decreases at constant force, but not as much as in the experiments. The predicted spring-back was significantly lower than the one observed in the tests. The experiment showed a spring-back to 1.9 mm when the force was released, whereas the model showed a spring-back to only 2.2 mm.

Fig. 4-15b shows the comparison of experimental and modeled data of the high force rate configuration of the NCF material. The observations from the comparison were very similar to the slower compaction. A good agreement during the compaction was followed by some deviations in the creep phase and significant differences for the spring-back. The differences can be explained by the deviations of the displacement-controlled configuration NCF_0.60_2, because the preforms were compacted to approximately 59% FVC in the force-controlled setups. The comparison of NCF_0.60_2 in Fig. 4-11 shows a very fast stress relaxation at the beginning and almost negligible time-dependent behavior of the model towards later times. The same behavior can be seen in Fig. 4-15, where the thickness decreases too quickly at the beginning of the creep phase and shows too little time-dependent behavior during the further creep and the spring-back.

(a)

(b)
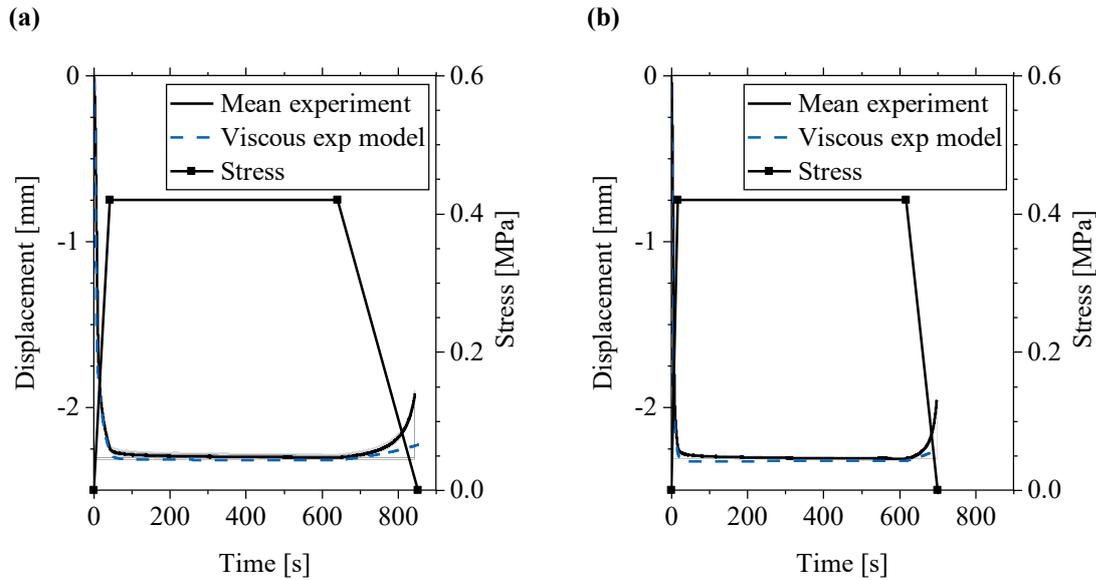
Fig. 4-15:   **Experimental data for force-controlled experiments, including minimum and maximum scatter area and results of the model of the NCF material: (a) slow compaction; (b) fast compaction.**

Fig. 4-16 provides a comparison of the simulation results for the displacement-controlled and force-controlled experiments with the weave material. In Fig. 4-16a, the thickness reduction is compared for both setups. The dashed line shows the displacement boundary condition of configuration WV_0.60-2, whereas the continuous line is the simulation result of the force-controlled experiment at a 100 N/s compaction rate. The force-controlled curve shows a steeper slope at the beginning and slowly flattens until reaching a plateau after about 200 s. However, both curves converge to the same displacement value. The final thickness is the same for the displacement-controlled and the force-controlled setups. Thus, according to Eq. (3-1), the final FVC is equal. Fig. 4-16b compares the stresses in thickness direction over time for both configurations. The dashed line is the resulting stress from the numerical simulation of configuration WV_0.60-2 and the continuous line is the stress boundary condition of the force-controlled simulation. The final stress at 700 s was almost equal, with -1.0 MPa for force-controlled and -0.98 MPa for displacement-controlled, respectively. The peak stress was at 101 s, whereas the constant stress of the force-controlled configuration was reached at 100 s. The peak stress of the displacement-controlled configuration was more than doubled, with a value of -2.1 MPa. Thus, the resulting peak stress can be reduced by 50% with slightly changing the evolution of the strain. In an RTM process, the challenge is to know the force which is necessary to achieve the desired FVC. As a result, the model developed in this work facilitates to design the process for minimizing peaks in tooling forces. It is possible either to design a force control or to adjust the displacement curve in order to avoid high peaks. This allows the use of a smaller press in the RTM process.

(a)   **(b)**
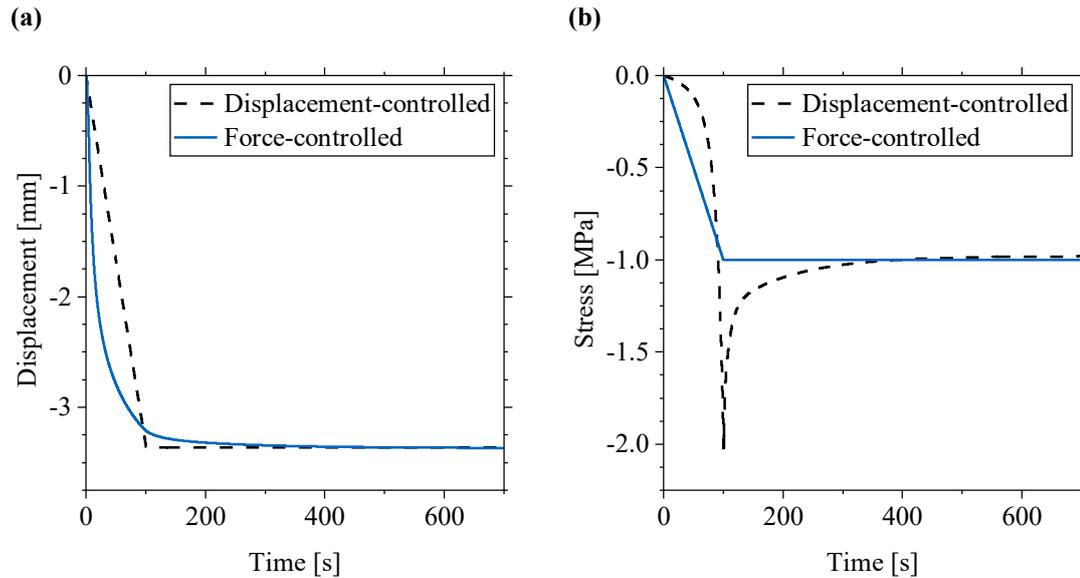
Fig. 4-16: **Comparison of displacement (a) and stress (b) for displacement-controlled and force-controlled simulations of the weave material.**

4.6 Discussion and conclusion of the 1D model

The content of this section is partly derived from the preprint of [P1].

A novel formulation of a viscoelastic material model was developed describing compaction and relaxation in a single set of formulas. As a result, the model can be used for non-constant strain rates or force-controlled setups with a smooth transition between the two phases. The necessary number of branches in the model was defined using the results of a parameter study. Very good agreement between the model stress response and the experimental tests for the two tested materials was obtained. By means of implementation into an FE code, the model can be applied to force boundary conditions. The compression, including creep and spring-back, could be predicted satisfactorily. None of the known material models from the literature has been applied and validated for the prediction of creeping and spring-back behavior. However, the model prediction of the spring-back was more accurate for the weave than for the NCF material. The deviation can partly be explained with comparably high velocities, especially during the compaction phase with the higher force rate. The maximum compaction velocity for the weave appearing at the beginning of the force-controlled compaction is 22.4 mm/min, whereas the maximum velocity is 27.8 mm/min for the NCF. Because the model has only been validated for velocities of up to 5 mm/min, there might be a deviation for higher compaction speeds.

In addition to calculating the preform thickness, this method can also be applied to reduce tooling forces in RTM processes. It was demonstrated that the peak compression

stress could be eliminated for the characterized material. The maximum stress for achieving the same final FVC was able to be reduced by 50% in the same process duration. This example clearly demonstrates the capabilities of the developed material model. Most of the existing models reviewed in Section 2.3 divide between the compaction and relaxation phase, requiring the ramp time between the phases to be known. In the case of the force-controlled setup, Fig. 4-16a shows a smooth transition between compaction and relaxation, thus making it impossible to define the beginning of relaxation. It can be assumed that stresses are relaxing at small strain rates which cannot be described by most of the models found in the literature.

The model was validated for two materials with very different compaction and relaxation behaviors. Together with the results of the parameter study, there is evidence to suggest that the model can be applied to a variety of fibrous preforms showing viscoelastic behavior. With the development of a compaction formula and its implementation in a FE code, research question 2 raised in Section 2.5 is fully answered.

5 Extension to a three-dimensional compaction process simulation model

A novel compaction material model was developed in Section 4.1 and implemented in a user-defined subroutine in Section 4.4. However, this methodology is limited to the prediction of the compaction response for flat geometries. To be applied for non-planar compaction cases, the model needs to be extended to include further deformation modes. The model extension focuses on the implementation of an out-of-plane shear model and the in-plane tensile and compression stiffness in a 3D solid element. Moreover, the frictional behavior between the preform and the tool is included in the contact definition. The applicability of the three-dimensional model is verified in two steps, single element tests and flat compaction tests with combined load cases. Afterwards, the model is calibrated and then validated with non-planar compaction experiments from Section 3.5. The fully validated model is used to perform a parameter study of geometric dimensions of the tool and the preform, for instance tool radius or preform thickness. From the knowledge gained, guidelines for the design of compaction processes are derived. At the end of this chapter, process-related, material-related and geometry-related guidelines are presented.

Because the material or element coordinate system may vary from the global coordinate system in non-planar cases, the following definition will be used throughout the following work:

Global coordinate system:

- x: Plane of the press
- y: Plane of the press
- z: Tool closing direction

Local or element orientation coordinate system:

- 1:   Fiber direction 1
- 2:   Orthogonal to 1, in-plane (fiber direction 2)
- 3:   Preform thickness direction

5.1 Implementation of a three-dimensional orthotropic material model

The content of this section has partly been published on the SAMPE Europe 2022 Conference [C5]. Fig. 5-1 shows the main deformation modes of a preform on macro-scale which have been considered by previous works [61,69,71,72]. Due to the orthotropic characteristic of the fibrous material, each deformation is described with a different stiffness. This stiffness can be dependent on the time, the FVC or both. The compaction in thickness direction has already been implemented in the user-defined material subroutine in Section 4.4. Moreover, the literature review showed that the out-of-plane shear deformation has a major impact on the non-planar compaction response. Thus, the material behavior observed in the experiments in Section 3.3 is added to the subroutine. Furthermore, the in-plane deformation modes elongation and extension are considered for the extension to a three-dimensional model. Because this work focuses on compaction cases where in-plane shear is not expected, this behavior is only discussed briefly.

The utilization of a user-defined material subroutine allows defining and implementing deformation modes independently. The stress-strain relation of an orthotropic material is defined by the following compliance matrix [266]:

$$
\begin{Bmatrix} \varepsilon_1 \\ \varepsilon_2 \\ \varepsilon_3 \\ \varepsilon_4 \\ \varepsilon_5 \\ \varepsilon_6 \end{Bmatrix} =
\begin{bmatrix}
\dfrac{1}{E_{11}} & -\dfrac{\nu_{12}}{E_{11}} & -\dfrac{\nu_{13}}{E_{11}} & 0 & 0 & 0 \\
-\dfrac{\nu_{12}}{E_{11}} & \dfrac{1}{E_{22}} & -\dfrac{\nu_{23}}{E_{22}} & 0 & 0 & 0 \\
-\dfrac{\nu_{13}}{E_{11}} & -\dfrac{\nu_{23}}{E_{22}} & \dfrac{1}{E_{33}} & 0 & 0 & 0 \\
0 & 0 & 0 & \dfrac{1}{E_{44}} & 0 & 0 \\
0 & 0 & 0 & 0 & \dfrac{1}{E_{55}} & 0 \\
0 & 0 & 0 & 0 & 0 & \dfrac{1}{E_{66}}
\end{bmatrix} \cdot
\begin{Bmatrix} \sigma_1 \\ \sigma_2 \\ \sigma_3 \\ \sigma_4 \\ \sigma_5 \\ \sigma_6 \end{Bmatrix}
\qquad (5\text{-}1)
$$

The strains ε_4, ε_5 and ε_6 denote shear strains and σ_4, σ_5 and σ_6 shear stresses respectively. This notation is chosen in order to be consistent with the subroutine in Appendix c. Each deformation mode shown in Fig. 5-1 corresponds to one or two entries on the diagonal of the compliance matrix. Entries outside of the diagonal indicate coupling factors between the deformation modes. Due to symmetry planes shown in Fig. 5-2, most of the coupling factors are zero. The only remaining coupling factors are the in-plane Poisson's ratio and the two out-of-plane Poisson's ratios.
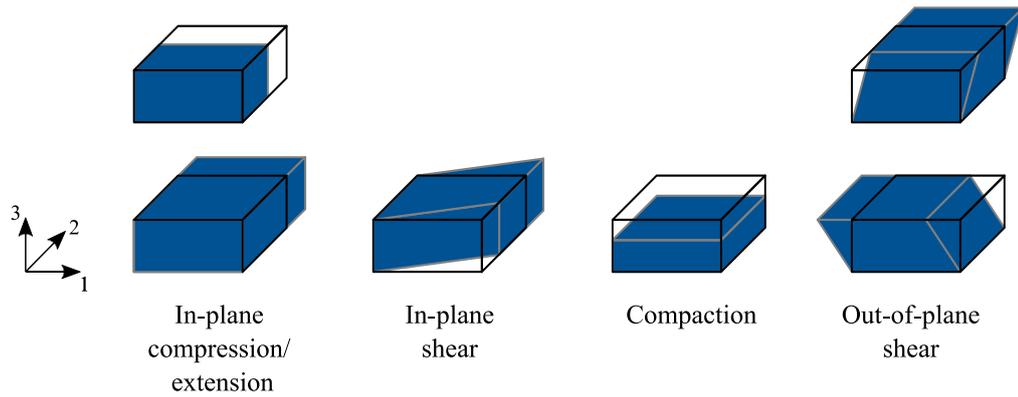
Fig. 5-1: Main deformation modes of a preform on macroscopic scale.
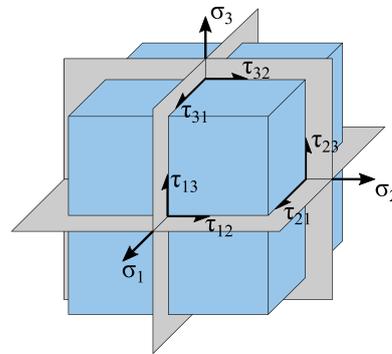
Fig. 5-2: Material symmetry planes for an orthotropic material (adapted from [170]).

The application of Eq. (5-1) in a three-dimensional user-subroutine facilitates to define each entry of the stiffness or compliance matrix respectively independently. The implementation of the viscoelastic model from Section 4.4 can directly be used for the E_{33} entry. Some assumptions are made here to simplify the model. These have to be reconsidered if the material or preform layup changes. Because all manufactured preforms have a balanced layup with a midplane-symmetry, it is assumed that $E_{11} = E_{22}$ and $E_{44} = E_{55}$. This assumption is only valid, if the fiber directions remain orthogonal in each element. For cases with significant in-plane shear, the reorientation of fibers has to be considered. Moreover, the Poisson's ratios ν_{12}, ν_{13} and ν_{23} in Eq. (5-1) are set to zero. With these assumptions Eq. (5-1) reduces to:

$$\begin{Bmatrix} \varepsilon_1 \\ \varepsilon_2 \\ \varepsilon_3 \\ \varepsilon_4 \\ \varepsilon_5 \\ \varepsilon_6 \end{Bmatrix} = \begin{bmatrix} \dfrac{1}{E_{11}} & 0 & 0 & 0 & 0 & 0 \\ 0 & \dfrac{1}{E_{11}} & 0 & 0 & 0 & 0 \\ 0 & 0 & \dfrac{1}{E_{33}} & 0 & 0 & 0 \\ 0 & 0 & 0 & \dfrac{1}{E_{44}} & 0 & 0 \\ 0 & 0 & 0 & 0 & \dfrac{1}{E_{44}} & 0 \\ 0 & 0 & 0 & 0 & 0 & \dfrac{1}{E_{66}} \end{bmatrix} \cdot \begin{Bmatrix} \sigma_1 \\ \sigma_2 \\ \sigma_3 \\ \sigma_4 \\ \sigma_5 \\ \sigma_6 \end{Bmatrix} \qquad (5\text{-}2)$$

The in-plane extension and compression are assumed to be dependent on the FVC according to Eq. (2-3). For this purpose, the fiber stiffness $E_f = 240\ GPa$ is taken from the data sheet [267]. Because fibers and fiber bundles tend to bend under compression, it is expected that the in-plane compression stiffness is significantly lower than the tensile stiffness. Hence, an in-plane stiffness reduction factor $f_{E_{11}}$ for cases with negative strain is introduced. Thus, the description of the in-plane stiffness E_{11} can be written as follows:

$$E_{11} = \begin{cases} V_{f1} \cdot E_f & , \varepsilon_1 \geq 0 \\ f_{E_{11}} \cdot V_{f1} \cdot E_f & , \varepsilon_1 < 0 \end{cases} \qquad (5\text{-}3)$$

It is important to state that V_{f1} represents the FVC in direction 1 and is assumed to be 50% of the global FVC for the modelled cases. A parameter study of in-plane stiffness reduction factor $f_{E_{11}}$ is performed in Section 5.4, because this property has not been characterized. The results of this study are used to understand the influence of this parameter on the material response and to calibrate the model.

The out-of-plane shear behavior is considered with the FVC dependent bilinear model presented in Section 3.3. The shear stiffness values are taken from Tab. 3-4 and implemented with a look-up table using linear interpolation between the measured FVC levels. Horizontal extrapolation was chosen in order to avoid extremely high or low stiffness values if the FVC exceeds the range from 0.45 to 0.60. In dependency of the FVC, the code checks if the current shear strain is below or above the interception of the two linear sections. The shear at which the stiffness changes needs to be provided in radiant in the code.

Negligible in-plane shear is expected, because only 0° and 90° layers are considered and the tested geometry shows only single curvature. Because no literature value for in-plane shear of a preform with activated binder could be found, the relation for in-plane isotropy

is applied. All entries of the compliance matrix according to Eq. (5-1) are summarized in Tab. 5-1.

Tab. 5-1: **Definition of the entries of the orthogonal compliance matrix for the compaction material model.**

Parameter	Value
E_{11}, E_{22}	Eq. (5-3)
E_{33}	Viscoelastic model (model parameters from Tab. 4-2)
E_{44}, E_{55}	Bilinear model (model parameters from Tab. 3-4)
E_{66}	$E_{11}/2(1-\nu_{12})$
$\nu_{12}, \nu_{13}, \nu_{23}$	0.0

The subroutine from Section 4.4 is extended to a three-dimensional case with three normal deformation modes (indicated with subscripts $j = 1\dots 3$) and three shear deformation modes (indicated with subscripts $j = 4\dots 5$). Thus, strains and stresses are denoted as vectors with six entries, whereas stiffness matrix and Jacobian matrix have the dimension 6×6. Relevant variables used in the subroutine are:

- Time: t
- Current time increment: Δt
- Strain: $\epsilon_{j,t+\Delta t}$
- Strain increment: $\partial \epsilon_{j,t+\Delta t}$
- Stress: $\sigma_{j,t+\Delta t}$
- Stiffness matrix: $K_{i,j,t+\Delta t}$
- Jacobian matrix: $J_{i,j,t+\Delta t}$

For all deformation modes except the compaction in thickness direction, the Jacobian matrix equals the stiffness matrix, because it is constant over time. Thus, the Jacobian matrix can be written as follows:

$$J_{i,j} = K_{i,j} \qquad for\ i,j \in \{1,2,4,5,6\} \qquad (5\text{-}4)$$

The stress is updated at the end of the time increment using the following linear dependency:

$$\sigma_i^{n+1} = \sigma_i^n + K_{i,j}\partial \epsilon_j^n \qquad for\ i,j \in \{1,2,4,5,6\} \qquad (5\text{-}5)$$

Furthermore, the frictional behavior characterized in Section 3.4 is considered in the contact definition and is discussed more in detail in Section 5.3.

5.2 Model verification with planar test cases

Applying the model to flat test geometries allows to separate the individual deformation modes and thus, to verify interactions between them. Moreover, the characterization experiments in Chapter 3 can be modeled in order to calibrate the model if necessary. The model is applied to single-element tests before it is utilized for more complex multi-element simulations.

5.2.1 Single element tests

The intention of these simple tests is to validate if the model shows the expected behavior for various load cases. For this purpose, a cube with 10 mm edge length is meshed with a single SOLID185 linear brick element. The element is oriented to have the directions 1 and 2 in-plane parallel to the fibers and the 3-direction indicating the thickness. The deformations were enforced by displacement boundary conditions on the surfaces. The corresponding surfaces were displaced by 5 mm in 50 s time. In order to verify relaxation effects, the position was held constant for another 20 s. The initial FVC was set to 0.33 for cases with compaction, whereas the remaining cases had a constant value of 0.5.

In a first series of tests, single deformation modes as depicted in Fig. 5-1 were applied to the element. Fig. 5-3 shows the stress responses for pure tension in-plane, compaction in thickness direction and out-of-plane shear. Material responses in the other directions are also plotted, in order to verify if stresses occur because of coupling effects. The stress response due to in-plane tension in Fig. 5-3a shows the expected behavior. Because of constant stiffness, the stress σ_1 shows a linear increase during the extension, followed by stress stagnation. Because the Poisson's ratios ν_{13} and ν_{15} were set to zero, no stresses are induced in thickness and out-of-plane shear direction. During the compaction in 3-direction (see Fig. 5-3b), the stress σ_3 shows the expected viscoelastic behavior with an exponential increase followed by stress relaxation during the holding phase. No stresses are induced in the other directions. Fig. 5-3c shows the stress responses of the single element subjected to pure shear. The shear stress σ_{13} shows a linear section at the beginning with high stiffness, followed by another linear section with lower stiffness. This correlates with the bilinear behavior implemented in Section 5.1, which reduces the stiffness after a defined shear strain. As with the previous deformation modes, no stresses occur in the other material directions.

(a)

(b)

(c)
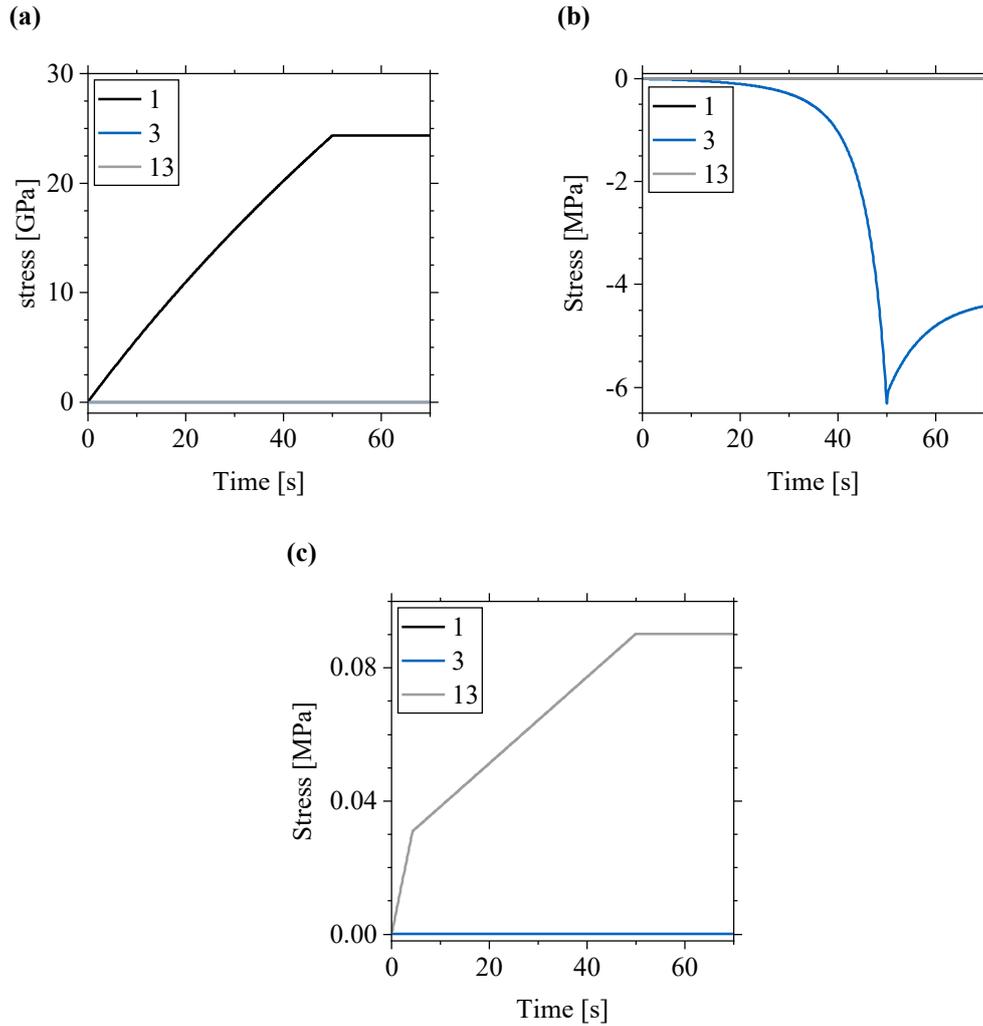
Fig. 5-3: **Stress response of a single element under different loading conditions: (a) pure tension in 1-direction; (b) pure compression in 3-direction; (c) pure shear in 13-direction.**

After the single deformation mode tests, the element is subjected to combined load cases. These tests ensure that in-plane extension and out-of-plane shear show the desired FVC dependency without affecting further material responses. First, the single element is extended in-plane while it is compacted in thickness direction. Two interesting observations can be made from the stress responses in Fig. 5-4a. On the one hand, the stress σ_1 shows an exponential increase due to the simultaneous compaction. This behavior can be explained with the FVC dependency, which leads to an increase of the in-plane stiffness. On the other hand, the compaction stress response is not affected by the simultaneous in-plane deformation. The progression of σ_3 is the same as for the pure compaction case in Fig. 5-3b. Fig. 5-4b shows the stress response of a combined compaction and out-of-plane shear load. Contrary to the pure shear test in Fig. 5-3c, the stress response is not bilinear anymore. The simultaneous FVC increase leads to an increase of the shear stiffness because of the linear interpolation implemented in Section 5.1.

Nevertheless, the σ_{13} stress shows the implemented kink followed by a reduced slope from the bilinear model. As with the single deformation, the compaction stress response is not affected by the shearing of the material. At last, the combination of extension and out-of-plane shear stress is analyzed. Contrary to the previous cases, the displacements cannot be defined on the surfaces because the model would be over-constrained. However, applying displacements to the edges leads to a combined extension-shear deformation. Two opposing edges have a displacement of 5 mm in 1-direction, while the other two have 0 mm and 10 mm displacement respectively. As expected, the deformations are independent. Both stress responses are the same as for the single deformation tests in Fig. 5-3a and Fig. 5-3c.
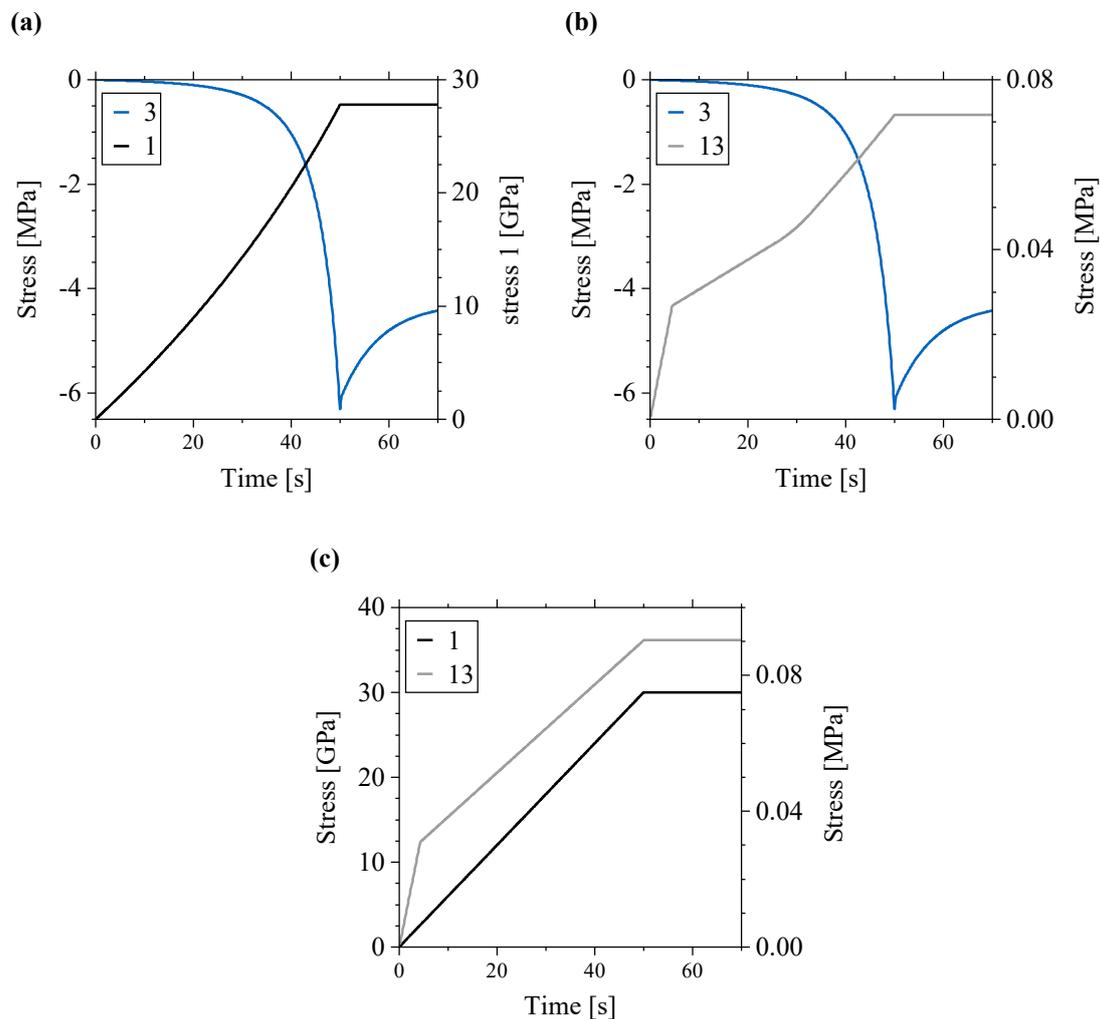
Fig. 5-4:   **Stress response of a single element under different loading conditions: (a) tension in 1-direction and compression in 3-direction; (b) compression in 3-direction and shear in 13-direction; (c) tension in 1-direction and shear in 13-direction.**

From the single element tests, it can be concluded that the material shows a reasonable behavior for various load cases. The single deformation cases demonstrated that the material answers with the expected stress responses without inducing stresses in other directions. The combined deformation cases showed that the material answers with the desired FVC dependencies for in-plane tension and out-of-plane shear. It is important to note that the real behavior for combined loading scenarios is unknown, because the coupling and interaction of different deformation modes is very challenging to characterize. The intention of these tests was to show if the material behaves as expected under the assumptions made.

5.2.2   Model validation with planar geometries

After the qualitative model verification, the three-dimensional model is used for a quantitative validation. For this purpose, the experimental tests in Chapter 3 are modeled with the correct specimen dimensions and results are compared to the test data. Because the compaction model was already validated in Section 4.3, the focus in this subsection is on the correct representation of the out-of-plane shear and the frictional behavior.

5.2.2.1   Calibration of the out-of-plane shear model

In order to validate the FVC dependent bilinear out-of-plane shear model, the experimental configurations in Tab. 3-3 were modeled in ANSYS Mechanical. Contrary to the experiments, only a single specimen with 90 mm x 40 mm in-plane dimensions and varying thickness according to Tab. 3-3 was modeled. The specimens were meshed with SOLID185 linear brick elements with 2.5 mm in-plane size and two elements over the thickness. Fig. 5-5 shows the mesh including the material orientation of the HV_45 configuration. For the planar models, the material is oriented parallel to the global coordinate system, with the in-plane-directions 1 and 2 in global x- and y- direction.
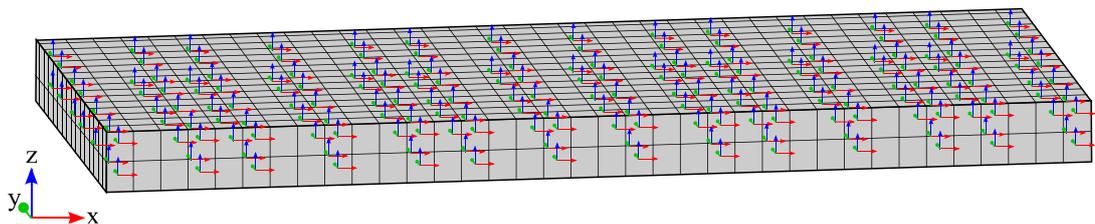
Fig. 5-5:   **Preform model of the out-of-plane shear simulation model with FVC 0.45 showing the material orientation (1-direction: red, 2-direction: green, 3-direction: blue).**

The boundary conditions are directly applied to the corresponding surfaces of the specimen without modeling the surrounding tool. All translational degrees of freedom were locked on the bottom side of the specimen. A constant velocity of 1 mm/min in global x-direction was applied to the top side of the model. The calculation was run with a

constant time step of 0.1 s for 170 s simulation time. The reaction force in x-direction of the boundary condition on top of the specimen was used for the evaluation of the simulation results.

Because only a single specimen was simulated, the reaction force needed to be multiplied by a factor of two in order to validate with the experimental data. Fig. 5-6 compares the simulation results with the bilinear model and the experimental results for the tested FVC levels. It can be seen that the simulation matches the material input extremely well for all configurations. At the transition to the lower stiffness, the simulation does not show a sharp kink as the model does. This can be explained with not all elements being subjected to the exact same shear deformation. Thus, some elements jump to lower stiffness one time step earlier or later than the others. Apart from the transition zone, the simulation results are located well inside the scatter area of the experimental measurements. Hence, the shear model can be used for more complex simulation models.
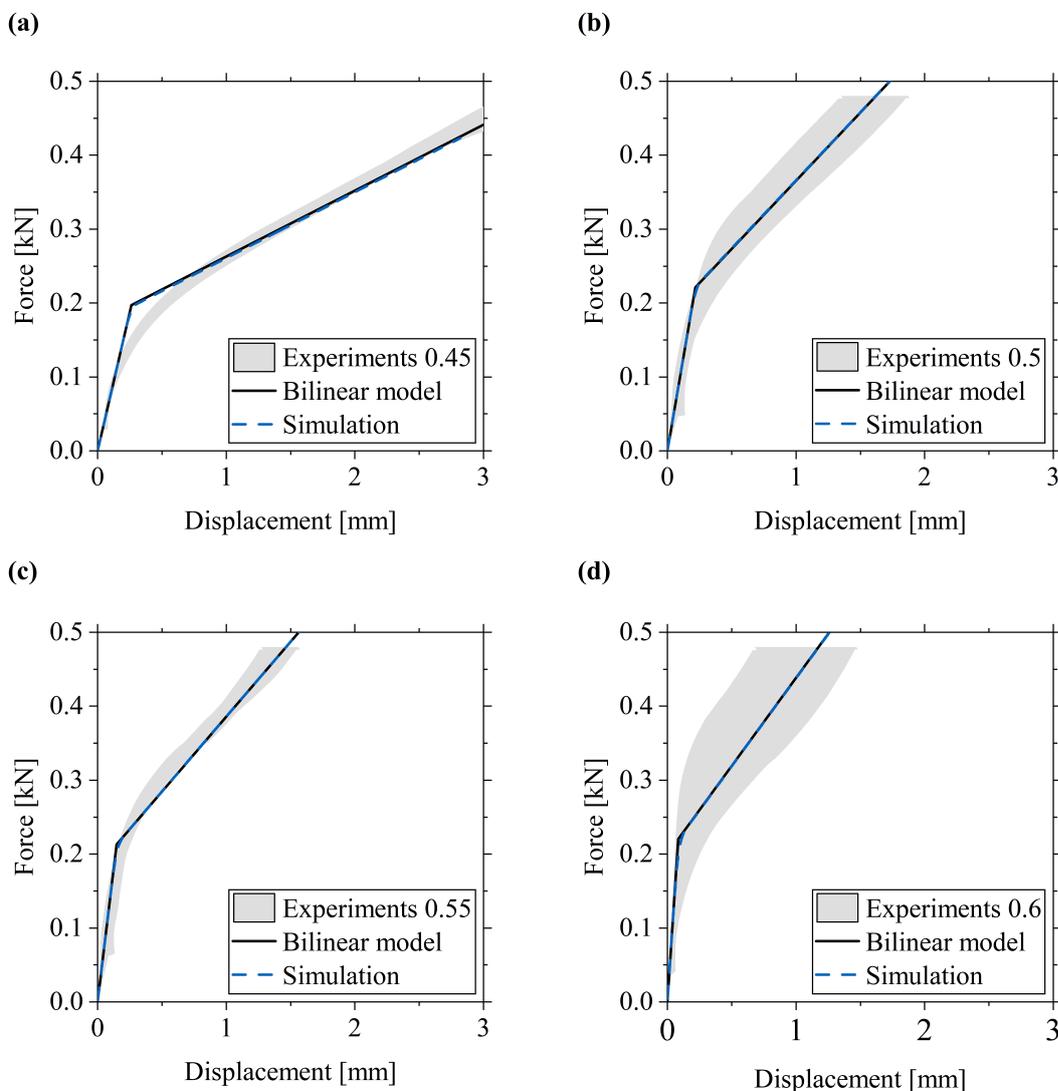
Fig. 5-6:   **Comparison of simulation results with the bilinear model and experimental results for varying FVC: (a) 0.45; (b) 0.45; (c) 0.45 and (d) 0.45.**

5.2.2.2 Validation of the tool-preform frictional behavior

A simple model was created for the validation of the frictional behavior between the tool and preform surface in ANSYS Mechanical together with Geschwandtner [S15]. The virtual model of the friction characterization test in Section 3.4 consists of one body representing the tool surface and a second body for the sled. The model setup at the beginning of the experiment is shown in Fig. 5-7, where the sled will be moved in positive x-direction. Because the material of the bodies is not relevant if only friction is tested, a standard steel material was assigned to them. Both bodies were meshed with an edge length of 5 mm using SOLID185 brick elements. All translational degrees of freedom were locked for the tool. A constant velocity of 1 mm/min in positive x-direction was applied to the preform while the translational degree of freedom in y-direction was locked. Additionally, a constant force of 85 N in negative z-direction was applied to the preform corresponding to the maximum weight in the friction experiments. The friction coefficient of 0.1 was defined in the interface definition. For this purpose, a frictional contact with symmetric behavior and small sliding option switched off was chosen. For all remaining contact settings, default options were kept. Contact definition is discussed more in detail for the non-planar compaction simulations in Section 5.3. The simulation ran for 12 s leading to a total displacement of the preform of 0.2 mm.
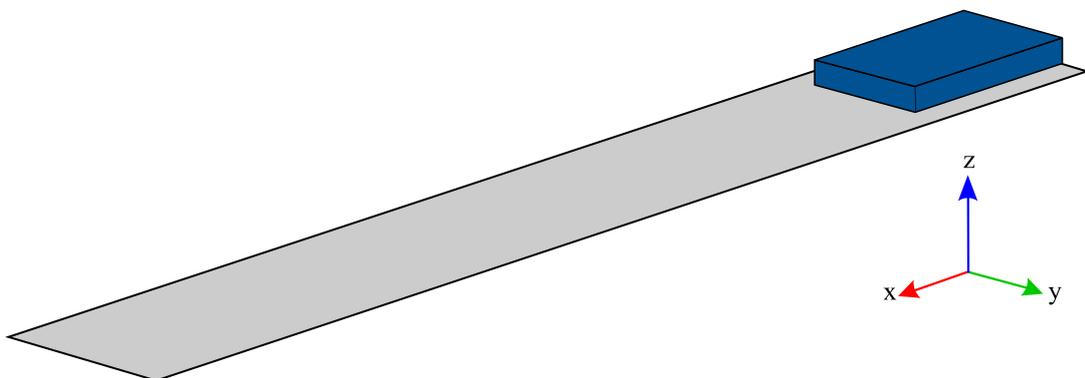
Fig. 5-7: **Simulation model of the friction characterization experiment.**

The reaction force in x-direction of the displacement boundary condition applied to the preform was used for the results analysis. Fig. 5-8 shows the evolution of the contact status and the friction force over time. As intended, the constant contact status (0: far-field, 1: near-field, 2: sliding and 3: sticking) of 2 indicates a sliding contact between the two surfaces over the whole duration of the simulation. The reaction in x-direction which equals the tangential friction force shows a constant value of 8.5 N.

According to Eq. (2-1), the friction coefficient of the virtual experiment can be calculated to 0.1. Thus, it can be stated that the behavior of the tool-preform interface provided correct results and can be applied to further cases.
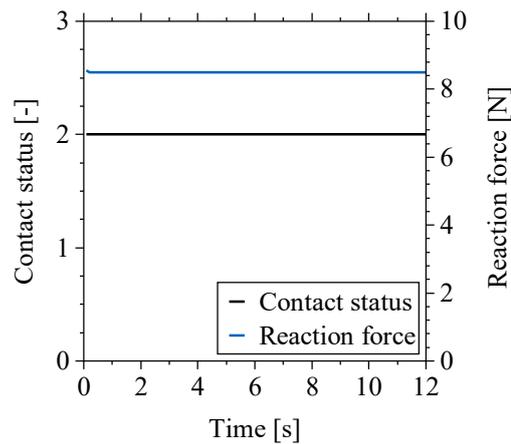
Fig. 5-8:   **Contact status and reaction force in x-direction of the virtual friction experiment.**

5.2.2.3   Planar compaction with combined shear and frictional behavior

This planar loading scenario was chosen in order to analyze the behavior of a preform which is subjected to compaction and out-of-plane shear loads. Because the shear is introduced by a tool displacement, the tool-preform interface shows sliding behavior with friction. Contrary to a non-planar compaction case, the individual load cases can be analyzed separately before the model is applied to an angled geometry in Section 5.3.

The simulation model consists of three parts, a lower tool, the preform and an upper tool, with standard steel material assigned to the tools. The setup consisting of two flat plates and a preform in blue is illustrated in Fig. 5-9a. The interfaces were defined as frictional contacts with a friction coefficient of 0.1. A symmetrical behavior with normal Lagrange formulation and nodal-normal from contact detection method was applied to the interface. Small sliding option was turned off and stabilization damping factor was set to zero in the contact settings. Linear eight-nodes brick elements (SOLID185) with reduced integration were used for the meshing of the preform and the tools. The preform material was oriented in a way that the 3-direction represents the thickness in global z-direction and 1- and 2- direction are parallel to the in-plane dimensions of the preform.

All degrees of freedom were locked for the lower tool, whereas the upper tool was used for load introduction into the preform. The material is compacted first and then sheared with displacements of the upper plate given in Fig. 5-9b. The compaction with 2 mm/min to a final thickness of 4.62 mm corresponds to the experimental configuration WV_0.55-2 in Tab. 3-1. The following shearing at FVC 0.55 with 1 mm/m corresponds to the configuration HV_55 in Tab. 3-3. Direct solver with zero damping was selected in the solver settings. An advantage of the user-defined material which is applied to the preform is that the FVC is calculated and stored in a user-variable automatically for each time step. Thus, the FVC can be visualized with a user-defined result.

(a)   (b)
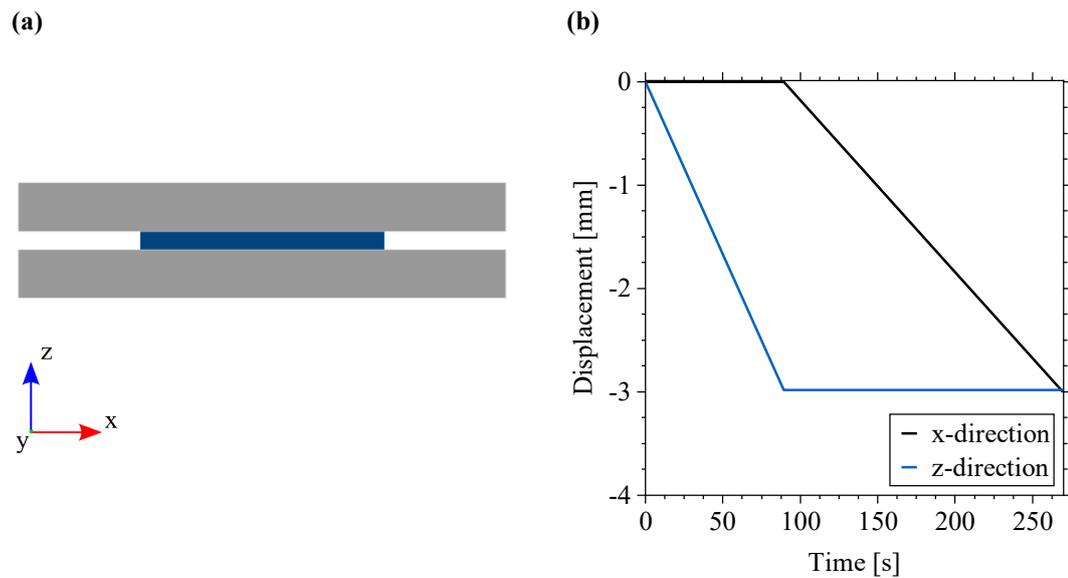
Fig. 5-9:   **Simulation of a planar compaction case: (a) model setup; (b) displacement boundary conditions.**

The material response in thickness direction can be seen in Fig. 5-10a, showing an exponential increase of the FVC until the vertical position of the upper plate is held constant. During the compression phase, the compaction stress increases exponentially followed by stress relaxation during the holding phase. As expected, the curve is exactly the same as the numerically predicted 0.55-2 curve in Fig. 4-13. This behavior equals pure compression experiments and thus, shows that the compaction is not influenced by the shear load as implemented.

The evolution of the contact status (0: far-field, 1: near-field, 2: sliding and 3: sticking) and the out-of-plane shear stress are shown in Fig. 5-10b. The evolution over time reveals that the contact surfaces are initially sticking and switch to sliding during the horizontal movement of the upper plate. Due to the out-of-plane shear to in-plane-extension coupling being defined as zero, the shear stress remains zero during the compaction. When the plate moves horizontally, the shear stress shows a linear increase followed by a linear increase with smaller stiffness. This behavior corresponds to the bilinear out-of-plane shear model. Once the maximum tangential contact force defined by the friction coefficient is reached, the surfaces are sliding. With a friction coefficient of 0.1, the sliding begins exactly when the shear stress is 10% of the compression stress. This results in a decrease of the shear stress converging to a constant value. With the sliding beginning after the transition point to lower out-of-plane shear stiffness, the importance of the bilinear model becomes obvious.

(a)   (b)
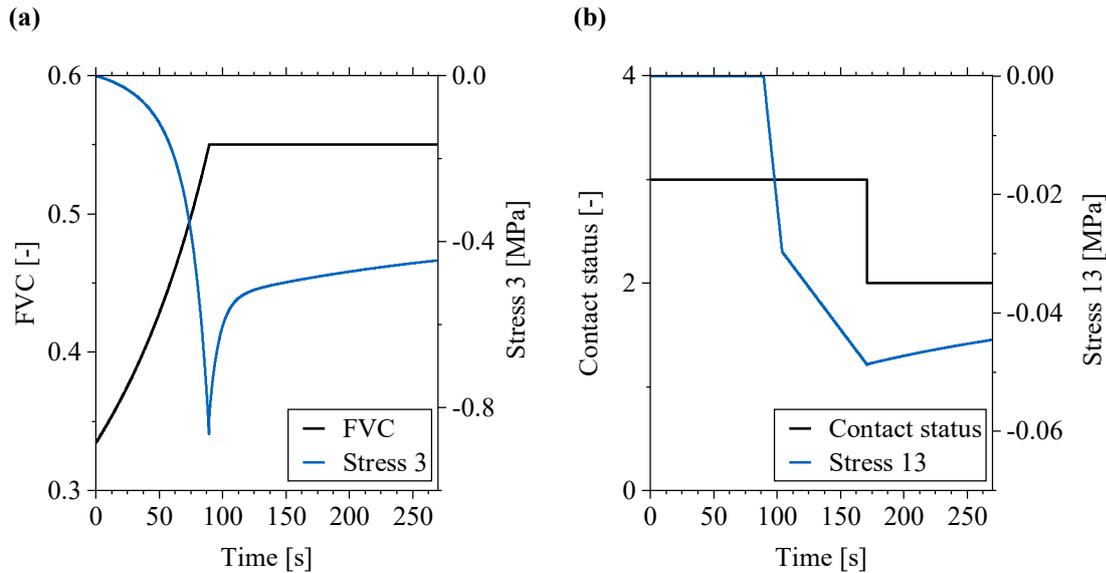
Fig. 5-10:   **Results of the planar compaction simulation with combined loads: (a) FVC and stress response in thickness direction; (b) contact status and shear stress response.**

5.3 Model setup of the non-planar compaction case

The model depicted in Fig. 5-11 consists of three parts, a lower tool, an upper tool and a preform in between. The tool geometries are imported as step files generated in the CAD environment CATIA. The preform geometry is modeled in the ANSYS built-in CAD tool DesignModeler by extruding the lower tool surface and trimming the side faces. A standard structural steel material from the database with a Young's modulus of 200 GPa is applied to the tools. The material of the preform is defined by an APDL command which calls the user-defined material (see Appendix c). An element orientation is defined for the preform part in order to have 1- and 2-direction parallel to the fiber orientation and 3 in thickness direction (see Fig. 5-11).

5.3.1 Boundary conditions and contact settings

Only two boundary conditions are defined for the non-planar compaction simulation, one for each tool. All degrees of freedom of the lower tool are constrained, whereas a displacement boundary condition in negative z direction is defined for the upper tool. The remaining translational degrees of freedom of the upper tool are set to zero.

The contact settings listed in Tab. 5-2 were found to deliver the best results in terms of model robustness and accuracy. Because initial simulation runs showed that the model is sensitive to penetration, a symmetric contact was chosen. A normal Lagrange contact

formulation was selected, because it enforces zero penetration, contrary to classic penalty-based formulations. This contact provides the highest accuracy and is most suitable for material nonlinearities and large sliding [268]. The default option small sliding is turned off due to relatively large sliding between the preform and the upper tool. Because damping would take energy out of the system and thus affect the compaction response, it is important to set the contact stabilization to zero. A program-controlled pinball radius proved to be sufficient for the studied cases. However, it might be necessary to increase the radius in case the initial gap is larger.
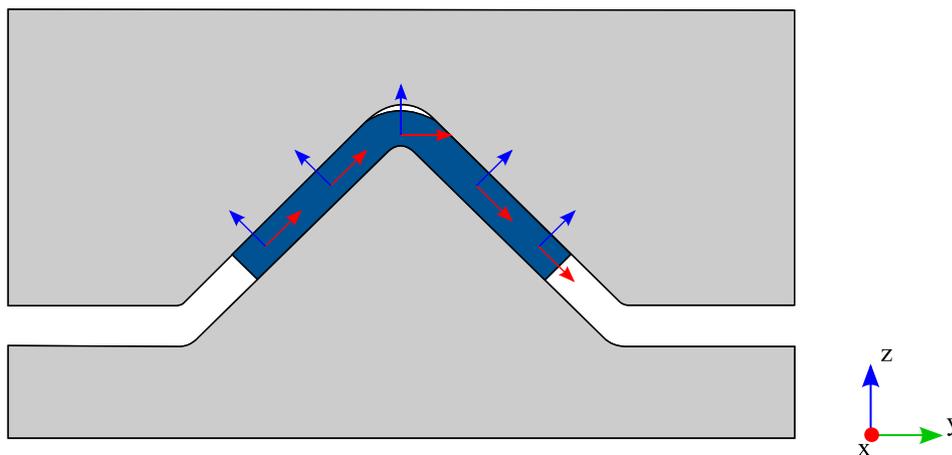
Fig. 5-11: **Model of the non-planar compaction with 3 mm inner radius and 8 mm outer radius including element orientation for the preform (1-drection: red, 3-direction: blue).**

Tab. 5-2: **Contact settings for the non-planar compaction simulations.**

Parameter	Value
Contact type	Frictional
Friction coefficient	0.1
Behavior	Symmetric
Formulation	Normal Lagrange
Small sliding	Off
Detection method	Nodal-projected normal from contact
Stabilization damping factor	0
Pinball radius (for upper tool)	Program-controlled
Interface treatment	Adjust to touch

5.3.2 Mesh convergence study

With material, element orientation, contact surfaces and boundary conditions set, the mesh size needs to be defined. For this purpose, a mesh convergence study was performed to find the optimum element size. A parametric mesh for the preform shown in Fig. 5-12 was chosen, because the present geometry does not allow meshing with uniform elements. This method ensures a good mesh quality in the radius due to equal number of divisions in the inner and outer radius. The initial configuration with design parameter $n = 1$ corresponds to an average mesh size of approximately 8 mm. For all subsequent configurations, n is doubled leading to half the mesh size. The tools were meshed with the respective number of divisions in the radius and the same mesh size on the flanges to ensure a good contact interface to the preform.
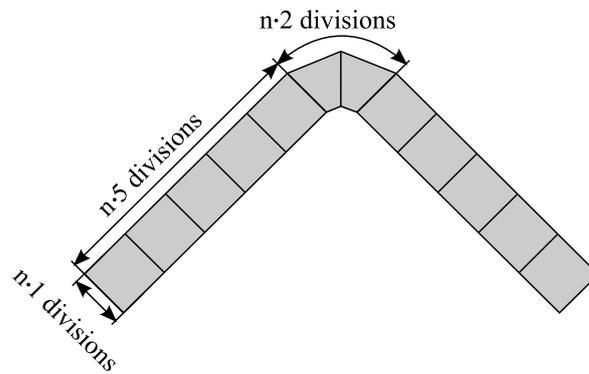
Fig. 5-12:   **Parametric mesh for the convergence study of the L-profile, showing $n = 1$.**

The reaction force of the upper tool boundary condition is chosen as response of interest for the study. The peak force and the relaxed force after 200 s are compared for different mesh sizes. The selected experimental configuration L_3_8_12 has its force maximum at the end of the compression after 110.3 s. Depending on the time step size, it cannot be assured that a time step is calculated at the exact time of the peak force. Thus, to ensure that the maximum stress always appears at the same time for all configurations, a constant time step of 0.5 s is selected for this study.

Fig. 5-13 shows the peak force and the relaxed force after 200 s for varying mesh design parameters n from 1 to 16. The results reveal a strong mesh dependency for large element sizes. However, peak stress and relaxed stress are converging towards larger numbers of mesh divisions. There is almost no change of the reaction force from $n = 8$ to $n = 16$. Consequently, a design parameter of $n = 8$ is chosen for the further course. Assuming the mesh size in the radius is more crucial for the model response, the in-plane mesh size on the flanges is increased to $n = 4$. The through-thickness mesh size is kept at $n = 8$ to achieve higher resolution of the results in thickness direction. The increase of the in-plane mesh size lead to an increase of the peak force of 0.2% and an increase

of the relaxed force of 0.4% compared to the $n = 8$ configuration. However, the total number of elements in the model could be reduced by 64%. Consequently, all further simulations will be run with the $n = 8$ configuration with increased flange mesh size.
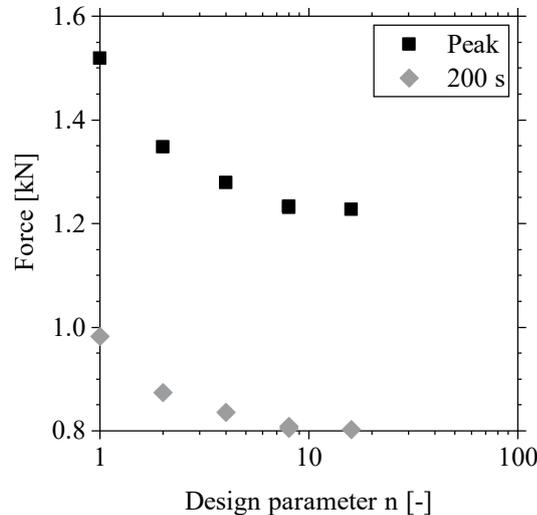
Fig. 5-13: **Convergence of peak force and relaxed force after 200 s for decreasing mesh size of the L-shaped preform.**

5.3.3   Adaption of thickness and fiber volume content from preforming

The preform was initially modeled with constant thickness. However, measurements after preforming in Section 3.5 revealed that the thickness is not uniform due to corner thinning. Because the thickness variation also affects the FVC distribution, only adopting the geometry in the simulation is not sufficient. A pre-compaction simulation step is used to achieve the correct thickness in the radius including a locally increased FVC. However, there is no direct way of transferring the FVC distribution from the pre-compaction step to the final compaction step. Applying two load steps in one simulation would add additional unrealistic stresses in the preform and is consequently not sufficient. Hence, the workflow shown in Fig. 5-14 was applied to overcome this issue.

During draping of the stacked layers, the outermost layer is pulled downwards and compresses the layers beneath in the radius. This effect leads to a reduced thickness in the radius. In order to recreate this effect in the simulation, the upper short edges on the flanges are pulled downwards in a 45° angle. As shown in Fig. 5-15b, the thickness in the radius is reduced without affecting the flange thickness. The mesh of the pre-compacted preform can directly be transferred as input geometry to a subsequent simulation, whereas no direct transfer of individual results is available. However, it is possible to export and import fields between simulation steps. Because strain and stress field are reserved with actual results, a temperature field can be used to transfer additional data.

Hence, the nodal FVC distribution including node locations after pre-compaction is exported into a text file. Afterwards, this file can be opened using "External Data" in ANSYS. Node locations and temperature variables are assigned to the respective columns of the text file. This information is transferred to the compaction simulation and mapped to the preform mesh as initial body temperature.

```
┌──────────────────────────┐        ┌──────────────────────────┐
│ Run precompaction        │───────▶│ Transfer "External Data" to│
│ simulation               │        │ compaction simulation     │
└──────────────────────────┘        └──────────────────────────┘
            │                                     │
            ▼                                     ▼
┌──────────────────────────┐        ┌──────────────────────────┐
│ Export nodel FVC data    │        │ Map imported body temperature│
│ in .txt file             │        │ to preform part           │
└──────────────────────────┘        └──────────────────────────┘
            │                                     │
            ▼                                     ▼
┌──────────────────────────┐        ┌──────────────────────────┐
│ Transfer deformed mesh to│        │ Set tempearture to FVC    │
│ compaction simulation    │        │ via subroutine            │
└──────────────────────────┘        └──────────────────────────┘
            │                                     │
            ▼                                     ▼
┌──────────────────────────┐        ┌──────────────────────────┐
│ Open .txt file as        │        │ Set tempearture to FVC    │
│ "External Data"          │        │ via subroutine            │
└──────────────────────────┘        └──────────────────────────┘
            │                                     ▲
            ▼                                     │
┌──────────────────────────┐                     │
│ Assign temperature field │─────────────────────┘
│ to FVC data              │
└──────────────────────────┘
```
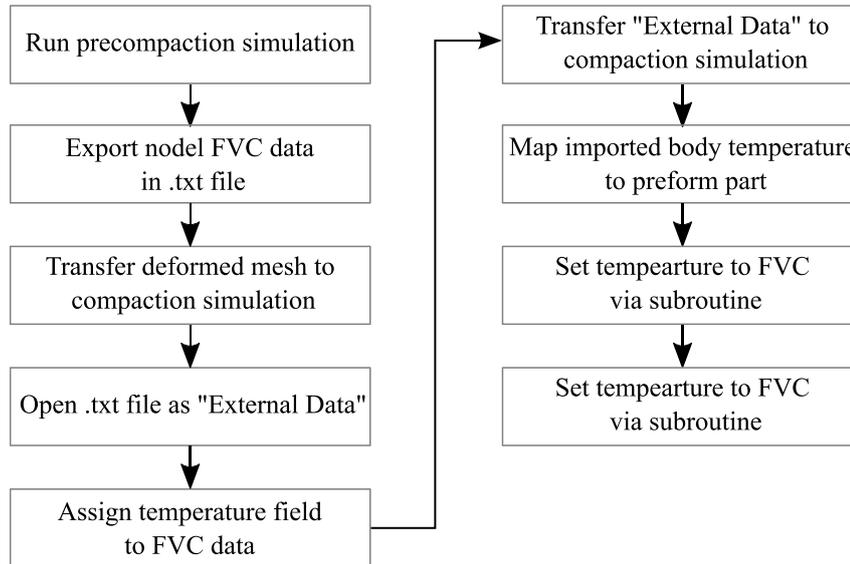
Fig. 5-14:   Flow-chart for the data transfer from pre-compaction to compaction simulation.

There are some minor changes necessary in the subroutine to reassign the temperature to the FVC. By default, the user material is assigned to defined temperature levels with linear interpolation. Knowing that the temperature ranges between 0 and 1, a horizontal interpolation can be enforced by assigning the same parameters to 0 and 1 (see APDL command in Appendix c). The temperature is mapped to the preform at the end of the first time step. Thus, the initial temperature is set to the initial FVC before pre-compaction to avoid steep increase within the first time step. In the material subroutine, the temperature derived from the mapping is assigned to the initial FVC. Based on this value, the FVC is computed by the subroutine for all following time steps.

Fig. 5-15 depicts the approach of the two-step compaction simulation showing the FVC distribution at different states. The initial state before pre-compaction in Fig. 5-15a shows a homogeneous FVC distribution. Pulling the outer edges downwards results in a thickness decrease in the radius and consequently higher FVC. The state in Fig. 5-15b is mapped to the subsequent compaction simulation as initial body temperature or FVC distribution respectively. Fig. 5-15c shows the FVC distribution at the end of the compaction of configuration L_3_8_12.
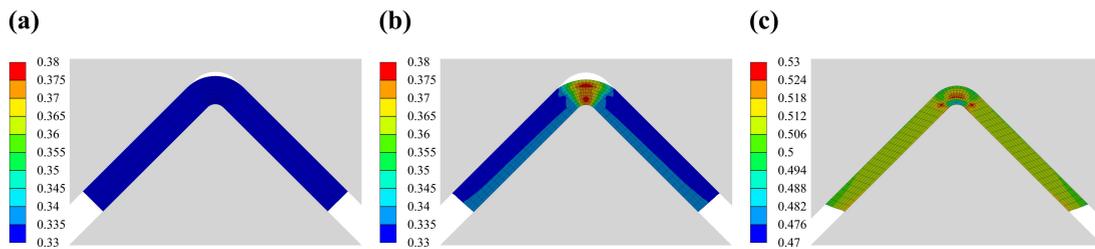
Fig. 5-15: **FVC distribution during the compaction of an L-shaped preform (configuration L_3_8_12): (a) initial state; (b) after pre-compaction; (c) after final compaction.**

5.4 Model calibration

The analysis of the model response with the method described above revealed that the reaction force does not match the force response from the experimental test. The peak force of the experimental configuration L_3_10_12 was at 1.8 kN, whereas the simulation showed a peak force of 1.2 kN. The deviation of the relaxed stress showed approximately the same magnitude. Hence, the model needs to be calibrated to the non-planar compaction case. In order to be able to adjust the model, it is necessary to identify possible root causes for the deviation between model and experiment. The following theoretical causes for the difference were identified:

- In-plane compression stiffness: From theoretical considerations, it seems to be reasonable that fibrous material behaves softer in compression than in extension. However, the in-plane compression behavior could not be characterized. In Section 5.1, a reduction factor $f_{E_{11}}$ was introduced in the model without knowing its quantity. After analyzing the impact of this parameter on the model response, it is calibrated to the material behavior observed in the experiments.

- Tool-preform friction: With the friction test setup used in Section 3.4, a maximum normal pressure of 0.02 MPa could be achieved, whereas a pressure of up to 2.0 MPa was measured during the compaction experiments. Even if the coefficient of friction has not shown a dependency on the normal pressure in the experiments, it cannot be excluded that friction increases at a very high pressure. Consequently, the influence of higher friction values on the compaction response is investigated.

- Combined shear and compaction: In Section 3.2, the compaction behavior was characterized independently on the out-of-plane shear. However, it can be assumed that lateral shift due to a shear load affects the compaction behavior. Based on numerical models, Chen [138] found that the degree of nesting influences the compaction response. Because this effect is difficult to control in experiments, it has not been characterized. Comparing the nesting configurations in Fig. 5-16 shows that there is less space for the fiber bundles to deform at maximum nesting. This could enforce an earlier yarn compression leading to higher

compaction forces. A parameter study is used to analyze the effect of increased compaction stiffness due to simultaneous shearing.

- Influence of the preforming process: Despite all efforts, the conditions during the preforming process for the flat and the curved specimens were not exactly the same. Compaction time, pressure and temperature were identical, but some differences originate from the tool geometry. The flat specimens were compacted between thin metal plates, whereas the angled preforms were compacted with thick steel tools. This affects the thermal flux from the tool to the preform. Moreover, the flat preforms were produced as large 400 mm x 400 mm plates with a distance of the heated plates of 7 mm, causing heat accumulation. In contrast, the angled specimens were manufactured individually with 60 mm x 100 mm in a comparably open press with approximately 100 mm plate distance. This allows more convection and thus, less heat accumulation. Mei et al. concluded that a different binder activation influences the mechanical behavior of the preform [220]. Varying the compaction stiffness and the out-of-plane shear stiffness allows to quantify the effect on the compaction behavior.

Besides the model calibration, the results of the parameter study were to investigate the influence of certain material parameters on the model response. Each material property influences the reaction force and the preform deformation in a different way.
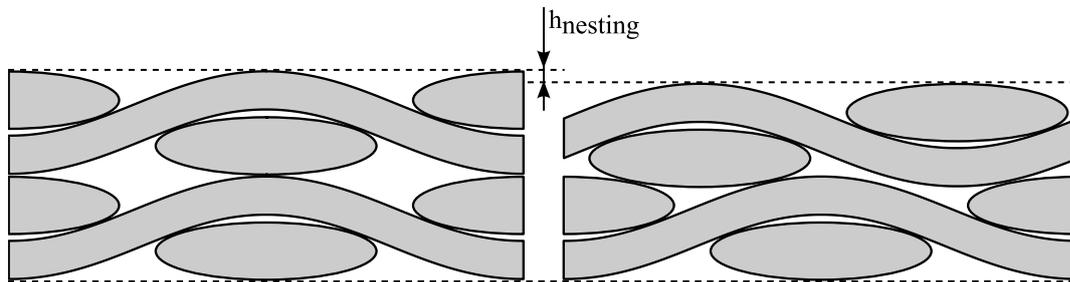
Fig. 5-16:   **Schematic illustration of nesting.**

5.4.1 Influence of in-plane compression stiffness

First, the influence of the in-plane compression stiffness on the model response is analyzed, because this property has not been characterized with experiments. It is assumed that the theoretical maximum compression stiffness equals the tensile stiffness according to Eq. (2-3). However, because fibers or yarns tend to bend or kink when compressed in lateral direction, the compression stiffness can be significantly lower. Thus, an in-plane stiffness compression reduction factor was $f_{E_{11}}$ introduced.

Fig. 5-17 shows the FVC distribution after 200 s for varying reduction factors from 1.0 to 0.001. The comparison reveals that the in-plane compression stiffness has a major impact on the model response. On the one hand, high values lead to empty spaces in the cavity. A gap near the inner radius appears, resulting from an uplift of the preform during

the tool closing. A smaller gap is still visible for a reduction factor of 0.1. Moreover, high compression stiffness causes an unrealistic deformation behavior near the upper radius of the cavity leading to two smaller gaps near the top. On the other hand, the in-plane compression stiffness influences the FVC distribution in the radius section. With a reduction factor of 0.001, the FVC is nearly homogeneous in the radius, whereas a significant gradient appears for a factor of 1.0.
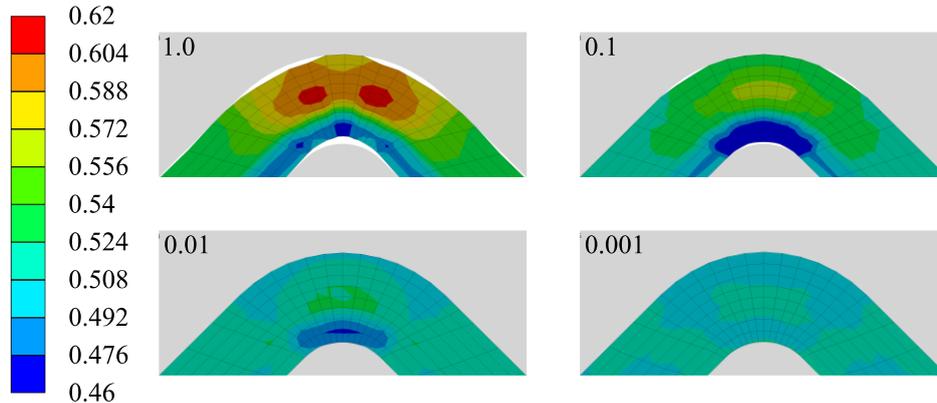
Fig. 5-17: FVC distribution after stress relaxation for varying in-plane stiffness compression reduction factors (1.0, 0.1, 0.01 and 0.001).

Fig. 5-18a depicts that the in-plane compression stiffness reduction factor has a major influence on the force response. For the highest value of $f_{E_{11}}$, the peak force and the relaxed force are significantly higher. However, for values of $f_{E_{11}} \leq 0.001$, the force response seems to be converging to a single curve. Thus, it can be assumed that the reaction force is independent on the in-plane compression stiffness for small $f_{E_{11}}$ values.

Because no gap could be observed in the experiments in Section 3.5, an in-plane stiffness compression reduction factor of less than 0.1 must be chosen. In order to determine the optimum value of the reduction factor, another parameter is introduced. Even though the gap between the preform and the upper mold is closed in all simulations with smaller factors, the time at which the gap vanishes is different. The gap closure time is defined as the point of time when the upper mold touches the preform in the middle of the radius. This time can be evaluated by the contact status change of the top nodes of the preform. Thus, small gaps located off-center such as the ones shown in Fig. 5-17 with $f_{E_{11}} = 1.0$ are ignored. Fig. 5-18b compares the closure time for varying in-plane stiffness reduction factors. With factors 1.0 and 0.1 the gap at the top vanishes comparably late at approximately 90 s. A further decrease of the factor leads to an earlier closure of the gap. A plateau with minimum closure time is reached between 0.002 and 0.0005 followed by higher values for smaller values of $f_{E_{11}}$. It was observed that simulations with $f_{E_{11}} < 0.001$ showed convergence issues, requiring more iterations to find a stable solution.

Based on the outcome of this study, an in-plane stiffness compression reduction factor of 0.001 is chosen for the following simulations. A final calibration of $f_{E_{11}}$ is conducted in Subsection 5.4.5 after studying the remaining parameters and their influence on the material response.

(a)   **(b)**
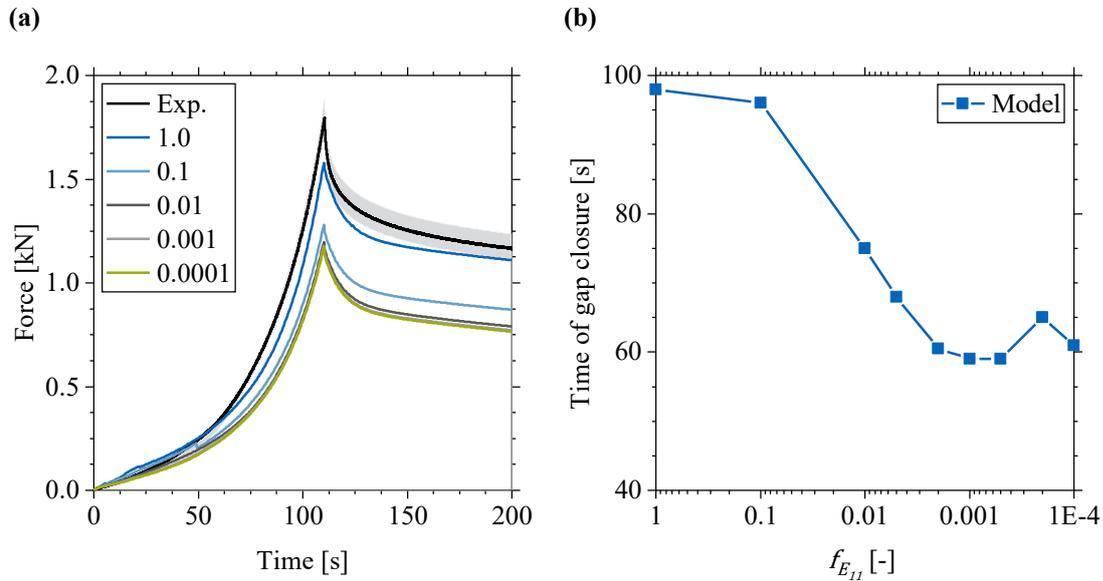
Fig. 5-18: **Influence of varying in-plane stiffness compression reduction factors $f_{E_{11}}$: (a) on the reaction force of the upper tool; (b) on the gap closure time.**

5.4.2 Influence of tool-preform friction

Fig. 5-19 compares the FVC distribution after stress relaxation for varying friction co-efficient values μ from 0.1 to 0.6. For each simulation, the same friction values were assigned to the upper tool-preform contact and the lower tool-preform contact. The comparison clearly proves that the friction coefficient has a significant influence on the final shape of the curved preform. Starting from a friction coefficient of 0.4, a gap remains near the outer radius of the cavity. Increasing the friction coefficient further to 0.6 results in a more pronounced gap. Moreover, the reduced thickness due to high friction forces leads to higher FVC values in the radius.

The influence of the tool-preform friction on the reaction force response of the upper tool is illustrated in Fig. 5-20. The friction coefficient was gradually increased from the measured value 0.1 up to 0.6. Further increasing of the friction coefficient lead to unstable simulations. The study reveals that the friction has a minor influence on the force response. Although an increase in force can be observed for high friction values, it is small compared to the influence of other parameters. Even the highest value of 0.6 leads to a compaction force which does not match the experimental data. Additionally, high

friction values cause a gap in the tool, which could not be observed in the experiments. Hence, it can be concluded that an uncertainty in the friction measurement is not the cause of the deviation between the model and the experimental force response.
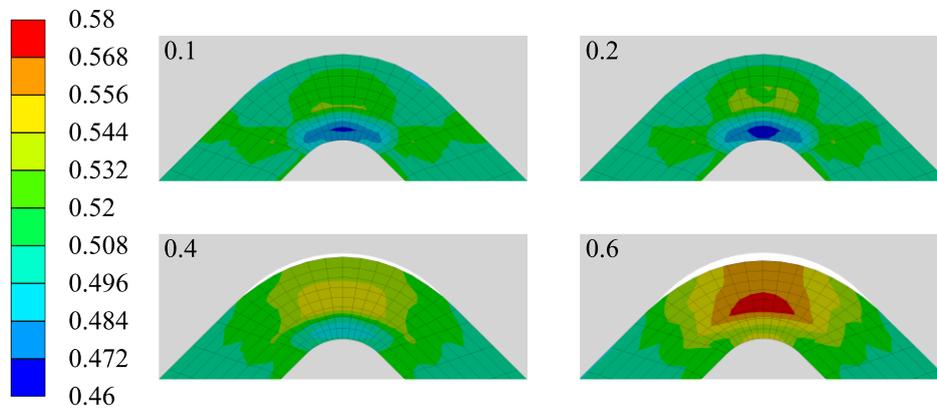
Fig. 5-19:   FVC distribution after stress relaxation for varying tool-preform friction coefficients.
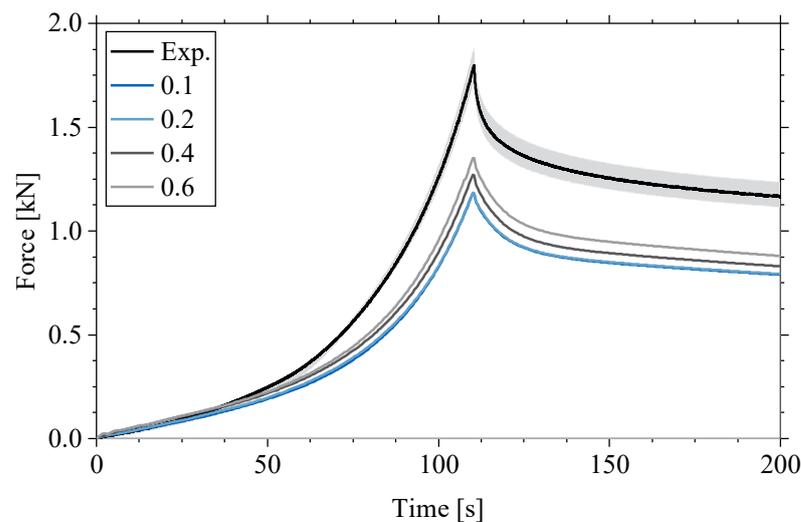
Fig. 5-20:   **Influence of varying tool-preform friction coefficient values on the reaction force of the upper tool.**

5.4.3   Influence of compaction stiffness

From the force response of the displacement-controlled experiments in Section 3.5, it is obvious that the non-planar compaction is strongly dominated by the through-thickness behavior. The factor $f_{E_{33}}$ is introduced to scale the compaction stiffness in the material model. With this factor, the influence of the compaction stiffness on the non-planar model response can be analyzed. Fig. 5-21a shows a comparison of the reaction force of

the upper tool for different scaling factors. This study reveals that the compaction stiffness has a strong influence on the force response. With a factor of $f_{E_{33}} = 2.0$, the force response is significantly increased to very high values. However, a factor of $f_{E_{33}} = 1.6$ results in a force response matching the peak force very well. Moreover, the reaction force of the model lies within the scatter of the experiments during compression and relaxation.

The variation of the compaction stiffness did not show any effect on the deformation of the preform during compaction. Only minor differences in the FVC distribution in the radius could be observed. The comparison of the gap closure time in Fig. 5-21b shows a slight increase towards later vanishing of the gap for higher compaction stiffnesses. Because the time of gap closure increases only by 3% between factors 1.5 and 2.0, it can be concluded that the influence is negligible for higher values.

(a)   **(b)**
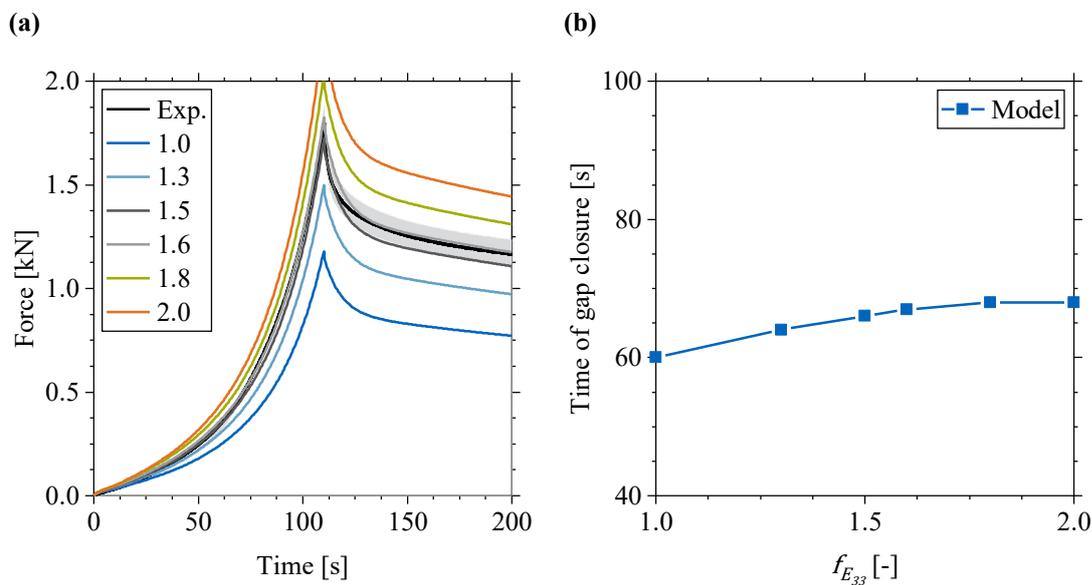
Fig. 5-21:   Influence of varying compaction stiffness scaling factors $f_{E_{33}}$: (a) on the reaction force of the upper tool; (b) on the gap closure time.

5.4.4 Influence of out-of-plane shear stiffness

Fig. 5-22a depicts a comparison of varying out-of-plane shear stiffness scaling factors $f_{E_{55}}$ from 1.0 to 16.0. This parameter study shows that the out-of-plane shear stiffness has a major impact on the force response of the model. With a scaling factor of $f_{E_{55}} = 16.0$, the model response almost matches the experiment at the peak. However, the model prediction shows deviations during the compaction phase. More significantly, the scaling factor of $f_{E_{55}} = 16.0$ results in a model response not being able to relax the

stresses to the experimental data, leading to major deviations. Thus, the experimental force response cannot be matched by calibrating the out-of-plane shear stiffness.

The influence of varying out-of-plane shear stiffness scaling factors $f_{E_{55}}$ on the time of gap closure is depicted in Fig. 5-22b. Compared to the compaction stiffness, the influence of the out-of-plane shear stiffness on the gap closure time is stronger. The tendency towards later gap closure for higher shear stiffness seems to be non-intuitive. Because of more shearing of the softer flanges, one would expect that the preform is more pulled downwards in the radius. However, a comparison of the z-displacement of the preform top node reveals that there is only a minor movement of 0.07 mm prior to tool contact in case of $f_{E_{55}} = 1.0$. In comparison, the top node with $f_{E_{55}} = 16.0$ shows a z-displacement of 0.65 mm prior to the initial contact with the upper tool. The greater movement of the top node together with less shear strain due to higher shear stiffness leads to higher FVC gradients in the material. Moreover, the in-plane compressive strains increase from maximum 0.02 with $f_{E_{55}} = 1.0$ by almost a factor of five to 0.10 with $f_{E_{55}} = 16.0$.

(a)   **(b)**
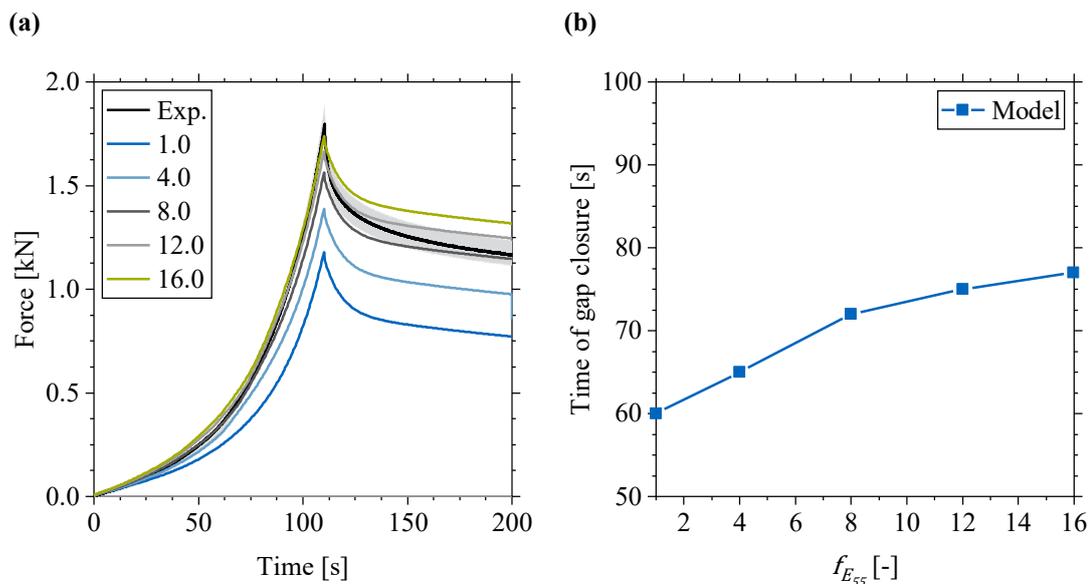
Fig. 5-22: Influence of varying out-of plane shear stiffness scaling factors $f_{E_{55}}$: (a) on the reaction force of the upper tool; (b) on the gap closure time.

As mentioned above, increasing the out-of-plane shear stiffness decreases the shear deformation in the flanges. This relation can be used for further calibration of the model, using the shear measurement from pictures described in Section 3.5. Fig. 5-23 compares the flange shear angle for varying $f_{E_{55}}$ values with experimental data of configuration L_3_8_12. The shear angle at the flanges decreases from 20.9° for $f_{E_{55}} = 1.0$ to 6.6° for $f_{E_{55}} = 16.0$. The horizontal experimental line indicates the average shear deformation of 21° measured from picture overlays. Only an out-of-plane shear stiffness factor of 1.0

guarantees a shear deformation which is close to the mean experimental data and inside the scatter area. Based on the finding in this subsection, the out-of-plane shear stiffness remains unchanged for all following simulations.
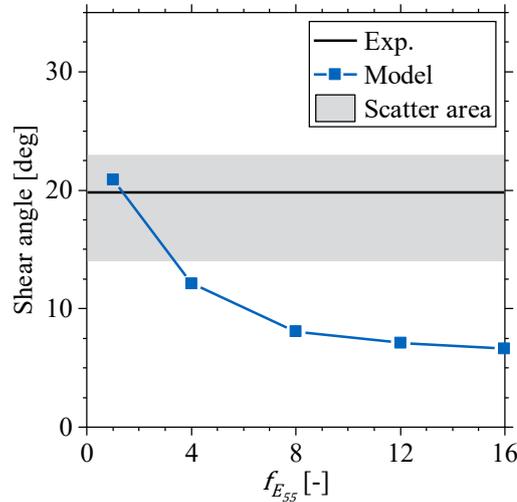
Fig. 5-23:   **Influence of varying out-of plane shear stiffness scaling factors $f_{E_{55}}$ on the shear angle at the end of the flange compared to experiments of configuration L_3_8_12.**

5.4.5 Calibration of the in-plane compression stiffness with experimental data

The study of the influence of the in-plane compression stiffness on the material response in Subsection 5.4.1 showed that only values smaller than 0.1 result in a reasonable final preform shape. Moreover, the factor $f_{E_{11}}$ had a significant effect on the time of gap closure. Since the results from the compaction stiffness study in Subsection 5.4.3 suggest a factor $f_{E_{33}} = 1.6$, which also influences the gap closure time, a final calibration step of $f_{E_{11}}$ is necessary. For this purpose, the study of the influence of the in-plane compression stiffness is repeated with a constant compaction stiffness factor of 1.6. The result of this parameter study with the influence on the force response is depicted in Fig. 5-24a. Consistent with the previous studies, the force signal converges for small values of $f_{E_{11}}$. The two lower curves with $f_{E_{11}} = 0.001$ and $f_{E_{11}} = 0.0001$ are in very good agreement with the experimental data.

The comparison of the gap closure time in Fig. 5-24b shows the same qualitative behavior as in Fig. 5-18b with a higher minimum. The closure times for $f_{E_{11}} = 0.001$ and $f_{E_{11}} = 0.0005$ differ from the experimental value only by one second. In addition, the force response and the final FVC distribution are nearly identical for both values. Because lower values of $f_{E_{11}}$ tend to make simulations more unstable, the greater value of 0.001 is chosen for all following calculations.
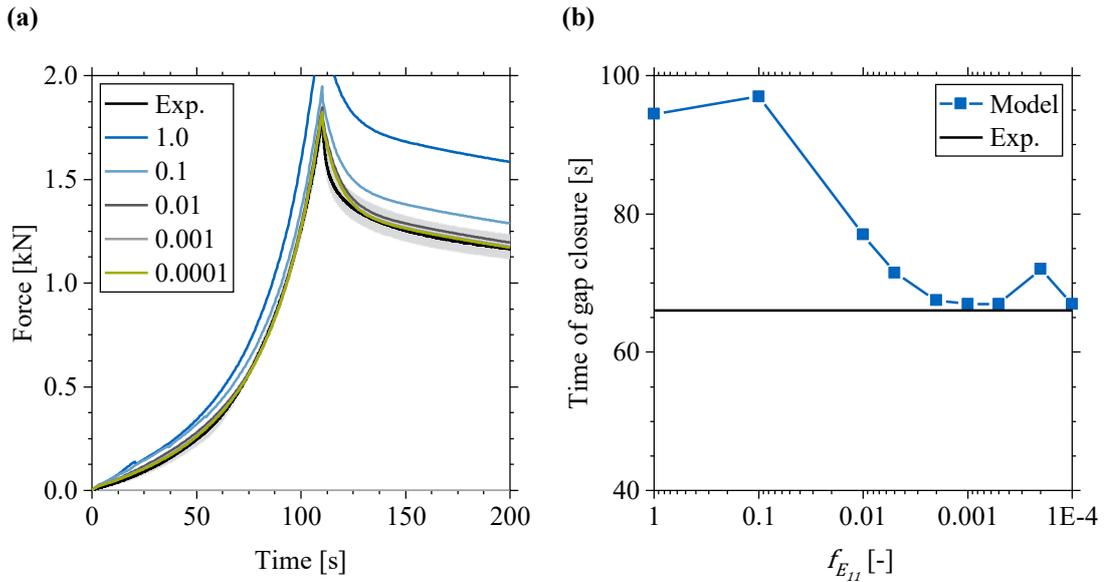
Fig. 5-24: Influence of varying in-plane stiffness compression reduction factors $f_{E_{11}}$ with increased compaction stiffness $f_{E_{33}} = 1.6$: (a) on the reaction force of the upper tool; (b) on the gap closure time.

5.4.6 Conclusion on the influence of the main material properties on the model response

The in-plane compression stiffness and the friction coefficient have the most significant influence on the preform deformation. High values for both properties lead to unrealistic preform deformation which did not appear during the experiments. Thus, upper bounds can be derived by comparing the deformation to experiments. Based on the results from the study, high in-plane compression stiffness and an uncertainty in the friction measurements can be ruled out as main cause for the deviation of the force response. The compaction stiffness and the out-of-plane shear stiffness both affect the force response without influencing the preform deformation. However, only an increased compaction stiffness allows matching the experimental force response, because high shear stiffness affects the qualitative force evolution during compaction. Thus, it can be concluded that the main cause for the deviation must originate from the compaction stiffness. Nevertheless, the cause for an increased compaction stiffness cannot be identified. The effect can be based on combined shear and compaction or a differing preform process. It is possible that the out-of-plane shear stiffness needs to be adjusted as well. However, because the contribution of increased shear cannot be great, this effect is neglected leading to a scaling factor of 1.0. The final set of material parameters used for all subsequent simulations are summarized in Tab. 5-3.

Tab. 5-3:   **Final material parameters after model calibration.**

Parameter	Value
In-plane compression stiffness reduction factor $f_{E_{11}}$	0.001
Compaction stiffness calibration factor $f_{E_{33}}$	1.6
Out-of-plane shear stiffness calibration factor $f_{E_{55}}$	1.0
Friction coefficient μ	0.1

5.5 Model validation with non-planar compaction experiments

Simulation models were created for all configurations in Tab. 3-8 using the material parameters defined in Tab. 5-3. First, the model response of displacement-controlled setups is compared to experimental data. Second, the displacement of the upper tool in the simulation model validated with experimental measurements of force-controlled tests. This section concludes with a discussion of the capabilities and limitations of the three-dimensional compaction model.

5.5.1 Results of displacement-controlled configurations

Fig. 5-25 compares the reaction force response of the upper tool boundary condition with the experimental results of the displacement-controlled non-planar compaction tests. The greatest deviation between model and experiment appears for configuration L_3_10_16. The difference is small at the beginning of the compaction phase and increases towards higher forces. This leads to an overestimation of the peak force by 17% compared to the mean experimental force response. The model shows a strong stress relaxation leading to a slight underestimation of the relaxed stress by 12% from experimental data. Nevertheless, the relaxed stress is very close to the scatter area of the experiments. The model responses of configurations L_3_8_12 and L_5_10_12 are almost identical, which is in good agreement with observations from the experiments. The model predicts the behavior of the material extremely well during compression and relaxation. There is only a minor deviation from the mean value at the end of the relaxation, still being inside the scatter area. The model prediction for configuration L_5_8_8 is in excellent agreement with experimental data. Especially, the compaction prediction is very satisfying with the peak force only being underestimated by 3.7% compared to the experimental mean value. During the stress relaxation, the model correlates well with the experiments, as indicated by the force response remaining inside the scatter area.

Interestingly, the experiments show a different behavior for configurations L_3_8_14 and L_5_10_14 with different tool radii. The greater tool radius leads to higher peak force and a higher level of relaxed forces. This behavior is qualitatively reproduced by the model, showing higher stresses for the greater radius with a difference being smaller than in the experiments. Experimental data and simulation results are in good agreement during the compaction phase for both configurations. For configuration L_3_8_14, the peak stress is underestimated by 8.3%, whereas the relaxed stress is overestimated by 9.3% in relation to the mean value. However, due to the comparably high scatter of the experiments, the relaxed stress is only 4.3% above the scatter area. The agreement with experimental data is significantly better for configuration L_5_10_14. The model underestimates the peak stress by only 2.4% and overestimates the relaxed stress by 3.3% relative to the mean experimental values. Remaining inside the experimental scatter area almost during the whole process, the agreement is extremely good.
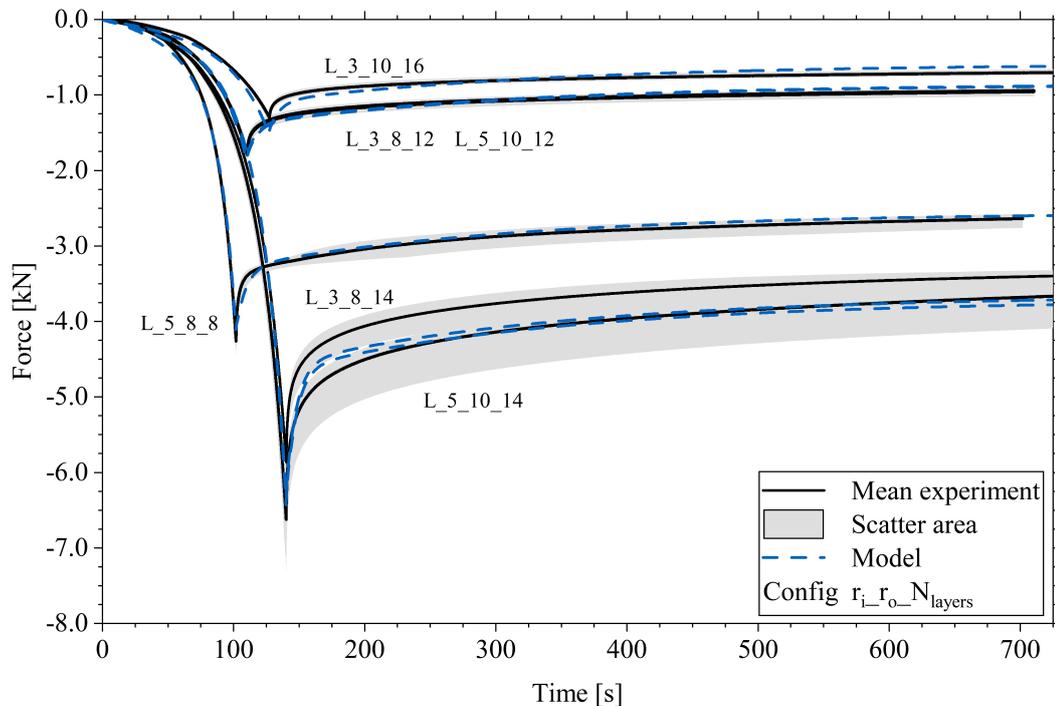
Fig. 5-25: Experimental data of the non-planar displacement-controlled compaction tests, including minimum and maximum scatter area and prediction of the three-dimensional compaction model.

In addition to validating the model with the experimental force response, the shape of the preform can be compared to further asses the accuracy of the model. As shown in Section 5.4, several material properties have a significant influence on the gap closure time. With the help of images derived from videos, which were taken during the experiments, it is possible to validate the tool closing process. The focus is placed on the

deformation of the preform in the radius and the vanishing of the gap over time. Fig. 5-26 compares the experiment with the process simulation at four different times. The time $t = 0\ s$ represents the beginning of the compaction experiment when the upper tool starts to move. The small thickness difference can be explained with experimental test L_5_10_12_05 being 0.17 mm thinner in the radius than the mean value for this configuration. The model was created using the mean geometric dimensions given in Tab. 3-10. As shown in Fig. 5-26, the model predicts the tool closing process is extremely well. At $t = 50\ s$, only a very small gap can be seen in the model and the experiment. Moreover, the model shows the change of the FVC distribution during the tool closing.
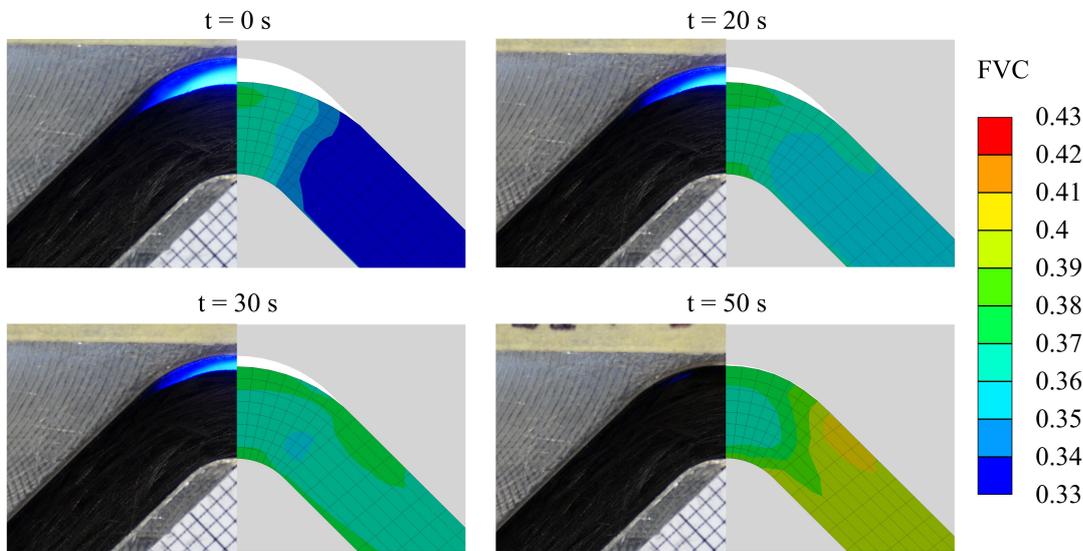
Fig. 5-26: **Comparison of experiment L_5_10_12_05 with the simulation at different times of the tool closing, with simulation showing the FVC distribution.**

Furthermore, the comparison of the flange deformation provides another possibility to validate the simulation. The closing of the tool leads to a combined compaction and shear deformation of the flange, which can be quantified by observing the outer edge of the flange. Fig. 5-27a compares the simulation result of the final deformed state of the flange with the experiment of configuration L_5_10_12. The comparison shows an excellent agreement between the simulation and the experimental result. While the thickness of the preform is defined by process parameters, the resulting out-of-plane shear angle depends on friction and the corresponding shear stiffness. Hence, the shear angle of the flange is an adequate means for validation.

Fig. 5-27b shows a comparison of the resulting shear angle of the simulation with the experiments for various configurations. The simulated shear angle is in excellent agreement with the experimental data. For all configurations, the simulation result lies within the scatter of the experiments. Moreover, the model prediction is close to the mean shear

angle of the experiments for most of the configurations. The largest discrepancy of two degrees appears for configurations L_3_10_16 and L_5_8_8. The comparison proves that the simulation is capable of predicting the preform deformation very well. Especially, the FVC dependent out-of-plane shear stiffness model implemented in the subroutine seems to be appropriate.

The validation in this section demonstrated that the model is capable of predicting the force response and the shape of the preform during the tool closing very well.

(a)   **(b)**
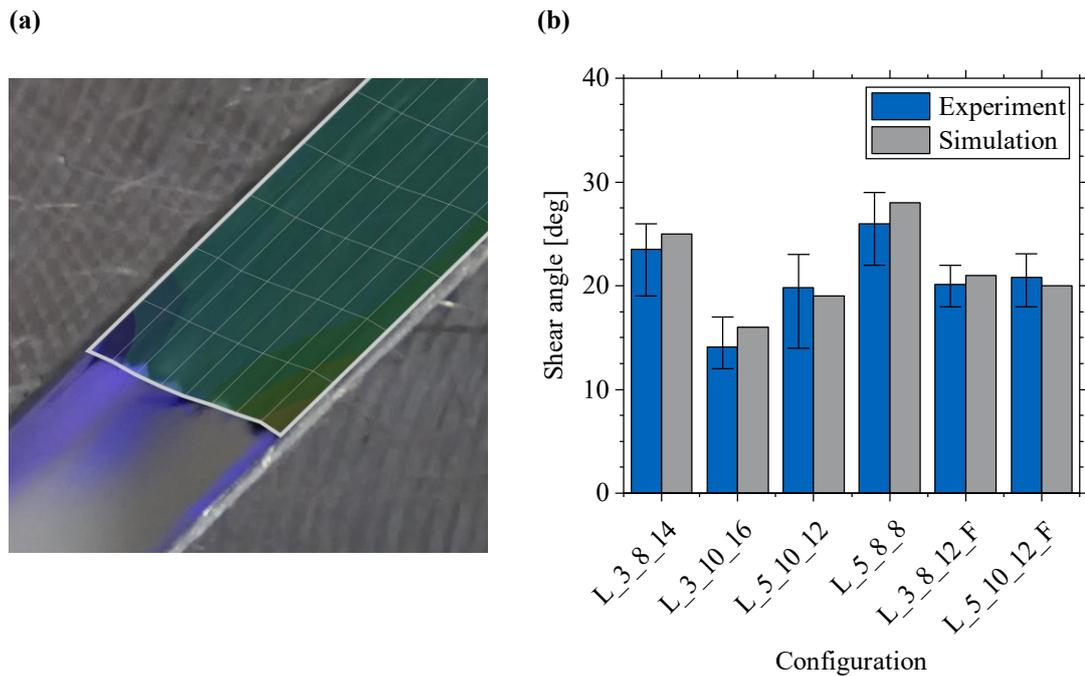
Fig. 5-27: **Shear angle measurement: (a) overlay of experiment and simulation for configuration L_5_10_12, simulation showing the FVC distribution; (b) comparison of simulation with experiment with error bars indicating the minimum and the maximum.**

5.5.2 Results of force-controlled configurations

Fig. 5-28 compares the displacement of the upper tool predicted by the model with the experimental displacement measurement. The comparison shows that the model response is in very good agreement with the experiments for both tool radii. The numerical prediction matches the measured data perfectly during the compaction phase. Moreover, the model shows the same creep behavior as the tests. The model slightly overestimates the displacement by 2.4% and 2.1% for the 3 mm and the 5 mm configuration respectively. Furthermore, the model shows a spring-back during the force release. However, the predicted final displacement differs by 10.5% and 10.2% from the experiments for the 3 mm and the 5 mm configuration respectively.

The validation of the out-of-plane shear angle of the flange in Fig. 5-27b shows a very good result of the model prediction for the force-controlled configurations. For the two tested configurations, the simulated shear angle is within the scatter range of the experiment and extremely close to the mean value.
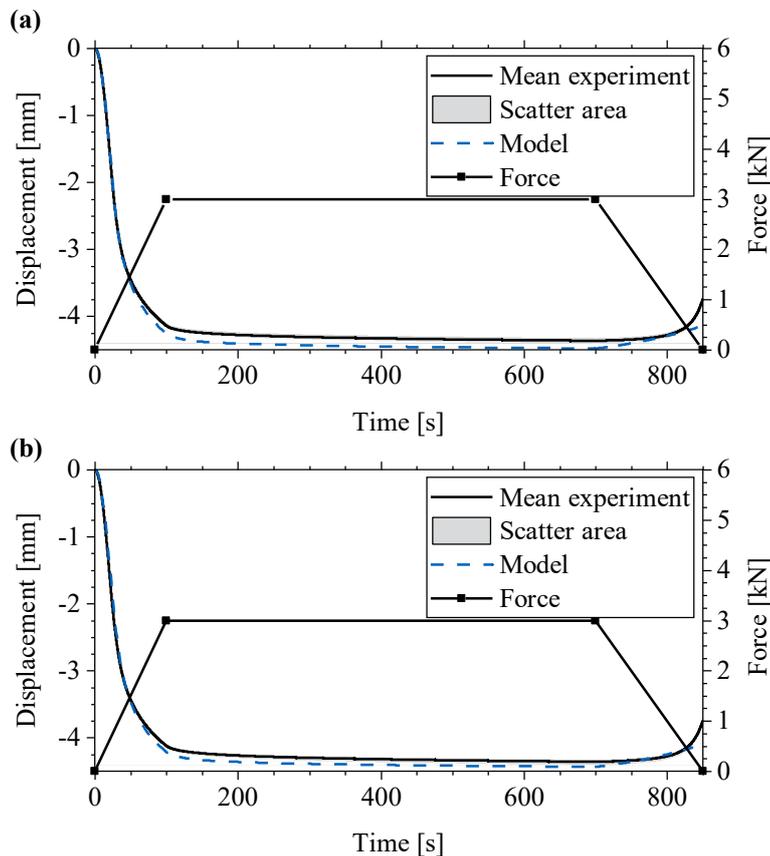
Fig. 5-28:   **Experimental data of the non-planar force-controlled compaction tests, including minimum and maximum scatter area and prediction of the three-dimensional compaction model: (a) 3 mm inner tool radius; (b) 5 mm inner tool radius.**

5.5.3   Discussion of model capabilities and limitations

Generally, the model prediction is in very good agreement with the experimental data. The validation proves that the model can be applied to displacement-controlled and force-controlled setups for different tool radii and varying preform thicknesses. Additionally to the displacement response and the force response, the validation proved that the model prediction of the preform deformation is very satisfying. The closing time, was in good agreement with videos taken during the experiment. This proves that the deformation in the radius is predicted correctly. Moreover, the modeled shear deformation of the flange matched the experimental results very well for all tested configurations.

The largest deviation of the reaction force between model and experiment occurred for L_3_10_16 being the preform with the most layers. There are two possible explanations for this behavior. On the one hand, the preform of this configuration is thicker and was compacted in the heated press for the same time as the thinner configurations. Thus, the middle layers of the preform were exposed to less heat, leading to reduced binder activation in the center. Having less adhesion between the layers gives the fibers more freedom to move which decreases the compaction stiffness. On the other hand, the preform with more layers has a higher potential for nesting. Hence, less force is needed to compact the preform. The simultaneous shear and compaction deformation might enforce the lateral shift of the layers leading to more nesting. This is in good agreement with the results from Chen et al [138]. They performed a virtual study of the impact of layer count with maximum nesting on the compressive force concluding that the force decreases for higher layer count. Dalfi et al. [269] came to the same conclusion that increasing the number woven fabric layers reduces the average thickness per layer when compacted with the same pressure. A precise conclusion on the cause of the model deviation for thick preforms requires more experiments with varying preform thicknesses and different FVC. Because the model predicts the force response of the thinner configuration L_5_8_8 very well, only the applicability of the model to very thick preforms is limited. However, if the focus is on predicting final stresses after relaxation, the model shows a good performance for all configurations.

Another uncertainty lies in the prediction of the force response with varying tool radii at high final FVC. The experiments showed clearly higher compaction forces for the 5 mm radius compared to the 3 mm radius. While the model is able to correctly predict the trend, the difference between the two configurations is significantly smaller. More experimental data is needed to clarify the influence of the tool radius on the force response, because the experiments showed nearly identical behavior for the twelve-layer configurations. Based on the available data, it cannot be ruled out that the root cause is a deviation in the experimental setup of configuration L_3_10_14. Nevertheless, the model results of the cases with small radii and high FVC must be regarded with caution.

5.6 Virtual study of geometry parameters

Based on the validated three-dimensional model, a parameter study of geometrical parameters was performed. The following properties were varied and investigated:

- Radius of the inner tool
- Initial thickness of the preform at constant FVC
- Initial FVC with constant preform thickness

The goal of this section is to gain deeper understanding of the influence of geometric variations on the compaction behavior. Moreover, the results were used to derive guidelines for the design of compaction processes.

The impact on the compaction behavior was evaluated with two different criteria. On the one hand the force response was analyzed for each parameter study. On the other hand, the closure time of the gap was compared. Although no gap occurred in the experiments, knowing the risk of race-tracking channels in the corner is valuable information. The later the gap between preform and upper tool vanishes, the higher the risk of an empty space remaining in the tool.

5.6.1 Tool radius study

For this study, the inner tool radius of configuration L_3_8_12 was reduced to 50% and the inner tool radius of L_5_10_12 was increased to 200%, resulting in four different models. Two studies were performed with 12 layers and 14 layers having the same thickness of the preform. The radius of the outer tool was adjusted to match the inner tool radius plus the final preform thickness of 5 mm to achieve a uniform cavity height. All preforms were compacted with the same tool displacement boundary condition.

Fig. 5-29a compares the reaction force on the lower tool for the four different tool radii with preforms consisting of 12 layers. The comparison shows a trend towards lower forces for larger tool radii, with the 10 mm radius model showing the lowest compaction force. All remaining configurations answer with almost the same force response. Generally, the tool radius has a minor impact on the force response. This is in good agreement with the experimental results shown in Fig. 3-23 where the closing force is almost identical for configuration L_3_8_12 and L_5_10_12. Fig. 5-29b shows the comparison of the time of gap closure for the different tool radii for preforms with 12 layers. There is a trend towards later closing times for larger tool radii. Thus, the risk for gaps remaining in the cavity decreases for larger tool radii. However, the closing time is independent of the tool radius for configurations with a radius less than 5 mm.

The experiments shown in Fig. 3-23 revealed that the compaction force increases with increasing tool radius for the 14 layers configurations L_3_8_14 and L_5_10_14. Because this is in contrast with the findings of the 12 layers configurations, the virtual radius study was repeated with more layers in the preform. Fig. 5-29c depicts the comparison of the reaction force on the lower tool for the varying tool radii with preforms consisting of 14 layers. The two configurations with larger radii show slightly higher peak forces and higher relaxed forces than the two configurations with smaller radii. However, the force during the compaction is nearly independent of the tool radius. Generally, the tool radius has a minor impact on the compaction force response. Fig. 5-29d shows that preforms with 14 layers lead to a later closing of the gap compared to the 12 layers preforms. However, the trend is the same as for 12 layers, showing constant closure times for smaller radii and a decrease for 10 mm tool radius.

(a)

(b)

(c)

(d)
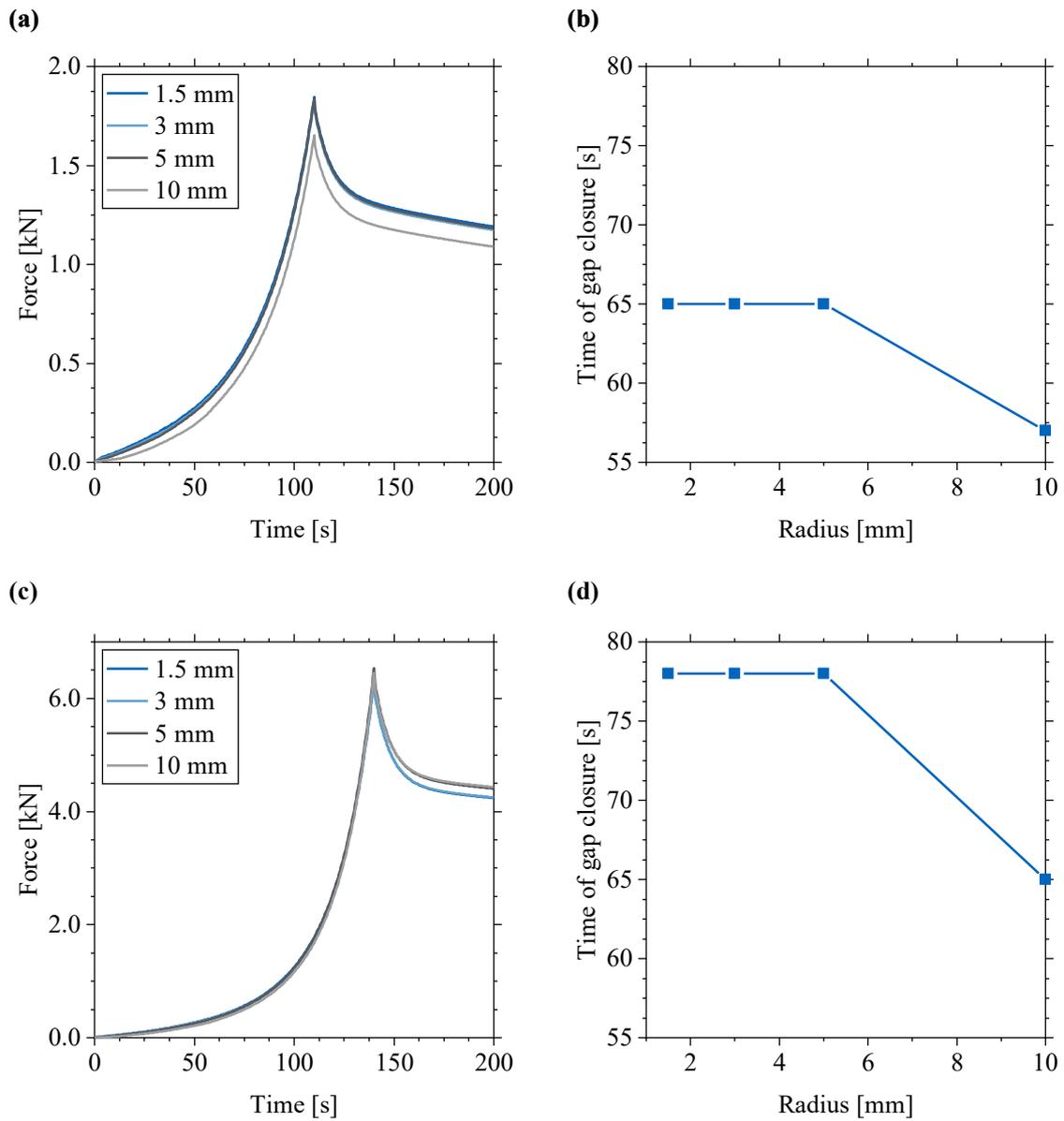
Fig. 5-29: **Influence of varying inner tool radii: (a) of a 12 layer preform on the compaction stress; (b) of a 12 layer preform on the time of gap closure; (c) of a 14 layer preform on the compaction stress; (d) of a 14 layer preform on the time of gap closure.**

5.6.2 Preform thickness study

The number of layers in the preform was varied for each configuration keeping the initial FVC constant. Thus, the initial thickness of the preform was adjusted for each simulation in this study. The preform properties used within this analysis are summarized in Tab. 5-4. The base line of this study is configuration L_3_8_12 with the same tool closing time of 110.3 s and a final nominal FVC in the flanges of 0.51 for all configurations.

Fig. 5-23a shows the compaction force occurring during the tool closing for varying preform thicknesses. Interestingly, an increasing thickness has a major influence on the

peak force. This effect can be explained with different compaction velocities to reach the same final FVC in the same period of time. For instance, the base line configuration with 7.6 mm thickness is compacted with 2.0 mm/min, whereas the 12.7 mm preform is compacted with 3.3 mm/min. Nevertheless, all forces are converging to the same relaxed force because of the same final FVC of all configurations. Thus, the models with very high thickness show a very pronounced force relaxation. Fig. 5-23b depicts the time of gap closure in dependency of the initial thickness of the preform. The diagram shows a significant shift towards later vanishing of the gap in the radius for an increasing number of layers in the preform. Hence, the risk for gaps remaining in the cavity increases with thicker preforms.

(a)

(b)
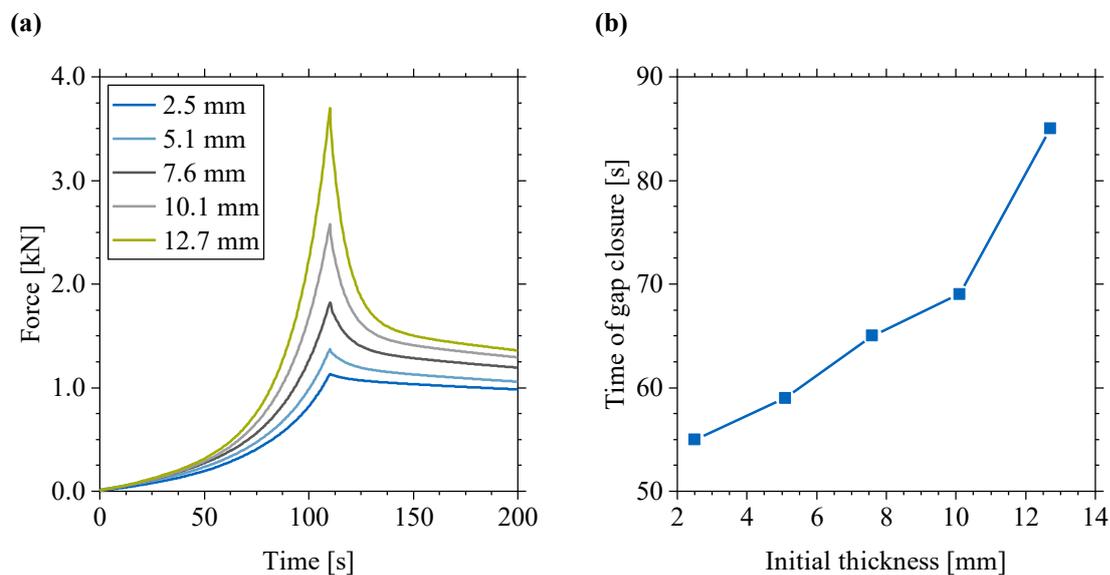
Fig. 5-30: **Influence of varying initial preform thickness with constant initial and final FVC: (a) on the reaction force of the upper tool; (b) on the time of gap closure.**

Tab. 5-4: **Initial and final preform properties for varying number of layers used for the virtual thickness study.**

Number of layers	Initial thickness [mm]	Initial FVC [-]	Final thickness [mm]	Final FVC [-]
4	2.53	0.33	1.67	0.51
8	5.01	0.33	3.33	0.51
12	7.6	0.33	5.0	0.51
16	10.13	0.33	6.67	0.51
20	12.67	0.33	8.33	0.51

5.6.3   Fiber volume content study

For the virtual study of the FVC, the number of layers in the preform was varied from 8 to 16 layers while the thickness was kept constant. The resulting initial FVC and the nominal final FVC according to Eq. (3-1) corresponding to a preform thickness of 5.0 mm are given in Tab. 5-5. All configurations were compacted with the same compaction velocity of 2 mm/min in 110.3 s.

The resulting reaction force for a varying initial and final FVC is depicted in Fig. 5-31a. As expected, the compaction force increases exponentially with increasing initial FVC. Interestingly, only a small portion of the peak stress is relaxed for the configurations with higher layer count. Fig. 5-31b compares the time of gap closure for different initial FVC of the preform. The diagram shows an exponential increase of the closure time for an increasing layer count. With a closure time of 89 s for the 16-layer configuration with 45% initial FVC, the gap in the cavity vanishes at the very end of the tool closing. Thus, the risk of a remaining gap in the cavity after tool closure is significantly higher for high FVCs.
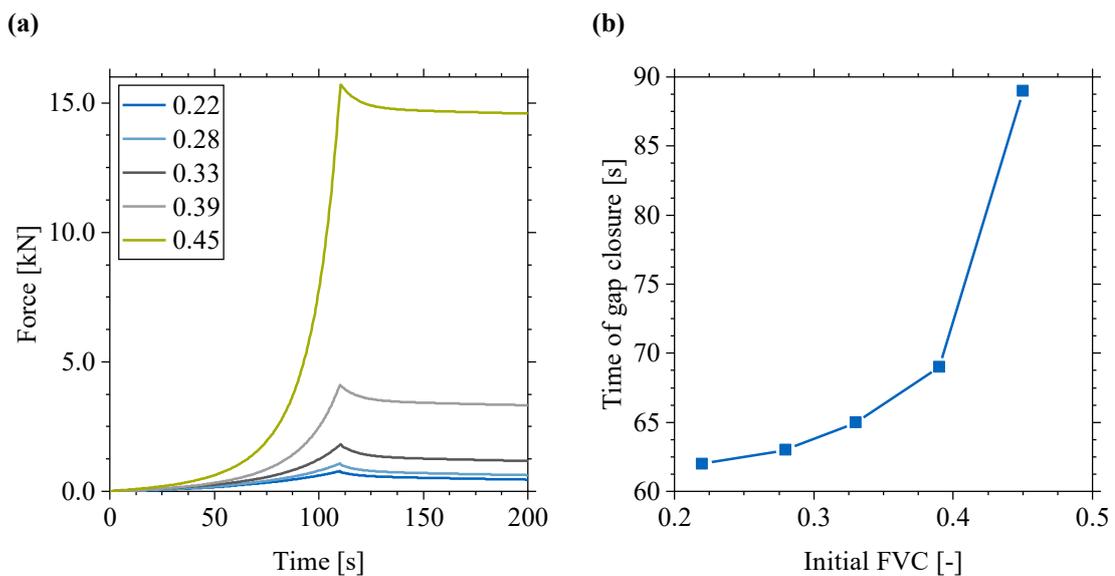
Fig. 5-31:   **Influence of varying number of layers at initial thickness: (a) on the reaction force of the upper tool; (b) on the time of gap closure.**

Tab. 5-5:   **Initial and final preform properties for varying number of layers used for the virtual FVC study.**

Number of layers	Initial thickness [mm]	Initial FVC [-]	Final thickness [mm]	Final FVC [-]
8	7.6	0.22	5.0	0.34
10	7.6	0.28	5.0	0.42
12	7.6	0.33	5.0	0.51
14	7.6	0.39	5.0	0.59
16	7.6	0.45	5.0	0.68

5.7 Derivation of guidelines for the preform compaction

Based on the findings in Sections 3.5, 4.5, 5.4 and 5.6, recommendations for the compaction of dry carbon fiber preforms were derived. These were divided into process-related, material-related and geometry-related guidelines. The guidelines contain valuable information for the early design phase when simulations cannot be performed because the material is not characterized yet or simulations are too time-consuming. The application of these recommendations can help to:

- Design a process for a smaller press because tooling forces are reduced
- Achieve a more robust process by reducing the risk of gaps
- Reduce FVC gradients in the final part and thus improve the part quality

With the results of this section, research question 3 is fully answered.

5.7.1 Process-related guidelines

Process-related parameters were concluded from the results of the 1D model in Section 4.5 and the non-planar experiments in Section 3.5:

- High closing velocities result in high peak forces, requiring a more powerful press for the compaction.
- Peak forces can be eliminated by adjusting the closing process, while achieving the same FVC in the same time.
- Significant thickness gradients in non-planar preforms originate from the draping process. These gradients can lead to defects after tool closing.

5.7.2 Material-related guidelines

The first section of Tab. 5-6 summarizes the main findings of the virtual study of material parameters in Section 5.4. The table gives an overview of how strong the influence of certain properties is on the force response and the preform deformation. From this information, the following material-related guidelines for the design of a compaction process can be obtained:

- The tool-preform friction has a major impact on the preform deformation. High friction values can result in gaps that remain in the radius of the cavity.
- The in-plane compression stiffness has a significant impact on the tool closing force and the risk of gaps in the cavity. To the author's knowledge, this has not been reported in the literature until now.
- The compression stiffness and the shear stiffness affect the force response but have a minor impact on the deformation behavior of the preform.

5.7.3 Geometry-related guidelines

The second section of Tab. 5-6 concludes the findings of the virtual study of geometric properties of the preform and the tool. It is important to note that the geometry parameters affect the preform deformation less than some of the material properties, such as the tool-ply friction. A more detailed overview that quantifies the impact of certain parameter variations is given in Fig. 5-32. Based on a scaling factor, Fig. 5-32a shows the influence of the inner tool radius, the preform thickness and the initial FVC on the peak force during the compaction. The comparison reveals that the FVC has the most significant impact on the reaction force with a maximum increase of the force by a factor of eight. Nevertheless, increasing the thickness of the preform by 67% doubles the maximum force during the compaction.

Fig. 5-32b compares the time of gap closure for varying tool radius, preform thickness and FVC, using the same scaling factor as mentioned above. All configurations were compacted in the same period of time of 110.3 s. Thus, the risk of empty regions remaining in the cavity is significantly higher for thick preforms and high FVC with gap closure times between 85 s and 90 s. An increased tool radius is the only parameter that was studied that leads to a decreased closing time.

The following guidelines can be concluded from Fig. 5-32a and Fig. 5-32b:

- The tool radius has a minor impact on the closing force. Small tool radii increase the risk of gaps in the tool.
- Thick preforms lead to higher compaction forces when the FVC is kept constant. Moreover, thick preforms increase the risk of gaps significantly.
- Preforms with high FVC lead to extremely high compaction forces. It is important to note that a high FVC increases the time of gap closure the most.

Tab. 5-6:   Influence of material and geometry properties on the tool closing force and the preform deformation (strong: ●●●, medium: ●●○, weak: ●○○, none: ○○○).

Property	Influence on the force response of the model	Influence on the preform deformation
Material-related		
In-plane compression stiffness	●●○	●●●
Compaction stiffness	●●●	●○○
Out-of-plane shear stiffness	●●○	●○○
Friction coefficient	●○○	●●●
Geometry-related		
Tool radius	●○○	●○○
Preform thickness	●●○	●●○
FVC of the preform	●●●	●●○
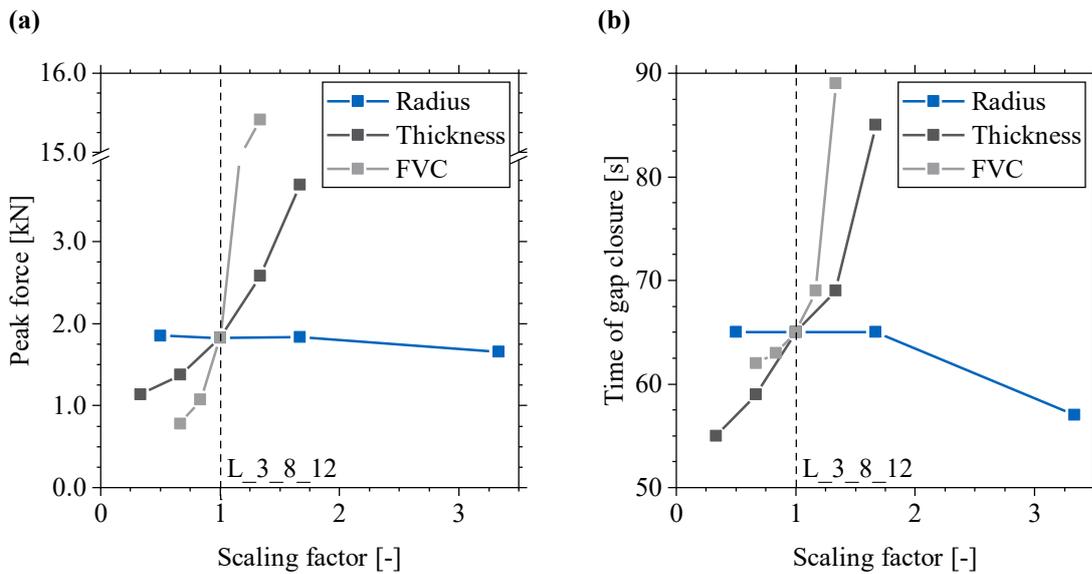
Fig. 5-32:   Impact of geometry parameter variation with reference configuration L_3_8_12 (inner tool radius 3 mm, initial thickness 7.6 mm and initial FVC 0.33): (a) on the peak force response; (b) on the time of gap closure.

6 Coupling of compaction process simulations with filling simulations

This chapter shows a further application of the developed compaction simulation method by coupling results such as FVC to subsequent filling simulations. The objective is to demonstrate the effect of the compaction state of the preform after tool closing on the filling behavior in an RTM process.

It is important to mention that the results of the filling simulations have not been validated within this work. This chapter focuses on demonstrating how compaction simulations can be embedded into a composite manufacturing process simulation chain. Moreover, the intention of the filling simulation results, presented here, is to highlight the importance of compaction simulations. First, the general methodology for the transfer of compaction results to filling simulations is presented. Second, a method for the creation of race-tracking channels in tool radii based on the mechanical contact status is illustrated. The approach is applied to two different geometries, a flat plate and an angled profile. Both examples demonstrate the influence of the transferred data. The workflow presented here has been developed together with Thalhamer in [S8] and Faron in [S13] and published jointly in [P3].

6.1 Data transfer to filling simulations

The content of this section is partly derived from the preprint of [P3].

The FVC, the material orientation and the geometry of the deformed preform are three main results from the compaction simulation that affect the filling behavior of the preform. FVC and material orientation directly influence the permeability of the reinforcement material. However, the deformed geometry defines the presence of potential race-tracking channels in the cavity and thus, has a major influence on the filling behavior.

The general concept of each data transfer is the same, with the work flow shown in Fig. 6-1. The methodology was initially developed together with Thalhamer [S8], enhanced with Faron [S13] and finalized within this thesis. First, the deformed mesh is transferred from the mechanical compaction simulation to the fluid model. For this purpose, the results are transferred to another mechanical model. With the compacted state as initial mesh of the second model, the deformed mesh can be transferred to ANSYS Fluent. Second, all remaining data such as material orientation, FVC and contact status are

exported into text files from the compaction simulation. Because the nodal information is exported with coordinates of the initial undeformed mesh, the data needs to be modified afterwards. For this purpose, nodal deformations in global x-, y- and z-direction are exported. A python script is used to read in the result file together with the nodal displacements and recalculate the final node positions. These updated nodal results are written into a cleaned text file, containing only necessary information for the subsequent import. It is important to note that ANSYS Fluent requires element information on the centroids. Thus, the nodal results from the mechanical simulation need to be interpolated to element centroids before further processing. For this purpose, the data interpolation available inside ANSYS Fluent is used. The final reduced file contains the coordinates of the element centroids in the first three columns, followed by the information to be transferred. For the FVC, a scalar is written into the fourth column, whereas the orientation must be defined by three rotation angles.
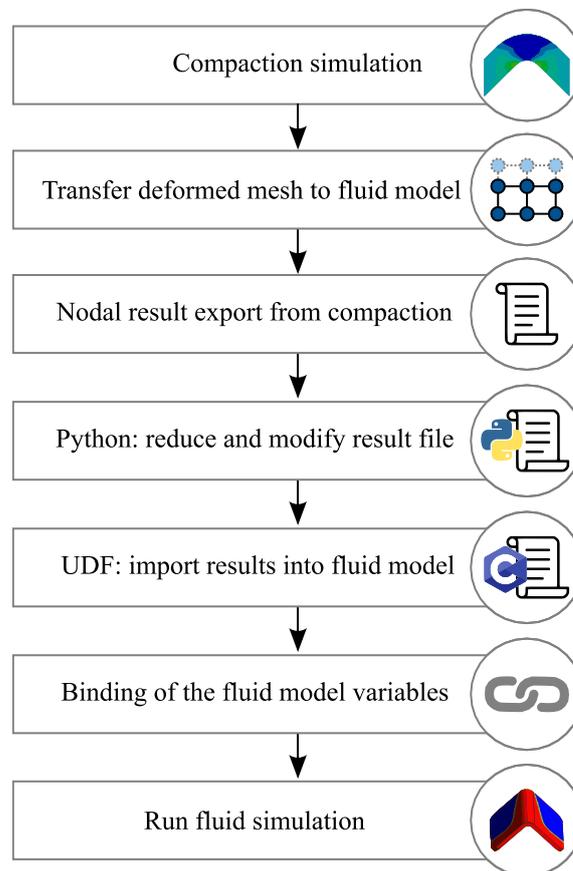
Fig. 6-1: **Flow chart of the data transfer between mechanical compaction simulation and fluid simulation.**

A user-defined function (UDF) in ANSYS Fluent is utilized to import the data from the reduced text file into the fluid model. Contrary to ANSYS mechanical, Fluent UDFs are written in C. The UDF reads in the coordinates of the reduced file and searches for the

corresponding cell in the mesh of the filling simulation. The respective information from the mechanical simulation is linked to the appropriate value of the cell. In order to avoid, that the modification of parameters is repeated at every time step, the function is only called at the beginning of the first time step. Similar meshes reduce the need of interpolation, and thus, provide a better mapping result.

Transfer of the FVC

The FVC, directly influences the permeability of the preform. The objective of the data transfer is to define the permeability distribution in the filling simulation, which is caused by the compaction during the mold closing. The method mentioned above is applied to create a reduced file with elementwise FVC data. The UDF, which is used for this data transfer, calculates the permeability for each cell. For the correlation between FVC V_f and permeability K, a Kozeny-Carman equation in the following form is used [234]:

$$K_j = \frac{\frac{1}{C_j} * \left(1 - V_f\right)^{n_j+1}}{V_f{}^{n_j}} \qquad (6\text{-}1)$$

C_j and n_j in Eq. (6-1) are fitting parameters for the permeability K in direction j. The fitting parameters given in Tab. 6-1 were derived from fitting to permeability data from [270]. As ANSYS Fluent works with porosities and viscous resistances, $1 - V_f$ and $1/K_j$ respectively are returned by the routine. Once the UDF has been loaded in the fluid model, the variables in the UDF need to be associated to the material parameters of the simulation. The porosity is bound to the porous zone of the fluid mixture and the permeabilities are connected with the viscous resistance of the resin phase.

Tab. 6-1:   **Fitting parameters for the Kozeny-Carman equation**

Parameter	Value
C_1	5.23994e+10
n_1	2.45998e+00
C_2	7.81982e+10
n_2	2.89996e+00
C_3	7.33998e+11
n_3	2.30000e+00

Transfer of the material orientation

The orientation of the material affects the permeability, as it is defined by an anisotropic tensor. For the current approach, the orientation is set in the mechanical simulation. However, the method can also be adapted to take the orientation input from a prior kinematic draping simulation. Using information from kinematic draping in ANSYS Composite PrepPost (ACP) is especially useful for more complex geometries. However, for the simple example of an L-profile, thickness and orientation can easily be defined manually. In order to receive element orientations, no separate result export is required, because the necessary data is stored in the solver input file. Thus, the python script reads in the element coordinates and the angles of rotation from the mechanical solver input. It is important to note that the rotations are provided in Euler angles with Z-X-Y rotation order. Afterwards, the script writes the elementwise rotations into a reduced file for the UDF. In ANSYS Fluent, the UDF reads in the reduced file and calculates the new orientations based on the rotation data. In a final step, the orientations are linked to the material properties to define the permeability directions.

Application of the data transfer to a simple plate

The method presented in this section was tested on a model with a quadratic preform that was locally compacted in the center. Fig. 6-2a shows the resulting FVC distribution after the mechanical simulation. In Fig. 6-2b, the calculated permeability K_1 of the fluid model is shown. Areas with higher degree of compaction show lower permeabilities, which proves that the data transfer and the mapping work very well. The result of the compacted geometry transfer is shown in Fig. 6-2c. The section cut shows the distribution of the z-coordinates on the deformed mesh where the reduced thickness in the compacted area in the center can clearly be seen.

(a)   **(b)**   **(c)**
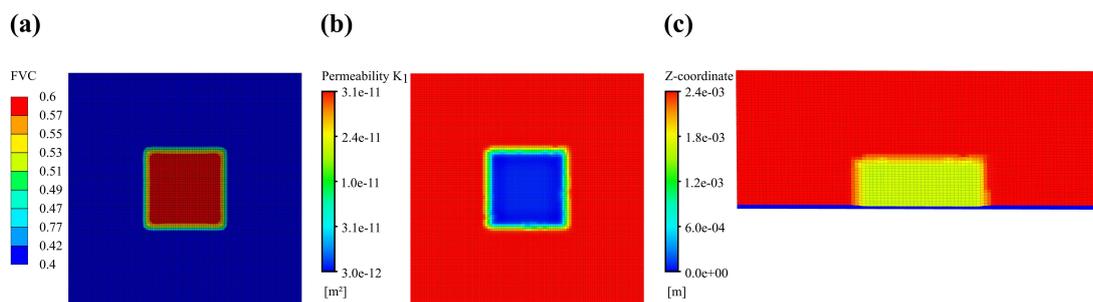
Fig. 6-2:   **Transfer of compaction results for a locally compacted plate: (a) FVC; (b) permeability K_1; (c) mid plane section cut with z coordinate.**

6.2 Generation of flow channels in empty cavities

The content of this section is partly derived from the preprint of [P3].

For the generation of the flow channels, the contact status was exported from the compaction simulation and imported into the fluid model. This methodology is illustrated in the flow chart in Fig. 6-3.
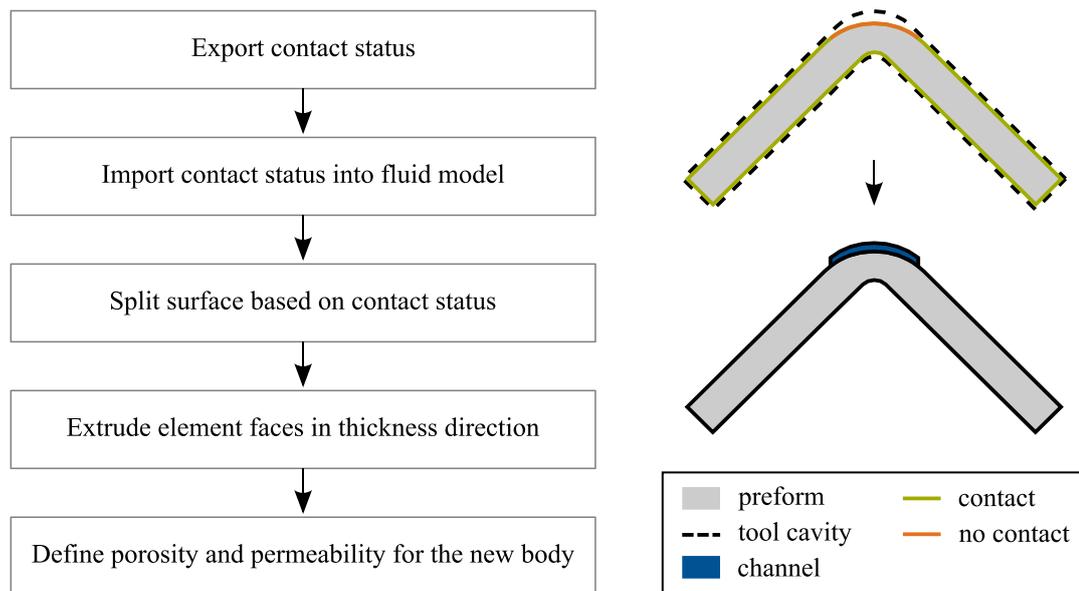
Fig. 6-3:   **Flow chart for the generation of flow channels based on the contact status of the compaction simulation.**

The general approach is the same as for the previously imported data. Fig. 6-4a shows the final FVC distribution of configuration L_3_8_12 with an increased tool ply friction of $\mu = 0.4$ from Subsection 5.4.2. In addition, the result shows a small gap between the preform and the upper mold in the radius. This gap can be detected by using the mechanical contact status, which has been imported into the filling simulation model (see Fig. 6-4b). The distribution on the top surface shows a change of the status from "near-field" to "sliding contact" in the region of the radius. The front side of the preform shows an interpolation of the contact status from top and bottom, performed automatically in ANSYS Fluent. However, the contact status on the top side shows a clear border where the gap is present in the cavity. By defining a new field variable in ANSYS Fluent, cells with a contact status between 0.8 and 1.2 (near-field contact) are marked. These marked cells are then used to split the surface of the preform. The element faces within the newly created surface are extruded using the built-in "extrude-face-zone-delta" function. This facilitates a normal extrusion of the selected face with constant thickness. The result analysis in the compaction simulation showed a gap height of 0.4 mm, which is

consequently chosen for the extrusion thickness. In a final step, a porosity of 1.0 and a permeability of 1e-8 m² are assigned to the newly created cell zone. The generated race-tracking channel can be seen in Fig. 6-4c, highlighted in blue.

(a)   **(b)**   **(c)**
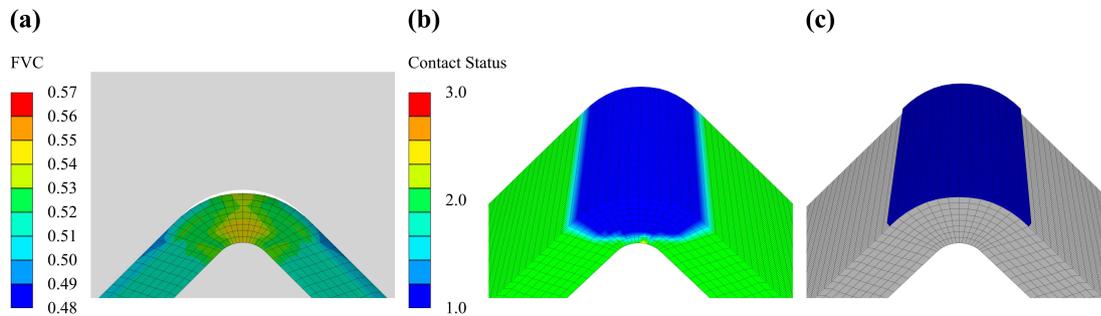
Fig. 6-4:   **Generation of a race-tracking channel: (a) fiber volume content; (b) contact status (status 1: near-field contact, 2: sliding contact and 3: sticking contact); (c) preform with flow channel created on top.**

6.3 Method for the filling simulations

The content of this section is partly derived from the preprint of [P3].

The developed method has been applied to the L-profile from Fig. 6-4. Two different models were created in ANSYS Fluent [271] with settings provided in Tab. 6-2.

Tab. 6-2:   **Parameter settings for the filling simulations in ANSYS Fluent.**

Parameter	Value
Solver type	Transient, pressure based
Number of phases	2 (resin and air)
Resin viscosity	0.054 kg/ms
Resin density	915 kg/m³
Air viscosity	1.7894e-05 kg/ms
Air density	1.225 kg/m³
Multiphase model	Eulerian
Formulation	Implicit
Inlet pressure	2 bar
Outlet pressure	0 bar

Both models were meshed with hexahedral elements, having a resin inlet and a resin outlet at the same locations with the same boundary conditions. The first model was set up without transferring data from the compaction simulation. For the second model, the new methodology was applied to transfer the FVC, the orientations, the displacements and to create the race-tracking channel on the radius. The material properties of the pre-form are derived from the data transfer of the compaction simulation. The permeability is calculated using Eq. (6-1) with parameters given in Tab. 6-1. A constant FVC of 0.5 and permeabilities derived from Eq. (6-1) were assumed for cases without imported compaction data. For the second model, the porosity in the channel was set to 1.0 and the permeability to of 1e-8 m².

6.4 Application of the coupled compaction and filling simulation

The content of this section is partly derived from the preprint of [P3].

Filling simulations were initially performed using the example of the locally compacted plate shown in Fig. 6-2. A resin inlet was placed on the left side with constant injection pressure and an outlet with 0 bar pressure was defined on the opposite side. It is important to note that the empty cavity in the area of the local compaction was not modeled in this case. The resulting fill factor at three different points in time are shown in Fig. 6-5. The picture on the left clearly shows that the resin flows significantly slower in the center due to the decreased permeability. In the further course of the injection, the compacted area gets filled from three sides almost causing an air entrapment in the center. The picture on the right shows the filling status towards the end of the injection with two flow fronts meeting behind the locally compacted area.

In the next step, filling simulations were performed for the L-shaped geometry shown in Fig. 6-4. In order to highlight the influence of FVC gradients, filling simulations with and without imported results from prior compaction are presented in Fig. 6-6. Contrary to the previous example, a race-tracking channel was modeled in the empty cavity. The resin was injected at one of the long edges of the profile, whereas the resin outlet was positioned on the opposite side. The filling pattern after 0.1 s proves that the race-tracking channel gets completely filled at the beginning of the injection. In the further course of the injection (e.g. after 2.0 s), the resin propagates to the flanches from the inlet and the channel on top of the radius. However, in the case without flow channel, the flow front remains always parallel to the resin inlet. The comparison of the injection after 10 s highlights that the presence of the race-tracking channel has a significant influence on the last filled elements and thus, the positioning of the resin outlets. These results prove that the presence of the flow channel has a major impact on the filling behavior. Hence, the influence of the adapted permeabilities cannot be seen in this example, because their

influence is less dominant. As a result of the increased FVC in the radius in Fig. 6-4a, the resin propagates slower in this region. The impact of decreased permeability due compaction can be better observed in the case of the locally compacted plate in Fig. 6-5.
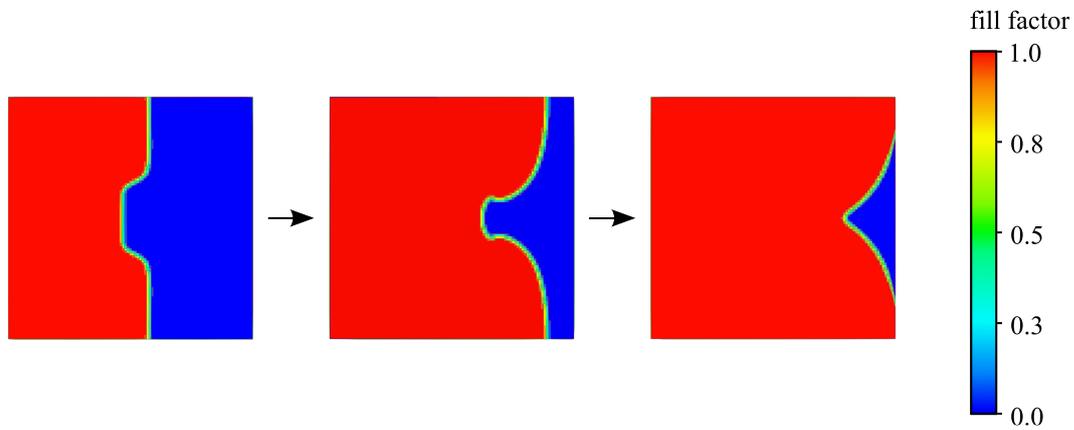
Fig. 6-5: **Filling behavior of the simple plate example with imported FVC and deformed mesh from compaction simulation.**
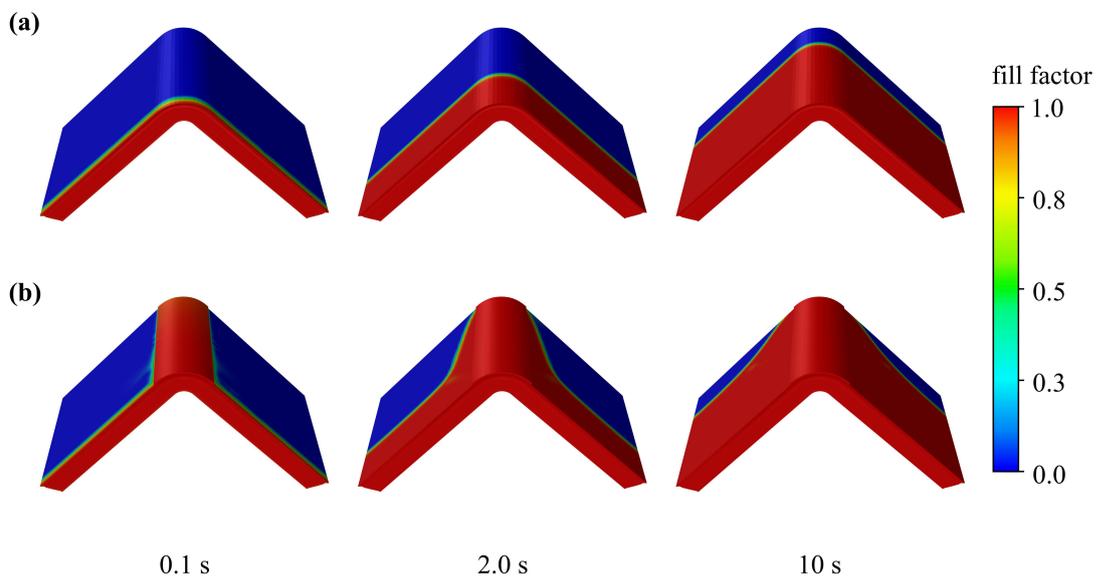
Fig. 6-6: **Comparison of filling behavior after 0.1 s, 2.0 s and 10 s injection time: (a) without imported compaction results; (b) with imported compaction results.**

6.5 Conclusions on the coupling with filling simulations

The content of this section is partly derived from the preprint of [P3].

In this chapter, a framework was developed that provides the possibility to utilize results from compaction simulations in subsequent filling simulations. With this approach, research question 4, raised in Section 2.5 was answered.

The presented methodology allows to transfer the FVC, material orientation and nodal displacements. In addition, the contact status is mapped onto the fluid model in order to generate race-tracking channels in empty cavities of the mold. The approach has been applied to a simple plate with local compaction and an L-profile with upper and lower mold. The example of the locally compacted plate demonstrated that the transfer of FVC and the corresponding adaption of permeabilities work very well. The functionality of the transfer of the deformed mesh and results with updated node locations to the infiltration model was verified for both models. The importance of transferring the contact status and generating race-tracking channels was demonstrated with the example of an L-profile. The developed methodology worked satisfactorily and highlighted the significant influence on the filling behavior compared to a model without imported compaction results. The resulting filling behavior of the angled preform is in very good agreement with observations made in literature [30,63].

The presented approach needs to be validated with injection experiments. In order to validate the filling simulations, the flow front position must be tracked at different locations inside the tool. This can either be achieved with multiple sensors (e.g. pressure or capacitive sensors) or a transparent tool with optical measurement as proposed by Bickerton et al. [30]. A major limitation of the current approach is that flow channels are generated with a uniform thickness. A better representation of gap geometry could be achieved by a stepwise layer extrusion of the race-tracking channel. Moreover, the extrusion based on contact status requires many manual steps in the graphical user-interface. Especially for more complex geometries, further automation with Python scripts is beneficial.

7 Conclusions

Numerous challenges in LCM processes, hindering a broader application for complex parts, can be related to process-induced FVC gradients. For instance, varying permeabilities and gaps in the tool can influence the filling behavior, resulting in defects such as resin-rich areas, dry spots or resin content gradients. These defects are significantly affecting residual stresses and part deformations after demolding. Moreover, mechanical properties show a great dependency on local FVC gradients in the final part. A non-uniform compaction of the preform is the root cause of these FVC gradients and the related part defects. Thus, predicting the compaction behavior with process simulations and avoiding compaction-related defects is of special importance. However, only very few material models are capable of predicting the anisotropic time-dependent behavior of preforms. To the author's knowledge, none of the existing models has proven to be applicable for non-planar displacement-controlled as well as force-controlled scenarios.

Four research questions were defined, the answers to which provide the necessary prerequisites for predicting the complex material behavior and integrating it into a process simulation chain. The models and solutions developed in this work provide a contribution to make LCM processes more robust and to reduce component scrap. This chapter summarizes the main contributions based on the defined research questions. Afterwards, an outlook is provided for future improvements and further applications of the newly developed modeling approach.

7.1 Summary of the main contributions

Material characterization of the main preform deformation mechanisms

A profound literature review revealed that the main deformation mechanisms during non-planar compaction are the through-thickness compaction and the out-of-plane shear behavior of the preform. Moreover, the review exposed that the friction at the tool-preform interface influences the material response during the compaction.

Initial tests showed that the machine deformation has a significant influence on the measured compaction force during the experiments. To overcome this issue, the compaction characterization method was improved using optical control of the upper plate movement. This ensured a constant closing velocity during the displacement-controlled compaction experiments. The compaction experiments were conducted with two textile materials, revealing interesting differences between woven fabric and NCF compaction behavior. Compaction forces are significantly higher for the woven fabric. For instance,

the relaxed force to reach 60% FVC is approximately 100% higher for the woven fabric compared to the NCF. This difference can be explained with less nesting effects occurring during the NCF compaction. In addition, the woven fabric shows a more pronounced stress relaxation of almost 60% compared to the one for the NCF material of approximately 30%.

Contrary to the compaction experiments, no method for the characterization of the out-of-plane shear of preforms was found in the literature. Thus, a new methodology for the characterization based on a double-lap shear test was developed. This method allows to test the out-of-plane shear stiffness at defined FVC levels. This was of particular importance as the results showed a strong dependency of the material behavior on the degree of compaction. The dependency can be explained with nesting, hindering lateral movement of the plies at high FVC. Additionally, a method for the result evaluation accounting for tape influence was developed. Using a linear regression algorithm allowed the identification of two sections with nearly constant stiffness for each test.

Non-planar compaction experiments were performed for the characterization of the behavior and the subsequent validation of the process model. Several configurations of L-shaped preforms with a varying number of layers and different tool radii were tested. Interestingly, the material response is clearly dominated by the through-thickness compaction. This can be seen in the same characteristic time-dependent material behavior that has been observed in the planar compaction tests. Thickness measurements of the specimens before the tests revealed that corner thinning lead to a reduced thickness in the radius by approximately 10% compared to the flange thickness. However, the initial gap on the outer tool radius vanished for all tested configurations.

Development of a one-dimensional compaction material model

A novel phenomenological formulation for the description of the time-dependent compaction behavior of dry carbon fiber preforms was developed. The incremental formulation makes the model suitable for an efficient FEA implementation. Furthermore, both compaction and relaxation phases are described in a single model, allowing an implementation without a case distinction.

The validation proved that the model is capable of predicting tooling forces in displacement-controlled setups over a wide range of FVCs and closing speeds. Moreover, the model predicts the creeping and the spring-back behavior of the material in force-controlled setups. Furthermore, the developed method can be used to reduce tooling forces in RTM processes. By eliminating the peak stress, the tooling forces, achieving the same FVC in the same time, could be reduced by 50%. The validation with two very different materials, a carbon fiber woven fabric and a carbon fiber NCF, demonstrated the broad applicability of the model. The results of a parameter study support the assumption that the model can be applied to a variety of fibrous preforms. Such a wide range of boundary conditions, preform and process properties could not be found for any of the models in the reviewed literature.

Extension to a three-dimensional material model and derivation of guidelines

After the validation of the through-thickness compaction model, the method was extended to a three-dimensional material model. The use of a general orthotropic material model allowed the separate definition of each stiffness matrix entry. Thus, the user-defined material could be extended by the bilinear out-of-plane shear model and an FVC-dependent in-plane tensile stiffness with reduced magnitude in compression. Simple single-element tests and planar geometry tests verified that the model shows the expected behavior. Combined load cases proved that the material answers with the desired coupling between the individual deformation modes.

Afterwards, the model was applied to non-planar cases, using the experimental configurations with L-shaped preforms. For this purpose, a new method was developed to account for the thinning effect and resulting changes of the FVC during preforming. A parameter study of the material properties was used to calibrate the model to one of the displacement-controlled experimental configurations. The study revealed that the compaction stiffness needs to be scaled by a factor of 1.6 in order to match the force response from experiments. Possible root causes are differences in the temperature introduction during preforming or a dependency of the compaction stiffness on the out-of-plane shear.

The model, calibrated to a single experimental configuration, was validated with the remaining displacement-controlled and force-controlled configurations. The force-response of the displacement-controlled configurations was in good agreement with experimental data. The model showed a satisfactory prediction for varying tool radii, FVC and number of layers. The largest deviation was observed for the thickest preform with 16 layers. This can be explained with lower core temperature, and thus differing binder activation during the preforming process or increased nesting of the higher number of layers. The predicted preform deformation in the radius section agrees well with the photographs captured during the experiments. A comparison of the upper tool displacement with the experimental data for the force-controlled configurations showed a very good agreement. The model predicted the compaction and creep of the material very well. Small deviations could be observed for the final thickness after force release.

The validated non-planar compaction simulation was further used for a virtual study of material parameters and geometrical dimensions. Together with results from the planar and non-planar compaction experiments, valuable guidelines for process, material and geometry were derived. High closing speed leads to high peak forces that can be eliminated by adjusting the velocity profile. Thus, a smaller press can be used to achieve the same FVC in the same time. Tool-preform friction and in-plane compression stiffness have a major impact on the preform deformation, whereas compression stiffness and out-of-plane shear stiffness mostly affect the closing force. Especially thick preforms and those with high FVC show an increased risk of gaps remaining in the cavity. The

tool radius has a minor impact on the closing force, but small tool radii increase the risk of gaps in the tool. These results are in good agreement with the findings from Dong [52], shown in Fig. 2-5. He concluded that FVC has the most significant influence on the formation of gaps, followed by stacking sequence and tool radius. The impact of preform thickness was not covered in his study.

Integration of the results into a virtual composite manufacturing chain

In addition to the development of a compaction model, a further objective of this work was the integration into a process simulation chain. This goal is of special importance as the local FVC gradients have a significant influence on the subsequent process steps. Thus, a methodology to transfer compaction simulation results into filling simulations was developed. This approach can be applied to transfer FVC, material orientation and nodal displacements. By importing the mechanical contact status and splitting the surfaces, a flow channel can be extruded at the location of the empty cavity in the tool. This allows to take race-tracking effects in tool radii into account. The example of a locally compacted plate proved that the method works very well for the adjustment of permeabilities based on the compaction state. With the example of the L-profile, the functionality of the orientation transfer and the contact status transfer was demonstrated. The qualitative results of the filling simulations are in good agreement with the behavior found in the literature [30,63]. These examples prove the importance of the integration of the compaction process into a composite manufacturing simulation chain.

7.2 Outlook

Future work on material characterization and validation experiments

The initial comparison of simulation results with the experimental data in Section 5.4 revealed a mismatch of the force response. A difference in the binder activation and an influence of the out-of-plane shear on the compaction stiffness were identified as two possible root causes. In order to gain a deeper understanding of the underlaying mechanisms, more experiments need to be carried out. The influence of binder activation can be analyzed with various preforming temperatures and preform thicknesses. The works form Dickert [272] and Wu et al. [118] suggest that the binder activation temperature has a significant influence on the compaction behavior of preforms. In order to exclude the influence of the tool on the mechanical properties of the preform, the planar test specimens should be produced in the same tool as the curved ones.

Another possible reason for the model deviation for the non-planar preforms is the coupling between the out-of-plane shear and the compaction. The experiments in Section 3.3 showed that the degree of compaction influences the shear stiffness. However, the influence of the lateral ply shift on the compaction response could not be studied.

According to Chen [138], there is a relation between the degree of nesting and the compaction response. Dalfi et al. [273] studied the influence of fabric architecture on the compaction response, concluding that fabrics that allow for more nesting show a different compaction response. Moreover, the number of layers influences the compaction response due to nesting effects [138,274]. The influence of nesting and out-of-plane shear on the compaction stiffness can be studied with two different approaches. One possibility is the experimental analysis of this relation. Fig. 7-1 shows a concept for a device that allows the testing of the compaction response of sheared preforms. A screw on the lower plate enforces a lateral displacement of the plates. An adhesive tape, as used in Section 3.3, transfers the load into the specimen causing shear in thickness direction. Another possibility to investigate the coupling behavior is to apply simulation models on a mesoscopic scale. A validated meso-model, similar to the one proposed by Nguyen et al. [186], allows simple modifications of the lateral shift and the evaluation of the compaction response of various configurations. The derived relation can be transferred to the macroscopic model.
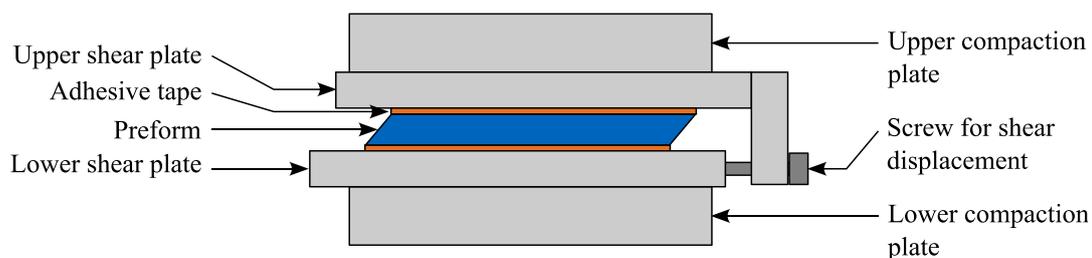
Fig. 7-1:   Concept for an experimental setup for the characterization of the influence of the out-of-plane shear on the compaction behavior.

A characterization of the in-plane compression stiffness can further enhance the model, because the study of material parameters in Section 5.4 showed its significant influence on the compaction response. Similar to the coupled out-of-plane shear compaction, the measurement of the compression stiffness is not straightforward. The main challenge is the possible dependency of the in-plane compression stiffness on the FVC as a higher degree of compaction hinders fibers from bending during in-plane compression.

To further improve the model, it is beneficial to validate the FVC distribution with experimental data. However, the FVC measurement during the compaction experiment is challenging. One option is to use a setup that can be observed with an optical microscope, as suggested by Dong in [71]. However, it is not clear if the resolution of such a setup is enough to measure the FVC. Moreover, it is only possible to see the front surface of the specimen that may be affected by edge effects. Another possibility is to freeze the compaction state by injecting a reactive resin that allows to cut out cross-sections for micrographs after curing. With this method, there are at least two challenges to be overcome. On the one hand, the resin injection probably requires an RTM tool because a

high pressure is needed to reach a complete filling at high FVC. The challenge will be to include the RTM tool in a UTM together with an optical measurement system for the tool displacement. On the other hand, the lubrication effect due to the resin injection may lead to a movement of fibers and fiber bundles affecting local FVC gradients. However, it is possible to repeat the characterization experiments from Chapter 3 using wet material. This will extend the field of application to coupled fluid-mechanical simulations such as CRTM process simulations.

Future improvements of the material model

The through-thickness compaction showed a very good agreement with experimental results for two different materials. However, there was a deviation for the prediction of the spring-back during force-controlled setups. The model can be further improved in order to achieve a higher accuracy for the spring-back prediction after force release. Moreover, the force response experiments showed a dependency on the strain rate when compacted to the same FVC. This behavior cannot be reproduced with the current model. More experiments are necessary to gain a deeper understanding, because the conducted tests did not show an evident relation between strain rate and relaxed stress.

The three-dimensional model can be further improved in multiple ways. One enhancement to the model is a description of the in-plane compression behavior based on experimental data. Another material property that has not been characterized is the in-plane shear stiffness. This is valid as no shear strains appeared for the selected setup with cross-ply layup and single curved preforms. However, in-plane shear stresses will be introduced, if layers with different orientations are added to the layup or if the preform is compacted on a more complex geometry. High in-plane shear strains can cause wrinkles making this property especially important. For this purpose, it is useful to extend the model by including in-plane shear. In addition, it was assumed that all Poisson's ratios can be set to zero. This assumption needs to be verified with experiments or in case a significant strain-strain coupling appears in the experiments, the Poisson's ratios need to be added to the model.

A single layer modeling approach was chosen for the three-dimensional model in order to achieve a higher computational efficiency. However, this reduces the capability of the model to predict effects occurring on ply level such as wrinkles and layer separations. Nevertheless, the main goal of a process simulation is to support in avoiding wrinkles, rather than predicting their exact shape. Thus, it is sufficient to implement a criticality factor, indicating the risk of wrinkles that occur at a specific location. This factor could be based on in-plane shear strains and in-plane compression strains. Moreover, the contact status needs to be considered in order to evaluate whether there is space in the cavity for the formation of wrinkles.

The literature review showed that various fibrous reinforcements including prepregs show the same qualitative behavior. Hence, it is interesting to apply the model to predict the compaction of prepregs and natural fibers.

Outlook on the integration into a complete manufacturing process simulation chain

The methodology developed in Chapter 6 demonstrated that results from compaction simulations can be transferred to a subsequent filling process step. Nevertheless, there is future work to be done in order to integrate further steps on both ends of the process chain.

On the one hand, the thickness measurement revealed that the preforming process leads to a significant thinning in the radius. For the current approach, the thickness was measured and adjusted in a pre-compaction simulation step. This is not feasible for more complex structures where thickness measurements are more complicated. The process simulation method can be enhanced by the simulation of the draping process in order to derive the thickness of the preform before compaction. The draping process can be simulated with the same material model used for compaction. However, it is important that the material properties of stacked layers differ from a preform with activated binder. This requires a repeated material characterization for the model input.

On the other hand, the compaction results can be transferred to simulation steps after the filling simulation. For instance, the results from compaction simulations can be used in a subsequent curing and part distortion simulation. Because local FVC gradients and resin-rich corners have a significant influence on residual stresses, the prediction of part distortions can be improved [28,29]. The transfer of results from compaction simulations into structural simulations is a further extension of the simulation chain. Compared to the transfer of data into the filling simulation, all the further transfers require less effort. As all steps from draping to structural analysis are mechanical simulations, the approach presented in Subsection 5.3.3 for the pre-compaction can be applied.

Another interesting extension of the developed methodology is to have a simultaneous coupling of compaction and infiltration simulation. Contrary to the current sequential approach, this method can be applied to cases where compaction and infiltration happen simultaneously. This is of particular interest for CRTM or VARTM processes, because the infiltration with resin influences the mechanical properties and the thickness of the preform. The method presented by Yang et al. in [275] can be applied to model CRTM processes in ANSYS. For the structural simulation, the material model subroutine developed in Section 5.1 can be applied.

Further application of the model in ongoing research projects

The material model and the process simulation methodology developed in this work is further enhanced within the scope of two ongoing research projects. Both projects aim for the application of the model to more complex geometries making the next step towards an industrial application. The ESKoRT project (Zentrales Innovationsprogramm Mittelstand (ZIM), funding reference KK5135803KP0) addresses the prediction of the compaction state of the demonstrator geometry shown in Fig. 7-2a. The main objective

is to use a validated compaction material model to minimize compaction-related defects based on the findings in Section 5.4. This is achieved by a virtual optimization of the mechanical preform properties and local adaption of the tool-preform friction. On the one hand, a systematic variation of binder content or binder activation temperature can be used to reduce local FVC gradients or to avoid gaps in the tool. On the other hand, local variations of the tool surface by sanding or coating can ensure a desired compaction behavior by changing the friction. The optimization of these material properties will make manufacturing processes more robust by avoiding manufacturing defects.

The FogeLRaP project (ZIM, funding reference KK5135803KP0) aims to predict gaps in the tool after compaction. Using the data transfer into the filling simulation presented in Chapter 6, the influence on the filling behavior can be predicted. The coupled process simulation supports to find an optimal filling strategy for varying preform quality. The integration of sensors in the tool to track the resin front and adaptive inlets and outlets allow to control the filling process. With the database of virtual filling strategies, the pressure in the tool can be adjusted to achieve a complete filling. This method will help to reduce scrap and improve the manufacturing process robustness.

(a)   **(b)**
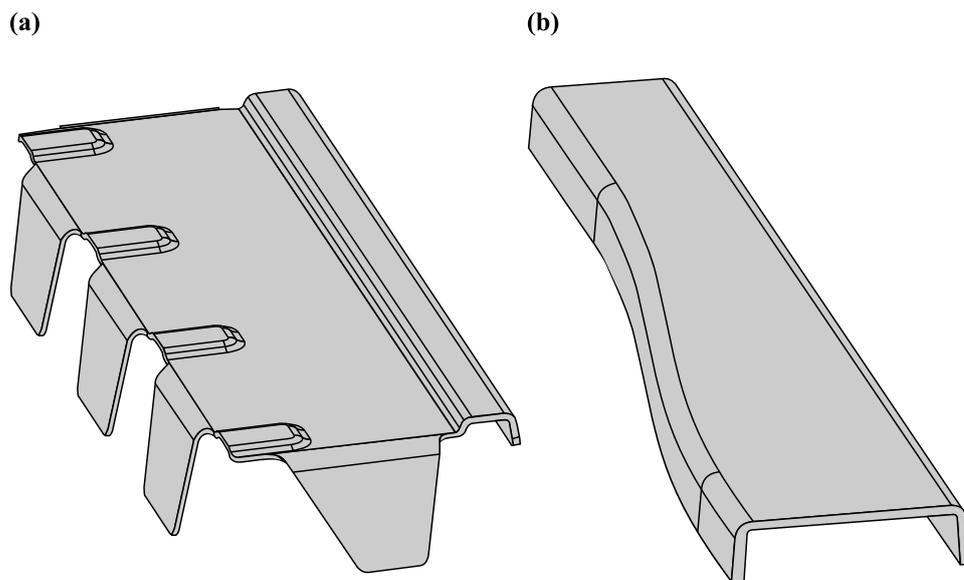
Fig. 7-2:   **Demonstrator parts of follow-up research projects: (a) ZIM project ESKoRT; (b) ZIM FogeLRaP.**

References

[1]   Lee JJ, Lukachko SP, Waitz IA, Schafer A. Historical and Future Trends in Aircraft Performance Cost and Emissions. Annu. Rev. Energy. Environ. 2001;26(1):167–200.

[2]   Federal Aviation Administration FAA. Advanced Materials Research Program. [July 06, 2022]; Available from: https://www.tc.faa.gov/its/cmd/visitors/data/AAR-430/advanced.pdf.

[3]   Murphy K. The Paperless Cockpit. The New York Times July 4th 2011, July 4th 2011; Available from: https://www.nytimes.com/2011/07/05/business/05pilots.html. [July 06, 2022].

[4]   Jaffrey D. American Airlines scraps paper manuals for tablets to cut fuel costs. Reuters; Available from: https://www.reuters.com/article/us-airlines-american-airlines-group-idUSKBN0H600320140911. [July 06, 2022].

[5]   McIlhagger A, Archer E, McIlhagger R (ed.). Polymer Composites in the Aerospace Industry: Elsevier; 2020.

[6]   The Boeing Company. 787 Airplane Characteristics for Airport Planning. [July 06, 2022]; Available from: https://www.boeing.com/resources/boeingdotcom/commercial/airports/acaps/787.pdf.

[7]   European Commission and Directorate-General for Mobility and Transport and Directorate-General for Research and Innovation. Flightpath 2050 Europe's vision for aviation maintaining global leadership and serving society's needs: Publications Office; 2012.

[8]   Smith F. The Use of composites in aerospace: Past, present and future challenges; 2013.

[9]   United States Government General Accountability Office. Aviations safety: status of FAA's actions to oversee the safety of composite airplanes.: Report to Congressional Requesters GAO-11-849; 2011.

[10]   Slayton R, Spinardi G. Radical innovation in scaling up: Boeing's Dreamliner and the challenge of socio-technical transitions. Technovation 2016;47(7):47–58.

[11]   Meola C, Boccardi S, Carlomagno Gm. Composite Materials in the Aeronautical Industry. In: Meola C, Boccardi S, editors. Infrared Thermography in the Evaluation of Aerospace Composite Materials: Elsevier; 2017, p. 1–24.

[12]   Sloan J. Exelis wins center wingbox strut contract for Airbus A350-1000. [July 06, 2022]; Available from: https://www.compositesworld.com/articles/exelis-wins-center-wingbox-strut-contract-for-airbus-a350-1000.

[13]   Roth YC, Weinholdt, M., Winkelmann, L. Liquid Composite Moulding – Enabler for the Automated Production of CFRP Aircraft Components. Seville, Spain; 2014.

[14]   Lengsfeld H. Composite technology: Prepregs and monolithic part fabrication technologies. Munich, Cincinnati: Hanser Publications; Hanser Publishers; 2016&#x5d.

[15]   Airbus Group. Global Market Forecast 2021 - 2024. [July 06, 2022]; Available from: https://www.airbus.com/sites/g/files/jlcbta136/files/2021-11/Airbus-Global-Market-Forecast-2021-2040.pdf.

[16]   Eiselin S. Airbus tritt bei A320-Produktion wieder aufs Gaspedal. [July 06, 2022]; Available from: https://www.aerotelegraph.com/airbus-tritt-bei-a320-produktion-wieder-aufs-gaspedal.

[17]   Hexcel. HexPly M21 Product Data; 2007.

[18]   Gardinger G. Resin transfer molding: An update: Fulfilling the promise of OOA composites without sacrificing pressure. [August 14, 2020]; Available from: https://www.compositesworld.com/articles/resin-transfer-molding-an-update.

[19]   Sloan J. High-rate, automated aerospace RTM line delivers next-gen spoilers. [August 20, 2020]; Available from: https://www.compositesworld.com/articles/high-rate-automated-aerospace-rtm-line-delivers-next-gen-spoilers.

[20]   Sendner F.-M. Schneiderbauer G. Advanced Multicell Flap': Ein One-Shot Fertigungsansatz für hochintegrale Landeklappen in RTM Technologie. Munich, Germany; 2021.

[21]   Nehls G. Spirit AeroSystems Europe delivers first set of A320 Family RTM spoilers. [May 07, 2022]; Available from: https://www.compositesworld.com/news/spirit-aerosystems-europe-delivers-first-set-of-a320-family-rtm-spoilers.

[22]   Mason H. Airbus begins assembly of first Wing of Tomorrow prototype: The program brings together more than 100 new technologies and composites innovations, including delivery of the first fixed trailing edge by GKN Aerospace. [June 30, 2022]; Available from: https://www.compositesworld.com/news/airbus-assembles-first-wing-of-tomorrow-prototype.

[23]   Balasubramanian K, Sultan MTH, Rajeswari N. Manufacturing techniques of composites for aerospace applications. In: Sustainable Composites for Aerospace Applications: Elsevier; 2018, p. 55–67.

[24]   Hammami A, Gauvin R, Trochu F, Touret O, Ferland P. Analysis of the Edge Effect on Flow Patterns in Liquid Composites Molding. Appl Compos Mater 1998;5(3):161–73.

[25] Siddig NA, Binetruy C, Syerko E, Simacek P, Advani S. A new methodology for race-tracking detection and criticality in resin transfer molding process using pressure sensors. Journal of Composite Materials 2018;52(29):4087–103.

[26] Mesogitis TS, Skordos AA, Long AC. Uncertainty in the manufacturing of fibrous thermosetting composites: A review. Composites Part A: Applied Science and Manufacturing 2014;57(5):67–75.

[27] Li J, Zhang C, Liang R, Wang B. Statistical characterization and robust design of RTM processes. Composites Part A: Applied Science and Manufacturing 2005;36(5):564–80.

[28] Radford DW. Volume fraction gradient induced warpage in curved composite plates. Composites Engineering 1995;5(7):923–34.

[29] Brauner C, Bauer S, Herrmann AS. Analysing process-induced deformation and stresses using a simulated manufacturing process for composite multispar flaps. Journal of Composite Materials 2015;49(4):387–402.

[30] Bickerton S, Sozer EM, Graham PJ, Advani SG. Fabric structure and mold curvature effects on preform permeability and mold filling in the RTM process. Part I. Experiments. Composites Part A: Applied Science and Manufacturing 2000;31(5):423–38.

[31] Liu B, Bickerton S, Advani SG. Modelling and simulation of resin transfer moulding (RTM)—gate control, venting and dry spot prediction. Composites Part A: Applied Science and Manufacturing 1996;27(2):135–41.

[32] Advani SG, Sozer EM. Process modeling in composites manufacturing. New York, NY: Marcel Dekker; 2002.

[33] Mayer N, Prowe J, Havar T, Hinterhölzl R, Drechsler K. Structural analysis of composite components considering manufacturing effect. Composite Structures 2016;140(1):776–82.

[34] Dix M, Beck S, Repper A, Hinterhölzl R. Integrierte Materialmodellierung für die CFK-Prozesssimulation. Lightweight Des 2013;6(5):24–9.

[35] ESI Group. PAM-COMPOSITES. [July 07, 2022]; Available from: https://www.esi-group.com/products/composites.

[36] Long AC (ed.). Design and manufacture of textile composites. Cambridge, Boca Raton: Woodhead; 2005.

[37] Gutowski TGP (ed.). Advanced composites manufacturing. New York, NY: Wiley; 1997.

[38] Vita A, Castorani V, Germani M, Marconi M. Comparative life cycle assessment of low-pressure RTM, compression RTM and high-pressure RTM manufacturing processes to produce CFRP car hoods. Procedia CIRP 2019;80:352–7.

[39] Svanberg JM., Holmberg AJ. Prediction of shape distortions Part I. FE-imple-
      mentation of a path dependent constitutive model. Composites Part A: Applied
      Science and Manufacturing 2004;35(6):711–21.

[40] Saseendran S, Berglund D, Varna J. Viscoelastic model with complex rheologi-
      cal behavior (VisCoR): incremental formulation. Advanced Manufacturing: Pol-
      ymer & Composites Science 2020;107:1–16.

[41] Brauner C, Peters C, Brandwein F, Herrmann AS. Analysis of process-induced
      deformations in thermoplastic composite materials. Journal of Composite Mate-
      rials 2014;48(22):2779–91.

[42] Groh F, Kappel E, Hühne C, Brymerski W. Investigation of fast curing epoxy
      resins regarding process induced distortions of fibre reinforced composites.
      Composite Structures 2019;207:923–34.

[43] Laurenzi S, Marchetti M. Advanced Composite Materials by Resin Transfer
      Molding for Aerospace Applications. In: Hu N, editor. Composites and Their
      Properties: InTech; 2012.

[44] Miranda Campos B, Bourbigot S, Fontaine G, Bonnet F. Thermoplastic matrix-
      based composites produced by resin transfer molding: A review. Polym. Com-
      pos. 2022;43(5):2485–506.

[45] Mallick PK. Thermoplastics and thermoplastic–matrix composites for light-
      weight automotive structures. In: Materials, Design and Manufacturing for
      Lightweight Vehicles: Elsevier; 2010, p. 174–207.

[46] Jayasekara D, Lai NYG, Wong K-H, Pawar K, Zhu Y. Level of automation
      (LOA) in aerospace composite manufacturing: Present status and future direc-
      tions towards industry 4.0. Journal of Manufacturing Systems 2022;62:44–61.

[47] Holmes M. High volume composites for the automotive challenge. Reinforced
      Plastics 2017;61(5):294–8.

[48] Fernberg P, Gong G, Mannberg P, Tsampas S. Development of novel high Tg
      polyimide-based composites. Part I: RTM processing properties. Journal of
      Composite Materials 2018;52(2):253–60.

[49] Tsampas S, Fernberg P, Joffe R. Development of novel high T g polyimide-
      based composites. Part II: Mechanical characterisation. Journal of Composite
      Materials 2018;52(2):261–74.

[50] Ageyeva T, Sibikin I, Kovács JG. A Review of Thermoplastic Resin Transfer
      Molding: Process Modeling and Simulation. Polymers 2019;11(10).

[51] Hamidi YK, Altan CM. 2.5 Process-Induced Defects in Resin Transfer Molded
      Composites. In: Comprehensive Composite Materials II: Elsevier; 2018, p. 95–
      106.

[52] Dong C. Experimental investigation on the fiber preform deformation due to mold closure for composites processing. Int J Adv Manuf Technol 2014;71(1-4):585–91.

[53] Menta V, Vuppalapati R, Chandrashekhara K, Schuman T, Sha J. Elevated-temperature vacuum-assisted resin transfer molding process for high performance aerospace composites. Polym. Int 2013;62(10):1465–76.

[54] Veers PS, Ashwill TD, Sutherland HJ, Laird DL, Lobitz DW, Griffin DA et al. Trends in the Design, Manufacture and Evaluation of Wind Turbine Blades. Wind Energ. 2003;6(3):245–59.

[55] Harismendy I, Del Río M, Edu Ruiz, Garcí JA. Modelling VARTM of Wind Turbine Blades under non-isothermal Boundary Conditions. Montréal (Québec), Canada; 2008.

[56] Causse P, Ruiz E, Trochu F. Influence of preforming on the quality of curved composite parts manufactured by flexible injection. Int J Mater Form 2013;6(3):341–62.

[57] Hsiao K-T, Heider D. Vacuum assisted resin transfer molding (VARTM) in polymer matrix composites. In: Advani SG, Hsiao K-T, editors. Manufacturing Techniques for Polymer Matrix Composites (PMCs): Compression resin transfer moulding (CRTM) in polymer matrix composites. Sawston, United Kingdom: Woodhead Publishing Ltd; 2012, p. 310–47.

[58] Gardinger G. The path to OOA wings with minimal fasteners: A review of the quest to eliminate both the autoclave and mechanical fasteners in composite wing structures. [February 15, 2022].

[59] Li J, Zhang C, Liang R, Wang B, Walsh S. Modeling and analysis of thickness gradient and variations in vacuum-assisted resin transfer molding process. Polym. Compos. 2008;29(5):473–82.

[60] Tackitt KD, Walsh SM. Experimental Study of Thickness Gradient Formation in the VARTM Process. Materials and Manufacturing Processes 2005;20(4):607–27.

[61] Holmberg JA, Berglund LA. Manufacturing and performance of RTM U-beams. Composites Part A: Applied Science and Manufacturing 1997;28(6):513–21.

[62] Dong CS, Tsai TC. Formation of Resin-Rich Zones in Composites Processing. AMR 2010;123-125:543–6.

[63] Koutsonas S. Modelling race-tracking variability of resin rich zones on 90° composite 2.2 twill fibre curved plate. Composites Science and Technology 2018;168:448–59.

[64] Devillard M, Hsiao K-T, Gokce A, Advani SG. On-Line Characterization of Bulk Permeability and Race-Tracking During the Filling Stage in Resin Transfer Molding Process. Journal of Composite Materials 2003;37(17):1525–41.

[65] Zaremba S. Bypassströmungen im Füllprozess textiler Strukturen: Charakterisierung, Abbildung und Optimierung. Doctoral dissertation, Technische Universität München. München: Dr. Hut; 2018.

[66] Hsiao K-T, Advani SG. Flow sensing and control strategies to address race-tracking disturbances in resin transfer molding. Part I: design and algorithm development. Composites Part A: Applied Science and Manufacturing 2004;35(10):1149–59.

[67] Bickerton S, Advani SG, Mohan RV, Shires DR. Experimental analysis and numerical modeling of flow channel effects in resin transfer molding. Polym. Compos. 2000;21(1):134–53.

[68] Potter K. Understanding the Origins of Defects and Variability in Composites Manufacture. Proceedings of ICCM17 - 17th International Conference on Composite Materials, Edinburgh, United Kingdom 2009.

[69] Walbran WA, Bickerton S, Kelly PA. Evaluating the shear component of reinforcement compaction stress during liquid composite moulding processes. Journal of Composite Materials 2013;47(5):513–28.

[70] Walbran WA, Bickerton S, Kelly PA. Simulation and experimental validation of mould tooling forces in RTM and CRTM for nonplanar components. Polym. Compos. 2015;36(4):591–603.

[71] Dong C. Model development for the formation of resin-rich zones in composites processing. Composites Part A: Applied Science and Manufacturing 2011;42(4):419–24.

[72] Koutsonas S. Compaction and bending variability measurements of a novel geometry 3D woven layer to layer interlock composite textile around a 90° curve plate 3.2 mm radius. Composites Communications 2017;5:40–5.

[73] Fong L, Xu J, James Lee L. Performing analysis of thermoformable glass fiber mats—deformation modes and reinforcement characterization. Polym. Compos. 1994;15(2):134–46.

[74] Bickerton S, Advani SG. Experimental investigation and flow visualization of the resin-transfer mold-filling process in a non-planar geometry. Composites Science and Technology 1997;57(1):23–33.

[75] Jain LK, Lutton BG, Mai Y-W, Paton R. Stresses and Deformations Induced during Manufacturing. Part II: A Study of the Spring-in Phenomenon. Journal of Composite Materials 1997;31(7):696–719.

[76] Brauner C, Pereira GC, Herrmann AS. Effects of fabric-based unbalances on process-induced distortions of composite materials. Journal of Composite Materials 2015;49(11):1291–300.

[77] Causse P, Ruiz E, Trochu F. Spring-in behavior of curved composites manufactured by Flexible Injection. Composites Part A: Applied Science and Manufacturing 2012;43(11):1901–13.

[78] Hamidi YK, Altan MC. Process Induced Defects in Liquid Molding Processes of Composites. International Polymer Processing 2017;32(5):527–44.

[79] Karahan M. The effect of fibre volume fraction on damage initiation and propagation of woven carbon-epoxy multi-layer composites. Textile Research Journal 2012;82(1):45–61.

[80] Khan B, Potter K, Wisnom M. Simulation of Process Induced Defects in Resin Transfer Moulded Woven Carbon Fiber Laminates and Their Effect on Mechanical Behaviour. Proceedings of 8th FPCM - The 8th International Conference on Flow Processes in Composite Material, Douai, France 2006.

[81] Geng Y, Jiang J, Chen N. Local impregnation behavior and simulation of non-crimp fabric on curved plates in vacuum assisted resin transfer molding. Composite Structures 2019;208:517–24.

[82] Cauberghs H. Effect of Tight Corners and Ply Terminations on Quality in Out-of-Autoclave Part.

[83] Ma Y, Centea T, Nutt SR. Defect reduction strategies for the manufacture of contoured laminates using vacuum BAG-only prepregs. Polym. Compos. 2017;38(9):2016–25.

[84] Feih S, Shercliff HR. Quality assessment of curved composite components in peel joint structures. Composites Part A: Applied Science and Manufacturing 2005;36(3):397–408.

[85] Hassan MH. A mini review on manufacturing defects and performance assessments of complex shape prepreg-based composites. Int J Adv Manuf Technol 2021;115(11-12):3393–408.

[86] Hassan MH, Othman AR, Kamaruddin S. A review on the manufacturing defects of complex-shaped laminate in aircraft composite structures. Int J Adv Manuf Technol 2017;91(9-12):4081–94.

[87] Hubert P, Poursartip A. Aspects of the Compaction of Composite Angle Laminates: An Experimental Investigation. Journal of Composite Materials 2001;35(1):2–26.

[88] Levy A, Hubert P. Vacuum-bagged composite laminate forming processes: Predicting thickness deviation in complex shapes. Composites Part A: Applied Science and Manufacturing 2019;126(4):105568.

[89] Hubert P, Schubert J, Bickerton S, Hickey C. Towards a design guideline for corners in composite parts. Proceedings of ICCM21 - International Conferences on Composite Materials;2017.

[90] Lightfoot JS, Wisnom MR, Potter K. A new mechanism for the formation of ply wrinkles due to shear between plies. Composites Part A: Applied Science and Manufacturing 2013;49:139–47.

[91] Li Y, Li M, Gu Y, Zhang Z. Numerical and Experimental Study on the Effect of Lay-Up Type and Structural Elements on Thickness Uniformity of L-Shaped Laminates. Appl Compos Mater 2009;16(2):101–15.

[92] Belnoue JP-H, Nixon-Pearson OJ, Thompson AJ, Ivanov DS, Potter KD, Hallett SR. Consolidation-Driven Defect Generation in Thick Composite Parts. Journal of Manufacturing Science and Engineering 2018;140(7):1343.

[93] Baran I, Cinar K, Ersoy N, Akkerman R, Hattel JH. A Review on the Mechanical Modeling of Composite Manufacturing Processes. Archives of computational methods in engineering state of the art reviews 2017;24(2):365–95.

[94] Svanberg JM., Hallander P NT. Variation in Shape Distortion due to Corner Thinning/Thickenning of Prepreg. Edinburgh, United Kingdom; 2019.

[95] Oakeshott JL. Warpage of carbon–epoxy composite channels. Plastics, Rubber and Composites 2003;32(3):104–13.

[96] Hubert P, Vaziri R, Poursartip A. A two-dimensional flow model for the process simulation of complex shape composite laminates. Int. J. Numer. Meth. Engng. 1999;44(1):1–26.

[97] Li M, Tucker CL. Modeling and simulation of two-dimensional consolidation for thermoset matrix composites. Composites Part A: Applied Science and Manufacturing 2002;33(6):877–92.

[98] Mezeix L, Seman A, Nasir MNM, Aminanda Y, Rivai A, Castanié B et al. Spring-back simulation of unidirectional carbon/epoxy flat laminate composite manufactured through autoclave process. Composite Structures 2015;124:196–205.

[99] Twigg G. An experimental method for quantifying tool–part shear interaction during composites processing. Composites Science and Technology 2003;63(13):1985–2002.

[100] Ma Y, Centea T, Nilakantan G, Nutt SR. Vacuum Bag Only Processing of Complex Shapes: Effect of Corner Angle, Material Properties and Processing Conditions. San Diego, CA, United States; 2014.

[101] Darrow DA, Smith LV. Isolating Components of Processing Induced Warpage in Laminated Composites. Journal of Composite Materials 2002;36(21):2407–19.

[102] Wiersma HW, Peeters LJB, Akkerman R. Prediction of springforward in continuous-fibre/polymer L-shaped parts. Composites Part A: Applied Science and Manufacturing 1998;29(11):1333–42.

[103] Huang CK, Yang SY. Warping in advanced composite tools with varying angles and radii. Composites Part A: Applied Science and Manufacturing 1997;28(9-10):891–3.

[104] Potter K, Khan B, Wisnom M, Bell T, Stevens J. Variability, fibre waviness and misalignment in the determination of the properties of composite materials and structures. Composites Part A: Applied Science and Manufacturing 2008;39(9):1343–54.

[105] Sousa P, Lomov SV, Ivens J. Methodology of dry and wet compressibility measurement. Composites Part A: Applied Science and Manufacturing 2020;128:105672.

[106] Kabachi MA, Danzi M, Arreguin S, Ermanni P. Experimental study on the influence of cyclic compaction on the fiber-bed permeability, quasi-static and dynamic compaction responses. Composites Part A: Applied Science and Manufacturing 2019;125:105559.

[107] Danzi M, Schneeberger C, Ermanni P. A model for the time-dependent compaction response of woven fiber textiles. Composites Part A: Applied Science and Manufacturing 2018;105:180–8.

[108] Grieser T, Mitschang P. Investigation of the compaction behavior of carbon fiber NCF for continuous preforming processes. Polym. Compos. 2017;38(11):2609–25.

[109] Lee SH, Han JH, Kim SY, Youn JR, Song YS. Compression and Relaxation Behavior of Dry Fiber Preforms for Resin Transfer Molding. Journal of Composite Materials 2010;44(15):1801–20.

[110] Somashekar AA, Bickerton S, Bhattacharyya D. An experimental investigation of non-elastic deformation of fibrous reinforcements in composites manufacturing. Composites Part A: Applied Science and Manufacturing 2006;37(6):858–67.

[111] Chen B, Cheng AH-D, Chou T-W. A nonlinear compaction model for fibrous preforms. Composites Part A: Applied Science and Manufacturing 2001;32(5):701–7.

[112] Kabachi MA, Stettler L, Arreguin S, Ermanni P. Concurrent characterization of through-thickness permeability and compaction of fiber reinforcements. Composites Part A: Applied Science and Manufacturing 2021;141(9):106203.

[113] Yong AXH, Aktas A, May D, Endruweit A, Lomov SV, Advani S et al. Experimental characterisation of textile compaction response: A benchmark exercise. Composites Part A: Applied Science and Manufacturing 2021;142(4):106243.

[114] Bublitz D, Colin D, Drechsler K. Implementation of a viscoelastic material model to predict the compaction response of dry carbon fiber preforms. Composites Part A: Applied Science and Manufacturing 2021.

[115] Robitaille F, Gauvin R. Compaction of textile reinforcements for composites manufacturing. I: Review of experimental results. Polym. Compos. 1998;19(2):198–216.

[116] Bickerton S, Kelly PA. Modelling the Viscoelastic Compression Behaviour of Fibrous Reinforcing Fabrics. Baltimore; 2002.

[117] Kim YR, McCarthy SP, Fanucci JP. Compressibility and relaxation of fiber reinforcements during composite processing. Polym. Compos. 1991;12(1):13–9.

[118] Wu W, Jiang B, Xie L, Klunker F, Aranda S, Ziegmann G. Effect of Compaction and Preforming Parameters on the Compaction Behavior of Bindered Textile Preforms for Automated Composite Manufacturing. Appl Compos Mater 2013;20(5):907–26.

[119] Kelly PA, Umer R, Bickerton S. Viscoelastic response of dry and wet fibrous materials during infusion processes. Composites Part A: Applied Science and Manufacturing 2006;37(6):868–73.

[120] Mbakop RS, Lebrun G, Brouillette F. Experimental analysis of the planar compaction and preforming of unidirectional flax reinforcements using a thin paper or flax mat as binder for the UD fibers. Composites Part A: Applied Science and Manufacturing 2018;109:604–14.

[121] Yenilmez B, Caglar B, Sozer EM. Pressure-controlled compaction characterization of fiber preforms suitable for viscoelastic modeling in the vacuum infusion process. Journal of Composite Materials 2017;51(9):1209–24.

[122] Graupner R, Drechsler K. Quantitative transversal permeability testing-challenges and enhancements. Proceedings of 14th Iinternational Conference on Flow Processing in Composite Materials 2018.

[123] May D, Kühn F, Etchells M, Fauster E, Endruweit A, Lira C. A reference specimen for compaction tests of fiber reinforcements. Advanced Manufacturing: Polymer & Composites Science 2019;5(4):230–3.

[124] Bickerton S, Buntain MJ, Somashekar AA. The viscoelastic compression behavior of liquid composite molding preforms. Composites Part A: Applied Science and Manufacturing 2003;34(5):431–44.

[125] Chen B, Lang EJ, Chou T-W. Experimental and theoretical studies of fabric compaction behavior in resin transfer molding. Materials Science and Engineering: A 2001;317(1-2):188–96.

[126] Wei K, Liang D, Mei M, Wang D, Yang X, Qu Z. Preforming behaviors of carbon fiber fabrics with different contents of binder and under various process parameters. Composites Part B: Engineering 2019;166:221–32.

[127] Francucci G, Rodríguez ES, Vázquez A. Experimental study of the compaction response of jute fabrics in liquid composite molding processes. Journal of Composite Materials 2012;46(2):155–67.

[128] Salit MS, Jawaid M, Yusoff NB, Hoque ME. Manufacturing of Natural Fibre Reinforced Polymer Composites. Cham: Springer International Publishing; 2015.

[129] Hautefeuille A, Comas-Cardona S, Binetruy C. Consolidation and compression of deformable impregnated fibrous reinforcements: Experimental study and modeling of flow-induced deformations. Composites Part A: Applied Science and Manufacturing 2020;131(4):105768.

[130] Buntain MJ, Bickerton S. Modeling forces generated within rigid liquid composite molding tools. Part A: Experimental study. Composites Part A: Applied Science and Manufacturing 2007;38(7):1729–41.

[131] Hubert P, Poursartip A. A method for the direct measurement of the fibre bed compaction curve of composite prepregs. Composites Part A: Applied Science and Manufacturing 2001;32(2):179–87.

[132] Gutowski TG, Dillon G. The Elastic Deformation of Lubricated Carbon Fiber Bundles: Comparison of Theory and Experiments. Journal of Composite Materials 1992;26(16):2330–47.

[133] Hall C, Ward C, Ivanov DS, Potter K. The Compaction of uncured toughened Prepreg Laminates in Relation to automated Forming. Proceedings of ECCM15 - 15th European Conference on Composite Materials 2012;2012.

[134] Lukaszewicz DH-JA, Potter K. Through-thickness compression response of uncured prepreg during manufacture by automated layup. Proceedings of the Institution of Mechanical Engineers, Part B: Journal of Engineering Manufacture 2012;226(2):193–202.

[135] Nixon-Pearson OJ, Belnoue J-H, Ivanov DS, Potter KD, Hallett SR. An experimental investigation of the consolidation behaviour of uncured prepregs under processing conditions. Journal of Composite Materials 2017;51(13):1911–24.

[136] Yang X, Wang Y, Mo F, Wei K, Duan S. Characterization of nesting effects on compression processes for plain woven fabrics in composites manufacturing. Journal of Reinforced Plastics and Composites 2017;36(20):1503–13.

[137] Potluri P, Sagar TV. Compaction modelling of textile preforms for composite structures. Composite Structures 2008;86(1-3):177–85.

[138] Chen B. Compaction of woven-fabric preforms: nesting and multi-layer deformation. Composites Science and Technology 2000;60(12-13):2223–31.

[139] Saunders RA, Lekakou C, Bader MG. Compression and microstructure of fibre plain woven cloths in the processing of polymer composites. Composites Part A: Applied Science and Manufacturing 1998;29(4):443–54.

[140] Robitaille F, Gauvin R. Compaction of textile reinforcements for composites manufacturing. III: Reorganization of the fiber network. Polym. Compos. 1999;20(1):48–61.

[141] Bréard J, Henzel Y, Trochu F, Gauvin R. Analysis of dynamic flows through porous media. Part II: Deformation of a double-scale fibrous reinforcement. Polym. Compos. 2003;24(3):409–21.

[142] Gras R, Leclerc H, Roux S, Otin S, Schneider J, Périé J-N. Identification of the Out-of-Plane Shear Modulus of a 3D Woven Composite. Exp Mech 2013;53(5):719–30.

[143] ASTM D2344/D2344M. Standard Test Method for Short-Beam Strength of Polymer Matrix Composite Materials and Their Laminates.

[144] DIN EN ISO 14125:2011-05. Fibre-reinforced plastic composites - Determination of flexural properties.

[145] Fan Z, Santare MH, Advani SG. Interlaminar shear strength of glass fiber reinforced epoxy composites enhanced with multi-walled carbon nanotubes. Composites Part A: Applied Science and Manufacturing 2008;39(3):540–54.

[146] Zahid S, Nasir MA, Nauman S, Karahan M, Nawab Y, Ali HM et al. Experimental analysis of ILSS of glass fibre reinforced thermoplastic and thermoset textile composites enhanced with multiwalled carbon nanotubes. J Mech Sci Technol 2019;33(1):197–204.

[147] Rosselli F, Santare MH. Comparison of the short beam shear (SBS) and interlaminar shear device (ISD) tests. Composites Part A: Applied Science and Manufacturing 1997;28(6):587–94.

[148] Schneider K, Lauke B, Beckert W. Compression Shear Test (CST) – A Convenient Apparatus for the Estimation of Apparent Shear Strength of Composite Materials. Appl Compos Mater 2001;8(1):43–62.

[149] ISO 1922:2018. Rigid cellular plastics — Determination of shear properties;83.100 Cellular materials.

[150] Cognard J-Y, Davies P, Sohier L. Advances in testing adhesively bonded composites. In: Cognard J-Y, editor. Advances in Structural Adhesive Bonding: Elsevier; 2010, p. 437–65.

[151] Lancaster JF. The use of adhesives for making structural joints. In: Metallurgy of Welding: Elsevier; 1999, p. 54–84.

[152] Duncan B. Developments in testing adhesive joints. In: Cognard J-Y, editor. Advances in Structural Adhesive Bonding: Elsevier; 2010, p. 389–436.

[153] Popov VL. Kontaktmechanik und Reibung. Berlin, Heidelberg: Springer Berlin Heidelberg; 2015.

[154] DIN EN 14882:2005-11, Mit Kautschuk oder Kunststoff beschichtete Textilien_-Bestimmung der Koeffizienten von Haftreibung und Bewegungsreibung; Deutsche Fassung EN_14882:2005. Berlin: Beuth Verlag GmbH. doi:10.31030/9626405.

[155] ASTM. ASTM 1894-01Test Method for Static and Kinetic Coefficients of Friction of Plastic Film and Sheeting. West Conshohocken, PA: ASTM International. doi:10.1520/D1894-01.

[156] Margossian A. Forming of tailored thermoplastic composite blanks. Doctoral dissertation, Technische Universität München. Munich: Dr. Hut; 2017.

[157] Colin D. Virtual development of non-crimp fabrics: numerical textile description at the scale of the filaments and forming simulation. Doctoral dissertation, Technische Universität München. Munich: Dr. Hut; 2022.

[158] Park JS, Lee SM, Joo BS, Jang H. The effect of material properties on the stick–slip behavior of polymers: A case study with PMMA, PC, PTFE, and PVC. Wear 2017;378-379:11–6.

[159] Gupta BS, Ajayi JO, Kutsenko M. Experimental methods for analyzing friction in textiles. In: Friction in Textile Materials: Elsevier; 2008, p. 174–221.

[160] Leutz DM. Forming simulation of AFP material layups. Doctoral dissertation, Technische Universität München. Munich: Dr. Hut; 2016.

[161] Najjar W, Pupin C, Legrand X, Boude S, Soulat D, Dal Santo P. Analysis of frictional behaviour of carbon dry woven reinforcement. Journal of Reinforced Plastics and Composites 2014;33(11):1037–47.

[162] Akkerman R.,Ubbink M. P. ,de Rooij M. B. and ten Thije R. H. W. Tool-Ply Friction In Composite Forming. In: AIP Conference Proceedings, Zaragoza (Spain), Apr. 2007, pp. 1080–1085.

[163] Thije RHW ten, Akkerman R, Ubbink M, van der Meer L. A lubrication approach to friction in thermoplastic composites forming processes. Composites Part A: Applied Science and Manufacturing 2011;42(8):950–60.

[164] DIN. DIN EN ISO 13934-1:2013-08, Textilien_- Zugeigenschaften von textilen Flächengebilden_- Teil_1: Bestimmung der Höchstzugkraft und Höchstzugkraft-Dehnung mit dem Streifen-Zugversuch (ISO_13934-1:2013); Deutsche Fassung EN_ISO_13934-1:2013. Berlin: Beuth Verlag GmbH. doi:10.31030/2017288.

[165] Cherif C. Textile Werkstoffe für den Leichtbau: Techniken - Verfahren - Materialien - Eigenschaften. Berlin, Heidelberg: Springer-Verlag Berlin Heidelberg; 2011.

[166] Syerko E, Comas-Cardona S, Binetruy C. Models of mechanical properties/behavior of dry fibrous materials at various scales in bending and tension: A review. Composites Part A: Applied Science and Manufacturing 2012;43(8):1365–88.

[167] Cao J, Akkerman R, Boisse P, Chen J, Cheng HS, Graaf EF de et al. Characterization of mechanical behavior of woven fabrics: Experimental methods and benchmark results. Composites Part A: Applied Science and Manufacturing 2008;39(6):1037–53.

[168] Sharma SB, Sutcliffe MPF, Chang SH. Characterisation of material properties for draping of dry woven composite material. Composites Part A: Applied Science and Manufacturing 2003;34(12):1167–75.

[169] Syerko E, Comas-Cardona S, Binetruy C. Models for shear properties/behavior of dry fibrous materials at various scales: a review. Int J Mater Form 2015;8(1):1–23.

[170] Schürmann H. Konstruieren mit Faser-Kunststoff-Verbunden. 2nd ed. Berlin, Heidelberg: Springer-Verlag Berlin Heidelberg; 2007.

[171] Penava, Ž., D. Penava, Ž. Knezić. Influence kinds of materials on the poisson's ratio of woven fabrics. Vela Luka, Kroatia; 2017.

[172] Sun H, Pan N, Postle R. On the Poisson's ratios of a woven fabric. Composite Structures 2005;68(4):505–10.

[173] Dixit A, Mali HS, Misra RK. Unit Cell Model of Woven Fabric Textile Composite for Multiscale Analysis. Procedia Engineering 2013;68:352–8.

[174] Bednarcyk BA, Stier B, Simon J-W, Reese S, Pineda EJ. Meso- and micro-scale modeling of damage in plain weave composites. Composite Structures 2015;121(8):258–70.

[175] van Wyk CM. Note on the Compressebility of Wool. Journal of the Textile Institute Transactions 1946;37(12):T285-T292.

[176] Green SD, Long AC, El Said BSF, Hallett SR. Numerical modelling of 3D woven preform deformations. Composite Structures 2014;108:747–56.

[177] Thompson AJ, El Said B, Ivanov D, Belnoue JP-H, Hallett SR. High fidelity modelling of the compression behaviour of 2D woven fabrics. International Journal of Solids and Structures 2018;154:104–13.

[178] Durville D, Baydoun I, Moustacas H, Périé G, Wielhorski Y. Determining the initial configuration and characterizing the mechanical properties of 3D angle-interlock fabrics using finite element simulation. International Journal of Solids and Structures 2018;154(8):97–103.

[179] Colin D, Bel S, Hans T, Hartmann M, Drechsler K. Virtual Description of Non-Crimp Fabrics at the Scale of Filaments Including Orientation Variability in the Fibrous Layers. Appl Compos Mater 2020;27(4):337–55.

[180] Chen Z-R, Ye L, Kruckenberg T. A micromechanical compaction model for woven fabric preforms. Part I: Single layer. Composites Science and Technology 2006;66(16):3254–62.

[181] Chen Z-R, Ye L. A micromechanical compaction model for woven fabric preforms. Part II: Multilayer. Composites Science and Technology 2006;66(16):3263–72.

[182] Jeong YJ, Kang TJ. Analysis of Compressional Deformation of Woven Fabric Using Finite Element Method. Journal of the Textile Institute 2001;92(1):1–15.

[183] Sherburn M. Geometric and Mechanical Modelling of Textiles: Doctoral dissertation, University of Nottingham. Nottingham; 2007.

[184] Grail G, Hirsekorn M, Wendling A, Hivet G, Hambli R. Consistent Finite Element mesh generation for meso-scale modeling of textile composites with preformed and compacted reinforcements. Composites Part A: Applied Science and Manufacturing 2013;55:143–51.

[185] Lin H, Sherburn M, Crookston J, Long AC, Clifford MJ, Jones IA. Finite element modelling of fabric compression. Journal of the Textile Institute 2008;16(3):35010.

[186] Nguyen QT, Vidal-Sallé E, Boisse P, Park CH, Saouab A, Bréard J et al. Mesoscopic scale analyses of textile composite reinforcement compaction. Composites Part B: Engineering 2013;44(1):231–41.

[187] Sirtautas J, Pickett AK, Lépicier P. A mesoscopic model for coupled drape-infusion simulation of biaxial Non-Crimp Fabric. Composites Part B: Engineering 2013;47(6–7):48–57.

[188] Wijaya W, Bickerton S, Kelly PA. Meso-scale compaction simulation of multilayer 2D textile reinforcements: A Kirchhoff-based large-strain non-linear elastic

constitutive tow model. Composites Part A: Applied Science and Manufacturing 2020;137:106017.

[189] Bertram A (ed.). Elasticity and Plasticity of Large Deformations. Cham: Springer International Publishing; 2021.

[190] Nasdala L (ed.). FEM-Formelsammlung Statik und Dynamik. Wiesbaden: Vieweg+Teubner Verlag; 2012.

[191] Hooke R. ut tensio, sic vis; sic vis. 1678.

[192] Brinson HF, Brinson LC. Polymer engineering science and viscoelasticity: An introduction. Boston, MA: Springer; 2008.

[193] Shaw MT, MacKnight WJ. Introduction to polymer viscoelasticity. 3rd ed. Hoboken, NJ: Wiley; 2005.

[194] Lion A (ed.). Beiträge zur Materialtheorie: Elementare Materialmodelle der linearen Visoelastizität im Zeitbereich; 2007.

[195] Kaliske M, Rothert H. Formulation and implementation of three-dimensional viscoelasticity at small and finite strains. Computational Mechanics 1997;19(3):228–39.

[196] Findley WN, Davis FA. Creep and Relaxation of Nonlinear Viscoelastic Materials. Newburyport: Dover Publications; 2013.

[197] Kelly P. Solid mechanics part I: An introduction to solid mechanics. Solid mechanics lecture notes; 2013.

[198] Yenilmez B, Caglar B, Sozer EM. Viscoelastic modeling of fiber preform compaction in vacuum infusion process. Journal of Composite Materials 2017;51(30):4189–203.

[199] Bunge C-A, Beckers M, Gries T (eds.). Polymer optical fibres: Fibre types, materials, fabrication, characterisation and applications. Duxford, United Kingdom: Woodhead Publishing is an imprint of Elsevier; 2017.

[200] Schapery RA. On the characterization of nonlinear viscoelastic materials. Polym. Eng. Sci. 1969;9(4):295–310.

[201] Simo J, Hughes T. Computational Inelasticity. New York: Springer-Verlag; 1998.

[202] Careglio C, Canales C, Papeleux L, Ponthot, J.P., Garino, C.G., Mirasso AE. An Implementation of the Generalized Maxwell Viscoelastic Constitutive Model. San Carlos de Bariloche; 2014.

[203] Schapery RA. Viscoelastic behavior and analysis of composite materials. Mechanics of Composite Materials:85–168.

[204] Lai J, Bakker A. 3-D schapery representation for non-linear viscoelasticity and finite element implementation. Computational Mechanics 1996;18(3):182–91.

[205] Schapery RA. Nonlinear Viscoelastic and Viscoplastic Constitutive Equations Based on Thermodynamics. Mechanics of Time-Dependent Materials 1997;1(2):209–40.

[206] Varna J, Pupure L, Joffe R. Incremental forms of Schapery's model: convergence and inversion to simulate strain controlled ramps. Mech Time-Depend Mater 2016;20(4):535–52.

[207] Haj-Ali RM, Muliana AH. Numerical finite element formulation of the Schapery non-linear viscoelastic material model. Int. J. Numer. Meth. Engng. 2004;59(1):25–45.

[208] Monsia MD. A Simplified Nonlinear Generalized Maxwell Model for Predicting the Time Dependent Behavior of Viscoelastic Materials. WJM 2011;01(03):158–67.

[209] Birzle AM, Wall WA. A viscoelastic nonlinear compressible material model of lung parenchyma - Experiments and numerical identification. Journal of the mechanical behavior of biomedical materials 2019;94:164–75.

[210] Xia Z, Shen X, Ellyin F. Cyclic deformation behavior of an epoxy polymer. Part II: Predictions of viscoelastic constitutive models. Polym. Eng. Sci. 2005;45(1):103–13.

[211] Gutowski TG, Cai Z, Bauer S, Boucher D, Kingery J, Wineman S. Consolidation Experiments for Laminate Composites. Journal of Composite Materials 1987;21(7):650–69.

[212] Vangheluwe L, Kiekens P. Modelling Relaxation Behaviour of Yarns Part I: Extended, Nonlinear Maxwell Model. Journal of the Textile Institute 1996;87(2):296–304.

[213] Ghosh A, Ishtiaque SM, Rengasamy RS. Stress–strain characteristics of different spun yarns as a function of strain rate and gauge length. Journal of the Textile Institute 2005;96(2):99–104.

[214] Kelly PA, Umer R, Bickerton S. Compaction of dry and wet Fibrous Materials during Infusion Processes 2004.

[215] Khan KA, Umer R. Modeling the viscoelastic compaction response of 3D woven fabrics for liquid composite molding processes. Journal of Reinforced Plastics and Composites 2017;36(18):1299–315.

[216] Matsuo M, Yamada T, Ito N. Stress Relaxation Behavior of Knitted Fabrics under Uniaxial and Strip Biaxial Excitation as Estimated by Corresponding

Principle between Elastic and Visco-Elastic Bodies. Textile Research Journal 2006;76(6):465–77.

[217] Somashekar AA, Bickerton S, Bhattacharyya D. Modelling the viscoelastic stress relaxation of glass fibre reinforcements under constant compaction strain during composites manufacturing. Composites Part A: Applied Science and Manufacturing 2012;43(7):1044–52.

[218] Xiong H, Hamila N, Boisse P. Consolidation Modeling during Thermoforming of Thermoplastic Composite Prepregs. Materials (Basel, Switzerland) 2019;12(18).

[219] Werlen V, Rytka C, Michaud V. A numerical approach to characterize the visco-elastic behaviour of fibre beds and to evaluate the influence of strain deviations on viscoelastic parameter extraction. Composites Part A: Applied Science and Manufacturing 2021;143(4):106315.

[220] Mei M, He Y, Wei K, Duan S, Li M, Yang X. Modeling the temperature-dependent viscoelastic behavior of glass fabric with binder in the compaction process. Polym. Compos. 2021;42(6):3038–50.

[221] Saunders RA, Lekakou C, Bader MG. Compression in the processing of polymer composites 2. Modelling of the viscoelastic compression of resin-impregnated fibre networks. Composites Science and Technology 1999;59(10):1483–94.

[222] Kelly PA. A viscoelastic model for the compaction of fibrous materials. Journal of the Textile Institute 2011;102(8):689–99.

[223] Belnoue JP-H, Nixon-Pearson OJ, Ivanov D, Hallett SR. A novel hyper-viscoelastic model for consolidation of toughened prepregs under processing conditions. Mechanics of Materials 2016;97:118–34.

[224] Valverde MA, Belnoue JP-H, Kupfer R, Kawashita LF, Gude M, Hallett SR. Compaction behaviour of continuous fibre-reinforced thermoplastic composites under rapid processing conditions. Composites Part A: Applied Science and Manufacturing 2021;149(7):106549.

[225] Blößl Y, Schledjewski R. A robust empirical model equation for the compaction response of textile reinforcements. Polym. Compos. 2021;42(1):297–308.

[226] Šajn D, Geršak J, Flajs R. Prediction of Stress Relaxation of Fabrics with Increased Elasticity. Textile Research Journal 2006;76(10):742–50.

[227] Dörr D, Henning F, Kärger L. Nonlinear hyperviscoelastic modelling of intra-ply deformation behaviour in finite element forming simulation of continuously fibre-reinforced thermoplastics. Composites Part A: Applied Science and Manufacturing 2018;109:585–96.

[228] Bickerton S, Buntain MJ. Modeling forces generated within rigid liquid composite molding tools. Part B: Numerical analysis. Composites Part A: Applied Science and Manufacturing 2007;38(7):1742–54.

[229] Gupta A, Kelly PA, Bickerton S, Walbran WA. Simulating the effect of temperature elevation on clamping force requirements during rigid-tool Liquid Composite Moulding processes. Composites Part A: Applied Science and Manufacturing 2012;43(12):2221–9.

[230] Walbran WA, Verleye B, Bickerton S, Kelly PA. Prediction and experimental verification of normal stress distributions on mould tools during Liquid Composite Moulding. Composites Part A: Applied Science and Manufacturing 2012;43(1):138–49.

[231] Kang MK, Lee WI, Hahn HT. Analysis of vacuum bag resin transfer molding process. Composites Part A: Applied Science and Manufacturing 2001;32(11):1553–60.

[232] Park J, Kang MK. A numerical simulation of the resin film infusion process. Composite Structures 2003;60(4):431–7.

[233] Advani SG, Hsiao K-T (eds.). Manufacturing Techniques for Polymer Matrix Composites (PMCs): Compression resin transfer moulding (CRTM) in polymer matrix composites. Sawston, United Kingdom: Woodhead Publishing Ltd; 2012.

[234] Bickerton S, Kelly PA. Compression resin transfer moulding (CRTM) in polymer matrix composites. In: Advani SG, Hsiao K-T, editors. Manufacturing Techniques for Polymer Matrix Composites (PMCs): Compression resin transfer moulding (CRTM) in polymer matrix composites. Sawston, United Kingdom: Woodhead Publishing Ltd; 2012, p. 348–80.

[235] Muthuvel B, Bhattacharyya D, Bickerton S. A parametric flow visualisation study on the impregnation and consolidation stages of the Wet Compression Moulding process. Part I: Process parameters. Composites Part A: Applied Science and Manufacturing 2021;150(5):106634.

[236] Acheson JA, Simacek P, Advani SG. The implications of fiber compaction and saturation on fully coupled VARTM simulation. Composites Part A: Applied Science and Manufacturing 2004;35(2):159–69.

[237] Govignon Q, Bickerton S, Kelly PA. Simulation of the reinforcement compaction and resin flow during the complete resin infusion process. Composites Part A: Applied Science and Manufacturing 2010;41(1):45–57.

[238] Chang C-Y. Simulation of dynamic mold compression and resin flow for force-controlled compression resin transfer molding. Journal of Polymer Engineering 2019;39(9):844–51.

[239] Walbran WA, Verleye B, Bickerton S, Kelly PA. Reducing setup costs: Tooling force prediction in resin transfer moulding (RTM) and compression RTM 2009.

[240] Correia NC, Robitaille F, Long AC, Rudd CD, Sˇimaˊcˇek P, Advani SG. Use of Resin Transfer Molding Simulation to Predict Flow, Saturation, and Compaction in the VARTM Process. Journal of Fluids Engineering 2004;126(2):210–5.

[241] Gao Z-S, Young W-B. Study of the bending induced gap in fiber preforming of woven fiber mats. Polym. Compos. 2002;23(2):239–48.

[242] Bickerton S, Sozer EM, Šimácek P, Advani SG. Fabric structure and mold curvature effects on preform permeability and mold filling in the RTM process. Part II. Predictions and comparisons with experiments. Composites Part A: Applied Science and Manufacturing 2000;31(5):439–58.

[243] ANSYS Inc. Ansys Mechanical: Finite Element Analysis (FEA) Software for Structural Engineering. [November 04, 2021]; Available from: https://www.ansys.com/products/structures/ansys-mechanical.

[244] Dassault systems. ABAQUS/CAE: Complete Solution for Abaqus Finite Element Modelling, Visualization, and Process Automation. [July 11, 2022]; Available from: https://www.3ds.com/products-services/simulia/products/abaqus/abaquscae/.

[245] Bickerton S, Kelly PA. Application of a Complete Tooling Force Analysis for Simulation of Liquid Composite Moulding Processes. KEM 2007;334-335:17–20.

[246] Simacek P, Advani SG. Desirable features in mold filling simulations for Liquid Composite Molding processes. Polym. Compos. 2004;25(4):355–67.

[247] Kelly PA, Bickerton S. A comprehensive filling and tooling force analysis for rigid mould LCM processes. Composites Part A: Applied Science and Manufacturing 2009;40(11):1685–97.

[248] Merotte J, Simacek P, Advani SG. Resin flow analysis with fiber preform deformation in through thickness direction during Compression Resin Transfer Molding. Composites Part A: Applied Science and Manufacturing 2010;41(7):881–7.

[249] Pillai KM, Tucker CL, Phelan FR. Numerical simulation of injection/compression liquid composite molding. Part 2: preform compression. Composites Part A: Applied Science and Manufacturing 2001;32(2):207–20.

[250] Martin FA, Warrior NA, Simacek P, Advani S, Hughes A, Darlington R et al. Simulation and Validation of Injection-Compression Filling Stage of Liquid Moulding with Fast Curing Resins. Appl Compos Mater 2019;26(1):41–63.

[251] Verleye B, Walbran WA, Bickerton S, Kelly PA. Simulation and experimental validation of force controlled compression resin transfer molding. Journal of Composite Materials 2011;45(7):815–29.

[252] Qiao Y, Zhang J, Zhang M, Hu H, Liu L, Zhai P et al. Numerical analysis on the flow–compaction behavior and the effect of interface permeability in thick composite plates during autoclave processing. J Mater Sci 2018;53(20):14412–22.

[253] Ganapathi AS, Joshi SC, Chen Z. Experimental and numerical investigation of process-induced deformations of glass/epoxy wind turbine blade spar cap. Journal of Composite Materials 2017;51(27):3791–806.

[254] Amini Niaki S, Forghani A, Vaziri R, Poursartip A. An Orthotropic Integrated Flow-Stress Model for Process Simulation of Composite Materials—Part I: Two-Phase Systems. Journal of Manufacturing Science and Engineering 2019;141(3):135.

[255] Sakhaei AH, Erland S, Dodwell TJ. A finite deformation Cosserat continuum model for uncured carbon fibre composites. Mechanics of Materials 2020;151(1):103611.

[256] Thompson AJ, McFarlane JR, Belnoue JP-H, Hallett SR. Numerical modelling of compaction induced defects in thick 2D textile composites. Materials & Design 2020:109088.

[257] Hexcel. G0926 D 1304 TCT INJECTEX E01 2F: Data Sheet; 2020.

[258] Teijin. Tenax Dry Reinforcement Non-Crimp Fabric DRNF PB1/PB3: Product Information on Safe Handling.

[259] Lomov SV, Verpoest I, Peeters T, Roose D, Zako M. Nesting in textile laminates: geometrical modelling of the laminate. Composites Science and Technology 2003;63(7):993–1007.

[260] Trochu F, Vernet N, Sun Y, Echaabi J, Makradi A, Belouettar S. Hybrid twin models of fiber compaction for composite manufacturing based on dual kriging. International Journal of Material Forming 2022(15).

[261] ISO 20505:2005. Fine ceramics (advanced ceramics, advanced technical ceramics) — Determination of the interlaminar shear strength of continuous-fibre-reinforced composites at ambient temperature by the compression of double-notched test pieces and by the Iosipescu test.

[262] OpenCV. about OpenCV. [June 18, 2022]; Available from: https://opencv.org/about/.

[263] Leibniz Rechenzentrum LRZ. Linux Cluster Segments: LRZ Linux Cluster Overview. [May 06, 2022]; Available from: https://doku.lrz.de/display/PUBLIC/Linux+Cluster+Segments.

[264] Bathe K-J. Finite element procedures. Boston, Mass.: Bathe; 2006.

[265] ANSYS Inc. Subroutines for Customizing Material Behavior: Subroutine UserMat (Creating Your Own Material Model). [November 09, 2021]; Available from: https://ansyshelp.ansys.com/account/secured?returnurl=/Views/Secured/corp/v231/en/ans_prog/Z7K4r1e5lcd.html%23UPFusermatjwf032800403.

[266] Society of Automotive Engineers, National Institute for Aviation Research (U.S.). Composite materials handbook. Warrendale, Pa.: SAE International on behalf of CMH-17 a division of Wichita State University; 2012.

[267] Teijin. Tenax Filament Yarn: Data Sheet.

[268] ANSYS Inc. Contact Formulation Algorithms. [July 14, 2022]; Available from: https://ansyshelp.ansys.com/account/secured?returnurl=/Views/Secured/corp/v202/en/aim_all/AIM/user_manual/aim_connections/topics/c_asm_contact_formulation.html?q=normal%20lagrange.

[269] Nasdala L. Materialmodelle. In: Nasdala L, editor. FEM-Formelsammlung Statik und Dynamik. Wiesbaden: Vieweg+Teubner Verlag; 2012, p. 171–216.

[270] Vollmer M., Tagscherer N, Zaremba S, Schultheiß D, Mertiny P, Drechsler K. Material characterization for compression resin transfer molding process simulation. Athens, Greece; 2018.

[271] ANSYS Inc. Ansys Fluent: Fluid Simulation Software. [November 09, 2021]; Available from: https://www.ansys.com/products/fluids/ansys-fluent.

[272] Dickert M. Einfluss von Binder auf die Herstellung von Faserkunststoffverbunden. Doctoral dissertation, Techn. Univ Clausthal-Zellerfeld. Clausthal-Zellerfeld: Universitätsbibliothek Clausthal; 2015.

[273] Dalfi HK, Yousaf Z, Selver E, Potluri P. Influence of yarn hybridisation and fibre architecture on the compaction response of woven fabric preforms during composite manufacturing. Journal of Industrial Textiles 2021;21:152808372110242.

[274] Walbran WA, Körber H (eds.). Fast and efficient permeability and compaction characterisation of dry textiles: considerations for a proposed technique; 2014.

[275] Yang B, Wang S, Tang Q. Modeling and 3D Simulation of the Mould Compression and Resin Flow for Force-Controlled Compression Resin Transfer Moulding. ms 2019;25(1).

[276] The SciPy community. scipy.optimize.minimize. [January 31, 2023]; Available from: https://docs.scipy.org/doc/scipy/reference/generated/scipy.optimize.minimize.html.

[277] The SciPy community. scipy.optimize.basinhopping. [January 31, 2023]; Available from: https://docs.scipy.org/doc/scipy/reference/generated/scipy.optimize.basinhopping.html#scipy.optimize.basinhopping.

A Appendix

a Data sheets

HexForce® HS06K CARBON FABRIC
G0926 D 1304 TCT INJECTEX E01 2F

HEXCEL®

Product Data Sheet

Textile Reinforcement for High Performance Composite

HexForce® reinforcements are available in a range of weave styles – from woven fabrics to multiaxials and specialties that offers a range of globally certified aerospace / industrial products in carbon, glass and aramid and specialty fibers that we sell under the HexForce® trademark.

DESCRIPTION		SI Units	US Units
Type of yarns	Warp	TENAX E HTA 40 E13 6K	
	Weft	TENAX E HTA 40 E13 6K	
Nominal weight		375 g/m²	11.06 oz/sqy²
Weave style		5H SATIN	
Width		1304 mm	51.3 in
Finish type		E01 2F	
Finish description			
Powder type		Epoxy powder	
Powder designation		Epoxy Powder E01 2.5% per side	

CHARACTERISTICS		SI Units	US Units
Nominal construction	Warp	4.6 yarn/cm	11.68 yarn/in
	Weft	4.6 picks/cm	11.68 picks/in
Weight distribution	Warp	50 %	
	Weft	50 %	
Thickness (*)		0.38 mm	0.01 in

*NB : The above average values are obtained with laminate at 55% of fibres in volume.

Other Informations
TRACERS Warp & Weft

For more informations

Hexcel is a leading worlwide supplier of composite materials to aerospace and industrial markets.
Our comprehensive range includes:

- HexTow® carbon fibers
- HexForce® reinforcements
- HiMax™ multiaxial reinforcements
- HiTape™ advanced reinforcements
- HexPly® prepregs

- HexMC® molding compounds
- HexFlow® RTM resins
- Redux® adhesives
- HexTool® tooling materials
- HexWeb® honeycombs

- Acousti-CAP® sound attenuating honeycomb
- Engineered core
- Engineered products

For US quotes, orders and product information call toll-free 1-800-688-7734. For other worldwide sales office telephone numbers and a full address list, please go to:

http://www.hexcel.com/contact/salesoffice

TEIJIN

Tenax® Filamentgarn

Produktdatenblatt (EU)

Markenname / Produktionsstandort	Faserfamilie & Zugeigenschaften	Präparations-eigenschaften	Filamentanzahl	Garnfeinheit (ohne Präparation)	Zusatzinformation	Zugfestigkeit [MPa]	Zug-E-Modul [GPa]	Bruchdehnung [%]	Filamentdurchmesser [µm]	Dichte [g/cm³]	Präparation	Präparationsgehalt [%]
Tenax®-J	HTA40	E15	1K	67tex	15S	4100	240	1,7	7,0	1,77	EP	2,5
Tenax®-E	HTA40	E13	3K	200tex		4100	240	1,7	7,0	1,77	EP	1,3
Tenax®-E	HTA40	E13	3K	200tex	15Z	4100	240	1,7	7,0	1,77	EP	1,3
Tenax®-J/E	HTA40	E13	6K	400tex		4100	240	1,7	7,0	1,77	EP	1,3
Tenax®-E	HTA40	E13	6K	400tex	10Z	4100	240	1,7	7,0	1,77	EP	1,3
Tenax®J	HTS40	E13	3K	200tex		4400	240	1,8	7,0	1,77	EP	1,3
Tenax®J	HTS40	E13	6K	400tex		4400	240	1,8	7,0	1,77	EP	1,3
Tenax®-E	HTS40	F13	12K	800tex		4400	240	1,8	7,0	1,77	PU	1,0
Tenax®-E	HTS40	F13	12K	800tex	10Z	4400	240	1,8	7,0	1,77	PU	1,0
Tenax®-E	HTS40	F13	24K	1600tex		4400	240	1,8	7,0	1,77	PU	1,0
Tenax®-E	HTS40	F13	24K	1600tex	5Z	4400	240	1,8	7,0	1,77	PU	1,0
Tenax®-E	HTS45	E23	3K	200tex		4500	235	1,9	7,0	1,77	EP	1,3
Tenax®-E	HTS45	E23	3K	200tex	15Z	4500	235	1,9	7,0	1,77	EP	1,3
Tenax®-E	HTS45	E23	12K	800tex		4500	240	1,9	7,0	1,77	EP	1,3
Tenax®-E	HTS45	E23	12K	800tex	10Z	4500	240	1,9	7,0	1,77	EP	1,3
Tenax®-E	HTS45	P12	12K	800tex		4500	240	1,9	7,0	1,77	TP	0,5
Tenax®E	STS40	E23	24K	1600tex		4300	240	1,8	7,0	1,78	EP	1,3
Tenax®-E	STS40	F11	24K	1600tex		4300	240	1,8	7,0	1,78	PU	0,17
Tenax®-J/E	STS40	F13	24K	1600tex		4300	240	1,8	7,0	1,78	PU	1,0
Tenax®-J/E	STS40	F13	48K	3200tex		4300	250	1,7	7,0	1,77	PU	1,0
Tenax®-J/E	STS40	F13	48K	3200tex	CP	4300	250	1,7	7,0	1,77	PU	1,0
Tenax®-J	UTS50	F13	12K	800tex		5100	245	2,1	7,0	1,78	PU	1,0
Tenax®-J	UTS50	F22	12K	800tex	S	5100	245	2,1	7,0	1,78	PU	0,8
Tenax®-J/E	UTS50	F24	24K	1600tex	DCP	5100	245	2,1	7,0	1,78	PU	2,0
Tenax®-E	ITS50	F23	24K	1600tex	D	5100	265	1,9	7,0	1,80	PU	1,0
Tenax®-J	IMS60	E13	24K	830tex		5800	290	2,0	5,0	1,79	EP	1,3
Tenax®-E	IMS65	E23	24K	830tex		6000	290	2,1	5,0	1,78	EP	1,3
Tenax®-E	IMS65	P12	24K	830tex		6000	290	2,1	5,0	1,78	TP	0,8
Tenax®-J	UMS40	F23	24K	800tex	S	4700	390	1,2	4,9	1,79	PU	1,0
Tenax®-J	UMS45	F22	12K	385tex		4600	425	1,1	4,7	1,83	PU	0,8
Tenax®-J	HTS40	A23	12K	1420tex	MC	2900	230	1,3	7,5*	2,70	PU	1,3

* inkl. 0,25 µm Nickel

Zur optimalen Typenauswahl steht Ihnen unser Verkauf gerne zur Verfügung. Die angegebenen Werte sind Richtwerte. Für die Auslegung von Bauteilen fordern Sie bitte über unseren Verkauf eine Spezifikation an.

Bitte geben Sie auf Ihrer Bestellung den Anwendungsbereich (Luftfahrt oder Industrie & Sport) an.

Die Ausfuhr oder Verbringung von Kohlenstofffasern kann genehmigungspflichtig sein, abhängig von der Endbestimmung und Endverwendung.

Tenax° Dry Reinforcement Non-Crimp Fabric
DRNF PB1/PB3

TEIJIN

Product Information on Safe Handling

Revision 01 (en), print date 18 July 2018, updated 18 July 2018

According to Regulation (EC) No 1907/2006 [REACH] Article 3(3) this product is classified as article, hence no obligation exists to create a safety data sheet as required by REACH Article 31/32. This Product Information was created in the style of REACH Annex II/Regulation (EU) 2015/830 to inform about a safe and careful handling with this product.

Chapter 1: Identification of the article and of the company

1.1	Product Identifier	Tenax® Dry Reinforcement Non-Crimp Fabric
1.1.1	Product types	Tenax®-E DRNF Tenax®-E DRNF PB1 Tenax®-E DRNF PB3
1.2	Recommended Use	Use to produce molded composite parts for aerospace application.
1.2.1	Uses advised against	None.
1.3	Details of the supplier	
1.3.1	Address	Teijin Carbon Europe GmbH Kasinostr. 19-21 42103 Wuppertal GERMANY Tel: +49 202 32-3225 Homepage: www.teijincarbon.com
1.3.2	Responsible department/ competent person	Dr Axel Leuchter General Manager Quality & Compliance E-Mail: safety@teijincarbon.com

Chapter 2: Hazards identifications

2.1	Classification	This product is an **article**, and hence does not require a classification and labelling according to EU regulations.
2.1.1	Self-Classification according to Regulation (EC) No 1272/2008 [CLP]	Not classified as hazardous. See chapter 3.
2.2	Self-Labelling elements according to Regulation (EC) No 1272/2008 [CLP]	Not subject to labelling.
2.2.1	Precautionary instruction	P280: Wear protective gloves.
2.2.2	Supplemental hazard information (EU)	**EUH208**: "Contains reaction product: bisphenol-A-(epichlorhydrin); epoxy resin (number average molecular weight ≤ 700) and 2-(chloromethyl)oxirane; Formaldehyde; Phenol. May produce an allergic reaction."
2.3	Oher hazards	
2.3.1	Product meets the criteria for classification acc. to Annex XIII of REACH Reg. (EC) No 1907/2006 as PBT or vPvB	Not applicable
2.3.2	Other hazards which do not result in classification	Risk of skin burns cause of hot melt.

Chapter 3: Composition/information of ingredients

3.1	Product type	This product is an **article** acc. to regulation (EC) 1907/2006 [REACH]. It does not contain any substances that are intended to be released under normal or foreseeable applications.
3.1.1	Description	Pre-impregnated carbon fiber composition.
3.2	Composition/information of ingredients	

TEIJIN CARBON EUROPE GMBH — Verfasser/Editor: Doris Ohms — Freigabe/Release: Birgit Deimann

b Drawings of the tools for non-planar compaction

The drawings of the tools which were used for the non-planar compaction experiments in Section 3.5 are shown here. The tools were designed to be used for preforming in the hot press and to be mounted into the UTM for the compaction tests. Standard steel was used for the manufacturing of these geometries. Moreover, this section depicts the technical drawings of the two positioning devices that were used to cut the preforms. The positioning devices were additively manufactured with Polylactide.

front view
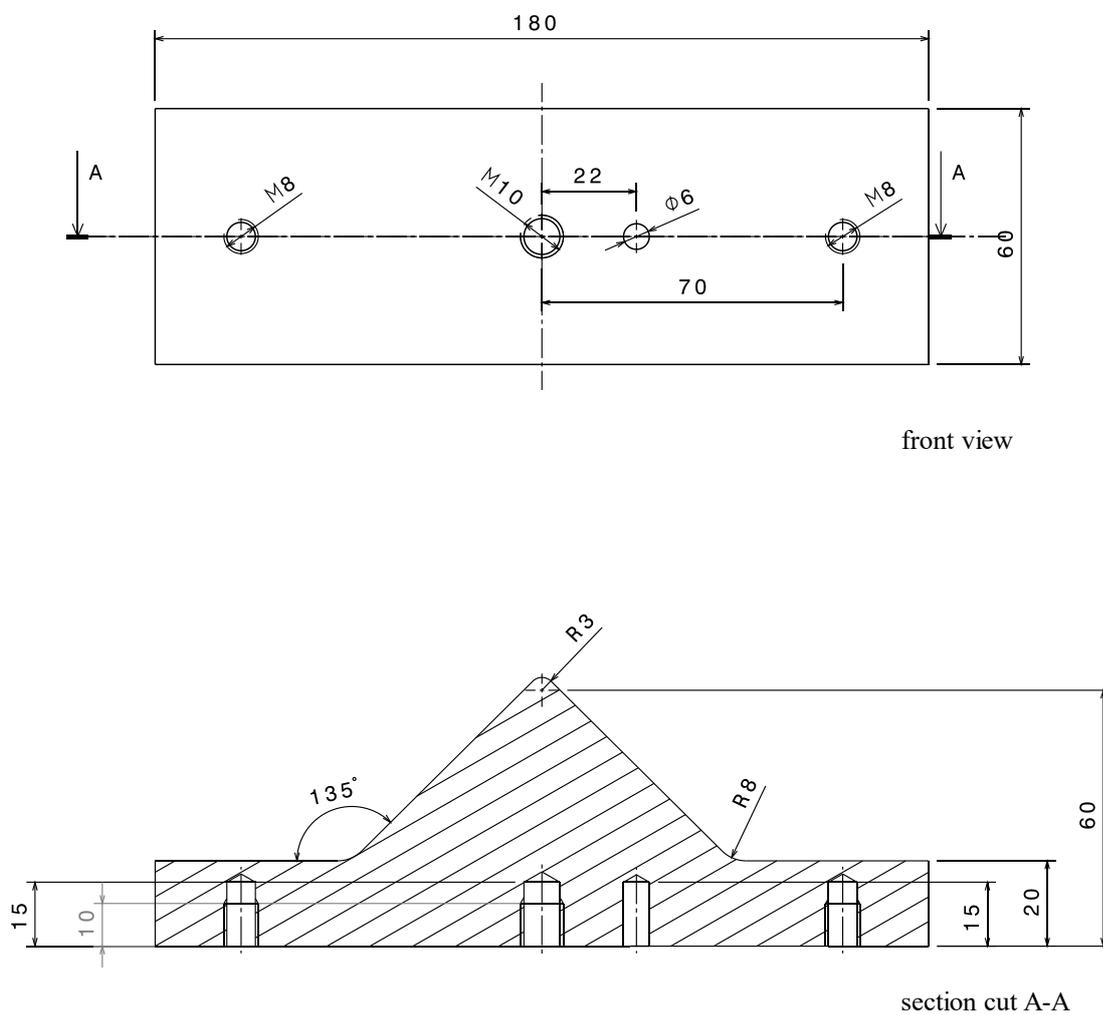
section cut A-A

Fig. A-1:   **Technical drawing of the 3 mm lower tool showing the front view and the section cut A-A.**
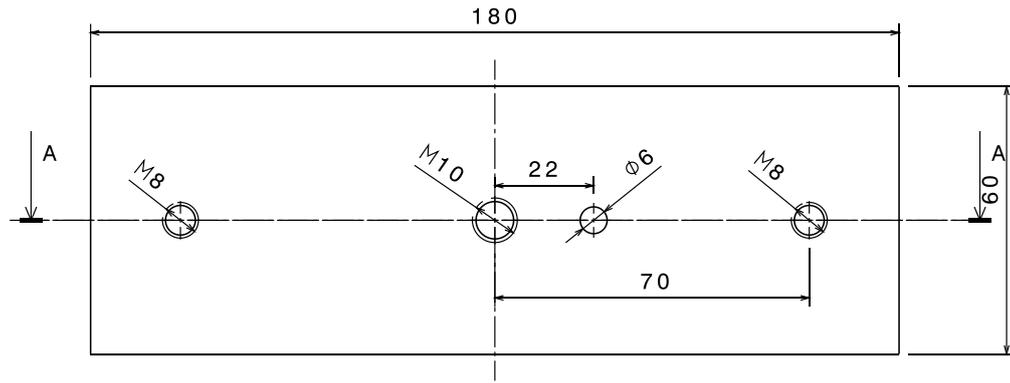
front view
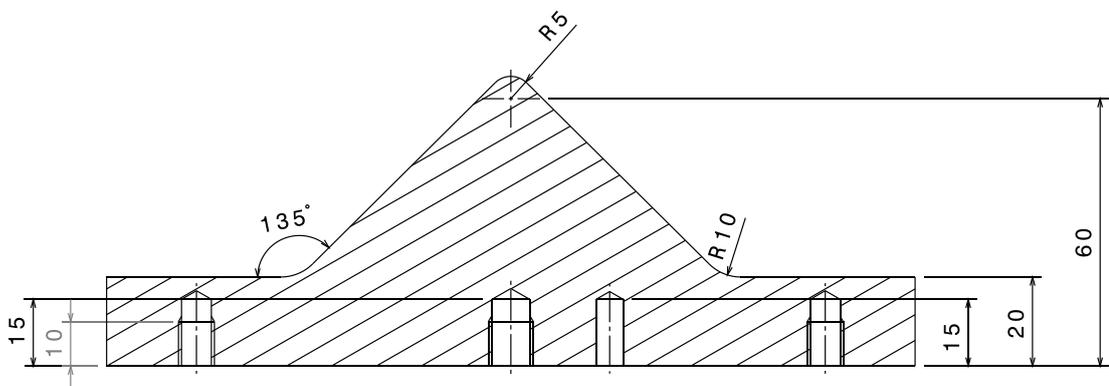
section cut A-A

Fig. A-2: **Technical drawing of the 5 mm lower tool showing the front view and the section cut A-A.**
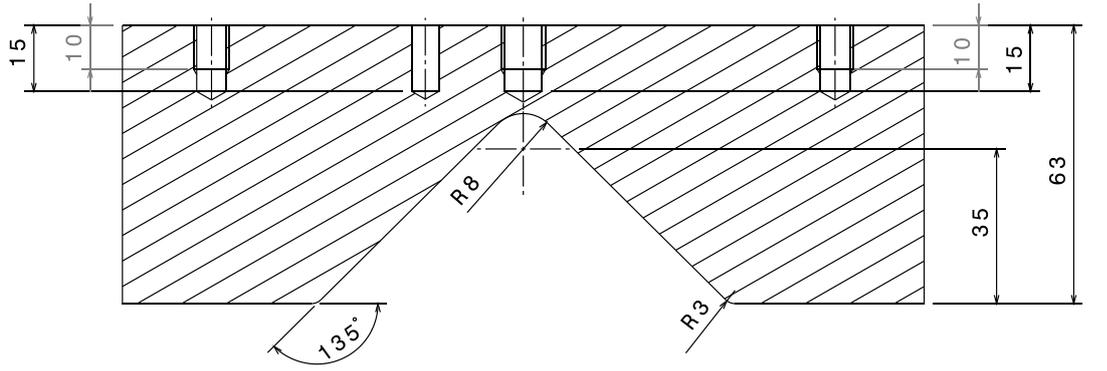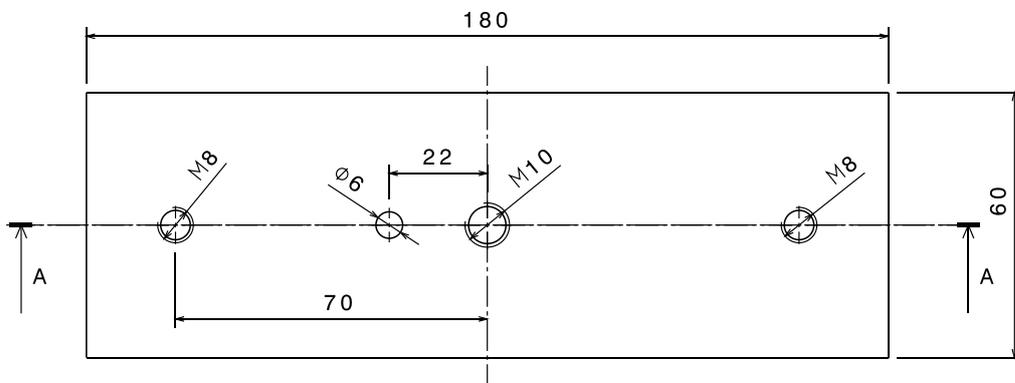
section cut A-A

front view

Fig. A-3:   Technical drawing of the 8 mm upper tool showing the front view and the section cut A-A.
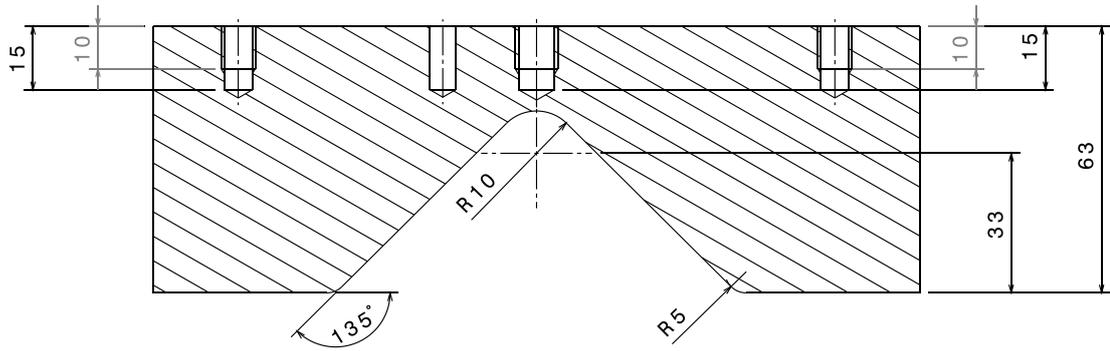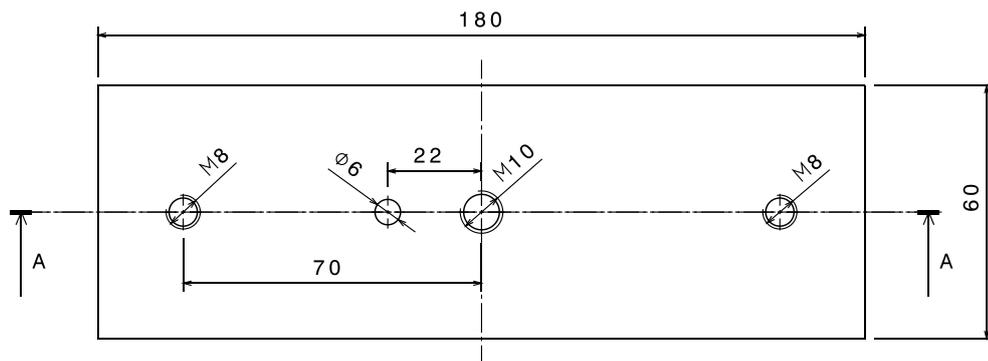
section cut A-A

front view

Fig. A-4:   **Technical drawing of the 10 mm upper tool showing the front view and the section cut A-A.**
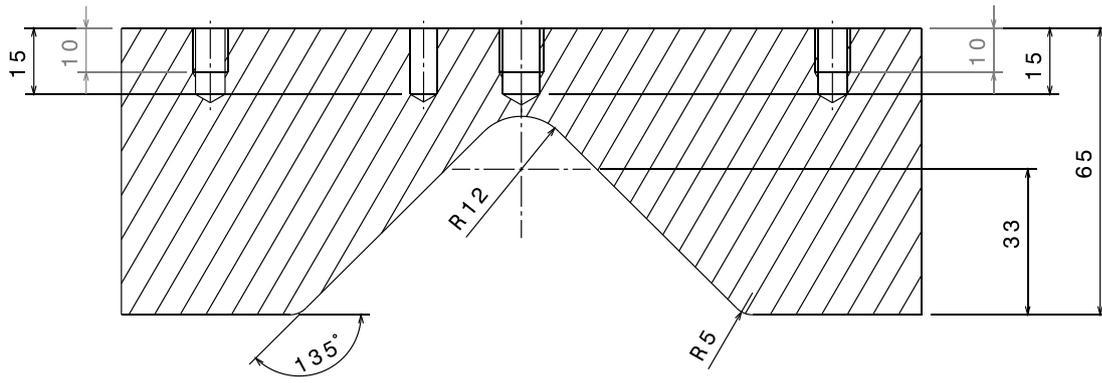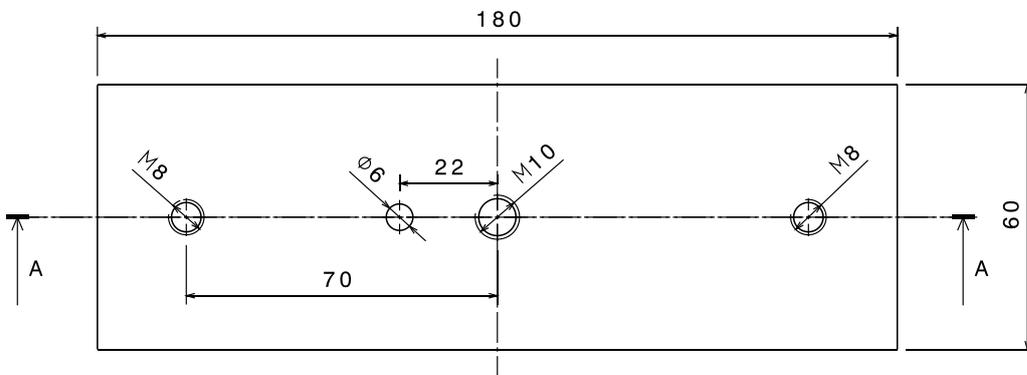
section cut A-A

front view

Fig. A-5:   **Technical drawing of the 12 mm upper tool showing the front view and the section cut A-A.**
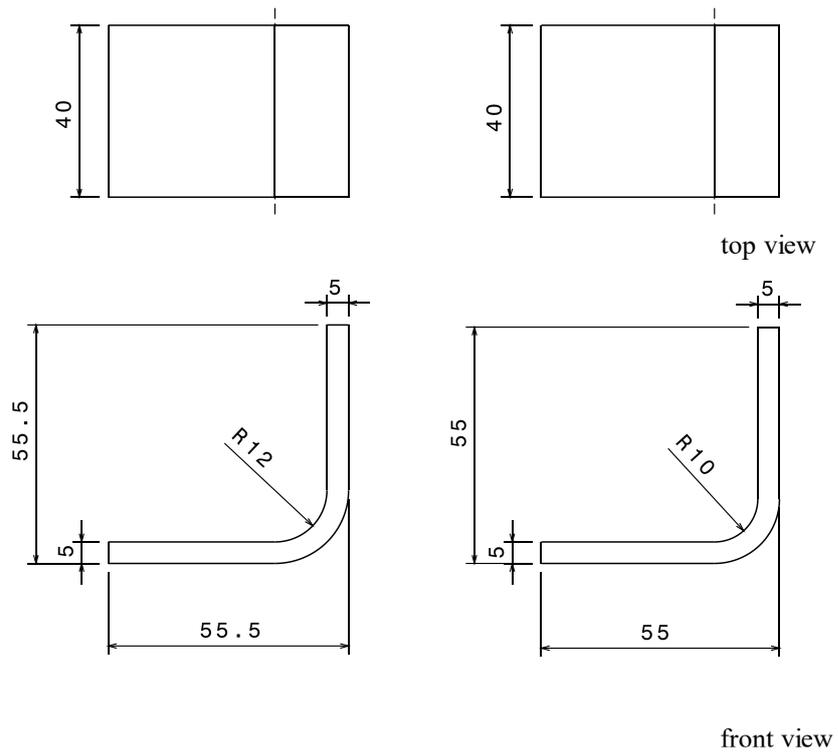
top view

front view

Fig. A- 6: **Technical drawing of the preform positioning device showing the top view and the front view.**

c Code for the implementation of the user-defined material

APDL command for the integration in ANSYS Workbench

The following command is used to apply the user-defined material to the preform geometry in ANSYS Workbench. This code replaces the default material for the preform with the usermat.F file. Moreover, specific parameters such as the initial FVC are transferred to the subroutine.

```
*set,Vf_0,0.3345          ! initial FVC
*set,young_1,120000.0      ! tensile stiffness in-plane
*set,fact,1.6              ! factor for comaction stiffness --> opt 1.6
*set,young_red,0.001       ! factor reduce in plane compression stiffness --> opt 0.01
*set,shear_fact, 1.0       ! factor for shear stiffness --> opt 1.0
*set,layer, 12.0           ! number of layers
ET,,SOLID186
ETCONTROL,OFF
tbdele,ALL,matid
tb,user,matid,2,5                                         ! User Material: user,mate-
rial ref num, num of temperatures, num of vars per temp
tbtemp,0.0                                                ! first temp.
tbdata,1,Vf_0,young_1,fact,young_red,shear_fact,layer     ! Young's modulus, posn ra-
tio
tbtemp,1.0                                                ! first temp.
tbdata,1,Vf_0,young_1,fact,young_red,shear_fact,layer     ! Young's modulus, posn ra-
tio
tb,state,matid,,20                                        ! mat1 has 1 state variable
tunif,Vf_0                                                ! Uniform temp of 1.0 for
all nodesAdd the following lines
/upf, usermat.F
```

Fortran code of the user-defined material subroutine

This appendix shows the Fortran code of the user-defined subroutine in its 3D implementation, which was used in Chapter 4 and Chapter 5. This code needs to be compiled with Microsoft Visual Studio Professional 2017 Version 15.0 and Intel Visual Fortran 2019.3.203, in order to be used in Ansys Mechanical 2020 R2.

```
c*************************************************************************
#include "impcom.inc"
c
     INTEGER
     &              matId, elemId,
     &              kDomIntPt, kLayer, kSectPt,
     &              ldstep,isubst,keycut,
     &              nDirect,nShear,ncomp,nStatev,nProp
     DOUBLE PRECISION
     &              Time,    dTime,   Temp,    dTemp,
     &              sedEl,   sedPl,   epseq,   epsZZ,   cutFactor
     DOUBLE PRECISION
     &              stress(ncomp  ), ustatev (nStatev),
     &              dsdePl  (ncomp,ncomp), stress_o(ncomp),
     &              Strain  (ncomp  ), dStrain (ncomp  ),
     &              epsPl   (ncomp  ), prop    (nProp  ),
     &              coords  (3),
```

```fortran
     &                    defGrad (3,3),    defGrad_t(3,3),
     &                    tsstif  (2), d_defGrad(3,3)
c
c**************** User defined part **********************************
c
c --- parameters
c
      INTEGER           mcomp
      DOUBLE PRECISION HALF, THIRD, ONE, TWO, SMALL, ONEHALF,
     &                 ZERO, TWOTHIRD, ONEDM02, ONEDM05, sqTiny
      PARAMETER       (ZERO        = 0.d0,
     &                 HALF        = 0.5d0,
     &                 THIRD       = 1.d0/3.d0,
     &                 ONE         = 1.d0,
     &                 TWO         = 2.d0,
     &                 SMALL       = 1.d-08,
     &                 sqTiny      = 1.d-20,
     &                 ONEDM02     = 1.d-02,
     &                 ONEDM05     = 1.d-05,
     &                 ONEHALF     = 1.5d0,
     &                 TWOTHIRD    = 2.0d0/3.0d0,
     &                 mcomp       = 6
     &                 )
c
c --- local variables
c
c      sigElp   (dp,ar(6  ),l)            trial stress
c      dsdeEl   (dp,ar(6,6),l)            elastic moduli
c      sigDev   (dp,ar(6  ),l)            deviatoric stress tensor
c      dfds     (dp,ar(6  ),l)            derivative of the yield function
c      JM       (dp,ar(6,6),l)            2D matrix for a 4 order tensor
c      pEl      (dp,sc     ,l)            hydrostatic pressure stress
c      qEl      (dp,sc     ,l)            von-mises stress
c      pleq_t   (dp,sc     ,l)            equivalent plastic strain at beginnig of time
c increment
c      pleq     (dp,sc     ,l)            equivalent plastic strain at end of time in-
c crement
c      dpleq    (dp,sc     ,l)            incremental equivalent plastic strain
c      sigy_t   (dp,sc     ,l)            yield stress at beginnig of time increments
c      sigy     (dp,sc     ,l)            yield stress at end of time increment
c      young    (dp,ar(3  ),l)            Young's modulus
c      posn     (dp,ar(3  ),l)            Poiss's ratio
c      sigy0    (dp,sc     ,l)            initial yield stress
c      dsigdep  (dp,sc     ,l)            plastic slop
c      twoG     (dp,sc     ,l)            two time of shear moduli
c      threeG   (dp,sc     ,l)            three time of shear moduli
c      stress_o (dp,ar(6  ),l)            stress at n
c
c --- temperary variables for solution purpose
c      i, j
c      threeOv2qEl, oneOv3G, qElOv3G, con1, con2, fratio
c
      EXTERNAL          vzero, vmove, get_ElmData
      DOUBLE PRECISION sigElp(mcomp), dsdeEl(mcomp,mcomp), G(mcomp),
     &                 sigDev(mcomp), JM    (mcomp,mcomp), dfds(mcomp),
     &                 sigi  (mcomp), strainEl(mcomp), dstress(ncomp)

      DOUBLE PRECISION var0, var1, var2, var3, var4, var5,
     &                 var6, var7
      DATA G/1.0D0,1.0D0,1.0D0,0.0D0,0.0D0,0.0D0/
c
      INTEGER          i, j
      DOUBLE PRECISION dsigdep, young(ncomp-3),                     ! Declare all
parameters here
     &                 posn(ncomp-3), engStrain(6), engdStrain,
     &                 Vf_0, Vf, Vf_ref, fit_A, fit_B, ratio,
     &                 Gxy, Gyz, Gzx, ref_layer, layer,
     &                 G_A45, G_B45, G_A50, G_B50,
     &                 G_A55, G_B55, G_A60, G_B60,
     &                 icpt,icpt45, icpt50, icpt55, icpt60,
     &                 deltaVf, tau_1, tau_2, tau_3,
     &                 a1, a2, a3, b1, b2, b3,
     &                 eps_dot,j_1, j_2, j_3,
     &                 eps_1, eps_2, eps_3, young_init,
```

```fortran
      &                    eps_1rel, eps_2rel, eps_3rel,
      &                    E_0, E_1, E_2, E_3, h_1, h_2, h_3,
      &                    delt, delt1, delt2, fact, fact2, shearfact
C*********************************************************************
c
      keycut   = 0
      cutFactor = 0.d0
      dsigdep  = 0.d0
      deltaVf  = 0.0d0
      Vf_ref=0.3345
      ref_layer = 12.0d0
c *** get Young's modulus and Poisson's ratio, initial yield stress and others
      Vf_0       = Temp                                  ! Initial FVF as
input from input file elasticBar.txt
      IF (Vf_0 .LT. 0.001) THEN
        Vf_0=0.3345
      END IF
      fact = prop(4)                                     ! In-plane stiff-
ness reduction factor
      fact2 = prop(3)                                    ! Compaction stiff-
ness scaling factor
      shearfact = prop(5)                                ! Out-of-plane
shear stiffness scaling factor
      layer = prop(6)                                    ! Number of layers
      young_init  = 0.3d0                                ! initial Young's
Modulus Z-axis
      G_A45        = 0.59d0
      G_B45        = 0.07d0
      G_A50        = 0.72d0
      G_B50        = 0.13d0
      G_A55        = 0.93d0
      G_B55        = 0.13d0
      G_A60        = 1.54d0
      G_B60        = 0.14d0
      icpt45       = 0.046d0
      icpt50       = 0.043d0
      icpt55       = 0.032d0
      icpt60       = 0.020d0
      posn(1)      = 0.00d0                              !pos_xy
      posn(5)      = 0.00d0                              !pos_zy
      posn(3)      = 0.00d0                              !pos_zx
C     --- Initializing Parameters                        ! Optimized parame-
ters
      fit_A        = fact2*0.0040d0
      fit_B        = 16.1292d0
      tau_1        = 7.90100288d0
      tau_2        = 214.570458d0
      tau_3        = 0.0558369852d0
      a1           = fact2*0.0227905286d0
      b1           = 16.494685d0
      a2           = fact2*0.0986589683d0
      b2           = 12.4436282d0
      a3           = fact2*3.53723871d0
      b3           = 9.99963659d0
      IF (ldstep .EQ. 1 .AND. isubst .EQ. 1) THEN
         ustatev(1) = 0.0d0
         ustatev(2) = 0.0d0
         ustatev(3) = 0.0d0
         ustatev(4) = a1
         ustatev(5) = a2
         ustatev(6) = a3
         ustatev(7) = 0.0d0
         ustatev(8) = 0.0d0
         ustatev(9) = 0.0d0
      END IF
      DO i=1,ncomp
         sigElp(i) = stress(i)
      END DO
C     --- Viscoelastic Model
      eps_dot = dStrain(3)/dTime                         ! Strain rate
      Vf = Vf_0/(1+Strain(3))                            ! Loacal FVF as a
function of Strain

C     --- Expressions for repeated use
```

```fortran
        IF (ldstep .EQ. 1 .AND. isubst .EQ. 1) THEN
           j_1 = 0.0
           j_2 = 0.0
           j_3 = 0.0
        ELSE
           j_1 = (1-EXP(-dTime/tau_1))/(dTime/tau_1)
           j_2 = (1-EXP(-dTime/tau_2))/(dTime/tau_2)
           j_3 = (1-EXP(-dTime/tau_3))/(dTime/tau_3)
        END IF
C       --- calculation of strains
        eps_1=EXP(-dTime/tau_1)*ustatev(1)+eps_dot*dTime*j_1        ! Brnach strains:
Derived from branch stress formulations
        eps_2=EXP(-dTime/tau_2)*ustatev(2)+eps_dot*dTime*j_2        ! Maxwell-springs
        eps_3=EXP(-dTime/tau_3)*ustatev(3)+eps_dot*dTime*j_3
C       --- calculation of Maxwell elements relative strains
        ratio = SQRT(layer/ref_layer)
        eps_1rel = ratio * (Strain(3) - eps_1)                     ! Relative branch
strains: Maxwell-dashpots
        eps_2rel = ratio * (Strain(3) - eps_2)
        eps_3rel = ratio * (Strain(3) - eps_3)
C       --- calculation of quasi-static stiffness modulus E_0

        E_0 = (fit_A/Vf)*exp(fit_B*Vf**2)                          ! Nonlinear Spring
for 1st branch: Modified from Danzi model
        young(1)   = Vf*prop(2)                                    ! Young's Modulus
X-axis
        young(2)   = Vf*prop(2)                                    ! Young's Modulus
Y-axis
C       --- adjust in plane stiffness
        IF (Strain(1) .LT. 0.0) THEN
           young(1) = fact*Vf*prop(2)
        ENDIF
        IF (Strain(2) .LT. 0.0) THEN
           young(2) = fact*Vf*prop(2)
        ENDIF
C       --- calculation of Maxwell elements stiffness E_1, E_2, E_3
        E_1 = a1*exp(abs(eps_1rel)*b1)                             ! Maxwell Spring
Stiffnesses: from Danzi model
        E_2 = a2*exp(abs(eps_2rel)*b2)
        E_3 = a3*exp(abs(eps_3rel)*b3)
C       --- calculation of internal stress variables
        IF (Time.EQ.0) THEN                                        ! Branch stresses
           h_1=0                                                   ! Initial value at
t=0 to avoid reaching singularity
           h_2=0
           h_3=0
        ELSE
           h_1= EXP(-dTime/tau_1)*ustatev(7)+(E_1*eps_dot*tau_1)   ! Branch stress
formulations: adapted and modified
     &    -(ustatev(4)*eps_dot*tau_1*EXP(-dTime/tau_1))            ! from Kaliske
model
           h_2= EXP(-dTime/tau_2)*ustatev(8)+(E_2*eps_dot*tau_2)
     &    -(ustatev(5)*eps_dot*tau_2*EXP(-dTime/tau_2))
           h_3= EXP(-dTime/tau_3)*ustatev(9)+(E_3*eps_dot*tau_3)
     &    -(ustatev(6)*eps_dot*tau_3*EXP(-dTime/tau_3))
        ENDIF
C       --- calculation of Trial Stress
        sigElp(3) = E_0*(Strain(3)+dStrain(3))+h_1+h_2+h_3         ! Viscoelastic
stress response
        IF (Time.EQ.0) THEN
           young(3) = young_init
        ELSE
           young(3)  = sigElp(3)/(Strain(3)+dStrain(3))
        END IF
c       IF (Strain(3) .GT. 0.0) THEN
c          young(3)  = prop(5)
c       END IF
C------- compute shear stiffness
C       -----FVC less than45%---
        IF (Vf.LT.0.45) THEN
           icpt = icpt45
           IF (abs(Strain(5)+dStrain(5)).LT.icpt) THEN
              Gyz = G_A45
           ELSE
```

```fortran
                Gyz = G_B45
              END IF
              IF (abs(Strain(6)+dStrain(6)).LT.icpt) THEN
                Gzx = G_A45
              ELSE
                Gzx = G_B45
              END IF
C       -----FVC greater than45% and less than50%---
        ELSE IF (Vf.GE.0.45 .AND. Vf.LT.0.50) THEN
              deltaVf = Vf-0.45
              icpt = icpt45 + deltaVf*(icpt50-icpt45)/0.05
              IF (abs(Strain(5)+dStrain(5)).LT.icpt) THEN
                Gyz = G_A45 + deltaVf*(G_A50-G_A45)/0.05
              ELSE
                Gyz = G_B45 + deltaVf*(G_B50-G_B45)/0.05
              END IF
              IF (abs(Strain(6)+dStrain(6)).LT.icpt) THEN
                Gzx = G_A45 + deltaVf*(G_A50-G_A45)/0.05
              ELSE
                Gzx = G_B45 + deltaVf*(G_B50-G_B45)/0.05
              END IF
C       -----FVC greater than50% and less than55%---
        ELSE IF (Vf.GE.0.50 .AND. Vf.LT.0.55) THEN
              deltaVf = Vf-0.50
              icpt = icpt50 + deltaVf*(icpt55-icpt50)/0.05
              IF (abs(Strain(5)+dStrain(5)).LT.icpt) THEN
                Gyz = G_A50 + deltaVf*(G_A55-G_A50)/0.05
              ELSE
                Gyz = G_B50 + deltaVf*(G_B55-G_B50)/0.05
              END IF
              IF (abs(Strain(6)+dStrain(6)).LT.icpt) THEN
                Gzx = G_A50 + deltaVf*(G_A55-G_A50)/0.05
              ELSE
                Gzx = G_B50 + deltaVf*(G_B55-G_B50)/0.05
              END IF
C       -----FVC greater than55% and less than60%---
        ELSE IF (Vf.GE.0.55 .AND. Vf.LT.0.60) THEN
              deltaVf = Vf-0.55
              icpt = icpt55 + deltaVf*(icpt60-icpt55)/0.05
              IF (abs(Strain(5)+dStrain(5)).LT.icpt) THEN
                Gyz = G_A55 + deltaVf*(G_A60-G_A55)/0.05
              ELSE
                Gyz = G_B55 + deltaVf*(G_B60-G_B55)/0.05
              END IF
              IF (abs(Strain(6)+dStrain(6)).LT.icpt) THEN
                Gzx = G_A55 + deltaVf*(G_A60-G_A55)/0.05
              ELSE
                Gzx = G_B55 + deltaVf*(G_B60-G_B55)/0.05
              END IF
C       -----FVC60%---
        ELSE IF (Vf.GE.0.60) THEN
              icpt = icpt60
              IF (abs(Strain(5)+dStrain(5)).LT.icpt) THEN
                Gyz = G_A60
              ELSE
                Gyz = G_B60
              END IF
              IF (abs(Strain(6)+dStrain(6)).LT.icpt) THEN
                Gzx = G_A60
              ELSE
                Gzx = G_B60
              END IF
        END IF
c        IF (abs(Strain(5)+dStrain(5)).LT.icpt55 ) THEN
c              Gyz = G_A55
c        ELSE
c              Gyz = G_B55
c        END IF
c        IF (abs(Strain(6)+dStrain(6)).LT.icpt55 ) THEN
c              Gzx = G_A55
c        ELSE
c              Gzx = G_B55
c        END IF
```

```fortran
      dsdeEl(1,1)=young(1)
      dsdeEl(1,2)=posn(1)
      dsdeEl(1,3)=posn(3)
      dsdeEl(1,4)=0
      dsdeEl(1,5)=0
      dsdeEl(1,6)=0
      dsdeEl(2,2)=young(2)
      dsdeEl(2,3)=posn(5)
      dsdeEl(2,4)=0
      dsdeEl(2,5)=0
      dsdeEl(2,6)=0
      dsdeEl(3,3)=young(3)                          ! Ezz calculated
from viscoelastic stress response
      dsdeEl(3,4)=0
      dsdeEl(3,5)=0
      dsdeEl(3,6)=0
      dsdeEl(4,4)=750.0d0                           !Gxy
      dsdeEl(4,5)=0
      dsdeEl(4,6)=0
      dsdeEl(5,5)=shearfact*Gyz                     ! Gyz
      dsdeEl(5,6)=0
      dsdeEl(6,6)=shearfact*Gzx                     ! Gzx
C     --- Symmetry of the Stiffness Matrix
      DO i=1,ncomp-1
         DO j=i+1,ncomp
            dsdeEl(j,i)=dsdeEl(i,j)                 ! dictating sym-
metry
         END DO
      END DO
C     --- calculate the material Jacobian matrix
      DO i= 1,ncomp
         DO j= 1,ncomp
            IF (i.EQ.3 .AND. i.EQ.j) THEN
               IF (Time.GT.0) THEN
                  dsdePl(i,j)= E_0 +                ! Specified Jaco-
bian in viscoelastic behavior
     &              (E_1-(ustatev(4)*EXP(-dTime/tau_1)))/(dTime/tau_1)! for compaction
direction (Z axis)
     &            + (E_2-(ustatev(5)*EXP(-dTime/tau_2)))/(dTime/tau_2)
     &            + (E_3-(ustatev(6)*EXP(-dTime/tau_3)))/(dTime/tau_3)
               ELSE
                  dsdePl(i,j)= E_0 + E_1 + E_2 + E_3
               END IF
            ELSE
               dsdePl(i,j) = dsdeEl(i,j)            ! Specified Jaco-
bain for the remaining directions
            END IF
         END DO
      END DO
C     --- update stresses
      stress(1)=sigElp(1)+dsdeEl(1,1)*dStrain(1)
      stress(2)=sigElp(2)+dsdeEl(2,2)*dStrain(2)
      stress(3)=sigElp(3)
      stress(4)=sigElp(4)+dsdeEl(4,4)*dStrain(4)
      stress(5)=sigElp(5)+dsdeEl(5,5)*dStrain(5)
      stress(6)=sigElp(6)+dsdeEl(6,6)*dStrain(6)
C     --- store state variables
      ustatev(1) = eps_1
      ustatev(2) = eps_2
      ustatev(3) = eps_3
      ustatev(4) = E_1
      ustatev(5) = E_2
      ustatev(6) = E_3
      ustatev(7) = h_1
      ustatev(8) = h_2
      ustatev(9) = h_3
      ustatev(10)= E_0
      ustatev(11)= Vf
      ustatev(12)= defGrad(1,1)-1
      ustatev(13)= defGrad(2,2)-1
      ustatev(14)= defGrad(3,3)-1
      ustatev(15)= stress(1)
      ustatev(16)= Strain(5)
      ustatev(17)= Strain(6)
```

```fortran
        ustatev(18)= deltaVf
        ustatev(19)= eps_dot
        ustatev(20)= ratio
C *** create Output                                              ! Activate these
commands by removing comment 'C'
C       IF (isubst .eq. 1) THEN                                  ! For exporting ad-
ditional parameters used in the
C          open (unit = 5, file = "ustatev.txt")                 ! material model
C          WRITE (5,*)
C       &  "Time, ecs_1,ecs,2"
C        END IF
C        WRITE (5,*) Time, ecs(1), ecs(2)
        RETURN
        END
```

d Implementation of the curve fitting algorithm

The curve fitting for the derivation of the model parameters shown in Tab. 4-2 is performed in two subsequent steps. First, the parameters of the free spring A and B are determined. Afterwards, the remaining parameters a_j, b_j and τ_j are derived with a second fitting step. Both fitting algorithms are implemented in Python using the optimize.minimize function in the SciPy extension [276].

Fitting of parameters A and B

This fitting procedure determines the parameters A and B by fitting Eq. (4-5) to the relaxed stresses of the experimental tests for different final FVC. Thus, two lists with the final FVC values and the corresponding relaxed stresses are needed as input.

Fig. A-7 shows the flow chart for the parameter fitting. The stresses are calculated with current values for A and B using Eq. (4-5). These stresses are subtracted from the relaxed experimental stresses defined in the input. The function optimize.minimize is used to minimize this difference in order to find the optimum values for A and B. Nelder-Mead method with a maximum number of iterations of 10000 is used for the optimization.
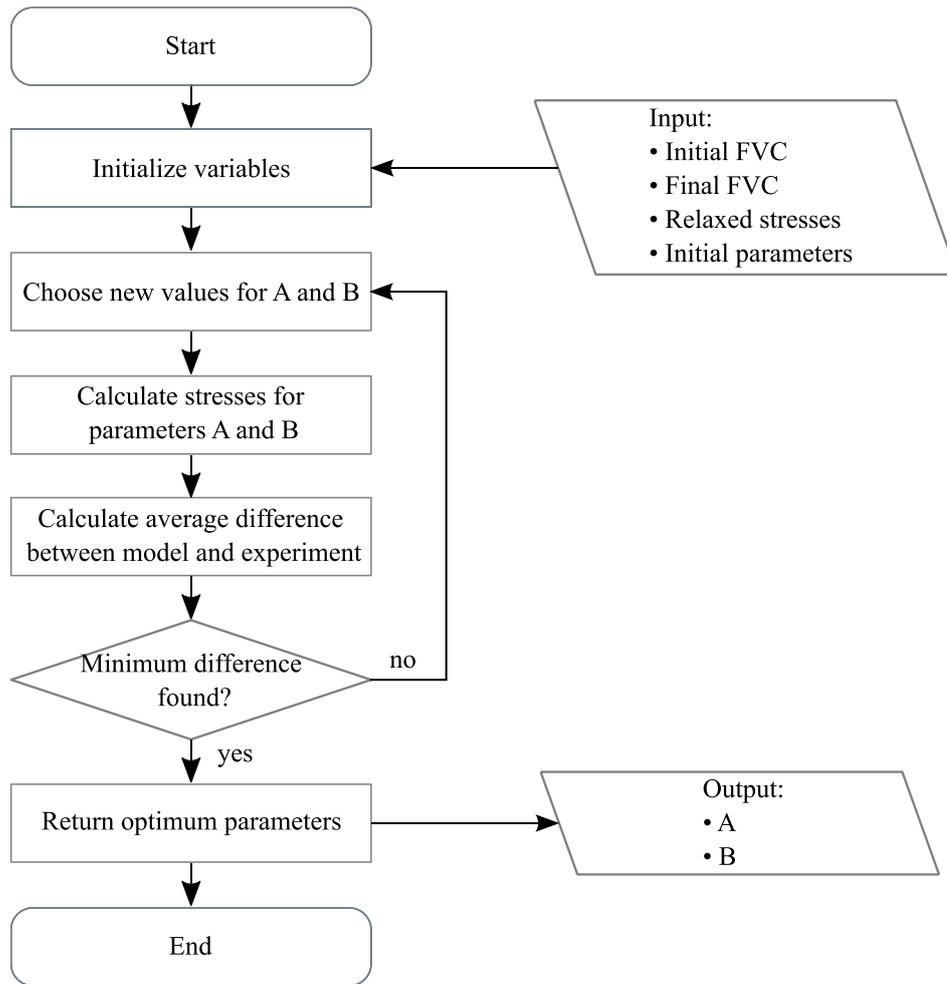
Fig. A-7:   **Flow chart for the fitting of parameters *A* and *B* in the free spring the *viscous exp* model.**

Fitting of parameters a_j, b_j and τ_j

The remaining fitting parameters a_j, b_j and τ_j for each branch j of the viscous *exp model* are derived with a very similar approach. However, the optimization with nine different parameters in case of a three-branch model is significantly more computationally expensive. The approach is depicted in the flow chart shown in Fig. A-8. Contrary to the fitting of single values in the previous section, this algorithm utilizes the whole stress history to find the optimum parameters. For this purpose, the script reads in the experimental stress data for each configuration. Stresses at each time step are saved in .csv files including the final FVC and the compaction velocity of the respective configuration. Afterwards, the stresses of the model are calculated according to Eq. (4-3),(4-4) and (4-5) for the same points in time experimental data was read in. Having model data and experimental data for the same points in time, facilitates the curve fitting, because data interpolation is not necessary. The square difference between experimental stress and model stress is calculated for each data point in time and normalized according to Eq. (4-1). Eq. (4-2) then allows calculating the total stress difference λ_{tot} considering

all selected configurations. The optimizer minimizes the λ_{tot} which represents the normalized area between experimental curves and model curves. For this fitting procedure, the basin-hopping procedure method was used. This two-phase method was developed to find the global minimum for complex problems [277]. SLSQP method was used as minimization method inside the basin-hopping with a maximum of 10000 iterations. 200 basin-hopping iterations showed satisfactory results with this method.
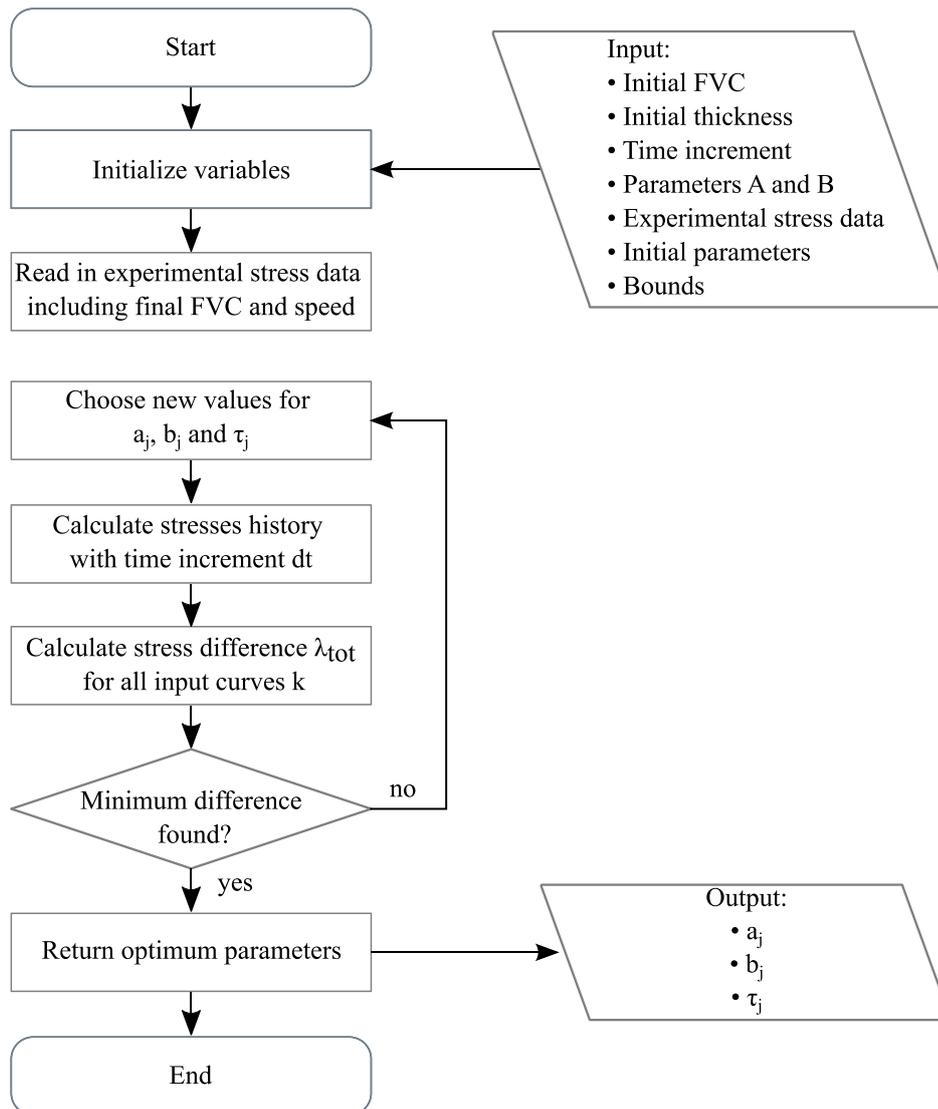

Fig. A-8:   **Flow chart for the fitting of parameters a_j, b_j and τ_j of the *viscous exp* model.**

e Tool-preform friction characterization

This appendix shows the results of all friction experiments performed to characterize the tool-preform interface. The experiments were performed for the following configurations:

- 0° orientation and 1 mm/min speed
- 0° orientation and 10 mm/min speed
- 90° orientation and 10 mm/min speed

The individual tests were named according the nomenclature "orientation-speed-number of additional weights-test repetition". The number of additional weights ranges from 0 to 4 and the number of repetitions from 1 to 6 for each configuration. Fig. A-9 shows how the orientation of the layers is defined for the friction experiments. An experiment in 0° direction means the material is pulled in the direction of the four warp yarns of the satin weave.
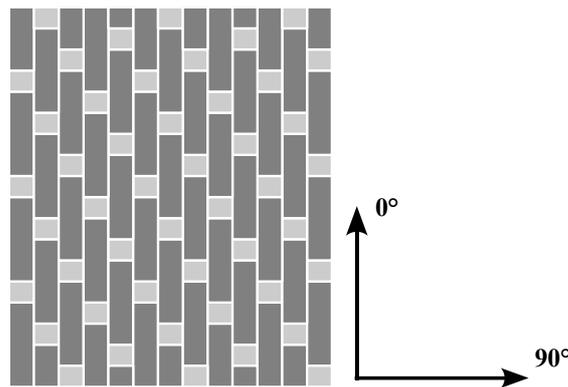

Fig. A-9:   **Definition of the orientation for the friction experiments.**

In Fig. A-10, Fig. A-11 and Fig. A-12 outliers are not included. These outliers were mostly a result of loosened fibers or fiber bundles perpendicular to the pulling direction accumulating under the specimen. This fiber accumulation caused significantly higher pulling forces during the experiments. Another reason for outliers was a damage in textile occurring while fixing the specimen on the sled.

The friction force for each repetition was evaluated from the point, the sled started to move until a displacement of 10 mm. A mean value and scatter were calculated for all force values during the movement of the sled. Afterwards a total mean value and scatter was derived from all repetitions of one configuration. These total mean values were used to calculate the friction coefficient according to Eq. (2-1).

(a)

(b)

(c)

(d)

(e)
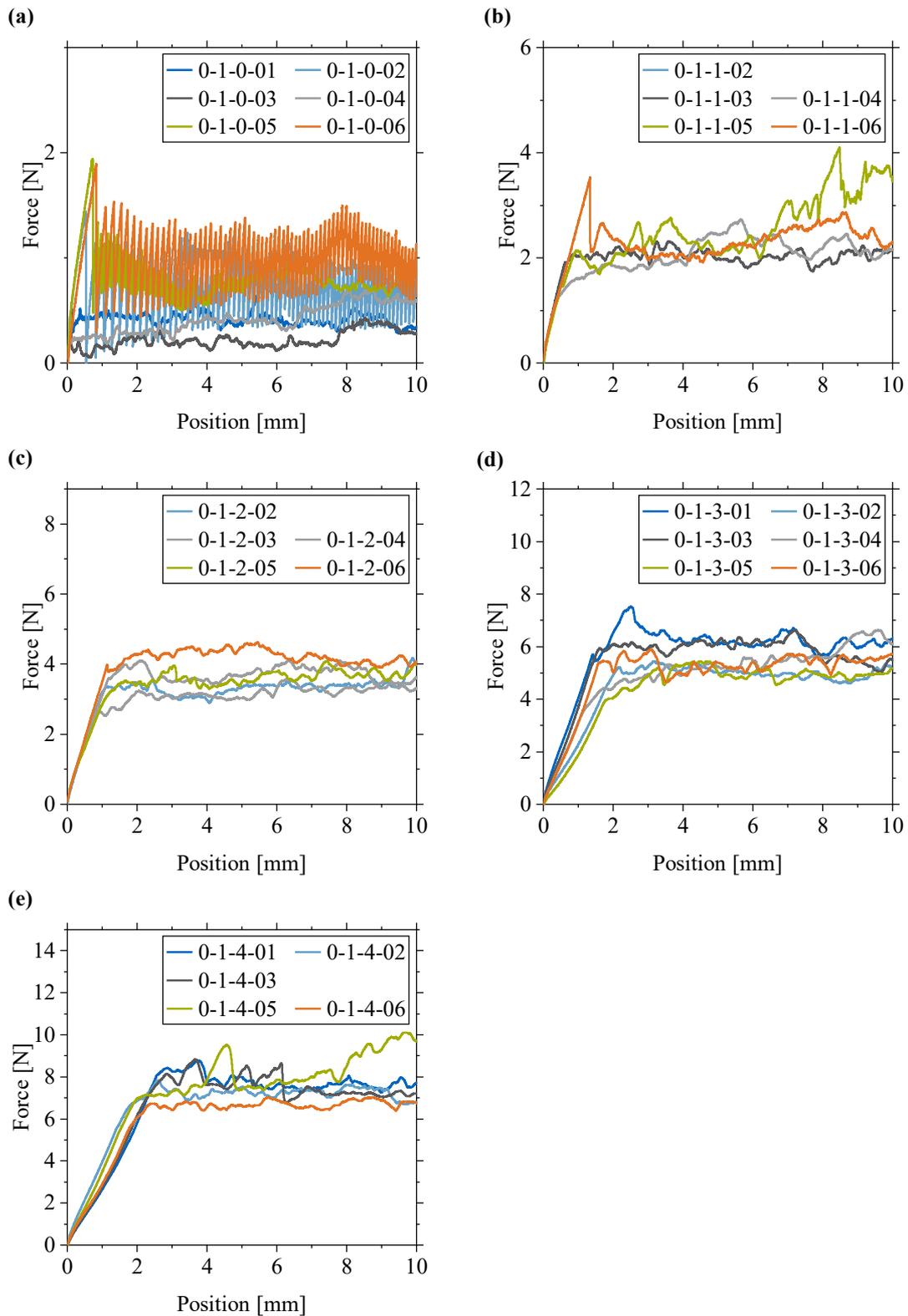
Fig. A-10: **Results of the friction characterization with 0° orientation and 1 mm/min speed: (a) zero additional weights; (b) one additional weight; (c) two additional weights; (d) three additional weights; (e) four additional weights.**

(a)

(b)

(c)

(d)

(e)
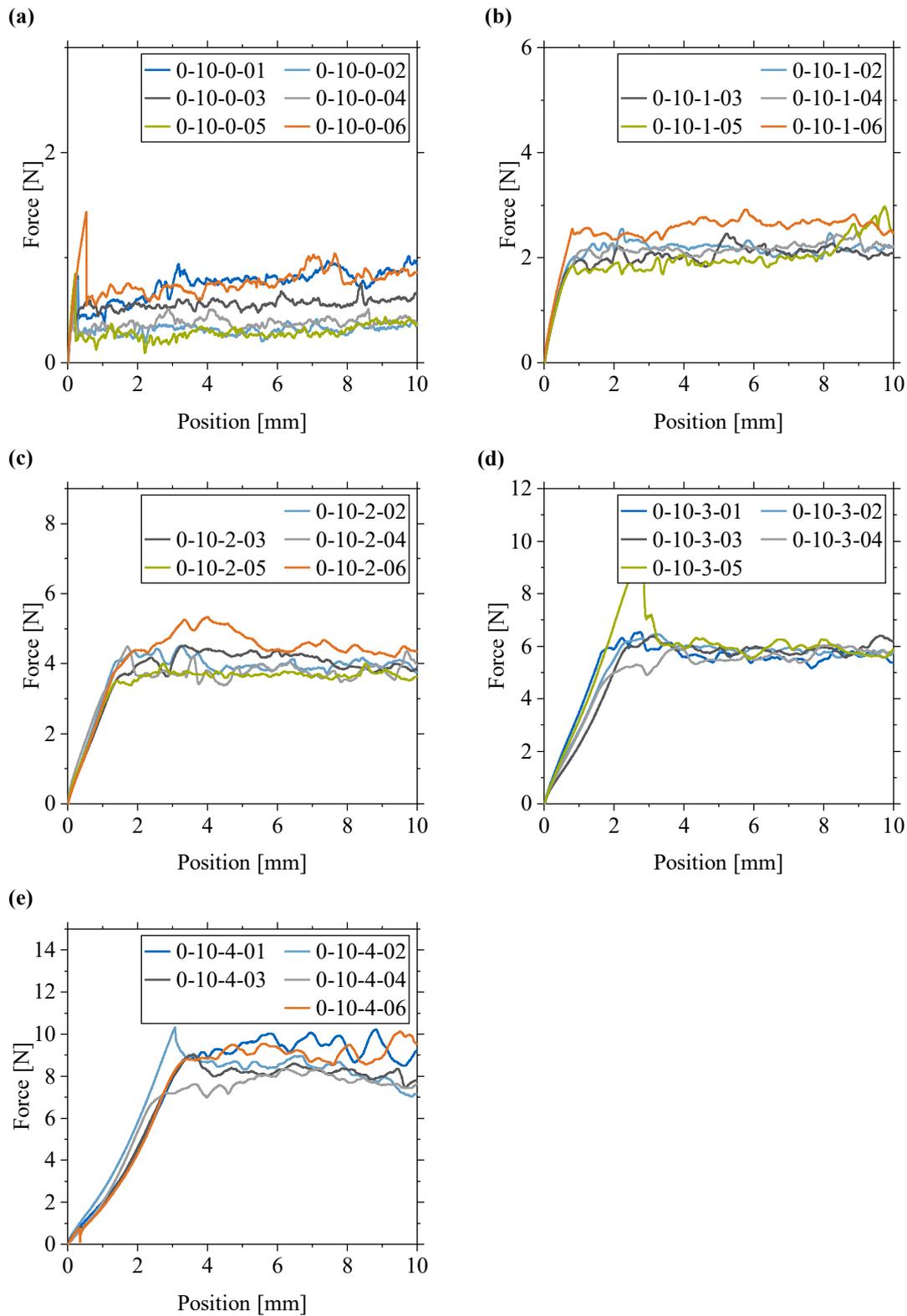
Fig. A-11:   **Results of the friction characterization with 0° orientation and 10 mm/min speed: (a) zero additional weights; (b) one additional weight; (c) two additional weights; (d) three additional weights; (e) four additional weights.**
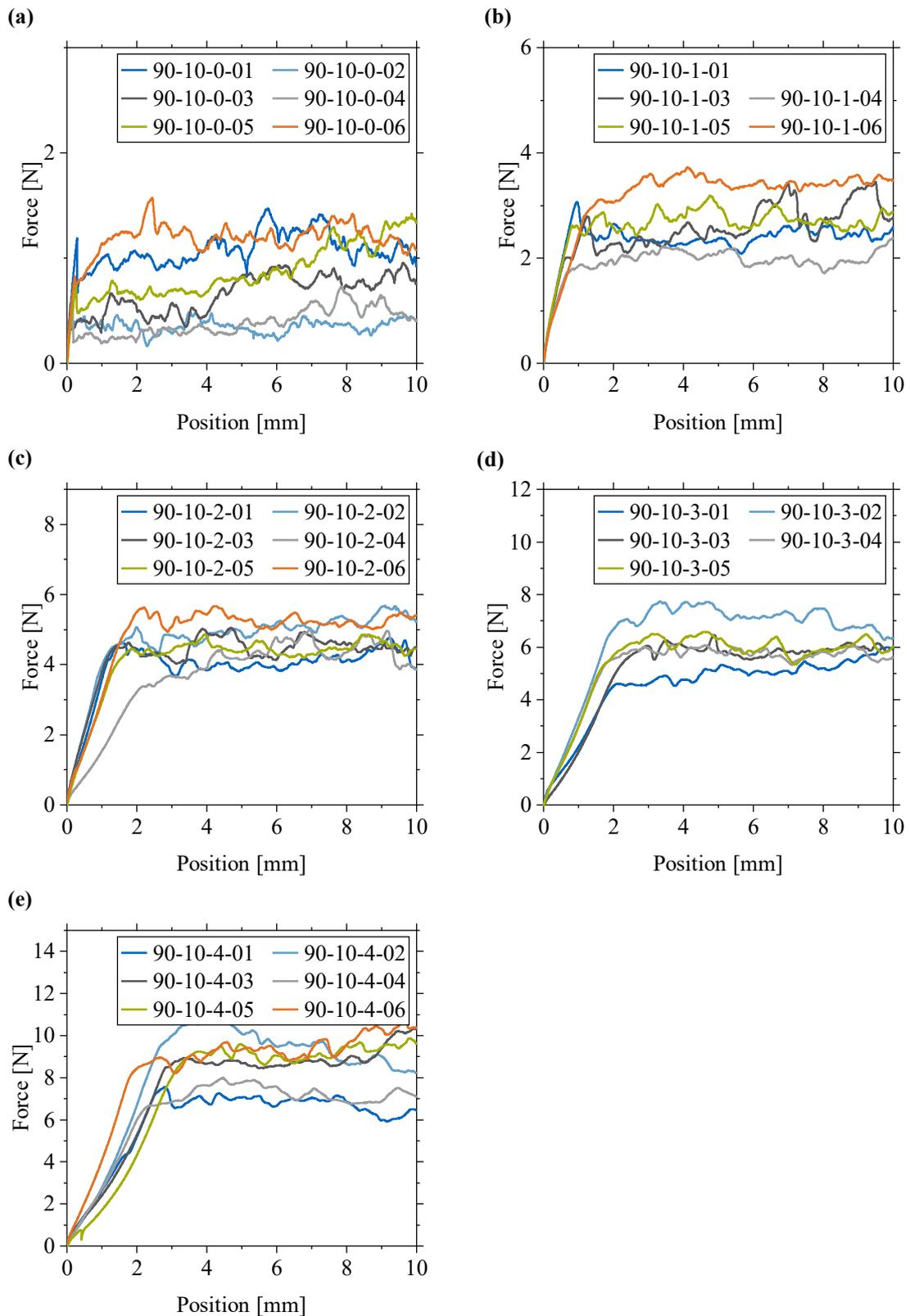
Fig. A-12:   Results of the friction characterization with 90° orientation and 10 mm/min speed:
(a) zero additional weights; (b) one additional weight; (c) two additional weights;
(d) three additional weights; (e) four additional weights.

B Publications

Scientific journal papers

[P1]   Bublitz D, Colin D, Drechsler K. Implementation of a viscoelastic material model to predict the compaction response of dry carbon fiber preforms. Composites Part A: Applied Science and Manufacturing 2021;42(4):106718.

[P2]   Etchegaray Bello M, Engelhardt R, Bublitz D, Drechsler K. Lab-scale experimental analysis of the cyclic compaction-recovery characteristics of uncured thermoset prepreg. Advanced Manufacturing: Polymer and Composites Science 2022

[P3]   Bublitz D, Thalhamer A, Schwöller J, Faron D, Colin D, Drechsler K. Chaining of Compaction with Flow Simulations to Predict the Filling Behavior in Resin Transfer Molding Processes. Materials Science Forum 2022; Volume 1060 MSF, 121 – 126

[P4]   Matschinski A, Bublitz D, Ihring T, Chen C, Grandl S, Schneider K, Pearce G, Drechsler K. Optimization of Continuous Fiber Path Planning for an Additively Manufactured Open-Hole Specimen. Materials Science Forum 2022; Volume 1060 MSF, 127 - 132

Confereneces

[C1]   Bublitz D, Angstl M, Colin D, Drechsler K. Implementation of a viscoelastic material model to predict the compaction behavior of dry carbon fiber preforms. in 30th SICOMP Conference - Manufacturing and Design of Composites, Trollhättan, Sweden, 2021.

[C2]   Bublitz D, Vollmer M, Nusser F. A novel method for the evaluation of compression RTM process simulations. ESI Forum in Germany 2019, Berlin, Germany, 2019

[C3]   Bublitz D, Angstl M, Colin D, Drechsler K. A novel method for the characterization of out-of-plane shear stiffness for dry carbon fiber preforms. in SAMPE Europe Conference 2021, Baden/Zürich, Switzerland, 2021.

[C4]   Vollmer M, Nusser F, Bublitz D, Baumann H, Graßl L, Zaremba S, Drechsler K. Increasing process robustness of the compression resin transfer molding process by reducing edge race-tracking. in SAMPE Europe Conference 2021, Baden/Zürich, Switzerland, 2021.

[C5]   Bublitz D, Rahman M, Schwöller J, Geschwandtner V, Drechsler K. Towards a three-dimensional compaction model for non-planar geometries. in SAMPE Europe Conference 2022, Hamburg, Germany, 2022.

[C6]   Steinhardt M, Böckl B, Denk A, Techmer D, Bublitz D, Drechsler K. Development of an experimental setup to determine the permeability of a single tow. in ECCM 20, Lausanne, Switzerland, 2022

[C7]   Seidel A, Khudiakova A, Bublitz D, Drechsler K. Numerical Simulation of Microscale Crack Propagation in Glass-Epoxy Composites Using Discrete Fibres, Matrix and Inter face. in ECCM 20, Lausanne, Switzerland, 2022

[C8]   Schauer C, Ongaki B, Bublitz D, Drechsler K. Influence of the Binder on Compaction, Shear and Friction for Carbon Fiber Preforms in the RTM-Process. in CAMX 2022, Anaheim, California USA, 2022

C Supervised student theses

The following student theses were written under my supervision during my employment at the TUM Chair of Carbon Composites:

[S1]   Weis P. "Entwicklung einer Auslegungsmethodik für Faserverbundquerblattfedern mit Radführungseigenschaften", Master's Thesis in cooperation with Forward Engineering GmbH, Chair of Carbon Composites, TUM, 2018.

[S2]   Schletterer M. " Implementierung eines Materialmodells für die Kompaktierung von Preforms im RTM-Prozess für Luftfahrtanwendungen", Bachelor's Thesis, Chair of Carbon Composites, TUM, 2018.

[S3]   Angstl M. "Modellierung der Kompaktierung von Preforms im RTM-Prozess für die Anwendung in der Luftfahrtindustrie", Bachelor's Thesis, Chair of Carbon Composites, TUM, 2018.

[S4]   Eberhardt P. "Calibration of a hyper viscoelastic material model for the compaction behaviour of preimpregnated carbon fibres", Bachelor's Thesis, Chair of Carbon Composites, TUM, 2018.

[S5]   Ordóñez DB. "Porosity Study of Carbon-Epoxy Prepreg Laminates through Materialography and X-ray Microtomography", Term project, Chair of Carbon Composites, TUM, 2019.

[S6]   Li S. "Entwicklung eines Werkzeugdesignprozesses für Hochtemperatur RTM-Verfahren in der Luftfahrt", Term project, Chair of Carbon Composites, TUM, 2018.

[S7]   Nusser F. "Simulative Comparison Study of Filling Behavior during RTM and CRTM Process at Occurring Race Tracking: Development of the Study Approach, Data Basis and Evaluation Method", Master's Thesis, Chair of Carbon Composites, TUM, 2019.

[S8]   Thalhamer A. "Virtual modelling of the filling behavior in the RTM-process for the manufacturing of jet engine components", Master's Thesis, Chair of Carbon Composites, TUM, 2019.

[S9]   Rahman M. "Viscoelastic Material Modeling and FEA of Compaction Behavior of Carbon Fiber Pre-forms during the RTM Process", Master's Thesis, Chair of Carbon Composites, TUM, 2019.

[S10]   Angstl M. " Experimentelle Charakterisierung des Kompaktierungsverhaltens von trockenen Kohlenstofffasergeweben ", Term project, Chair of Carbon Composites, TUM, 2019.

[S11]   Schletterer M. "Materialcharakterisierung von Silikon zur Weiterentwicklung eines Finite Elemente Mo-dells für einen Fiber Patch Placement Greifer", Term project in cooperation with Cevotec GmbH, Chair of Carbon Composites, TUM, 2020.

[S12]   Schwöller J. "Simulation of the Compaction Behavior of Carbon Fiber Preforms during the RTM Process", Master's Thesis, Chair of Carbon Composites, TUM, 2020.

[S13]   Faron D. "Virtual Development of an RTM Filling Strategy and Coupling of Compaction and Filling Simulations for the Manufacturing of Jet Engine Components", Term project, Chair of Carbon Composites, TUM, 2020.

[S14]   Schletterer M. "Entwicklung einer neuartigen Methode zur Messung des Schubs in Carbonfasergeweben", Master's Thesis, Chair of Carbon Composites, TUM, 2021.

[S15]   Geschwandtner V. "Charakterisierung der Reibwerte von Carbonfaserpreforms für die Verwendung in Prozesssimulationen", Bachelor's Thesis, Chair of Carbon Composites, TUM, 2021.

[S16]   Kaustubh. "Development of a computational efficient model for the simulation of the compaction of carbon fiber preforms", Term project, Chair of Carbon Composites, TUM, 2021.

[S17]   Varsha Kannan P. "Viscoelastic Material Modeling and FEA of Compaction Behavior of Carbon Fiber Pre-forms during the RTM Process", Master's Thesis, Chair of Carbon Composites, TUM, 2022.

Parts of the above listed theses contributed to the underlying doctoral dissertation, as indicated in the text.